AD-A207 018 Approved UMENTATION PAGE No. 0704-0188 1a. REPORT SECURITY CLASSIFICATION 16. RESTRICTIVE Δ **Unclassified** 2a. SECURITY CLASSIFICATION AUTHORITY 3. DISTRIBUTION/AVAILABILITY OF REPORT Unlimited Approved for public release; 2b. DECLASSIFICATION / DOWNGRADING SCHEDULE distribution unlimits. 5. MONITORING ORGANIZATION REPORT NUMBER(5)* 4. PERFORMING ORGANIZATION REPORT NUMBER(S) AFOSR-TR. 89-047 7a. NAME OF MONITORING ORGANIZATION 69. NAME OF PERFORMING ORGANIZATION 6b. OFFICE SYMBOL (If applicable) Carnegie Mellon University Air Force Office of Scientific Research 6c. ADDRESS (City, State, and ZIP Code) 7b. ADDRESS (City, State, and ZIP Code) Pittsburgh, PA 15213-3890 Bolling Air Force Base, Washington, DC 20332 SULLDEN 8a. NAME OF FUNDING / SPONSORING 8b. OFFICE SYMBOL 9. PROCUREMENT INSTRUMENT IDENTIFICATION NUMBER **ORGANIZATION** (If applicable) AFOSR-84-0341 **AFOSR** Sc. ADDRESS (City, State, and ZIP Code) 10. SOURCE OF FUNDING NUMBERS Bolling Air Force Base, Washington, DC 20332 WORK UNIT ACCESSION NO. PROGRAM PROJECT TASK ELEMENT NO. 11. TITLE (Include Security Classification) High Density Ion Implanted Contiguous Disk Bubble Technology (Unclassified) 12. PERSONAL AUTHOR(S) M. H. Kryder, M. Alex, A. Cowen, D. Greve, A. Guzman, K. Nitzberg, M. Ramesh, P. Rasky 13a. TYPE OF REPORT 13b. TIME COVERED 14. DATE OF REPORT (Year, Month, Day) 15. PAGE COUNT Final Scientific FROM 9/30/84 TO9/29/88 1989 March 31 434 16. SUPPLEMENTARY NOTATION 18. SUBJECT TERMS (Continue on reverse if necessary and identify by block number) COSATI CODES Bubble Memory, Ion Implantation, Garnet, Silicon-on-FIELD GROUP SUB-GROUP Insulator, Silicon-on-Garnet ABSTRACT (Continue on reverse if necessary and identify by block number) The main thrust of research carried out under this program was to develop high density ionimplanted contiguous-disk bubble memory devices. These devices offer order of magnitude higher bit density than presently manufactured bubble memory devices for a given lithographic resolution. In one phase of the research, a computer simulator was constructed and used to model the operation of ion-implanted contiquous-disk bubble devices. Input parameters for the simulator include the geometry of the implanted patterns, magnetic characteristics of the bubble film, implanted layer thickness, conductor geometry, amplitude and phase of currents in conductors, and the frequency and amplitude of the drive field. The fields acting upon the bubble include those from the conductors, implanted/unimplanted boundaries and charged walls. Using the model, the operation of various gates for ion-implanted devices was analyzed, including a trapping transfer gate and a dual conductor block replicate gate. A novel true-20. DISTRIBUTION / AVAILABILITY OF ABSTRACT 21. ABSTRACT SECURITY CLASSIFICATION **☑** UNCLASSIFIED/UNLIMITED ☐ SAME AS RPT. ☐ DTIC USERS Unclassified 22b TELEPHONE (Include Area Code) 22c. OFFICE SYMBOL (202) 767-4931 22a. NAME OF RESPONSIBLE INDIVIDUAL New **DD Form 1473, JUN 86** Previous editions are obsolete. SECURITY CLASSIFICATION OF THIS PAGE

Unclassified

Block #19 Continued; -

swap gate for ion-implanted bubble devices was also devised and simulated. The simulated bias margins of both propagation structures and gates were found to correspond well with experimental measurements.

In a second phase of the research, propagation structures for ion-implanted bubble devices were studied to determine optimal track designs in both minor and major loop propagation structures. It was found that diamond shaped propagation structures performed best and had the widest bias field margins. A special track design for a non-rectangular major loop was also studied and design criteria for it were specified. It was found that to achieve isotropic propagation margins it is necessary to not only utilize garnet materials with nearly isotropic magnetostriction, but also the proper ion implantation dose. It is believed that the reason the isotropy of propagation depends on the ion implantation dose is that to achieve true isotropy, a small magnetostrictive anisotropy must be tuned to cancel the magnetocrystalline anisotropy. This can only be achieved for a given range of stress induced by the ion implantation.

To improve the performance of the ion-implanted contiguous-disk bubble devices and make it possible to perform logical functions on the memory chip, research was carried out on the design, fabrication and testing of magnetic bubble logic gates. Gates were designed to perform Control, And, Or and Exclusive-Or logical functions, utilizing both bubbles that deflect from a field gradient and also bubbles that do not deflect from the gradient. These logic gates were fabricated utilizing dual-conductor, perforated-sheet, current-access bubble technology. The gates were tested while in operation at a 100 kHz data rate using a high-speed magneto-optic camera system to observe the magnetic bubble domains, optically. Bias field operating margins of 6%, 11% and 3% of the nominal bias field were obtained for the Control, And/Or, and Exclusive-Or gates, respectively, with drive currents of 2 mA/micrometer in the bottom conductor sheet and 3.4 mA/micrometer in the top conductor sheet.

To make possible higher frequency operation and to place more detectors on a bubble chip, magnetodiode bubble detectors were also investigated. To build these detectors, we developed silicon-on-garnet technology. The current-voltage characteristics of silicon magnetodiodes are sensitive to magnetic fields, and we showed that the devices could be integrated with ion-implanted contiguous-disk bubble propagation patterns to construct novel selfaligned magnetic bubble sensors. The results of magnetic field calculations appropriate to the design and placement of bubble domain sensors showed that diode base widths comparable to the bubble domain diameter are optimal. Work on the laser annealed polysilicon-on-garnet technology has resulted in MOSFET's which have channel electron mobilities in the 100 to 200 cm²/V.sec range. Gate breakdown voltages for this type of FET are 3 to 4 volts. MOSFET's fabricated using a low temperature process onto bubble substrates coated with plasma-deposited SiO2 have higher breakdown voltages which exceed 20 V, but channel electron mobilities which are lower than for the laser annealed devices.

Individual reports describing each of the above areas are contained in this final report.

CARNEGIE MELLON

Department of Electrical and Computer Engineering

HIGH DENSITY ION IMPLANTED CONTIGUOUS DISK BUBBLE TECHNOLOGY

FINAL REPORT

September 30, 1984 - September 29, 1988

APOSR- 18- 59-4476

Carnegie Mellon 089

HIGH DENSITY ION IMPLANTED CONTIGUOUS DISK BUBBLE TECHNOLOGY

FINAL REPORT

September 30, 1984 - September 29, 1988

approved for public release: distribution unlimited.

AIR PORCE OFFICE OF SCIENTIFIC RESEARCH (AFSC)
NOTICE OF TRANSCIONAL TO DTIC
This becomes to not not some reviewed and is
againsted for probabilities as they AFR 190-12.
Distribution is inscribed.
MATTHIES I RETIFIER
Chief, Technical Information Division



TABLE OF CONTENTS

			Section	Pages
Section	1:	Characterization of Silicon and Silicon on Garnet Magnetodiodes with Applications to the Detection of Magnetic Bubble Domains in an Ion-Implanted Contiguous-Disk Memory	Pages	1-88
		Paul H. L. Rasky		
Section	2:	Simulation, Fabrication, and Testing of Logic Gates Designed for Deflecting and Non- Deflecting Bubbles	Pages	1-65
		Allen Bruce Cowen		
Section	3:	Propagation in One Micron Ion-Implanted Contiguous Disk Bubble Memory Devices	Pages	1-42
		Kathy R. Nitzberg		
Section	4 :	Simulation of Gates for Ion-Implanted Magnetic Bubble Devices	Pages	1-196
		Michael Alex		

Characterization of silicon and silicon on garnet magnetodiodes with applications to the detection of magnetic bubble domains in an ion-implanted contiguous-disk memory

Final Report

Paul H.L. Rasky

Department of Electrical and Computer Engineering Carnegie Mellon University Pittsburgh, PA. 15213

> Advisors: Prof. David W. Greve Prof. Mark H. Kryder

> > November 1988

Acknowledgements

Our magnetic bubble domain stretchers were in part evaluated using a number of computer simulation programs written by J. C. Wu. D. N. Shenton, Z. Cendes, A. J. Butler and B. Shyamkumar provided code for and assisted the authors with the two dimensional finite element simulations reported in this document. Magnetic bubble substrates were grown and/or provided by C. S. Krafft, R. O. Campbell, B. Warren, M. Ramesh, and S. Santhanam. The plasma silicon nitride layers used in some of our device structures were deposited at Yale University by T. Tamagawa. The laser processing used in some of our processes was carried out at the Westinghouse Research and Development Center (in Pittsburgh) with the assistance of P. Rai-Choudhury, S. Dutta, P. McMullin, P. Palaschak, and B. Cifone. The masks we used in a number of processes were fabricated at the National Nanofabrication Facility at Cornell University with the assistance of B. Whitehead, S. Burgess, D. Costello, J. Comeau, R. Tiberio, G. Galvin and E. Wolf. Some of the ion implants used in our work were provided by A. Guzman, J. Tabacchi, and D. Junker. C. Bowman, R. Harris, S. Santhanam, R. S. Wilson, J. Brown, and other members of the clean room staff are acknowledged for the technical assistance they provide throughout the project. D.-L. Chen, M. K. Hatalis, B.-C. Hseih, J. Pickering, and P. A. Potyraj all provided assistance with processing and equipment maintenance. Moreover, they, along with T. Y. Chou, M. Racanelli and H. T. Han, provided countless hours of intriguing discussion on models and modeling. The TEM data presented in this report is in large part the work of A. Zeltser, in conjunction with D. E. Laughlin. Discussions with A. A. Thiele, P. Asselin, J. C. Wu, M. Alex, R. Ramesh, W. Eppler, S. Jo, R. Smith, and H.-P. D. Shieh on magnetics proved helpful on many occasions. B. T. Smith, B. Barris and M. Hess provided secretarial services at various points during the project. Finally, we wish to acknowledge F. Bruno, J. Schubert, D. Delotti, and B. E. Smith of the ECE machine shop for providing support services on what must have felt like a day-to-day basis.

Table of Contents

1.	Introduction	1
	1.1 Magnetic bubbles: background and domain propagation	1
	1.2 The architecture of bubble memories	3
	1.3 Magnetic bubble detectors	4
	1.4 References	10
2.	Magnetic field calculations for the design and placement of bubble domain	12
	sensors.	
	2.1 Introduction	12
	2.2 Design of magnetic bubble domain sensors	12
	2.3 Design of magnetic bubble domain stretchers	14
	2.4 Simulation results for the differential magnetodiode bubble sensor: fringing fields	18
	2.5 References	24
3.	Fabrication of silicon on garnet devices	25
	3.1 Introduction	25
	3.2 Fabrication of silicon on garnet magnetodiodes	25
	3.3 Structural characteristics of silicon on garnet devices	29
	3.4 Summary	38
	3.5 References	39
4.	The effects of thermal processing on magnetic bubble films	40
	4.1 Introduction	40
	4.1.1 Static properties of magnetic bubbles	40
	4.1.2 Dynamic properties of magnetic bubbles	42
	4.1.3 Temperature dependence of bubble film parameters	42
	4.2 Characterization of magnetic bubble films	43
	4.3 Laser annealed devices with a single layer spacer	44
	4.3.1 Process	44
	4.3.2 Results	45
	4.4 Laser annealed devices with a double layer spacer	46
	4.4.1 Process	46
	4.4.2 Results for a 1 micron bubble film family	47
	4.4.3 Conclusions for the 1 micron bubble film family	47
	4.4.4 Results for a 2 micron bubble film family	47
	4.5 Low temperature devices with a single layer spacer	51
	4.5.1 Process	51
	4.5.2 Results	53
	4.6 Summary 4.7 References	55 56
_		
5.	Theory and characterization of silicon magnetodiodes	58
	5.1 Introduction	58
	5.1.1 Positive resistance devices	58
	5.1.2 Negative resistance devices	60
	5.2 Magnetodiodes on silicon substrates	62
	5.2.1 Device fabrication	62
	5.2.2 Results	63

	5.3 Magnetodiodes on bubble substrates	66
	5.3.1 Device fabrication	66
	5.3.2 Results	66
	5.4 Summary	69
	5.5 References	70
в.	Silicon on Garnet MOSFET's	72
	6.1 Introduction	72
	6.2 Laser annealed MOSFET's with a single layer spacer	72
	6.2.1 Device fabrication	72
	6.2.2 Electrical Characteristics	73
	6.3 Laser annealed MOSFET's with a double layer spacer	73
	6.3.1 Device fabrication	74
	6.3.2 Electrical Characteristics	76
	6.3.3 Conclusions	79
	6.4 Low temperature MOSFET's with a single layer spacer	80
	6.4.1 Device fabrication	81
	6.4.2 Electrical characteristics	82
	6.5 Summary	83
	6.6 References	87
7.	Conclusions	22

List of Figures

Figure	1-1:	Bubble domains.	1
Figure	1-2:	Stripe domains.	2
Figure	1-3:	Ion-Implanted contiguous-disk propagation pattern with charged walls.	2
Figure	1-4:	Bubble propagation along ion-implanted tracks.	3
Figure	1-5:	Major/minor loop organization of a magnetic bubble memory chip.	4
Figure	1-6:	Channel-bar detector using straight-bar Permalloy elements. The two	5
		bars serve as detector and reference detector, but both respond to the	
		bubble, increasing the figure of merit.	
Figure	1-7:	Magnetoresistive sensing.	5
Figure	1-8:	Silicon on garnet magnetodiode cross section.	6
Figure	1-9:	I(V) characteristic for a magnetodiode.	7
Figure	1-10:	Differential magnetodiode bubble sensor.	8
Figure		Circuit diagram for the design of figure 1-10.	9
Figure		Theory of operation for the design of figure 1-10.	9
Figure		Geometry assumed in equations (2.1) and (2.2).	13
Figure	2-2:	Plots of H _x as a function of x and z.	14
Figure	2 -3:	Average value of H _x as a function of z and diode width w.	15
Figure:	2-4:	Design for a differential magnetodiode bubble sensor. Field values are	16
		given in Oersteds (oe), and we note that this design was not chosen for	
		fabrication.	
Figure:	2-5:	Design for a differential magnetodiode bubble sensor. Field values are	17
		given in Oersteds (oe).	
Figure:	2-6:	(A) Vector plot of B(H) resulting from an energized hairpin stretcher.	19
		The effect of the magnetic bubble film is not included in this figure; we	
		only indicate its position and the position of a bubble domain. The	
		silicon magnetodiodes and the Al-Cu conductors are assumed to be non-	
		magnetic materials. (B) Magnified plot of B(H) over the right	
		magnetodiode.	
Figure:		Scale drawing of an idealized silicon on garnet cross section.	20
Figure	2-8:	(A) Scale drawing of the structure for the "no bubble" simulation case -	21
		see figure 2-7 for dimensions. (B) Plot of B for the right magnetodiode.	
Figure	2-9:	(A) Scale drawing of the structure for the "bubble" simulation case -	22
		see figure 2-7 for dimensions. (B) Plot of B for the right magnetodiode.	
Figure	2 -10:	X ·	23
		region for the left and right magnetodiodes for the simulation cases of	
		figures 2-8 and 2-9	
Figure	2-11:	Direction and average value of B _v acting over the width of the n- base	23
		region for the left and right magnetodiodes for the simulation cases of	
		figures 2-8 and 2-9	
Figure	3-1:	Structure after laser recrystallization.	26
Figure	3-2:	Selective doping of the magnetodiode structure.	27
Figure	3-3:	Structure after a 30min. 850°C wet oxidation.	27
Figure		Structure after the propagation implant.	28
Figure		Structure after contact windows are opened.	28
_		•	

Figure 3-6: Figure 3-7:	Final structure for the differential magnetodiode bubble sensor. Bright field photograph of a (Bi _{0.4} Dy _{0.7} Lu _{1.2} Sm _{0.2} Y _{0.5})[Fe _{4.45} Ga _{0.55}]O ₁₂ bubble film (AH45) after processing that was taken with transmitted light. The black areas are decomposed bubble film regions which were covered with an insufficient amount of LPCVD SiO ₂ prior to the LPCVD Si ₃ N ₄ and polysilicon	29 30
Figure 3-8:	depositions. (A) Bright field reflected photograph of a sample (092887-2 loc#1) with the structure shown in figure 3-1 after a 1hr. 625°C N ₂ anneal. (B) SEM micrograph of a sample (092887-2 loc#3) similar to the one shown in (A) after a 1.0 min. etch in 1 part of [1 part 0.15 M K ₂ Cr ₂ O ₇ + 2	32
Figure 3-9:	parts 49% HF] and 1 part deionized water; this is a diluted Secco etch. (A) TEM micrograph of a silicon on garnet cross section with a single sputtered SiO_2 spacer layer. The process used to fabricate this structure on bubble wafer AT15 had five steps: (1) deposit 1μ m of spacer SiO_2 by sputtering at 700 W/20 mtorr Ar, (2) deposit 0.6μ m of polysilicon by LPCVD at 625° C/0.4 torr, (3) deposit 1μ m of cap SiO_2 by sputtering at 700 W/20 mtorr Ar, (4) laser recrystallization of the polysilicon layer at approximately 1415° C (substrate temperature = 350° C), and (5) Wet O_2 oxidation at 850° C for 50 min. (cap oxide from step 3 was removed after the recrystallization step.). We also point out that the samples we examined with $SiO_2 + Si_3N_4$ spacers had a fabrication process similar to that listed in section 4.4.1. (B) Selected area diffraction for one of the	33
Figure 3-10:	grains shown in part (A).	35
Figure 3-11:		36
Figure 3-12:	(A) SEM micrograph of bubble wafer AC44 after a wet silicon etch for island definition; a thin pattern S ₁ O ₂ remains on the silicon island. The process used to fabricate this structure is the same as the one described in figure 3-9 with the following exceptions: (1) 0.5 µm of polysilicon, (2) 200°C substrate temperature for laser anneal, and (3) 90 min. oxidation. (B) SEM micrograph of bubble wafer AC47 after the wet silicon island etch (step 7 in the text).	37
Figure 4-1: Figure 4-2:	Structure of a Bloch wall Stripe head (wall) velocity as a function of ΔH , where ΔH is an applied pulse field parallel to the bias field. H_d is the dynamic coercivity; H_c is the static coercivity, and μ_w is the domain wall velocity.	41 44

Figure 5-1:	Schematic representation of the possible regimes of high-level double-injection behavior in a structure with a small density of deep centers, starting with the semiconductor regime. The manner in which the low-level regimes merge into the high-level regimes is also shown schematically (the "junction drop" regime shows up distinctly only for lower temperatures or for wide band-gap materials, i.e., when E_g/kT is large enough). Depending on material parameters, some of these regimes	59
Figure 5-2:	may not appear. SOS magnetodiode structure. d = base length, w = base width, b =	59
	film thickness.	
Figure 5-3:	Drawing of a current filament in a $p+\pi n+$ device, where π stands for a lightly doped p-type base.	61
Figure 5-4:	Characteristic curve of a filamentary double-injection device.	61
Figure 5-5:	Energy-band diagram for a double-injection device with a deep-level impurity.	62
Figure 5-6:	(A) Current - voltage characteristic for a magnetodiode fabricated on a silicon substrate, both log and linear plots are given (MI and IF, respectively). (B) Failure mode for the device (020586 MDSL R1C2 after 14th) of part (A).	64
Figure 5-7:	(A) Diode forward current I_D (in amps) with an applied in-plane magnetic field; the field was swept between $+$ and $-$ 16kG. See part B of this figure for device orientation and sign conventions. The diode is $25\mu m$ wide and was fabricated on a silicon substrate. Otherwise, the structure is identical to that of figure 5-8. (B) Orientation of the magnetodiode (MD) during the measurements; the bottom interface is closest to the paddle.	65
Figure 5-8:	Silicon on garnet cross section	66
Figure 5-9:	I-V characteristic for a silicon on garnet magnetodiode; a plot of the diode resistance (VMD/IF) is also given. The composition of the bubble film is (Sm Tm Lu) ₃ [Fe Ga] ₅ O ₁₂ .	68
Figure 5-10:	* * * ==	68
Figure 5-11:	Al-Si short between the ohmic contacts of a magnetodiode (AF24 R1C4 MDSL 2-19-88/8:30P). The short appears as a narrow white streak. The composition of the bubble film is (Sm Tm Lu) ₃ [Fe Ga] ₅ O ₁₂ .	69
Figure 6-1:	Cross section of a silicon on garnet MOSFET with a sputtered SiO ₂	73
5	spacer layer. The spacer is $\sim 1 \mu m$ thick.	_
Figure 6-2:	Drain characteristics for a silicon on garnet MOSFET with a non-zero gate leakage current. See figure 6-1 for a cross section of this device (wafer L10A).	74
Figure 6-3:	Drain characteristics for a silicon on garnet MOSFET with a catastrophic gate leakage current. See figure 6-1 for a cross section of this device (wafer L10A).	75

Figure 6-4: Figure 6-5:	Cross section of a silicon on garnet MOSFET with a double spacer. Drain characteristics for a device with the structure shown in figure 6-4; current is in μ A, and voltage is in volts. The SiO ₂ spacer layer is 0.41 μ m thick, and the Si ₃ N ₄ film is 0.85 μ m thick (devices with 0.24 μ m of Si ₃ N ₄ have similar drain characteristics). The composition of the magnetic bubble layer is Sm _x Tm _y Lu _{3-(x+y)} (Fe _{5-z} Ga _z)O ₁₂ . This MOSFET has a channel length/width ratio of 17μ m/35 μ m.	75 76
Figure 6-6:	(A) Zero-bias channel conductance (amps/volt) as a function of gate voltage (volts); a potential of 0.1 V (zero bias for practical purposes) is applied between the source and drain. The SiO ₂ spacer layer is 0.41 μ m thick and the Si ₃ N ₄ film is 0.24 μ m thick. This MOSFET has a length/width ratio of 17μ m/35 μ m. The composition of the magnetic bubble layer is Sm _x Tm _y Lu _{3-(x+y)} (Fe _{5-z} Ga _z)O ₁₂ . See figure 6-4 for the relevant cross section. (B) First order model of a silicon-on-garnet MOSFET with top (intended) and bottom (unintended) conduction channels.	78
Figure 6-7:	Plots of the gate leakage current I _g (in amps) vs. the gate voltage V _g (in volts) with the drain and source at ground potential (V _{ds} = 0 V) for three sets of spacers: (1) the solid plot is for a MOSFET fabricated on a [Sm _{1.2} Tm _{0.1} Lu _{1.7}](Fe _{5-z} Ga _z)O ₁₂ bubble substrate coated with a 1 μ m thick SiO ₂ spacer (wafer AC44); (2) the dashed plot is for a MOSFET fabricated on a [Sm _x Tm _y Lu _{3-(x+y)}](Fe _{5-z} Ga _z)O ₁₂ bubble substrate coated first with 0.41 μ of SiO ₂ and next with 0.24 μ m of Si ₃ N ₄ (wafer AF24), and (3) the dotted plot is for a MOSFET fabricated on a [Sm _x Tm _y Lu _{3-(x+y)}](Fe _{5-z} Ga _z)O ₁₂ bubble substrate coated first with 0.41 μ of SiO ₂ and next with 0.85 μ m of Si ₃ N ₄ (wafer AF25). The channel length/width ratios for these three cases are:(1) 12.5 μ m/25 μ m, (2)	79
Figure 6-8:	$17\mu\text{m}/35\mu\text{m}$, and (3) $17\mu\text{m}/35\mu\text{m}$. A plot of the gate leakage current I _g (in amps) vs. the gate voltage V _g (in volts) with the drain and source at ground potential (V _{ds} = 0 V) for a MOSFET on a silicon substrate coated with 0.41μ of SiO ₂ (first layer on the silicon substrate) and $0.24\mu\text{m}$ of Si ₃ N ₄ (second layer on the silicon substrate 020586-2). The channel length/width ratio of the MOSFET is $17\mu\text{m}/35\mu\text{m}$.	80
Figure 6-9:	Cross section of a low temperature silicon on garnet MOSFET with a single SiO ₂ spacer.	81
Figure 6-10:	Drain characteristics for a low temperature silicon on garnet MOSFET with the st. cture shown in figure 6-9 after hydrogen passivation. The SiO_2 spacer is $0.1\mu m$ thick, and the channel length/width ratio is	82
Figure 6-11:	7.9μ m/ 75μ m. (A) A plot of the drain current I_d (in μ A) vs. time (in seconds) for a low temperature silicon on garnet MOSFET before hydrogen passivation with the source at 0V, the gate at 15V, and drain at 10V.	84

The channel length/width ratio of this device is $7.9\mu m/75\mu m$, and we note that the composition of the bubble film is $[Bi_{0.4}Dy_{0.7}Sm_{0.2}Lu_{1.2}Y_{0.5}](Fe_{4.45}Ga_{0.55})O_{12}$. (B) Same as part (A) of this figure, but after hydrogen passivation.

Figure 6-12:

(A) A plot of the drain current I_d (in μ A) vs. time (in seconds) for a low temperature MOSFET fabricated on a silicon substrate coated with a 1μ m thick plasma SiO₂ spacer, before hydrogen passivation with the source at 0V, the gate at 15V, and drain at 10V. The channel length/width ratio of this device is 7.9μ m/75 μ m. (B) Same as part (A) of this figure, but after hydrogen passivation.

85

List of Tables

Table 4-1: Room magnetic temperature properties 45 of $(Sm_{0.35}Gd_{0.55}Tm_{1.2}Y_{0.9})[Fe_{4.61}Ga_{0.25}Al_{0.14}]O_{12}$ bubble film (#166) before and after a $1\mu m/700W/2hr/20$ mtorr/Ar sputtered SiO₀ deposition. Note, this deposition was done in two parts: 1hr for the top bubble film and 1hr for the bottom film. **Table 4-2:** Room temperature values of $4\pi M_g$ and l at four key points in our first 46 silicon on garnet process. We note that the composition of this particular bubble film (#198) is $(Sm_{0.3}Gd_{0.4}Tm_{0.73}Y_{1.57})[Fe_{4.6}Ga_{0.4}]O_{12}$ Room temperature magnetic properties of a 1µm bubble film (AH43) **Table 4-3:** 48 after key silicon on garnet process steps. Process steps are listed in the order in which they were performed. The composition of the bubble film is $(Bi_{0.4}Dy_{0.7}Lu_{1.2}Sm_{0.2}Y_{0.5})[Fe_{4.45}Ga_{0.55}]O_{12}$ Table 4-4: Room temperature magnetic properties of a 2µm bubble film (AP84) 50 after key silicon on garnet process steps. Process steps are listed in the order in which they were performed. The composition of the bubble film is $(Bi_{0.3}Dy_{1.0}Lu_{1.0}Sm_{0.2}Y_{0.5})[Fe_{4.36}Ga_{0.64}]O_{12}$ **Table 4-5:** Values of the static coercivity, dynamic coercivity, and domain wall **52** mobility for a $2\mu m$ (Bi_{0.3}Dy_{1.0}Lu_{1.0}Sm_{0.2}Y_{0.5})[Fe_{4.36}Ga_{0.64}]O₁₂ bubble film (AP100) before and after an 860°C LPCVD SiO₂ deposition. Values of the static coercivity, dynamic coercivity, and domain wall **Table 4-6:** 52 mobility for a $2\mu m$ (Bi_{0.3}Dy_{1.0}Lu_{1.0}Sm_{0.2}Y_{0.5})[Fe_{4.36}Ga_{0.64}]O₁₂ bubble film (AP102) before and after an 860° C O_2 anneal. Room temperature values of $4\pi M_s$, l, and K_u after the listed process Table 4-7: 54 steps for a $1\mu m \; (Bi_{0.4} Dy_{0.7} Lu_{1.2} Sm_{0.2} Y_{0.5}) [Fe_{4.45} Ga_{0.55}] O_{12} \; bubble film$ (AH68). Values of the static coercivity, dynamic coercivity, and domain wall Table 4-8: 54 temperature $(Bi_{0.4}Dy_{0.7}Lu_{1.2}Sm_{0.2}Y_{0.5})[Fe_{4.45}Ga_{0.55}]O_{12}$ bubble film (AH68) after

the listed steps.

Chapter 1

Introduction

The subject of this report is the merging of silicon and magnetic bubble devices; specifically, the detection of magnetic bubbles with silicon magnetodiodes. In this introduction, we will cover three main topics. First, we will give an overview of bubble physics and bubble memory. Next, we will consider the problem of magnetic bubble detection. We will then, in our third topic, describe the properties of the silicon magnetodiode that may make it a useful bubble sensor.

1.1 Magnetic bubbles: background and domain propagation

Magnetic bubbles are right circular cylinders of magnetization that exist in a thin film of appropriate composition. The magnetization in these cylinders is oriented perpendicular to the plane of the film, and we show this in figure 1-1. An applied magnetic field, also perpendicular

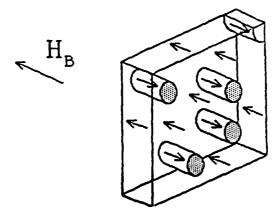


Figure 1-1: Bubble domains.

to the plane of the film, stablizes the domain size and position. The bubble domains will expand into stripe domains if this bias field is lowered below a critical value. Figure 1-2 shows an example c. stripe domains. A bubble domain will move within the film if it is exposed to a bias field gradient: the motion will be in the direction of decreasing magnetic field as the energy associated with the interaction of the magnetization and the applied magnetic field will be lowered for such a case. This field gradient can be created in a number of ways [1.1-1.4], and we will consider the scheme in which this gradient is created by a charged wall. A charged wall is a positive (negative) magnetic line charge that results from the convergence (divergence) of an in-

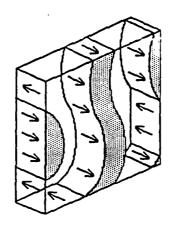


Figure 1-2: Stripe domains.

plane magnetization. The required in-plane magnetization is created by implanting hydrogen ions into the bubble film [1.5, 1.6], and it is caused to be convergent (divergent) at the boundaries between implanted and non-implanted regions through the action of a stress induced uniaxial anisotropy parallel to the boundaries [1.7] and an applied in-plane magnetic field. When the applied in-plane field rotates, it moves the charged walls around the ion-implanted contiguous-disk propagation pattern shown in figure 1-3. If a bubble is near a charged wall of the proper

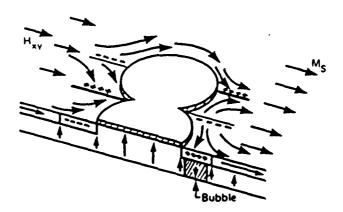


Figure 1-3: Ion-Implanted contiguous-disk propagation pattern with charged walls. sign (positive for the bubble shown in figure 1-3), it will be attracted to the charged wall, and the bubble will move with this wall if the wall is in motion. Recall that the top of the bubble shown in figure 1-3 is a negative magnetic charge. We illustrate this motion in figure 1-4, and we note that the bubbles actually propagate along the implanted/non-implanted boundary for about one third to one fourth of a cycle of the in-plane rotating field [1.8]. For the remainder of the cycle, the bubbles will stay in the pattern cusps if the negative charged wall is not overly strong.

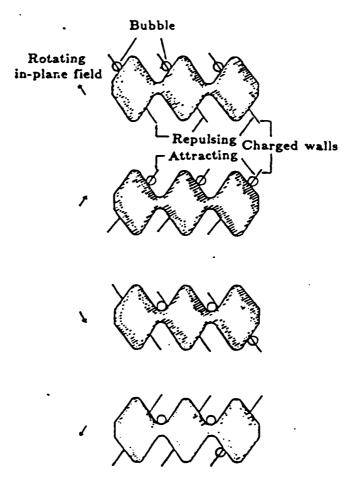


Figure 1-4: Bubble propagation along ion-implanted tracks.

1.2 The architecture of bubble memories

Since magnetic bubbles are stable in the presence of an applied bias field, it is not necessary for them to be in motion unless data is being written to or read from the bubble memory. A typical read/write bubble memory architecture is shown in figure 1-5 [1.9]. Information is written to the memory by the following scheme: a bit of binary information is input to a bubble nucleator [1.10], and this nucleator generates a bubble for one of the two logic levels, at most once per cycle of in-plane field. We will consider the case in which a bubble is generated for the logic 1 state - no bubble is generated for the logic 0 state. Once the data bit is written, it is transferred to the next bit position in the major (horizontal) loop, and the process then repeats itself until a bit of information is positioned over each of the minor (vertical) storage loops shown in figure 1-5. The transfer gates subsequently place this word of information in the minor storage loops. This word will propagate around these loops in a synchronous

fashion, and when it is necessary to output this word to another subsystem, it will be positioned at the topmost bit positions of the minor loops. The transfer gates will then place this word in the major loop for propagation to the bubble detector. The bubble detector checks the bit stream fed to it for the presence of bubbles, and when it finds bubbles, it will output a logic 1; if it does not sense a bubble, it will output a logic 0.

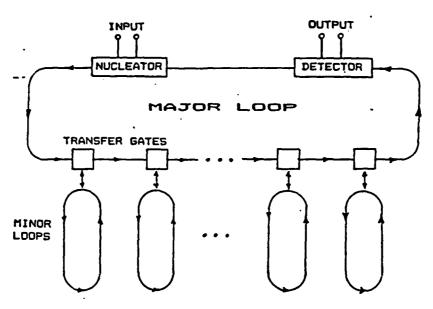


Figure 1-5: Major/minor loop organization of a magnetic bubble memory chip.

1.3 Magnetic bubble detectors

Magnetic bubble detectors based on the magnetooptic, magnetoresistive, and semiconductor Hall effect have been demonstrated [1.11]. The most common bubble detectors are the permalloy (21.5% Fe and 78.5% Ni) magnetoresistive sensors. Figure 1-6 shows an example of this type of sensor that has been integrated with an ion-implanted contiguous-disk propagation pattern. The two permalloy elements (the solid black bars) are connected in a differential fashion. When a bubble is at the mouth of the sensor, the Al-Cu stretcher (the cross hatched hairpin) is activated, and a magnetic field opposite to the bias field is established in the ion-implanted channel between the two sensor elements. The magnitude of this opposing field is large enough to lower the net field in the channel below that required for bubble stripe out; the bubble therefore expands into the channel, and some of its flux intercepts the magnetoresistive sensors. This fringing flux adds to the in-plane drive field on one of the permalloy elements and subtracts from the drive field on the other permalloy element. These field perturbations cause a change in the resistance of each sensor. The resistance changes are superimposed on the cyclic

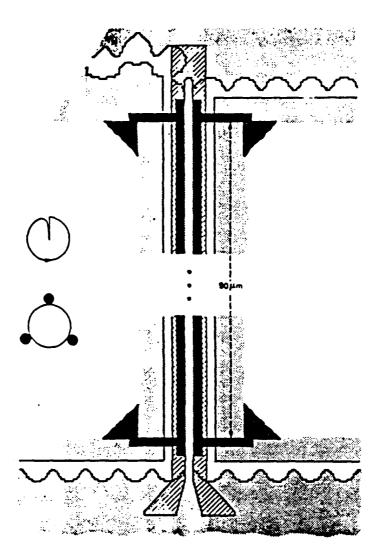


Figure 1-6: Channel-bar detector using straight-bar Permalloy elements. The two bars serve as detector and reference detector, but both respond to the bubble, increasing the figure of merit.

Ì

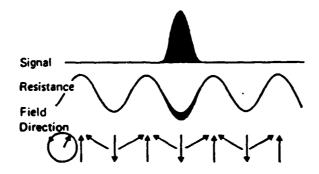


Figure 1-7: Magnetoresistive sensing.

change in resistance caused by the in-plane rotating field. Figure 1-7 shows this cyclic variation and the perturbation due to the presence of a stripe domain; here, we have shown the case when the perturbing flux lowers the resistance of the permalloy element. This change in resistance results from a change in the resistivity of the permalloy [1.12, 1.13]. We can increase the change in resistance by making the sensor longer, thinner, and narrower. Nelson et al. report a 3 mV output signal for the design of figure 1-6 with 2.5 mA driven into a 320 Ω magnetoresistive element.

A sensor output voltage of 3 mV is small, but most permalloy magnetoresistive senors give outputs similar to this value: Bobeck et al. report values in the 1-40 mV range [1.14]. Dealing with such small signals can be difficult, and we would therefore like to replace the magnetoresistive sensor with one of higher sensitivity. Silicon magnetodiodes, p+(n-)n+ diodes, have reported sensitivities in the 1-30 V/kgauss range [1.15, 1.16], and with such a device, it would be possible to achieve output signals in the 0.1 to 3.0 V range. Our past work shows that it is possible to fabricate silicon magnetodiodes on magnetic bubble substrates [1.17, 1.18]. Silicon on garnet MOSFET's are also possible [1.19], and these devices could be used to amplify the output of silicon on garnet magnetodiodes. With time, it might even be possible to fabricate single-chip silicon on garnet computers.

The structure of a silicon on garnet magnetodiode is shown in figure 1-8. Magnetodiodes

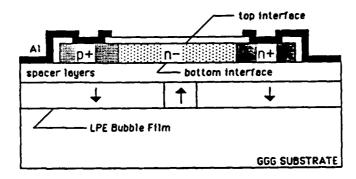


Figure 1-8: Silicon on garnet magnetodiode cross section.

have current - voltage characteristics that are dependent on the magnitude and direction of an applied magnetic field B. Figure 1-9 shows the type of characteristics that are seen when the applied magnetic field is in-plane and perpendicular to the diode current. The field induced current dependence is a consequence of the interfacial properties of the device. If the magnetic field deflects current carriers to the top interface, which is of high quality (low surface

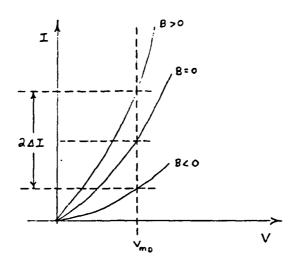


Figure 1-9: I(V) characteristic for a magnetodiode.

recombination velocity, s), they will recombine at a smaller rate than if the field deflects them to the bottom interface, which is of low quality (high surface recombination velocity, s). A smaller recombination rate will cause the concentration of electrons and holes in the n- base to increase if the diode is biased at constant voltage. This increase in carrier concentrations causes a higher diode current as the base conductivity has increased with respect to the B = 0 case.

We have attempted to integrate ion-implanted contiguous-disk propagation patterns for magnetic bubbles with silicon magnetodiodes, and figure 1-10 shows the structure we have been fabricating. The circuit diagram for this design is shown in figure 1-11. In this case, ΔI is the change in magnetodiode current brought about when magnetic fields are present in the n- base. If no fields are present, ΔI is zero, and the ammeter reads zero. The stretcher, stripe domain, and in-plane drive fields may each play a role in determining ΔI , but at this point, we will focus only on how the field from the stripe domain will alter the magnetodiode current. Assume that a magnetic bubble has striped out into the channel between the n- base regions. The flux from this stripe domain will intercept the magnetodiodes as shown in figure 1-12, and the Lorentz force (F = qv x B) will act on the currents I (Σ qv) as indicated. The left magnetodiode will then be operating along the B>0 curve shown in figure 1-9 while the right magnetodiode will be operating along the B < 0 curve. Both of these diodes are biased at the same constant voltage which in turn means that their currents can no longer be equal. The difference in their currents, $2\Delta I$, now forces a non-zero reading on the ammeter. The effect of the stretcher and in-plane drive fields can be taken into account by a similar analysis, and superposition can be applied to calculate the true ammeter reading. The ammeter readings are different for the bubble/no bubble cases even when the other fields are included.

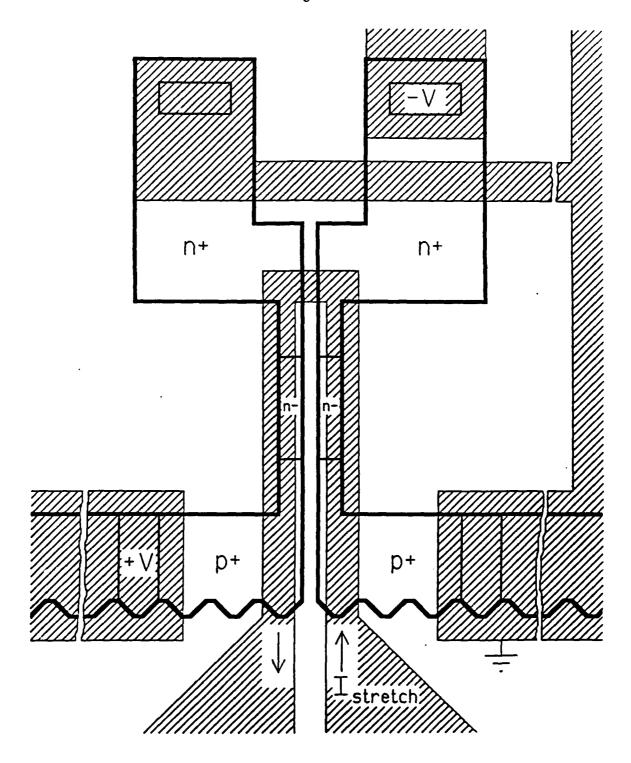


Figure 1-10: Differential magnetodiode bubble sensor.

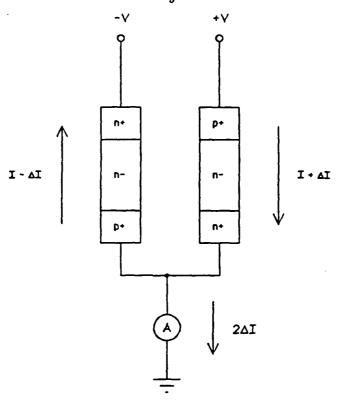


Figure 1-11: Circuit diagram for the design of figure 1-10.

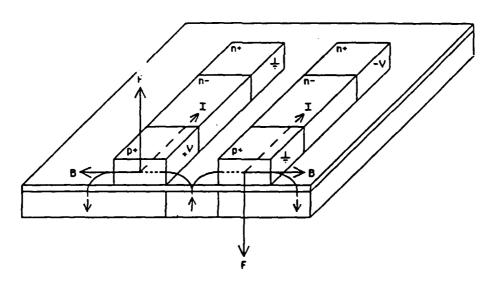


Figure 1-12: Theory of operation for the design of figure 1-10.

1.4 References

- [1.1] A. H. Bobeck and H. E. D. Scovil, "Magnetic Bubbles," Scientific American, Vol. 224, No. 6, June 1971, pp. 78-90.
- [1.2] A. J. Perneski, "Propagation of Cylindrical Magnetic Domains in Orthoferrites," IEEE Transactions on Magnetics, Vol. MAG-5, September, 1969, pp. 554-557.
- [1.3] R. Wolfe, J. C. North, W. A. Johnson, R. R. Spiwak, L. J. Varnerin, and R. F. Fischer, "Ion Implanted Patterns For Magnetic Bubble Propagation," Proceedings of the AIP 18th Annual Conference on Magnetism and Magnetic Materials, 1972, pp. 339-343.
- [1.4] A. H. Eschenfelder, "Magnetic Bubble Technology," Second Edition, Springer-Verlag, 1981, ch. 4 and 5.
- [1.5] Y. S. Lin, G. S. Almasi, and G. E. Keefe, "Contiguous-Disk Bubble Domain Devices," IEEE Transactions on Magnetics, Vol. MAG-13, No. 6, November, 1977, pp. 1744-1764.
- [1.6] J. C. North, R. Wolfe, and T. J. Nelson, "Applications Of Ion Implantation to Magnetic Bubble Devices," J. Vac. Sci. Technol., Vol. 15, No. 5, Sept./Oct., 1978, pp. 1675-1684.
- [1.7] Douglas A. Saunders, "Stress-induced Magnetic Anisotropies in Ion-implanted, Contiguous-disk, Magnetic Bubble Devices," Ph.D. Dissertation, Carnegie Mellon University, Pittsburgh, Pennsylvania, September, 1987, pp. 8-11 & 35-36.
- [1.8] Soonchul Jo, "Propagation in Submicron Ion Implanted Magnetic Bubble Computer Memory Devices," Ph.D. Dissertation, Carnegie Mellon University, Pittsburgh, Pennsylvania, July, 1987, pp. 5-6.
- [1.9] Douglas A. Saunders, "Stress-induced Magnetic Anisotropies in Ion-implanted, Contiguous-disk, Magnetic Bubble Devices," Ph.D. Dissertation, Carnegie Mellon University, Pittsburgh, Pennsylvania, September, 1987, pp. 6.
- [1.10] Jiin-chuan Wu, "Solid State Magnetic Devices: Magnetic Bubble Logic Devices and Vertical Bloch Line Memory," Ph.D. Dissertation, Carnegie Mellon University, Pittsburgh, Pennsylvania, August, 1986, pp. 25.
- [1.11] G. S. Almasi, "Magnetic Bubble-Domain Detection: Review and Outlook," IEEE Transactions on Magnetics, Vol. MAG-9, No. 4, December, 1973, pp. 663-669.
- [1.12] K. Patel, W. Clegg, and R. M. Pickard, "Theoretical Considerations on the Design of Magnetic Bubble Detectors," J. Appl. Phys., Vol. 49, No. 9, September 1978, pp. 4843-4848.

- [1.13] A. Bobeck, and E. Della Torre, "Magnetic Bubbles," North-Holland, 1975, pp. 184-193.
- [1.14] A. Bobeck, I. Danylchuk, F. C. Rossol, and W. Strauss, "Evolution of Bubble Circuits Processed by a Single Mask Level," IEEE Transactions on Magnetics, Vol. MAG-9, No. 3, September 1973, pp. 474-480.
- [1.15] A. Mohaghegh, S. Cristoloveanu and J. De Pontcharra, "Double- Injection Phenomena Under Magnetic Field in SOS Films: A New Generation of Magnetosensitive Microdevices," IEEE Transactions on Electron Devices, Vol. ED-28, No. 3, March 1981, pp. 237-242.
- [1.16] S. Cristoloveanu, A. Chovet, and G. Kamarinos, "Non-Uniform Recombination in Thin Silicon-on-Sapphire Films," Solid-State Electronics, Vol. 21, pp. 1563-1569.
- [1.17] P. H. L. Rasky, D. W. Greve, and M. H. Kryder, "The State of Silicon-on-Garnet Devices," Magnetic Technology Center Annual Report for 1986-1987, Carnegie Mellon University, 1987, pp. 355-372.
- [1.18] D. W. Greve, M. H. Kryder, and P. H. L. Rasky, "Integration of Semiconductor and Magnetic Bubble Devices: SOI on Garnet," Mat. Res. Soc. Symp. Proc., Vol. 53, 1986, pp. 375-382.
- [1.19] P. H. L. Rasky, D. W. Greve, M. H. Kryder, and S. Dutta, "The Feasibility of Silicon on Garnet Technology," J. Appl. Phys., Vol. 57, No. 1, April 15, 1985, pp. 4077-4079.

Ì

Chapter 2

Magnetic field calculations for the design and placement of bubble domain sensors.

2.1 Introduction

In the previous chapter we introduced our silicon-magnetodiode magnetic-bubble sensor and the first order theory of its operation. The influence of device geometry on the characteristics of the differential magnetodiode bubble sensor will be the subject of this chapter. It will be shown that we have selected a reasonable n- base width, thickness for each of the spacer layers, stretcher conductor design, and thickness for the silicon film.

2.2 Design of magnetic bubble domain sensors

If the width of the n- base is too large, the change in current ΔI for a single magnetodiode due to the bubble's fringing field will be too small compared to the diode's current I in the absence of the bubble's fringing field to insure reliable bubble detection. This is because the bubble's fringing field intercepts only a very limited portion of the n- base. If the diode's n- base is too narrow, ΔI will be smaller than its optimum value, and some of the bubble's fringing flux will be wasted. Finding the optimum diode width is thus related to the bubble's fringing magnetic field.

When a bubble stripes out into the channel shown in figure 1-10, it will have a large length to width ratio (at least 35), and this will allow us to model the domain as an infinite stripe to a good approximation. Calculation of the expanded bubble domain's fringing field is simplified in this case. Patel, Clegg, and Pickard have made this calculation for the geometry shown in figure 2-1; the result is given in equations (2.1) and (2.2) [2.1].

$$H_{x} = \frac{M_{B}}{2\pi} \left\{ \log \left[z^{2} + \left(\frac{W}{2} - x \right)^{2} \right] - \log \left[z^{2} + \left(-\frac{W}{2} - x \right)^{2} \right] - \log \left[(z + h)^{2} + \left(-\frac{W}{2} - x \right)^{2} \right] + \log \left[(z + h)^{2} + \left(-\frac{W}{2} - x \right)^{2} \right] \right\}$$
(2.1)

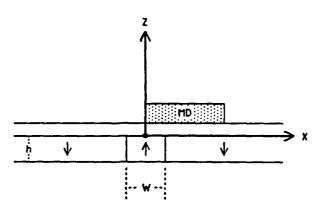


Figure 2-1: Geometry assumed in equations (2.1) and (2.2).

$$H_{z} = \frac{M_{B}}{\pi} \left[\tan^{-1} \left(\frac{\frac{1}{2}W - x}{z} \right) - \tan^{-1} \left(-\frac{\frac{1}{2}W - x}{z} \right) - \tan^{-1} \left(-\frac{\frac{1}{2}W - x}{z} \right) \right]$$

$$- \tan^{-1} \left(-\frac{\frac{1}{2}W - x}{z + h} \right) + \tan^{-1} \left(-\frac{\frac{1}{2}W - x}{z + h} \right)$$
(2.2)

We will focus our attention on equation (2.1) since the magnetosensitivity of the magnetodiode arises as a result of H_x, the x component of the magnetic field intensity. Figure 2-2 shows plots of H_x as a function of x for representative values of z where $M_B = 100$ A/m, $W = 2\mu m$, and h = $2\mu m$. These plots can be used for any M_B if values read from the plot are multiplied by $M_{\rm p}/100$. Note that $H_{\rm x}$, for all plots, drops to less than 5% of $M_{\rm b}$ by $x=4\mu{\rm m}$ and less than 0.6% of M_R by x=10 μ m. A diode base width much larger than 10 μ m is certainly not required. If we determine the area under each curve shown in figure 2-2 and divide by typical diode base widths, we have the plots shown in figure 2-3. These plots give the average value of H_x acting over the diode's width. For any given diode width, the average field is larger the closer the diode is to the bubble film, and in the ideal case, we would like to put the diode directly on the bubble substrate. This, unfortunately, can not be done with the process we plan to use. This process demands that the diode be placed on the order of 0.5-0.6µm above the bubble film: if it is placed much less than that value, the bubble film will melt during laser recrystallization of the silicon. The optimal base width based on the results of figure 2-3 is $2\mu m$. Widths smaller or larger than this optimum value will produce smaller $\Delta I/I$ figures of merit. In fixing the diode width, we must also keep in mind that the portion of the magnetodiode directly above the bubble domain in figure 2-1 does not exist in the design of figure 1-10. If it did exist, we would not have a sensor as both diodes would be shorted together. Furthermore, if it did exist, the ionimplanted channel would also be absent. The n- base regions shown in figure 1-10 are $3\mu m$ wide,

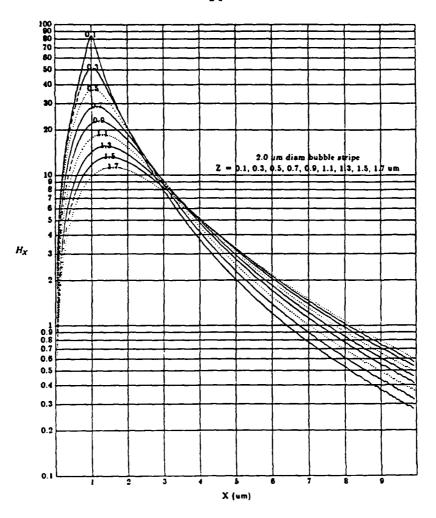


Figure 2-2: Plots of H_x as a function of x and z.

and we note that this choice of width simplifies sensor fabrication without being too far from the optimum value.

2.3 Design of magnetic bubble domain stretchers

The stretcher design shown in figure 1-10 was selected from a variety of designs which were evaluated with the aid of computer simulation programs written by J. C. Wu [2.2]. The first program, Expand, calculates the z component of magnetic field intensity H_z produced by the stretcher when it is energized. The second program, Edge, calculates the highly localized demagnetizing field that exists at the edges of the bubble propagation pattern (the implanted/non-implanted boundaries). The third program, Simulate, uses the results of Expand and Edge to predict how a bubble will behave in a structure such as the one shown in figure 1-10. A forth program, Drawf, takes the output of Expand and Edge, the field values, and plots constant field contours. Drawe, a fifth program, displays the results of Simulate as a slow-motion

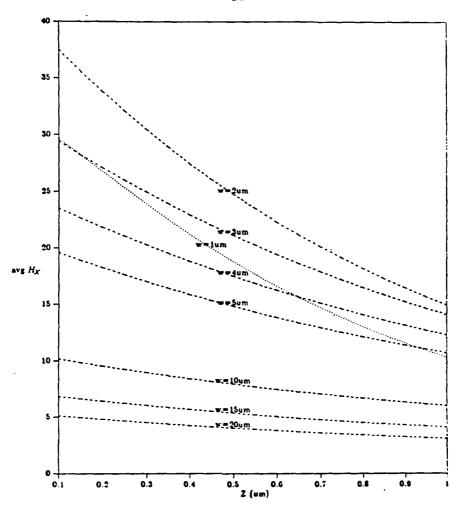


Figure 2-3: Average value of H_x as a function of z and diode width w.

video movie: dynamic events appear as they would in real time, but at a slower pace. Potential problems/design flaws can be identified and resolved before fabrication. Consider the design shown in figure 2-4. Expand predicts it will stripe out the bubble, but the path of the expanding domain does not include the ion-implanted channel between the n- base regions. The stripe instead turns in toward the left conductor of the hairpin stretcher and continues to expand in the direction of the steepest positive field gradient. The demagnetizing field produced by the implanted/non-implanted transitions tends to keep the expanding stripe in the implanted channel, but it is not sufficiently strong to prevent the stripe from crossing the transition region: the stretching field overpowers it. A proper design insures that the expanding domain never sees an increasing field gradient except in the direction in which the stripe is intended to expand. The stretcher design shown in figure 1-10 is one such design. Field contours for this design are shown in figure 2-5. The bubble starts its expansion at the mouth of the sensor where H_g is 60.0 oe, and the maximum field it sees, H_g=72 oe, is nearly 85μm from this initial position. That is an

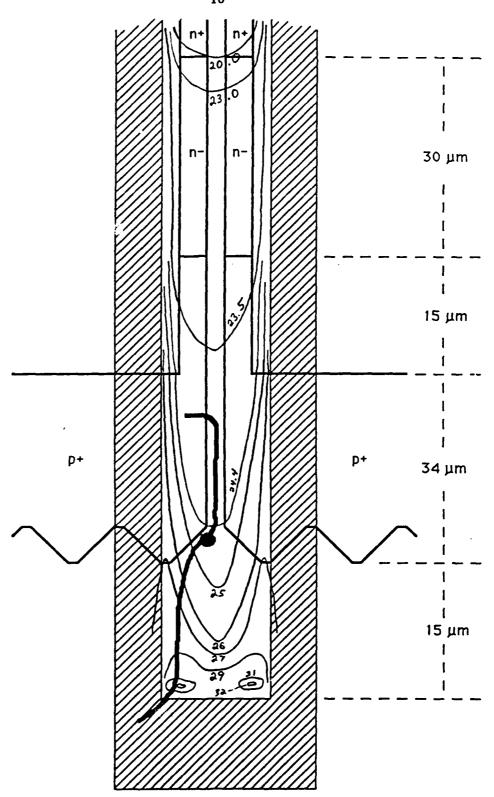


Figure 2-4: Design for a differential magnetodiode bubble sensor. Field values are given in Oersteds (oe), and we note that this design was not chosen for fabrication.

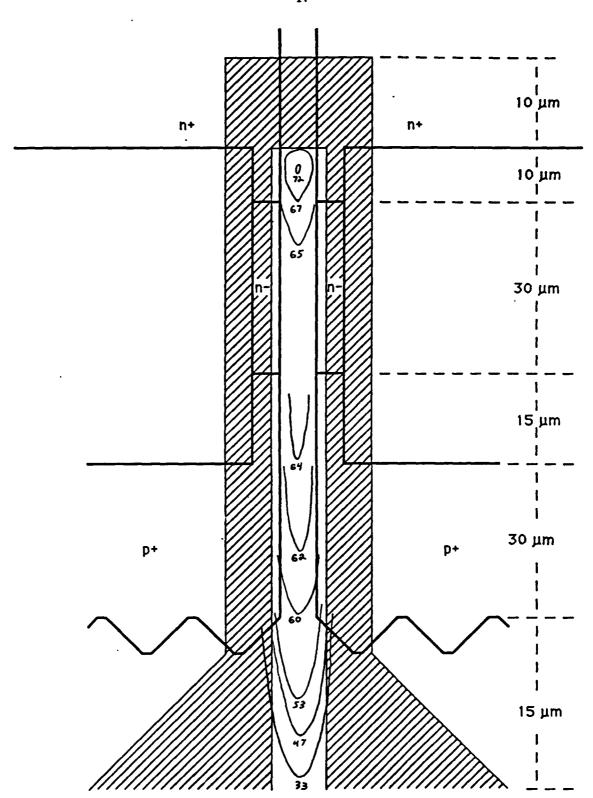


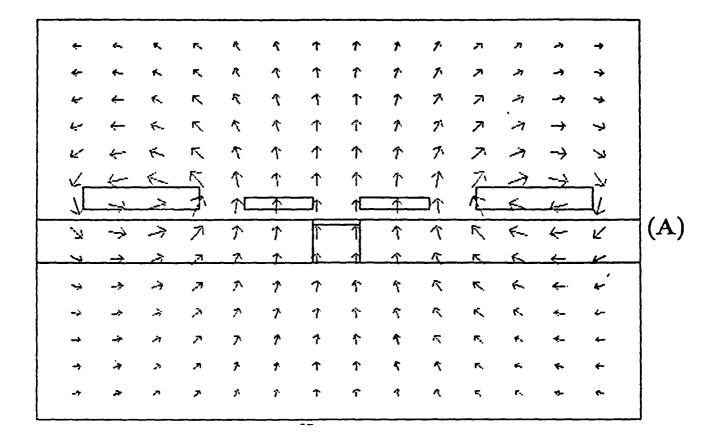
Figure 2-5: Design for a differential magnetodiode bubble sensor. Field values are given in Oersteds (oe).

increasing field gradient of 0.14 $oe/\mu m$ on average. Also note that the maximum field seen by the expanding stripe is located past the critical n- base region, near the position where stripe expansion will cease.

Designs such as the one shown in figure 2-4 were considered because the in-plane field component of H, H_x, can be much smaller than H_z over the width of the magnetodiode; twenty times smaller is typical. Figure 2-6 shows a vector plot of H for a cross section taken through the n- base of the design shown in figure 2-4. A finite element program called Magnetostat made the field calculation, and another finite element program, Meshmaker, generated the required mesh [2.3]. While it is true that H_x can be very small over the width of the magnetodiode during the expansion of a bubble domain, it is not true that H, will be small within the bubble film. In fact, if we assume similar expansion fields in the implanted channel, the maximum value of H_x for the design of figure 2-4 can be at least twice as large as the maximum value of H_x for the design of figure 2-5. This is a problem as the combined effect of H_x from the stretcher and the in-plane drive field (the field that propagates the bubbles) may be the nucleation of additional bubble domains: large in-plane fields can produce strong charged walls, and strong charged walls produce strong demagnetizing fields. When the demagnetizing field is on the order of H_k - $4\pi M_s$, a domain of reverse magnetization, a bubble, will be nucleated [2.4]. Here H_k is the anisotropy field, and $4\pi M_s$ is the saturation magnetization; both of these parameters are for the bubble film.

2.4 Simulation results for the differential magnetodiode bubble sensor: fringing fields

A cross section taken through the n- base regions for the sensor design shown in figures 1-10 and 2-5 is shown in figure 2-7. This cross section is very close to how an actual device cross section appears. A $0.50\text{-}0.55\mu\text{m}$ silicon layer is used. The $5\mu\text{m}$ width and $1\mu\text{m}$ thickness of the Al-Cu stretcher conductor are such that electromigration is not a problem during bubble expansion [2.5]. The current density in the Al-Cu conductor during bubble expansion will be about $2 \times 10^{10} \text{A/m}^2$ (100mA total); the bias field will be at approximately 235 oe. We determined the current needed to reliably expand a bubble domain from computer simulations using the program Simulate; our initial projections, the ones we first used in Simulate, were derived from the results reported by Nelson et al. [2.6]. Material parameters for the bubble film, such as the saturation magnetization [500 gauss] and the thickness of the ion-implanted drive



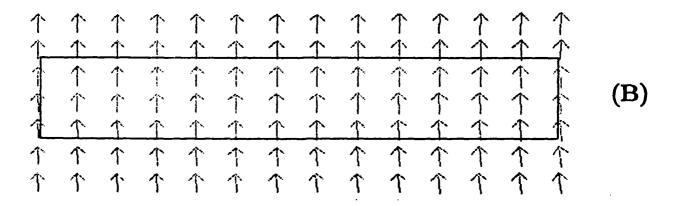


Figure 2-6: (A) Vector plot of B(H) resulting from an energized hairpin stretcher. The effect of the magnetic bubble film is not included in this figure; we only indicate its position and the position of a bubble domain. The silicon magnetodiodes and the Al-Cu conductors are assumed to be non-magnetic materials. (B) Magnified plot of B(H) over the right magnetodiode.

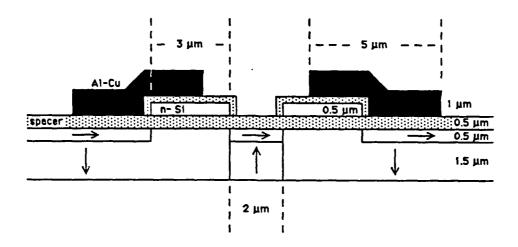


Figure 2-7: Scale drawing of an idealized silicon on garnet cross section.

layer $[0.5\mu\mathrm{m}]$, were taken from the literature [2.7, 2.8, 2.9]. Finite element simulations using this and the other information were made to determine how much of the stripe's flux would intercept the sensor's magnetodiodes. The simulation cases we considered are shown in figures 2-8(A) and 2-9(A). Vector plots of the resulting magnetic field minus the bias field are shown in part B of these figures for the right magnetodiode. The direction and average value of B_x acting over the width of the n- base region for the left and right magnetodiodes are diagramed in figure 2-10; the calculations are valid midway between the top and bottom interfaces. We have also made the corresponding calculations for B_y , and the results are given in figure 2-11. Notice how the average values of B_y for each magnetodiode are essentially the same for the bubble/no bubble case. This is not true for B_x : $\Delta B_x^{\text{total}}$ (ΔB_x^{left} - $\Delta B_x^{\text{right}}$) is 94.43 gauss. This result will be used in section 5.2.2 to estimate the current output of our sensor.

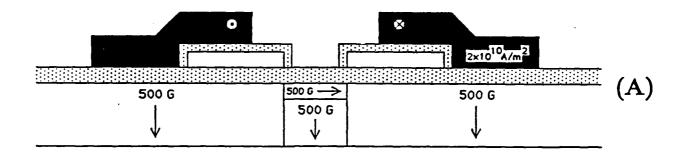
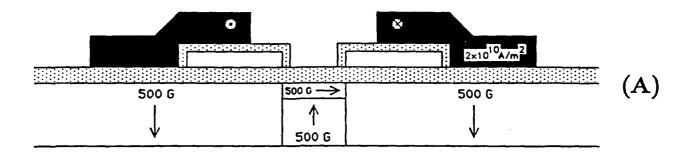




Figure 2-8: (A) Scale drawing of the structure for the "no bubble" simulation case - see figure 2-7 for dimensions. (B) Plot of B for the right magnetodiode.



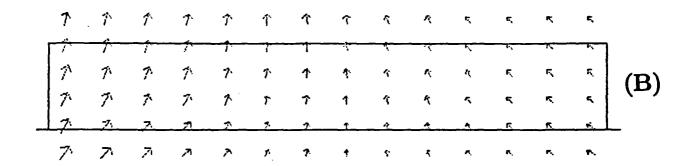


Figure 2-9: (A) Scale drawing of the structure for the "bubble" simulation case - see figure 2-7 for dimensions. (B) Plot of B for the right magnetodiode.

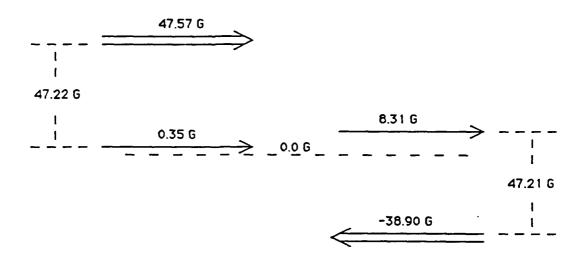


Figure 2-10: Direction and average value of B_x acting over the width of the n-base region for the left and right magnetodiodes for the simulation cases of figures 2-8 and 2-9



Figure 2-11: Direction and average value of B_y acting over the width of the n-base region for the left and right magnetodiodes for the simulation cases of figures 2-8 and 2-9

2.5 References

- [2.1] K. Patel, W. Clegg, and R. M. Pickard, "Theoretical Considerations on the Design of Magnetic Bubble Detectors," J. Appl. Phys., Vol. 49, No. 9, September 1978, pp. 4843-4848.
- [2.2] J. C. Wu, Department of Electrical and Computer Engineering, Carnegie Mellon University, 1986.
- [2.3] D. N. Shenton and Z. Cendes, Department of Electrical and Computer Engineering, Carnegie Mellon University, 1986.
- [2.4] A. H. Eschenfelder, "Magnetic Bubble Technology," Second Edition, Springer-Verlag, 1981, pp. 5.
- [2.5] S. Vaidya, T. T. Sheng, and A. K. Sinha, "Linewidth Dependence of Electromigration in Evaporated Al 0.5 %Cu, Appl. Phys. Lett., Vol. 36, No. 6, March 15, 1980, pp. 464-466.
- [2.6] T. J. Nelson, R. Wolfe, S. L. Blank, P. I. Bonyhard, W. A. Johnson, B. J. Roman, and G. P. Vella-Coleiro, "Design of Bubble Device Elements Employing Ion-Implanted Propagation Patterns," The Bell System Technical Journal, Vol. 59, No. 2, February 1980, pp. 229-257.
- [2.7] A. H. Eschenfelder, "Magnetic Bubble Technology," Second Edition, Springer-Verlag, 1981, pp. 184.
- [2.8] S. L. Blank, R. Wolfe, L. C. Luther, R. C. LeCraw, T. J. Nelson, and W. A. Biolsi, "Design and Development of Single-Layer, Ion-Implantable, Small Bubble Materials for Magnetic Bubble Devices," J. Appl. Phys., Vol. 50, No. 3, March 1979, pp. 2155-2160.
- [2.9] T. J. Nelson, R. Wolfe, S. L. Blank, and W. A. Johnson, "Reliable Propagation of Magnetic Bubbles with 8μm period Ion Implanted Propagation Patterns," J. Appl. Phys., Vol. 50, No. 3, March 1979, pp. 2261-2263.

Chapter 3

Fabrication of silicon on garnet devices

3.1 Introduction

From a structural point of view, all of our silicon on garnet devices are somewhat similar: there is, in all cases, a silicon film on a magnetic bubble substrate that is isolated from the magnetic bubble film by one or more spacer layers. One might, therefore, expect to see this similarity manifested in the different fabrication processes as a group of common or closely related fabrication steps/procedures. This is in fact the case, and because of this, we need not consider each process in great detail; a brief listing of key steps will suffice for all but the first or parent process. In this chapter, we will consider the parent process in detail, and will introduce some of its subtle aspects.

3.2 Fabrication of silicon on garnet magnetodiodes

We will now describe a silicon on garnet fabrication process for the structure shown in figure 1-10. The cross sections shown in this section are either parallel or perpendicular to the channel shown in figure 1-10.

The substrates we start with are (111) GGG (Gd₃Ga₅O₁₂), and each substrate has a single [SmLuYDyBi]₃(GaFe)₅O₁₂ bubble film on it. Two spacer layers are deposited on these bubble substrates: the first is a 0.35µm SiO₂ passivation layer, and the second is a 0.25µm Si₃N₄ barrier layer. Both of these films are deposited by low pressure chemical vapor deposition (LPCVD); the SiO₂ is deposited at 860°C, and the Si₃N₄ is deposited at 800°C. These films isolate the 0.55µm silicon device layer from the bubble substrate. The 0.55µm device quality silicon layer is formed in a four part process: (1) the silicon is deposited on the composite spacer in polycrystalline form at 625°C by LPCVD; (2) the polysilicon is doped n- by ion implanting phosphorus at 180 keV at a dose of 2.75 x 10¹⁰ cm⁻², 2.75 x 10¹¹ cm⁻², or 2.75 x 10¹² cm⁻²; (3) a 1µm SiO₂ cap layer is deposited on the polysilicon by rf sputtering or plasma enhanced CVD (chemical vapor deposition) at 300°C [3.1], and (4) the grain size of the polysilicon is increased by laser recrystallization [3.2]. The cross section of our structure after recrystallization is shown in figure 3-1.

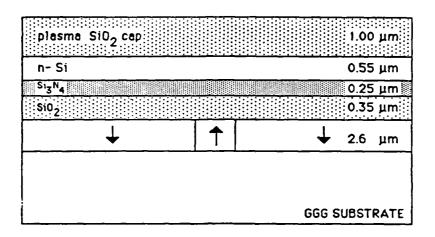


Figure 3-1: Structure after laser recrystallization.

We next selectively dope the recrystallized silicon layer n+ and p+ by the method outlined in figure 3-2. The first and second SiO_2 implant mask layers are $1\mu m$ thick, and they are deposited at 300° C by plasma enhanced CVD. The areas where SiO_2 will be absent are defined in photoresist using standard photolithographic procedures; these windows are then opened with a buffered HF etch. The n+ dopant, phosphorus, is implanted at 90 keV with a dose of 2.5 X 10^{15} cm⁻², and the p+ dopant, boron, is implanted at 60 keV with a dose of 2.5 X 10^{15} cm⁻².

After the p+ doping, the top two SiO_2 layers are etched off. The large grain polysilicon is then oxidized at 850° C in a wet oxygen ambient. Alignment markers for the next process step are made visible during this oxidation since oxide thicknesses are a function of the dopant concentration in the silicon film [3.3]. Suprem-III was used to calculate the oxide thicknesses over the n+, n-, and p+ regions [3.4]; figure 3-3 shows the results of these calculations.

The device islands and ion-implanted contiguous-disk propagation patterns are defined in a single photolithographic procedure: positive photoresist remains in places where devices are desired and where in-plane drive layers are not. The resist patterns are stabilized with a deep ultraviolet flood and a 110-120°C hard bake in air. We then etch off the SiO₂ and silicon in the unmasked regions. The SiO₂ is removed with a buffered HF etch, and the silicon is removed with a Cl₂ reactive ion etch. Propagation patterns are subsequently created by implanting hydrogen ions at 190kev. Figure 3-4 shows the silicon on garnet structure perpendicular to figure 3-3 after

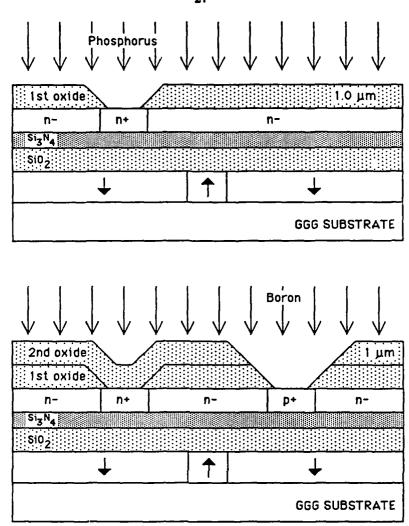


Figure 3-2: Selective doping of the magnetodiode structure.

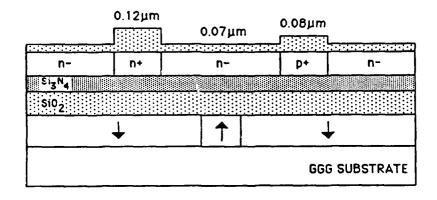


Figure 3-3: Structure after a 30min. 850°C wet oxidation.

this implant step. Notice how the in-plane drive layer in the bubble film is only formed in the unmasked areas; the propagation patterns are said to be self-aligned to the silicon magnetodiodes, and the spacing between the bubble and detector is thus minimized.

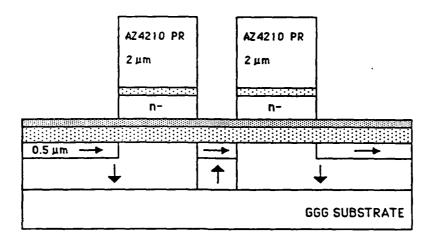


Figure 3-4: Structure after the propagation implant.

Following the propagation implant, the photoresist implant mask is removed with an air plasma in a barrel etcher. A 0.15μ m plasma SiO_2 layer is then deposited at 300° C. The Al-Cu stretcher shown in figure 1-10 would be shorted to the magnetodiodes if this oxide layer were absent; we would in effect have a sensor with a single node. Contact windows are defined in photoresist after the plasma SiO_2 deposition. These windows are opened with a buffered HF etch. We show the now nearly complete silicon on garnet structure in figure 3-5.

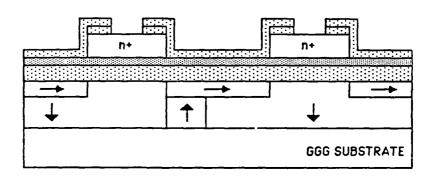


Figure 3-5: Structure after contact windows are opened.

Our magnetodiode fabrication process is complete once the Al-Cu conductor layer is

deposited and patterned. The Al-Cu is deposited by DC magnetron sputtering. Interconnect patterns are defined with photolithography, and unwanted portions of the conductor are etched away using a wet chemical etch. After this, we remove the resist with acetone. The final magnetodiode structure is shown in figure 3-6.

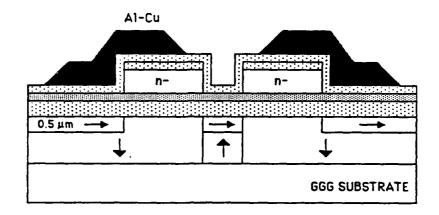


Figure 3-6: Final structure for the differential magnetodiode bubble sensor.

3.3 Structural characteristics of silicon on garnet devices

Having introduced a silicon on garnet fabrication process (in section 3.2), we will now consider the subtle aspects of such a process. Process induced decomposition of bubble films will be considered first. We will next take up the issue of capping layers for the laser recrystallization of silicon layers and the need for cap densification. Following this, we focus on the structural characteristics of silicon on garnet device structures as determined from cross sectional TEM work. The last topic we will deal with is the stability of silicon on garnet spacer layers during device fabrication.

As discussed in section 3.2, the first layer deposited on the bubble substrate is a passivation layer since it prevents decomposition of the bubble film during the LPCVD Si₃N₄ and polysilicon depositions. To see that this is the case, we will consider the effects of an experiment in which this oxide film is absent from (or is very thin in) a few areas of a $(Bi_{0.4}Dy_{0.7}Lu_{1.2}Sm_{0.2}Y_{0.5})[Fe_{4.45}Ga_{0.55}]O_{12}$ bubble substrate. This process has five steps which we will now list.

1. Support the bubble wafer in two small areas near the edge of the wafer with 3mm diameter quartz rods. The rods are in intimate contact with the bubble film at these spots, and because of this, the film deposited in these areas during step 2 is at best very thin.

- 2. Deposit $0.40\mu m$ of SiO₂ by LPCVD at $860^{\circ}C/0.85$ torr from SiH₄ and N₂O.
- 3. Support the bubble wafer in two different small areas near the edge of the wafer with 3mm diameter quartz rods.
- 4. Deposit $0.30\mu m$ of $\mathrm{Si_3N_4}$ by LPCVD at $800^{\circ}\mathrm{C}/0.4$ torr from $\mathrm{SiH_4}$ and $\mathrm{NH_3}$.
- 5. Deposit $0.65\mu m$ of polysilicon by LPCVD at $625^{\circ}C/0.4$ torr from SiH_4 .

Figure 3-7 shows a bright field photograph taken with transmitted light of an area masked by a quartz rod in step 1 (the large black area) and the surrounding areas which were unmasked (the large light areas). It is clear that the nitride and/or polysilicon deposition(s) initiated some form of chemical decomposition in the area which was not covered with a sufficient amount of SiO₂.

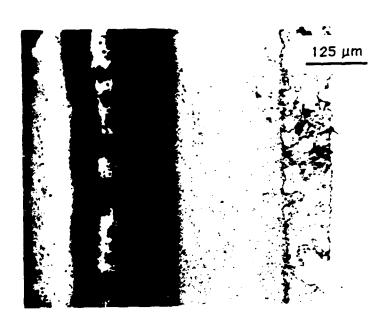


Figure 3-7: Bright field photograph of a $(Bi_{0.4}Dy_{0.7}Lu_{1.2}Sm_{0.2}Y_{0.5})[Fe_{4.45}Ga_{0.55}]O_{12}$ bubble film (AH45) after processing that was taken with transmitted light. The black areas are decomposed bubble film regions which were covered with an insufficient amount of LPCVD SiO₂ prior to the LPCVD Si₃N₄ and polysilicon depositions.

We have found that recrystallized polysilicon films have flatter surfaces if the polysilicon is capped with a SiO_2 film during the laser recrystallization. In our early work, we used $1\mu m$ thick SiO_2 caps that were deposited by rf sputtering; these caps were not densified prior to the laser recrystallization. Some of our later attempts at laser recrystallization employed plasma SiO_2

caps since this material was expected to contain less contamination than the sputtered SiO₂. These attempts however were not initially successful for undensified caps: the recrystallized silicon films had a high density of discontinuities, and we speculate that these holes formed during the laser anneal as a result of gas evolution from the plasma SiO₂ cap. This is plausible as films deposited by plasma enhanced CVD are known to contain a large amount of hydrogen which is bonded to silicon as Si-H and to oxygen as Si-OH and H₂O [3.1]. We tested our hypothesis of gas evolution induced defects with an experiment: we attempted recrystallization employing plasma SiO₂ caps that were densified in nitrogen for 1hr. at 625°C or 850°C. The structure of the samples used in these attempts is identical to that shown in figure 3-1, and the process used to fabricate the samples is the same as that given at the beginning of section 3.2 except that the densification step is added between steps (3) and (4). Figure 3-8(A) shows a bright field reflected light photograph of a sample that was laser annealed with increasing power (top to bottom in the photo) after a 1hr. 625°C N₂ anneal. It is clear that this 625° anneal has done little to improve the results: discontinuities can be seen in the bottom two thirds of the laser scan. Between these discontinuities, the silicon film is large grain and polycrystalline as can be seen from the SEM micrograph shown in figure 3-8(B). The 1hr. 850°C N₂ anneal, however, proved to be very effective, and we saw no signs of discontinuities in the laser recrystallized silicon film. It therefore appears that our results are consistent with the evolution of gas during the laser annealing.

The Si_3N_4 spacer layer of section 3.2 is called a barrier layer since it is intended to prevent bubble film ions that diffuse out of the bubble film from reaching the silicon device layer. The results of sections 6.2 and 6.3 show that the nitride layer is at least a partial diffusion barrier. The contamination that does get through (by way of cracks etc.) is of particular concern: it may be an electrically active part of the silicon device as mentioned in section 5.3.2 or it may be inactive and form structural defects like precipitates. Work by Honda et al. led us to believe that precipitates of iron with cross sectional areas on the order of 4.3 x $10^{-3} \mu m^2$ (0.05 μ x 0.086 μ) may have been present in our laser recrystallized material [3.5], and we therefore set out to investigate this possibility. Single (SiO₂ only) and double (SiO₂+Si₃N₄) spacer layer silicon on garnet structures were examined by TEM in cross section with 1 nm resolution [3.6]. No precipitates were seen for either type of structure, and based on solid solubility data for Fe in silicon we can therefore estimate that the concentration of iron in our recrystallized silicon films is less than 2 x 10^{15} cm⁻³ [3.7]. Figure 3-9(A) shows a TEM micrograph of a typical silicon on

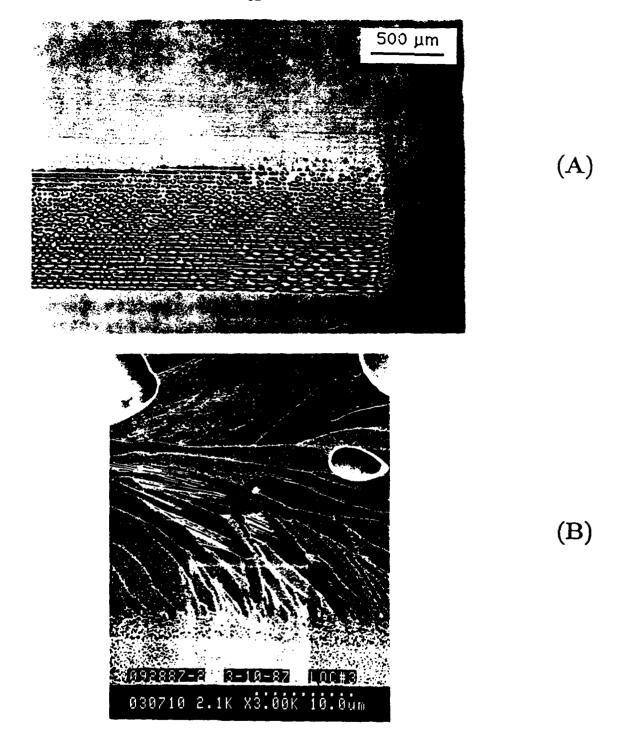


Figure 3-8: (A) Bright field reflected photograph of a sample (092887-2 loc#1) with the structure shown in figure 3-1 after a 1hr. 625°C N₂ anneal. (B) SEM micrograph of a sample (092887-2 loc#3) similar to the one shown in (A) after a 1.0 min. etch in 1 part of [1 part 0.15 M K₂Cr₂O₇ + 2 parts 49% HF] and 1 part deionized water; this is a diluted Secco etch.

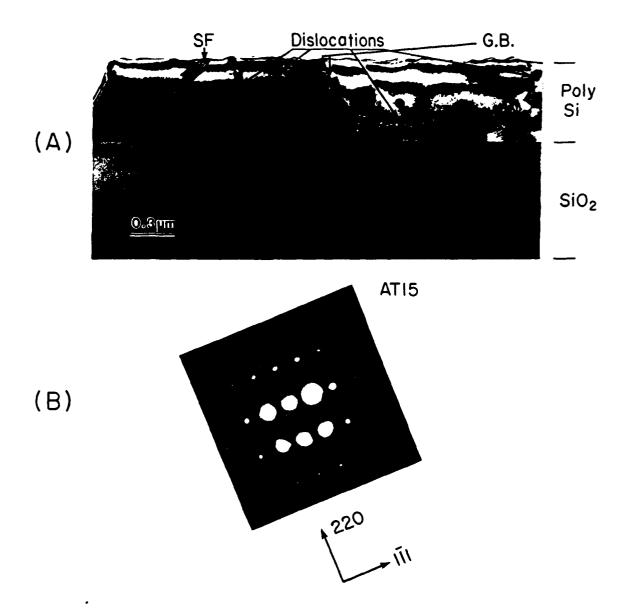


Figure 3-9: (A) TEM micrograph of a silicon on garnet cross section with a single sputtered SiO₂ spacer layer. The process used to fabricate this structure on bubble wafer AT15 had five steps: (1) deposit 1μm of spacer SiO₂ by sputtering at 700 W/20 mtorr Ar, (2) deposit 0.6μm of polysilicon by LPCVD at 625°C/0.4 torr, (3) deposit 1μm of cap SiO₂ by sputtering at 700 W/20 mtorr Ar, (4) laser recrystallization of the polysilicon layer at approximately 1415°C (substrate temperature = 350°C), and (5) Wct O₂ oxidation at 850°C for 50 min. (cap oxide from step 3 was removed after the recrystallization step.). We also point out that the samples we examined with SiO₂ + Si₃N₄ spacers had a fabrication process similar to that listed in section 4.4.1. (B) Selected area diffraction for one of the grains shown in part (A).

garnet cross section. The top layer is a laser recrystallized polysilicon film that is separated from the bubble film by a 1μ m sputtered SiO₂ layer. Dislocations, stacking faults, and grain boundaries are identified in part (A) of this figure; part (B) of the figure shows the selected area diffraction pattern for one of the grains shown in part (A). The laser processing which formed these large grains also damaged the top 0.9μ m - 0.16μ m of the bubble film: its crystal structure had changed from crystalline to polycrystalline, and the most likely cause was partial melting of the bubble film during laser recrystallization of the silicon device layer. Figure 3-10 shows a cross sectional TEM micrograph of a damaged bubble layer along with the diffraction patterns for a damaged (part (B)) and intact (part (C)) portion of the bubble film. This damaged layer is found for both spacer systems. Samples with the SiO₂ + Si₃N₄ spacers had a similar set of defects, both in the silicon and bubble films. Highly damaged portions of the bubble film can be detected with an optical microscope if transmitted light is used. The damage can be seen by focusing on the bubble film and looking for grainy/small bubble-like patterns similar to those shown in the center of figure 3-11.

Spacer layers are the first films on the bubble substrate, and the stability of these layers during device fabrication will in large part determine the structure of the silicon on garnet devices. Device structures with the LPCVD $SiO_2 + Si_3N_4$ spacers, discussed in section 3.2, have only minor structural problems: to date, the worst problem we have seen with this material system is a minor amount of stress induced cracking and/or peeling of the recrystallized silicon plus spacer layers. Stress induced spacer/device silicon cracking has also been a minor problem in silicon on garnet device structures with the sputtered SiO_2 spacer layer (see figure 3-12(A)). These types of problems are not surprising given that the thermal expansion coefficients of SiO_2 and garnet are 5 x 10^{-7} $^{\circ}C^{-1}$ and \sim 8 x 10^{-6} $^{\circ}C^{-1}$, respectively [3.8, 3.9]. We also know SiO_2 and Si_3N_4 are not well matched with respect to stress: SiO_2 is 2 - 4 x 10^9 dyn/cm² compressive with Si_3N_4 being 1.2 - 1.8 x 10^{10} dyn/cm² tensile [3.10].

One can match stress values for the SiO_2 and Si_3N_4 if the latter film is deposited by plasma enhanced CVD (plasma Si_3N_4 is 1 - 8 x 10^9 dyn/cm² compressive [3.10]). This matching, however, can be problematic since plasma Si_3N_4 films contain substantial quantities of hydrogen - 10 to 30 % is common - and our films are known to contain 30 % hydrogen [3.11]. We nonetheless tried to fabricate silicon devices on magnetic bubble substrates coated with sputtered SiO_2 (first spacer on the garnet substrate) and plasma Si_3N_4 . The process we used had seven steps which we will now list.

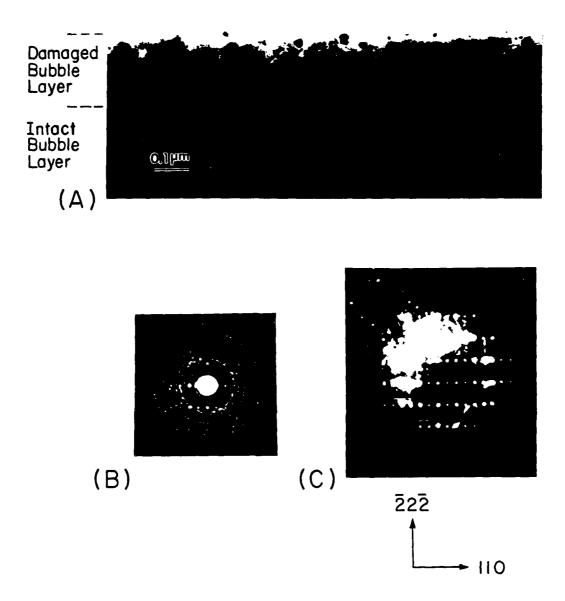


Figure 3-10: (A) Cross sectional TEM micrograph of the damaged and intact portions of a bubble film (AT15) which was processed according to the schedule given in figure 3-9. (B) Selected area diffraction for the damaged portion of the bubble film. (C) Same as part (B), but for the intact portion of the bubble film.

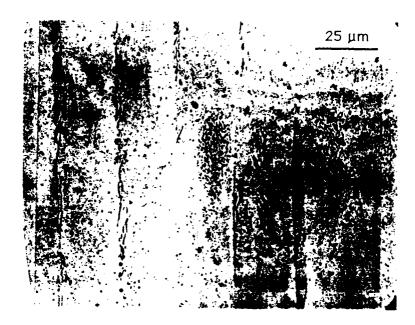


Figure 3-11: Bright field transmitted photograph of some damage to a magnetic bubble film (AH43). This is the same film considered in table 4-3, and we point out that this photo was taken just after the laser recrystallization step.

- 1. Deposit $0.4\mu \text{m}$ of SiO_2 by sputtering at 700 W/20 mtorr Ar from a SiO_2 target.
- 2. Deposit $0.3\mu m$ of Si_3N_4 by plasma enhanced CVD at $350^{\circ} C$ from 4% SiH_4 in He and NH_3 .
- 3. Deposit $0.50\mu m$ of polysilicon by LPCVD at $625^{\circ}C/0.4$ torr from SiH₄.
- 4. Deposit 1μ m of SiO₂ by sputtering at 700 W/20 mtorr Ar from a SiO₂ target (this film is the laser recrystallization cap).
- 5. Laser recrystallize the polysilicon layer at approximately 1415°C (substrate temperature = 200°C).
- 6. Wet O₂ oxidation at 850°C (this layer after patterning will be the mask for the silicon island etch).
- 7. Wet silicon island etch using the ${
 m SiO}_2$ mask grown in the last step.

Figure 3-12(B) shows the results of this process. Areas marked LA were laser annealed while those marked NLA were not. The composite spacer is identified as SiO2/Si3N4 in the figure, and we note the rectangle near the NLA marking is a polysilicon island (as are the long narrow horizontal areas near the top and bottom of the SEM micrograph). We note that most of the

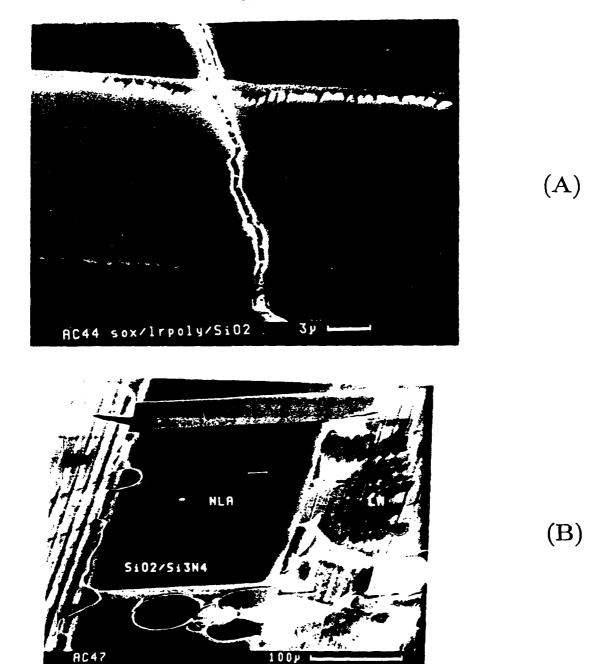


Figure 3-12: (A) SEM micrograph of bubble wafer AC44 after a wet silicon etch for island definition; a thin pattern SiO₂ remains on the silicon island. The process used to fabricate this structure is the same as the one described in figure 3-9 with the following exceptions: (1) 0.5μm of polysilicon, (2) 200°C substrate temperature for laser anneal, and (3) 90 min. oxidation. (B) SEM micrograph of bubble wafer AC47 after the wet silicon island etch (step 7 in the text).

layers {the sputtered SiO₂, plasma Si₃N₄, and LPCVD polysilicon} in the LA areas flaked and peeled off in the processing that followed the laser recrystallization. This is probably due to poor post-laser anneal adhesion of the Si₃N₄ plus recrystallized silicon layers to the sputtered oxide spacer, and we speculate that this poor adhesion is related to the evolution of hydrogen gas from the nitride spacer film during the laser anneal. It is also possible that stress effects play a role in this problem.

3.4 Summary

Section 3.2 described a silicon on garnet fabrication process that can be used to fabricate silicon magnetodiodes that are self-aligned to ion-implanted contiguous-disk bubble-propagation patterns, and section 3.3 introduced some of the subtle aspects of such a process, one example being the need to passivate the magnetic bubble film with a layer of SiO, before the 800°C LPCVD Si_3N_4 and $625^{\circ}C$ polysilicon depositions. We also found that it is necessary to densify plasma SiO₂ caps in nitrogen at 850°C for 1hr. prior to the laser recrystallization of polysilicon device layers. Cross sectional TEM work led to two key findings for all of the samples we examined: (1) iron concentrations in silicon on garnet films do not exceed approximately 2 x 10¹⁵ cm⁻³, and (2) laser recrystallization of the silicon layer in silicon on garnet structures will damage the top $0.9\mu m$ - $0.16\mu m$ of the magnetic bubble film. This damage occurs even though the SiO_2 and/or Si_3N_4 spacer layers place the silicon layer $0.7\mu m$ to $1.0\mu m$ above the bubble film. Stress induced spacer/device silicon cracking is another type of damage found in silicon on garnet device structures with the sputtered SiO₂ or LPCVD SiO₂ + Si₃N₄ spacer system; it tends, however, to be a minor problem. Finally, sputtered SiO₂ + plasma Si₃N₄ spacers did not prove to be effective in silicon on garnet device structures, and we speculate that this is a result of not densifying the nitride layer prior to the polysilicon deposition.

3.5 References

- [3.1] S. M. Sze (editor), "VLSI Technology," McGraw Hill, 1983, pp. 120-126.
- [3.2] R.A. Laff and G.L. Hutchins, "Laser Fabrication of Large-Area Arrays: Thin-Film Silicon Isolated Devices on Fused Silica Substrates," IEEE Transactions on Electron Devices, Vol. ED-21, 1974, pp. 743.
- [3.3] S. K. Ghandhi, "VLSI Fabrication Principles," Wiley, 1983, pp. 383.
- [3.4] C. P. Ho and S. E. Hansen, "SUPREM III A Program for Intergrated Circuit Process Modeling and Simulation," Technical Report No. SEL 83-001, Integrated Circuits Laboratory, Department of Electrical Engineering, Stanford University, Stanford, CA 94305.
- [3.5] K. Honda, T. Nakanishi, A. Ohsawa, and N. Toyokura, "Catastrophic breakdown in silicon oxides: The effect of Fe impurities at the SiO₂-Si interface," J. Appl. Phys., Vol. 62, No. 5, September 1, 1987, pp. 1960-1963.
- [3.6] A. Zeltser and D. E. Laughlin, Department of Metallurgical Engineering and Materials Science, Carnegie Mellon University, 1988.
- [3.7] A. G. Milnes, "Deep Impurities in Semiconductors," Wiley, 1973, pp. 28.
- [3.8] S. Wolf and R. N. Tauber, "Silicon processing for the VLSI era," Volume 1: process technology, Lattice Press, 1986, pp. 199.
- [3.9] G. Winkler, "Magnetic Garnets," Friedr. Vieweg & Sohn, 1981, pp. 37.
- [3.10] S. Wolf and R. N. Tauber, "Silicon processing for the VLSI era," Volume 1: process technology, Lattice Press, 1986, pp. 192 & 199.
- [3.11] D. W. Greve, depositions at Yale University, August, 1985.

Chapter 4

The effects of thermal processing on magnetic bubble films

4.1 Introduction

This chapter deals with the stability of magnetic bubble films. We will begin by introducing the theory of magnetic bubble domains and the parameters used to characterize magnetic bubble films. Following this, we will outline the methods used to determine these important film parameters. The results of past magnetic measurements will be presented at the end of this chapter; these measurements show how the silicon-on-garnet magnetodiode fabrication process alters the fundamental room temperature magnetic properties of the bubble film.

4.1.1 Static properties of magnetic bubbles

In a useful bubble film, the magnetization $(4\pi M_s)$ is oriented perpendicular to the plane of the film. The magnetization is in this orientation if the uniaxial magnetic anisotropy energy density K_u exceeds the demagnetization energy $2\pi M_s^2$ [4.1]. If K_u is less than $2\pi M_s^2$, part of the magnetization will lie in the plane of the film to minimize the demagnetizing field H_d ; the remaining magnetization will still be perpendicular to the plane of the film. Here we have neglected the magnetoelastic and crystalline anisotropy energy densities as they are second order corrections to K_u . Magnetoelastic considerations become important when one is describing ionimplanted contiguous-disk bubble propagations patterns: if ions, such as H^+ , are implanted into a bubble film, the implanted layer will be put into compression [4.2]. The resulting stress gives rise to an anisotropy K_i which will either enhance or reduce the uniaxial anisotropy of the film. This can be written as:

$$K_u^i = K_u^0 + K_i \tag{4.1}$$

where K_u^i is the value of the uniaxial anisotropy after implantation, and K_u^o is the original growth induced anisotropy. Eschenfelder shows that K_i can be written as:

$$K_{i} = \frac{3}{2} \frac{E\lambda_{111}}{1 - v} \frac{\delta a_{o}^{f}}{a_{o}^{f}}$$
 (4.2)

where E is Young's modulus; v is Poisson's ratio; λ_{111} is the magnetostrictive coefficient for the [111] direction; $\mathbf{a_o^f}$ is the lattice constant for the bubble film, and $\delta \mathbf{a_o^f}$ is the expansion of the garnet lattice that results because of the implanted ions [4.3]. The magnetostriction coefficient λ_{111} represents the strain that is induced in a crystal when the material is magnetized to saturation in the [111] direction. This parameter is the one that determines the sign of K_i as all other quantities in equation 4.2 are positive. If λ_{111} is sufficiently large and negative, K_i will counteract K_u and the magnetization will be pulled into the plane of the film. If λ_{111} is positive, K_i will only strengthen K_u : the magnetization remains perpendicular to the plane of the film. It is impossible to fabricate ion-implanted contiguous-disk propagation patterns in this later case. The magnetostriction coefficient λ_{111} is thus a very important parameter of the bubble film.

Various domain patterns are possible when the magnetization is perpendicular to the plane of the film. In the case of a thin film with no externally applied magnetic fields, the magnetization will be oriented up in one half of the film and down in the other half. A transition region, called a domain wall and shown in figure 4-1, will bridge these two orientations because it is energetically unfavorable for the magnetization to alter its direction abruptly. The

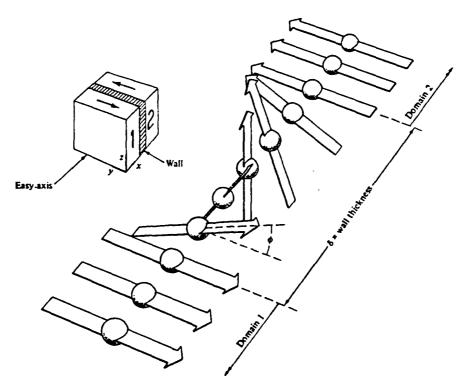


Figure 4-1: Structure of a Bloch wall

thickness of the domain wall is determined by minimizing the sum of the the anisotropy energy density, $E_K = K_u \sin^2 \theta$, and the exchange energy density, $E_x = A(d\theta/d\delta)^2$ [4.4]. Here A is the exchange constant for the material in question; θ is the orientation of the magnetization with respect to the normal of the film, and $d\theta/d\delta$ is the incremental rotation of the magnetization per increment of domain wall width. Domain walls add a positive component of energy to the system, but the resulting decrease in magnetostatic energy more than offsets this positive energy component [4.5, 4.6]. Now consider the case where an external magnetic field is applied perpendicular to the plane of the bubble film. Thiele studied this situation in detail and showed theoretically that an isolated bubble (a right circular cylinder of magnetization) is stable for a range of field values [4.7, 4.8]. If the bias field is lowered too much, the bubble will expand rapidly into a stripe domain. The bubble will "collapse" if the bias field is raised too much - the magnetization exists as a single domain in this case. The size of the bubble (its diameter as a function of the applied field), the stripe-out field, and the collapse field are easily found from a graphical calculation (see [4.9]). We must know I, the characteristic length, and h, the thickness of the bubble film, before the calculation can be carried out. The characteristic length is defined by $l=\sigma_{\rm w}/4\pi M_{\rm s}^2$ where $\sigma_{\rm w}$ is the wall energy density per unit area; it represents the value of h for which the increase in wall energy [due to the presence of the bubble] is balanced by a decrease in the magnetostatic energy, again due to the presence of the bubble domain [4.10].

4.1.2 Dynamic properties of magnetic bubbles

A magnetic bubble will move if it is exposed to a gradient in the bias field. The domain velocity for such a case is $1/2\mu_{\rm w}(|\Delta H_{\rm B}|-8H_{\rm c}/\pi)$, where $\mu_{\rm w}$ is the wall mobility; $\Delta H_{\rm B}$ is the change in bias field across the diameter of the bubble, and $H_{\rm c}$ is the domain wall coercive field [4.8]. No net bubble motion will occur when $|\Delta H_{\rm B}|$ is less than $8H_{\rm c}/\pi$. When motion does take place, we need to replace $H_{\rm c}$ by $H_{\rm d}$ where $H_{\rm d}$ is the dynamic coercivity of the bubble film. This dynamic coercivity is usually smaller than $H_{\rm c}$ (the static coercivity). A high quality bubble material should have a large $\mu_{\rm w}$ and a small $H_{\rm c}$ ($H_{\rm d}$).

4.1.3 Temperature dependence of bubble film parameters

The magnetic properties of a bubble film will depend on the film constituents as well as the location of these constituents within the film. In our work, we deal only with garnets, and we point out that these materials have a cubic crystal structure with a structural formula that is written as

$$\left\{RE_3^{3+}\right\} \left[Fe_2^{3+}\right] \left(Fe_3^{3+}\right) O_{12}$$
 (4.3)

Here, {RE} indicates a dodecahedral site (interstice) occupied by a rare earth ion and surrounded by 8 oxygens; [Fe] indicates an octahedral site occupied by an iron ion and surrounded by a total of 6 oxygens; (Fe) indicates a tetrahedral site occupied by an iron ion and encased by 4 oxygens [4.11]. The ions on these sites comprise three coupled magnetic sublattices, and we note that it is necessary to dilute these sublattices with non-magnetic ions like Y³⁺ (for the rare earth sites) and Ga³⁺ and/or Al³⁺ (for the iron sites) if one wants small diameter bubble films [4.12]. Such site substitutions for the diluents are preferential and temperature dependent: as an example, as grown Ga³⁺ substitutions tend to bifurcate about the tetrahedral and octahedral sites as 90% and 10%, but when a bubble film is annealed at an elevated temperature, some of the nonmagnetic Ga will transfer from (1/()) to (1/()) sites (4.13, 4.14, 4.15, 4.16, 4.17). An equal amount of iron, by necessity, must accompany this Ga transfer in the inverse direction. This forced transfer of iron from one sublattice to another will cause the net magnetization of the film to change since the octahedral and tetrahedral sublattice magnetizations are anti-parallel to one another. Ionic redistributions of large rare earth ions on the dodecahedral sites primarily affect K_u, and with respect to redistributions of ions on the octahedral or tetrahedral sites at a given temperature, these {} redistributions/exchanges are more difficult to effect [4.18, 4.19, 4.20].

4.2 Characterization of magnetic bubble films

The material parameters K_u , λ_{111} , $4\pi M_s$, l, h, μ_w , H_c , and H_d characterize the bubble film. Since our objective is to make silicon on garnet detectors integrated with propagation patterns, we have made measurements at critical points in our device fabrication process to determine these parameters for our bubble films. Ferromagnetic Resonance (FMR) measurements were made to determine K_u and λ_{111} ; we used the method employed by Krafft [4.21], but we did neglect the cubic crystalline anisotropy field. Krafft included this field component in his formulation. This cubic field is typically on the order of -100 to -200 oe for the [111] direction, and it represents a minor contribution to the uniaxial anisotropy field H_k ($H_k=2K_u/M_s$) [4.22]. The characteristic length, l, was determined from zero field stripe width measurements, and the saturation magnetization, $4\pi M_s$, was found from bubble collapse field measurements [4.23]. An optical interference technique, implemented at CMU by Krafft, was used to determine the thickness of all bubble films [4.24]. Stripe head motion experiments were made to determine the parameters μ_w , H_c , and H_d . These parameters are defined graphically in figure 4-2; v is the

velocity of the stripe head, and all fields represent pulsed values above the static bias field. The reader is referred to [4.25] for the theory and experimental details of the stripe head motion experiment.

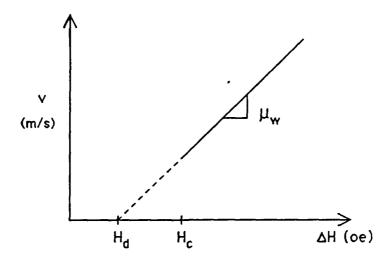


Figure 4-2: Stripe head (wall) velocity as a function of ΔH , where ΔH is an applied pulse field parallel to the bias field. H_d is the dynamic coercivity; H_c is the static coercivity, and μ_w is the domain wall velocity.

4.3 Laser annealed devices with a single layer spacer

High temperature processing is required in our first silicon on garnet process, and from the comments in section 4.1.3, we expected this kind of processing to alter the room temperature magnetic properties of a bubble film. It is therefore important to monitor the room temperature bubble film parameters like $4\pi M_8$ and l after all high temperature steps. Section 4.3.2 presents the results of such measurements to determine $4\pi M_8$ and l after a number of critical process steps. We will, however, first begin by introducing the important process steps in the next section (4.3.1).

4.3.1 Process

The substrates we started with are (111) GGG (Gd₃Ga₅O₁₂), and each substrate had a single bubble film on it. Device fabrication involved a large number of processing steps, but at this point, we are only interested in those steps which alter the magnetic nature of the bubble film (a more complete description of the current process can be found in section 6.2.1). Four of the steps in this first process which may change the room temperature magnetic properties of the bubble films we used are:

- 1. The sputter deposition of the $1\mu m SiO_2$ spacer layer,
- 2. Low pressure chemical vapor deposition of the $0.75\mu m$ polysilicon layer at $625^{\circ}C/0.4$ torr,
- 3. Laser recrystallization of the polysilicon layer at approximately 1415°C, and
- 4. the 850°C wet oxidation of the recrystallized silicon layer.

We point out that the above steps are listed in the order they are performed in the fabrication process.

4.3.2 Results

We found that the deposition of the $1\mu m$ SiO₂ spacer layer by sputtering did not alter the room temperature values of $4\pi M_s$ and I for a typical bubble film: the values listed in table 4-1 are within experimental error for the measurements we made. The polysilicon deposition does,

Film 166 Sample 166-54-30	4πM _S (G)	1 (μm)
As grown	634	0.1740
After sputtered SiO ₂ dep.	647	0.1782
After 625°C LPCVD poly-Si dep.	547	0.1989

h=1.28µm

Table 4-1: Room temperature magnetic properties of a $(Sm_{0.35}Gd_{0.55}Tm_{1.2}Y_{0.9})[Fe_{4.61}Ga_{0.25}Al_{0.14}]O_{12}$ bubble film (#166) before and after a $1\mu m/700W/2hr/20$ mtorr/Ar sputtered SiO_2 deposition. Note, this deposition was done in two parts: 1hr for the top bubble film and 1hr for the bottom film.

however, change both $4\pi M_s$ and l for the $(Sm_{0.35}Gd_{0.55}Tm_{1.2}Y_{0.9})[Fe_{4.61}Ga_{0.25}Al_{0.14}]O_{12}$ bubble film: $4\pi M_s$ decreases by 100 G and l increases by 0.0207 μ m, both with respect to the "after sputtered SiO_2 " values given in table 4-1. Films with different compositions, $(Sm_{0.3}Gd_{0.4}Tm_{0.73}Y_{1.57})[Fe_{4.6}Ga_{0.4}]O_{12}$ for example, may respond very differently to a given process step. Table 4-2 shows that this later bubble film (the only film we shall deal with for the remainder of this section) is essentially unaffected by the 625°C polysilicon deposition with respect to changes in $4\pi M_s$; there is, however, a small change in l. The laser recrystallization

Film 198	4πM _S (G)	l (μm)
As grown	687	0.1130
After 625°C LPCVD poly-Si dep.	691	0.1270
After laser anneal (LA area)	775	0.0928
(NLA area)	672	0.1215
After 20 min./850°C /0 ₂ annea1/(LA area)	673	0.1172
(NLA area)	689	0.1247

h=1.27µm

Table 4-2: Room temperature values of 4πM₈ and l at four key points in our first silicon on garnet process. We note that the composition of this particular bubble film (#198) is (Sm_{0.3}Gd_{0.4}Tm_{0.73}Y_{1.57})[Fe_{4.6}Ga_{0.4}]O₁₂

step does cause a substantial change to both $4\pi M_s$ and l. In this case, $4\pi M_s$ in the laser annealed area (LA area) is 103 Gauss larger than it is in the non-laser annealed area (NLA area), and l is 0.0287 μ m smaller in the LA area than it is in the NLA area. The $4\pi M_s$ and l values for the LA and NLA areas are reasonably well matched after the 850°C oxidation, however.

4.4 Laser annealed devices with a double layer spacer

High temperature processing is also required in our second silicon on garnet process, and as in section 4.3, we need to know which bubble film parameters will be changed by this processing. Section 4.4.1 introduces the high temperature processing steps of this second process. The effects of these process steps on the room temperature magnetic properties of two magnetic bubble films is considered in sections 4.4.2 and 4.4.4.

4.4.1 Process

In this section, as in section 4.3.1, we are only interested in those steps which alter the magnetic nature of the bubble film (a more complete description of the current process can be found in section 6.3.1). Five of the steps in this second process which may change the room temperature magnetic properties of the bubble films we used are:

1. Deposit $0.35\mu m$ - $0.41\mu m$ of LPCVD SiO_2 at $860^{\circ}C$ and 0.8-0.9 torr.

- 2. Deposit $0.24\mu m$ $0.85\mu m$ of LPCVD $\mathrm{Si_3N_4}$ at $800^{\circ}\mathrm{C}$ and 0.4 0.7 torr.
- 3. Deposit 0.55 \mu m of LPCVD polysilicon at 625 °C and 0.4 torr.
- 4. Laser recrystallization of the polysilicon layer at approximately 1415°C.
- 5. Wet O_2 (gate) oxidation at 850°C. The resulting SiO₂ layer is \sim 0.1 μ m thick.

We point out that the above steps are listed in the order they are performed in the fabrication process.

4.4.2 Results for a 1 micron bubble film family

Table 4-3 lists the room temperature values for $4\pi M_g$, l, and K_u for a $(Bi_{0.4}Dy_{0.7}Lu_{1.2}Sm_{0.2}Y_{0.5})[Fe_{4.45}Ga_{0.55}]O_{12}$ bubble film after a number of key processing steps. This is a 1μ m bubble film, and we point out that the values reported in table 4-3 are only approximate due to errors in the measurement of the zero field stripe width that are on the order of 10%. With this in mind, note that $4\pi M_g$ is essentially the same at the beginning and the end of the silicon on garnet process; K_u decreases by 20%, and l increases by 49%. These values are all with respect to the as grown ones. After the 850°C wet oxidation step, we observed some slightly non-ideal domain nucleation in randomly selected areas: a stripe domain would frequently nucleate additional ones as the bias field was lowered below stripe-out (at a rate of on the order of 10-30 oe/sec.). Long stripe domains also had a somewhat jagged appearance, and isolated bubble domains were still right-circular cylindrical in structure for bias fields between stripe-out and collapse.

4.4.3 Conclusions for the 1 micron bubble film family

The non-ideal domain structure and nucleation reported in section 4.4.2 are probably linked to an increase in H_c^{static} and/or H_c^{dynamic} , and we will show in the next section that these parameters do increase for a 2 μ m bubble film at a number of points in the fabrication process.

4.4.4 Results for a 2 micron bubble film family

Table 4-4 lists the room temperature values for $4\pi M_s$, l, K_u , λ_{111} , H_c^{static} , $H_c^{dynamic}$, and μ_w for a $(Bi_{0.3}Dy_{1.0}Lu_{1.0}Sm_{0.2}Y_{0.5})[Fe_{4.36}Ga_{0.64}]O_{12}$ bubble film after a number of key processing steps. This is a $2\mu m$ film, and we note that "LA area" indicates that a particular portion of the bubble film was annealed when the laser recrystallized the polysilicon directly

	4πM _S	1	K _u	
AH43	(gauss)	(µm)	(erg/cm ³)	
As Grown	587	0.1209	46,382	23°C
0.41µm LPCVD SiO ₂	477	0.1448		64 min. 860°C
0.24µm LPCVD Si ₃ N ₄	460	0.1553		11 min. 800°C
0.55 µm LPCVD Poly-Si	469	0.1632	41,409	50 min. 625*C
After Laser Anneal	565	0.0871	41,963	350-1412°C
0.1 µm Wet Oxidation	593	0.1796	37,114	50 min. 850°C

 $h = 1.21 \, \mu m$

Table 4-3: Room temperature magnetic properties of a 1μm bubble film (AH43) after key silicon on garnet process steps. Process steps are listed in the order in which they were performed. The composition of the bubble film is (Bi_{0.4}Dy_{0.7}Lu_{1.2}Sm_{0.2}Y_{0.5})[Fe_{4.45}Ga_{0.55}]O₁₂

above the area of interest. Likewise, "NLA area" indicates that an area was not scanned with the laser. The combined effect of the oxide, nitride, and polysilicon depositions is to lower $4\pi M_s$ by 64 G. Laser recrystallization, on the other hand, increases the magnetization in the scanned area (LA area) by 32 G. The magnetization in the non-laser annealed area, which was held at 350° C during the laser step, is for experimental purposes at the post-polysilicon deposition value of 397 G. An additional 17 G decrease in $4\pi M_s$ for the NLA area is seen after the 850° C oxidation, and it is interesting to note that there is a non-uniform recovery of the magnetization in the LA area (426 G to 400 G in some locations). Two noteworthy changes to I take place. The first occurs when the polysilicon is recrystallized, and in this case, we notice that the 0.1293 μ m post-laser anneal value is 0.0403 μ m smaller than the post-polysilicon deposition value. The second change in I occurs when we oxidize the polysilicon, and for this situation, we see that the 0.1615 μ m post-oxidation value is 0.0322 μ m larger than the post-laser recrystallization value. It's clear that these changes in I essentially cancel one another. A similar trend for K_u is observed: K_u first decreases from the as grown value of 52,034 erg/cm³ to the post-silicon

deposition value of 3341-12,122 erg/cm³, and then increases to the post-laser recrystallization and post-oxidation values of 28,918 erg/cm³ and 43,427 erg/cm³, respectively. The most we can say regarding the behavior of λ_{111} due to the very wide resonances observed during FMR is that we saw no significant changes in this parameter. The behavior of H_c^{static} and H_c^{dynamic} is, however, another story: H_c^{static} and H_c^{dynamic} after the polysilicon deposition are 19.57 oe and 26.78 oe larger than the corresponding as grown values. Further processing does not significantly alter H_c^{static} , but H_c^{dynamic} does increase after the 850°C wet oxidation for high pulse fields (64.7 - 90.6 oe). We indicate low field and high field values in table 4-4 by LF and HF, respectively. In our case, increases in H_c^{static} and H_c^{dynamic} are accompanied by corresponding decreases in μ_w with the exception of the HF entry in table 4-4: the post-silicon deposition and post-laser recrystallization values for μ_w are approximately a factor of two lower than the as grown value. Notice that the LF μ_w value after the 850°C oxidation is 9.2 times smaller than the as grown value.

The oxide, nitride, and polysilicon layers are deposited in a single set of processing steps in our present fabrication process, and this made it impractical to make magnetic measurements after the oxide and nitride depositions (hence the missing entries in table 4-4 for these steps). We still, however, need to know which process step or steps cause H_c^{static} and H_c^{dynamic} to increase as well as why these increases are so large. It was to this end that we conducted three additional experiments. The first one consisted of measuring H_c^{static} , H_c^{dynamic} , and μ_w for a bubble film with the same composition as AP84 before and after the LPCVD SiO_2 deposition. Table 4-5 lists the results from this experiment: H_c^{static} and H_c^{dynamic} after the oxide deposition are 25.81 oe and 31.56 oe larger than the corresponding as grown values. Comparing these values with the 19.57 oe and 26.78 oe increases seen after the oxide + nitride + polysilicon depositions, we conclude that the nitride + polysilicon depositions produce at most small changes to Hstatic and H^{dynamic}. We further conclude that the nitride + polysilicon depositions produce at most small changes to μ_w : compare the decrease seen after the SiO₂ deposition (a factor of 2.92) with that seen after the oxide + nitride + polysilicon depositions (a factor of 2.19 - table 4-4). So, it's clear that the 860°C LPCVD SiO, deposition is the problem step, and in our second experiment, we sought to identify which part of the LPCVD oxide deposition was causing the problems. Our assertion was and is that the pre-deposition phase of the oxide deposition is responsible for the rise in H_c^{static} and H_c^{dynamic}. To establish this claim, we conducted an experiment in which a sample spent most of its time in this state: we cycled one half of a bubble wafer (film AP102)

AP84		4πM _S (6)	l (μη)	K _u (erg/cm ³)	۱۱۱۸	HStatic Hc (oe)	Hagnar	nic μw (0e) (m/oe-sec)
As grown		461	0.1684	52,034	1.70 × 10 ⁻⁶ to 6.73 × 10 ⁻⁶	5.43	3.29	0.46
0.35 μm LPCVD Si0 ₂ 860°C/0.85 torr/62 min.	'n.	[1			
0.25 µm LPCVD SI3N4 800°C/0.40 torr/25 min.	- e	i	1	l	1		1	1
0.55 µm LPCVD poly-Si 625°C/0.40 torr/47 min.	:: <u>:</u>	397	9691.0	3341 to 12,122	-0.93 x 10 ⁻⁶ to 3.20 x 10 ⁻⁶	25.00	30.07	0.21
5 cm/sec beam scan speed	LA area	426	0.1293	28,918	2.11 × 10 ⁻⁶ to 8.51 × 10 ⁻⁶	29.78	31.92	0.17
size, 350-1415°C	NLA	394	0.1644	1	1	29.78	34.50	0.24
850°C wet oxidation 50 min.	LA area	400 - 436	0.1615	43,427	-9.7 x 10 ⁻⁶ to 3.49 x 10 ⁻⁶	32.35	22.05 LF 60.00 HF	0.05 LF 0.36 HF
02 120 • P = 1 atm	NLA	377	0.1654	1	1			1
h = 2.84 um IF = 1 ow field	_	F - Winh fleld						

Table 4-4: Room temperature magnetic properties of a $2\mu m$ bubble film (AP84) after key silicon on garnet process steps. Process steps are listed in the order in which they were performed. The composition of the bubble film is $(Bi_{0.3}Dy_{1.0}Lu_{1.0}Sm_{0.2}Y_{0.5})[Fe_{4.36}Ga_{0.64}]O_{12}$

with the same composition as AP84 through the 860° C LPCVD SiO_2 step without adding the N_2O and SiH_4 deposition gases (that is, we conducted a vacuum anneal). The characterization of this sample did not proceed far beyond visual inspections as the bubble film suffered a significant amount of decomposition during the anneal: it was noticeably blackened (our as grown bubble films are yellow to dark yellow in color), and the film surface, which should have been mirror-like, was clearly roughened by this second experiment. Coercivity measurements were not possible as we were unable to observe domains in the post-processed sample. Our assertion appears correct, and we further speculate that loss of oxygen from the bubble film during the pre-deposition period is directly linked with the increases in H_c^{static} and H_c^{dynamic} . In our third experiment, we proved that this is in fact the case by showing that a bubble film (the 2nd part of AP102) can withstand the 860° C SiO_2 deposition temperature for needed period of time if excess oxygen is present. Table 4-6 summarizes three interesting results from this atmospheric pressure O_2 annealing experiment: (1) the post-anneal value of H_c^{dynamic} is only 0.54 or larger than the as grown value; (2) the post-anneal value of H_c^{dynamic} is 1.51 or lower than the as grown value, and (3) the post-anneal value of H_c^{dynamic} is a factor of 1.74 higher than the as grown value.

4.5 Low temperature devices with a single layer spacer

Bubble films with process induced coercivity increases are highly undesirable; it is for this reason that we developed a "low coercivity" fabrication process. Oxygen loss is less of a problem in this process as the maximum temperature of this third process is 600°C. The results of section 4.5.2 show that the static and dynamic coercivities of the bubble film for the low temperature process are in fact a factor of three lower than the values reported for the laser annealed process reported in section 4.4.4. First, however, we will introduce the low temperature process in section 4.5.1.

4.5.1 Process

In this section, as in section 4.4.1, we are only interested in those steps which alter the magnetic nature of the bubble film (a more complete description of the current process can be found in section 6.4.1). Six of the steps in this second process which may change the room temperature magnetic properties of the bubble films we used are:

- 1. Deposit the 1μ m plasma SiO_2 spacer at 300° C.
- 2. Low pressure chemical vapor deposition of the $0.1\mu m$ amorphous Si layer at $545^{\circ}C/2.0$ torr.

AP100	H ^{static} (oe)	H <mark>dynam</mark> ic (oe)	μ _W (m/oe-sec)
As grown	5.34	5.23	0.76
0.35 μm LPCVD SiO ₂ 860°C/0.85 torr/62 min.	31.15	36.79	0.26

h ≈ 2.9 μm

Table 4-5: Values of the static coercivity, dynamic coercivity, and domain wall mobility for a $2\mu m$ (Bi $_{0.3}$ Dy $_{1.0}$ Lu $_{1.0}$ Sm $_{0.2}$ Y $_{0.5}$)[Fe $_{4.36}$ Ga $_{0.64}$]O $_{12}$ bubble film (AP100) before and after an 860°C LPCVD SiO $_2$ deposition.

AP102	H ^{static} (oe)	H ^{dynam} ic (oe)	μ _W (m/oe-sec)
As grown	5.34	6.36	0.57
860°C O ₂ anneal @ 1 atm with same temp/time cycle as a 0.35μm LPCVD SiO ₂ dep	5.88	4.85	0.99

h ≈ 2.9 μm

Table 4-6: Values of the static coercivity, dynamic coercivity, and domain for a 2μm (Bi_{0.3}Dy_{1.0}Lu_{1.0}Sm_{0.2}Y_{0.5})[Fe_{4.36}Ga_{0.64}]O₁₂ bubble film (AP102) before and after an 860°C O₂ anneal.

- 3. Crystallization of the amorphous silicon layer in vacuum at 550°C for 72 hrs.
- 4. Low pressure chemical vapor deposition of the 0.1 μ m SIPOS (Semi-Insulating POly-Silicon) gate material at 600° C/0.4 torr.
- 5. Oxidation of the SIPOS film for 24 hrs. in wet oxygen at 600°C.
- 6. Hydrogen plasma passivation at 300°C/0.7 torr/250 W for 5hrs.

For more information on this process, see section 6.4.1.

4.5.2 Results

To minimize damage to the silicon devices, we made magnetic measurements only toward the end of our low temperature process. Table 4-7 lists the room temperature values of $4\pi M_{\star}$, l, and K_u after process steps 5 and 6 for a 1 μm (Bi_{0.4}Dy_{0.7}Lu_{1.2}Sm_{0.2}Y_{0.5})[Fe_{4.45}Ga_{0.55}]O₁₂ bubble film (AH68). The net effect of steps 1-5 is to lower $4\pi M_e$ by 62 G, increase 1 by 0.0466 μ m, and increase K, by 3872 erg/cm³ with respect to the as grown values. Step 6, the hydrogen passivation, does not change the post-600°C wet oxidation values of $4\pi M_s$, l, and K_u to any significant degree. As grown values for H_c^{static} , H_c^{dynamic} , and μ_w are not available for AH68, and this is why the corresponding entries in table 4-8 are missing. We can, however, give ranges into which we think these parameters would fall based on characterization of 6 other bubble films with very similar compositions: H_c^{static} is expected to be in the 5.15 - 8.68 oe range; $H_c^{\rm dynamic}$ should be in the 3.29 - 11.28 oe range, and $\mu_{\rm w}$ is expected to fall in the 0.43 - 0.76 m/(oe-sec) range. The H_c^{static} , $H_c^{dynamic}$, and μ_w values given after the 600°C SIPOS oxidation are for the back film (the surface without devices) of AH68 since we did not want to risk damaging the silicon devices at that point in the process. It's clear that these values are essentially no different than the as grown values. We further expect that actual values for the top film (the one with devices) are not very different from the ones just quoted (both films are on the same GGG substrate and are grown at the same time). The values listed after the hydrogen passivation are also no worse than the as grown values given above, and we in addition point out that the general domain appearance was excellent: that is, we saw the expected serpentine domain structure and no signs of non-ideal domain nucleation

AH68	4πM _S (G)	l (μm)	K _u (erg/cm ³)
As grown values (from Ramesh)	650	0.0972	53,717
600° C wet oxidation 24 hrs. @ P = 1 atm 0_2 + H_2 0	588	0.1438	57,753
Hydrogen plasma passivation 300°C/0.7 torr/250 W/5 hrs.	591	0.1469	57,589

 $h = 1.46 \mu m$

Table 4-7: Room temperature values of $4\pi M_s$, l, and K_u after the listed process steps for a $1\mu m$ (Bi $_{0.4}$ Dy $_{0.7}$ Lu $_{1.2}$ Sm $_{0.2}$ Y $_{0.5}$)[Fe $_{4.45}$ Ga $_{0.55}$]O $_{12}$ bubble film (AH68).

AH68	H ^{static} (oe)	H ^{dynamic} (oe)	μ _Ψ (m/oe-sec)
As grown			
600°C wet oxidation 24 hrs./1 atm/ 0 ₂ + H ₂ 0 data for backside film	5.94	4.47	1.17
Hydrogen plasma passivation 300°C/0.7 torr/250 W/5 hrs. data for frontside film	9.00	8.21	2.17

Table 4-8: Values of the static coercivity, dynamic coercivity, and domain wall mobility at room temperature for a 1μ m (Bi $_{0.4}$ Dy $_{0.7}$ Lu $_{1.2}$ Sm $_{0.2}$ Y $_{0.5}$)[Fe $_{4.45}$ Ga $_{0.55}$]O $_{12}$ bubble film (AH68) after the listed steps.

4.6 Summary

At the beginning of this chapter in sections 4.1.1, 4.1.2 and 4.1.3, we introduced the static and dynamic properties of magnetic bubbles and established that high temperature processing can be expected to alter, at the very least, $4\pi M_s$ and K_u . Section 4.2 detailed the methods used to extract these and other bubble film parameters. Our first experimental work, presented in section 4.3, considered the effects of fabricating laser annealed devices with a single layer spacer $(Sm_{0.35}Gd_{0.55}Tm_{1.2}Y_{0.9})[Fe_{4.61}Ga_{0.25}Al_{0.14}]O_{12}$ on and $({\rm Sm_{0.35}Gd_{0.55}Tm_{1.2}Y_{0.9}})[{\rm Fe_{4.61}Ga_{0.25}Al_{0.14}}]{\rm O_{12}} \ \ {\rm bubble\ films.\ The\ most\ significant\ finding\ of\ most\ significant\ finding\ significant\ signi$ this work is that films containing the Al diluent are much more sensitive to process induced changes in $4\pi M_g$ than are films that contain only the Ga diluent. Our second set of experimental work, presented in sections 4.4.2 and 4.4.4, considered the effects of fabricating with laser annealed devices double layer $(\mathrm{Bi}_{0.4}\mathrm{Dy}_{0.7}\mathrm{Lu}_{1.2}\mathrm{Sm}_{0.2}\mathrm{Y}_{0.5})[\mathrm{Fe}_{4.45}\mathrm{Ga}_{0.55}]\mathrm{O}_{12} \ \ \mathrm{and} \ \ (\mathrm{Bi}_{0.3}\mathrm{Dy}_{1.0}\mathrm{Lu}_{1.0}\mathrm{Sm}_{0.2}\mathrm{Y}_{0.5})[\mathrm{Fe}_{4.36}\mathrm{Ga}_{0.64}]\mathrm{O}_{12}$ bubble films. In this case, the most significant finding of the work is that loss of oxygen from the bubble film during the pre-deposition phase of the LPCVD SiO₂ spacer deposition leads to major increases in the bubble film's static and dynamic coercivities. The third set of experimental work we did demonstrated that such changes can be avoided by keeping process temperatures at or below 600°C, and we thus conclude that low temperature silicon on garnet fabrication processes are an important development.

4.7 References

- [4.1] A. H. Eschenfelder, "Magnetic Bubble Technology," Second Edition, Springer-Verlag, 1981, pp. 2.
- [4.2] A. H. Eschenfelder, "Magnetic Bubble Technology," Second Edition, Springer-Verlag, 1981, pp. 126.
- [4.3] A. H. Eschenfelder, "Magnetic Bubble Technology," Second Edition, Springer-Verlag, 1981, pp. 326.
- [4.4] A. H. Eschenfelder, "Magnetic Bubble Technology," Second Edition, Springer-Verlag, 1981, pp. 28.
- [4.5] J. A. Cape and G. W. Lehman, "Magnetic Domain Structures in Thin Uniaxial Plates with Perpendicular Easy Axis," Journal of Applied Physics, Volume 42, Number 13, December, 1971, pp. 5732-5756.
- [4.6] Charles Kittel, "Physical Theory of Ferromagnetic Domains," Reviews of Modern Physics, Volume 21, Number 4, October, 1949, pp. 541-583.
- [4.7] A. A. Thiele, "The Theory of Cylindrical Magnetic Domains," The Bell System Technical Journal, Volume 48, Number 10, December, 1969, pp. 3287-3335.
- [4.8] A. A. Thiele, "Device Implications of the Theory of Cylindrical Magnetic Domains,"
 The Bell System Technical Journal, Volume 50, Number 3, March, 1971, pp. 725-773.
- [4.9] Jiin-chuan Wu, "Solid State Magnetic Devices: Magnetic Bubble Logic Devices and Vertical Bloch Line Memory," Ph.D. Dissertation, Carnegie Mellon University, Pittsburgh, Pennsylvania, August, 1986, pp. 10.
- [4.10] A. H. Eschenfelder, "Magnetic Bubble Technology," Second Edition, Springer-Verlag, 1981, pp. 32-33.
- [4.11] A. H. Eschenfelder, "Magnetic Bubble Technology," Second Edition, Springer-Verlag, 1981, pp. 171.
- [4.12] A. H. Eschenfelder, "Magnetic Bubble Technology," Second Edition, Springer-Verlag, 1981, pp. 163-187.
- [4.13] A. J. Kurtzig and M. Dixon, "Control of the Magnetization of Bubble Garnets by Annealing," J. Appl. Phys., Vol. 43, No. 6, June, 1972, pp. 2883-2885.
- [4.14] P. Roschmann, W. Tolksdorf, and F. Welz, "Annealing Effects on Cation Distribution in Diamagnetically Substituted Single Crystal Yttrium Iron Garnet," IEEE Transactions on Magnetics, Vol. MAG-14, No. 5, September, 1978, pp. 704-706.

- [4.15] P. Roschmann, "Redistribution Kinetics of Ga and Al Substitutions in Yttrium Iron Garnet," Journal of Magnetism and Magnetic Materials, 15-18, 1980, pp. 1305-1306.
- [4.16] L. Schultz, E. A. Giess, R. T. Hodgson, and T. O. Sedgwick, "Permanent local modification of the magnetic bubble properties of epitaxial garnet films by laser annealing," J. Appl. Phys., Vol. 50, No. 9, September, 1979, pp. 5902-5905.
- [4.17] B. Petek, E. A. Giess, and R. T. Hodgson, "Measurement of Fe-Ga ion interchange by pulsed laser heating and fast cooling of magnetic bubble films," J. Appl. Phys., Vol. 52, No. 6, June, 1981, pp. 4170-4175.
- [4.18] G. Winkler, "Magnetic Garnets," Friedr. Vieweg & Sohn, 1981, pp. 129-131.
- [4.19] A. J. Kurtzig, and F. B. Hagedorn, "Noncubic Magnetic Anisotropies in Bulk and Thin-Film Garnets," IEEE Transactions on Magnetics, Vol. MAG-7, September, 1971, pp. 473-476.
- [4.20] D. C. Cronemeyer, E. A. Giess, E. Klokholm, B. E. Argyle, and T. S. Plaskett, "Annealing of LPE Garnet Films," AIP Conference Proceedings, No. 5, 1972, pp. 115-119.
- [4.21] Charles Stuart Krafft, "Deuterium Implantation in Magnetic Garnets," Ph.D. Dissertation, Carnegie Mellon University, Pittsburgh, Pennsylvania, September 5, 1984, pp. 22-43.
- [4.22] J. O. Artman, Private Communication, October, 1987.
- [4.23] Charles Stuart Krafft, "Characterization of Magnetic Garnet Materials," Masters Thesis, Carnegie Mellon University, Pittsburgh, Pennsylvania, December 12, 1980, pp. 89-94.
- [4.24] Charles Stuart Krafft, "Characterization of Magnetic Garnet Materials," Masters Thesis, Carnegie Mellon University, Pittsburgh, Pennsylvania, December 12, 1980, pp. 12, eqn. 2.4.
- [4.25] Jiin-chuan Wu, "Solid State Magnetic Devices: Magnetic Bubble Logic Devices and Vertical Bloch Line Memory," Ph.D. Dissertation, Carnegie Mellon University, Pittsburgh, Pennsylvania, August, 1986, Chapter 4 and Appendix A.2.

Chapter 5

Theory and characterization of silicon magnetodiodes

5.1 Introduction

In this chapter we will summarize the large body of literature which exists on magnetodiodes [5.1]. We will then discuss the various ways of characterizing magnetodiodes. Finally, we present measurements of magnetodiode I(V) characteristics in sections 5.2.2 and 5.3.2. These results are important as they allow us to predict the performance of our differential magnetodiode sensor and the type of equipment required for testing.

5.1.1 Positive resistance devices

Magnetodiode sensitivities are highest when the magnetodiode is operated in one of the high-level double-injection regimes [5.2]. High-level indicates that the concentration of injected carriers is comparable to or larger than the concentration of donors, acceptors, and trap levels. In double injection both electrons and holes are important to the conduction process. Figure 5-1 shows the double injection regimes, beginning with the semiconductor regime, that are possible for a semiconductor with a small density of deep centers (traps) [5.3]. The magnetosensitivity in the ohmic region is purely magnetoresistive and has been shown to be negligible in SOS magnetodiodes for magnetic fields less than 5 T [5.2]. The current - voltage (I(V)) characteristics in the semiconductor regime for a n-type double-injection device are given by the Lampert-Rose relation [5.4]:

$$I = \frac{9}{8} bwe \mu_n \mu_p (n_o - p_o) \tau \frac{V^2}{d^3}$$
 (5.1)

where τ is the lifetime for the injected carriers; μ_n and μ_p are the electron and hole mobilities; e is the charge of an electron, and n_o and p_o are the equilibrium concentrations of electrons and holes in the n- base region. The geometry we are assuming is shown in figure 5-2. The Lampert-Rose relation can be used for a double injecting magnetodiode if the lifetime is replaced by a parameter which takes into account the effects of an applied magnetic field. This parameter, the effective lifetime τ_{eff} , has been calculated as [5.4]

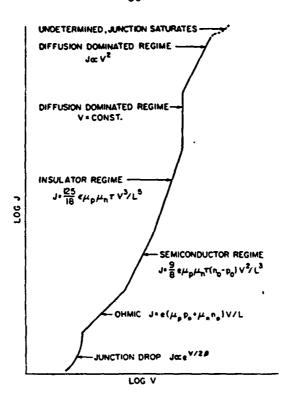


Figure 5-1: Schematic representation of the possible regimes of high-level double-injection behavior in a structure with a small density of deep centers, starting with the semiconductor regime. The manner in which the low-level regimes merge into the high-level regimes is also shown schematically (the "junction drop" regime shows up distinctly only for lower temperatures or for wide band-gap materials, i.e., when E_g/kT is large enough). Depending on material parameters, some of these regimes may not appear.

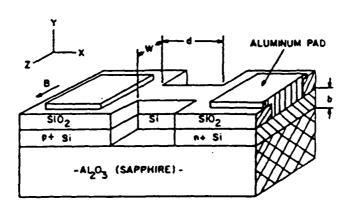


Figure 5-2: SOS magnetodiode structure. d = base length, w = base width, b = film thickness.

$$\bar{\tau}_{\text{eff}}^{1} = \bar{\tau}_{v}^{1} + L_{\text{B}}^{-1} \frac{s_{2} \exp(b/2L_{\text{B}}) + s_{1} \exp(-b/2L_{\text{B}})}{\exp(b/2L_{\text{B}}) - \exp(-b/2L_{\text{B}})}$$
(5.2)

where L_B^{-1} is given by $e(\mu_n + \mu_p)(BV/2kTd)$; τ_v is the bulk lifetime; B is the Z component of the magnetic field; s_1 is the surface recombination velocity of the top interface, and s_2 is the surface recombination velocity of the bottom interface. The magnetic field B deflects current carriers to the top or bottom interface, and since the surface recombination velocities of these interfaces are different, the mean density of carriers will be enhanced or reduced. This enhancement or reduction will change the conductivity of the n- base, and the conductivity change will cause a change in diode voltage and/or current. Equation (5.2) assumes an exponential distribution of carriers between the top and bottom interfaces; Cristoloveanu et al. show that this is a reasonable approximation to the actual situation [5.5]. These authors also describe a simple method to experimentally determine the parameters τ_v , s_1 , and s_2 : one constructs plots of I vs. V^2 , for three different values of B, and measures the slope of each plot. It follows from equation (5.1) that this measurement gives three different values of τ_{eff} ; these values can be used along with equation (5.2) to set up a system of three equations with three unknowns. The parameters τ_v , s_1 , and s_2 are found by solving this system of equations.

5.1.2 Negative resistance devices

Current filaments can be formed in magnetodiodes when the density of deep centers is large. A current filament is a nonuniform distribution of current density in a sample with a uniform electric field - figure 5-3 shows a drawing of a current filament. We are interested in filamentary double-injecting devices as these devices exhibit magnetic sensitivities larger than those of non-filamentary magnetodiodes. Sensitivities exceeding 20 V/T are possible for filamentary double-injecting magnetodiodes [5.2]. The characteristic curve for a filamentary double-injection device is shown in figure 5-4, and we show the energy-band diagram for a device with such a characteristic in figure 5-5. The device is assumed to have a single deep-lying donor trap. The current - voltage characteristic will remain linear as long as the hole (minority carrier) lifetime τ_p is less than transit time, the time required for holes to transverse the base region. As the hole lifetime becomes equal to the transit time, the bulk current conduction is changed from an ohmic to a one-carrier space-charge-limited current mechanism. This latter regime is described by the relation

Except as noted, the material in this paragraph is taken from reference [5.6]

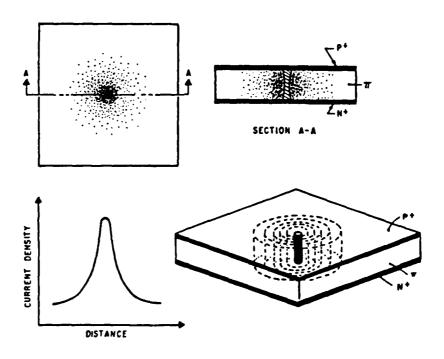


Figure 5-3: Drawing of a current filament in a $p+\pi n+$ device, where π stands for a lightly doped p-type base.

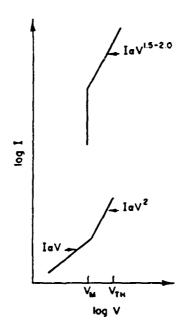


Figure 5-4: Characteristic curve of a filamentary double-injection device.

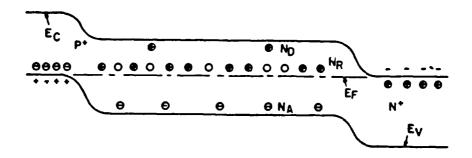


Figure 5-5: Energy-band diagram for a double-injection device with a deep-level impurity.

$$J = \frac{9}{8} \epsilon \mu_{\rm p} \frac{V^2}{d^3} \tag{5.3}$$

where ϵ is the dielectric constant of the semiconductor. The V² region continues as long as the electron (majority carrier) lifetime τ_n is less than the transit time. The conduction mechanism shifts from a one-carrier space-charge-limited current to a two-carrier space-charge-limited current when the majority-carrier transit time becomes equal to its lifetime. Majority-carrier transit then becomes significant as the majority-carrier traps are filled, and negative resistance sets in. The current increases while the voltage decreases for two reasons: (1) the lifetime of the majority carriers increases, and (2) the space charge in the base is reduced by the presence of a similar number of carriers of both signs. Current filaments may exist in the negative resistance region, the region where current increases at constant voltage, and in the high-current power-law region. In the high-current postbreakdown region, marked by voltages greater than $V_{M'}$. Lampert's model for an insulator has been used to describe device behavior. The model, however, does not explain all of the experimental results found for the postbreakdown region, and we thus refer the reader to [5.6] for more information on the nature of this region.

5.2 Magnetodiodes on silicon substrates

5.2.1 Device fabrication

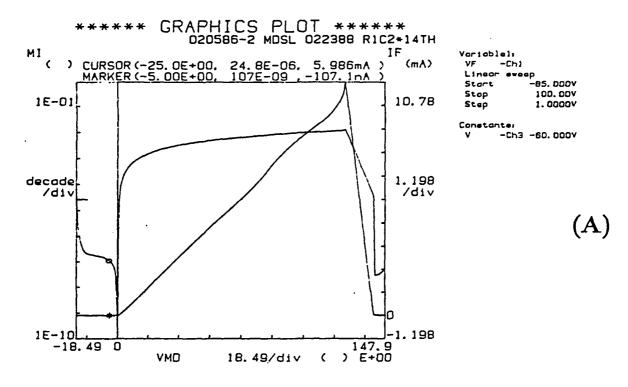
In this case, the fabrication process is identical to that described in section 5.3.1 with the exception that a silicon substrate is used.

5.2.2 Results

We have fabricated silicon magnetodiodes on silicon substrates coated with SiO_2 and Si₃N₄. These devices have dc I(V) characteristics similar to the one shown in figure 5-6(A). If the diode is biased above 136V, the device silicon melts and a open circuit results as shown in figure 5-6(B). Figure 5-7(A) shows a plot of the magnetodiode current for another, but similar, magnetodiode as the magnetic field is swept between plus and minus 16kG at a rate of approximately 1.1kG/sec; the diode's forward voltage drop, 30 V, is well below the breakdown value of 136V. Current maxima are at +16kG and current minima are at -16kG. The geometry pertinent to this measurement is shown in figure 5-7(B). Current is perpendicular to and out of the plane of the paper. The magnetic field is positive when directed to the right and is negative when directed to the left. The force $(F = qv \times B)$ on electrons and holes is directed away from the paddle when the magnetic field is positive and is directed toward the paddle when the magnetic field is negative. The magnetodiode's bottom interface is closest to the paddle. So, from the discussion of magnetodiodes given in chapter 1, we see that the locations of experimental maxima and minima are exactly where they should be. The data given in figure 5-7(A) can also be used to calculate the magnetic sensitivity $(\Delta I/\Delta B)$ for the represented device since ΔI is directly proportional to ΔB for a constant diode bias voltage [5.2]. The calculation we made using this data shows that $\Delta I/\Delta B$ is on the order of 2.5 x $10^{-4}\mu A$ per gauss per μm of diode width for our devices. This result and the result for ΔB from the end of chapter 2 can be used to predict the worst case differential current signal expected from the design of figure 1-10. Each diode in this design is $3\mu m$ wide, and each diode sees a flux $\Delta B/2$. It therefore follows that the sensor's differential current output, shown in figure 1-11 as $2\Delta I$, is given by

$$\Delta I_{\text{Diff}} = 2 \left(\frac{94.43 \text{ gauss}}{2} \right) \left(3 \mu \text{m} \right) \left(2.5 \times 10^{-4} \frac{\mu \text{A}}{\text{gauss-}\mu \text{m}} \right) = 71 \text{ nA}.$$
 (5.4)

This result assumes that the current in each diode is 0.136 mA, and it, the result, probably underestimates the $2\Delta I$ signal expected from our proposed differential magnetodiode sensor as the magnetosensitivity of $2.5 \times 10^{-4} \mu A/G$ - μ m was measured for a non-double injection device. The device of figure 5-7 did not exhibit the V^2 current law for the range of voltages we considered. Future devices should not have this problem since they will have more ideal base doping profiles and base lengths. Signals larger than 71nA are thus expected, but 71nA is still large enough to demonstrate magnetic bubble detection.



YMC () = VF-V-IF+1.33E3 MI () = ABS(IF)

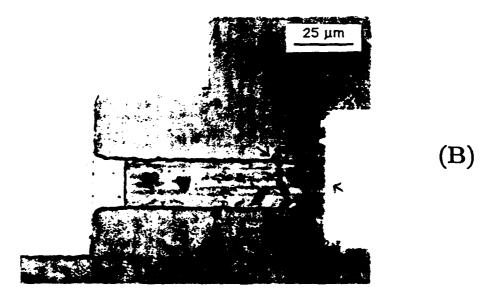


Figure 5-6: (A) Current - voltage characteristic for a magnetodiode fabricated on a silicon substrate, both log and linear plots are given (MI and IF, respectively). (B) Failure mode for the device (020586 MDSL R1C2 after 14th) of part (A).

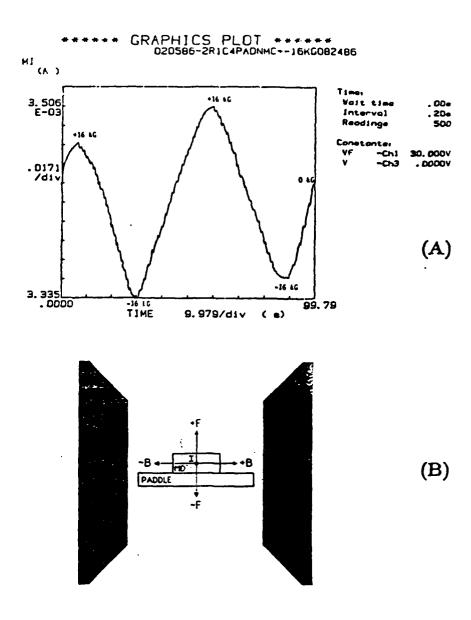


Figure 5-7: (A) Diode forward current I_D (in amps) with an applied in-plane magnetic field; the field was swept between + and - 16kG. See part B of this figure for device orientation and sign conventions. The diode is 25μm wide and was fabricated on a silicon substrate. Otherwise, the structure is identical to that of figure 5-8. (B) Orientation of the magnetodiode (MD) during the measurements; the bottom interface is closest to the paddle.

5.3 Magnetodiodes on bubble substrates

5.3.1 Device fabrication

The substrates we start with are (111) GGG (Gd₃Ga₅O₁₂), and each substrate has a single $[Sm_xTm_yLu_{3-(x+y)}](Fe_{5-z}Ga_z)O_{12}$ bubble film on it. Two spacer layers are deposited on these bubble substrates: the first is a 0.41 μ m SiO₂ passivation layer, and the second is a 0.24 μ m Si₃N₄ barrier layer. Both of these films are deposited by low pressure chemical vapor deposition (LPCVD); the SiO₂ is deposited at 860° C/0.8-0.9 torr, and the Si₃N₄ is deposited at 800° C/0.7 torr. These films isolate the 0.55 μ m silicon device layer from the bubble substrate. The 0.55 μ device quality silicon layer is formed in a two part process: (1) the silicon is deposited on the composite spacer in polycrystalline form at 625° C/0.4 torr by LPCVD, and (2) the grain size of the polysilicon is increased by laser recrystallization [6.2]. Device islands are next defined, etched, and doped n+/p+ in the contact regions by ion implantation. We then grow a 0.1 μ m SiO₂ oxide layer from the large grain polysilicon film in a wet oxygen ambient at 850° C, open contacts to the n+ and p+ regions, deposit aluminum, and pattern the aluminum layer to form the necessary electrodes. The completed structure is shown in figure 5-8. Base lengths for this structure were taken from the work of Karakushan et al. [5.7] with the assumption that silicon on garnet material is similar to SOS material.

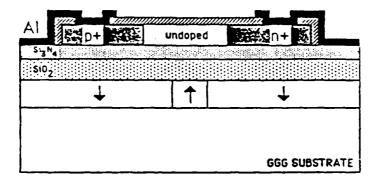


Figure 5-8: Silicon on garnet cross section

5.3.2 Results

Silicon on garnet magnetodiodes fabricated with the process described in section 5.3.1 have I-V characteristics that are of the negative resistance type, but they deviate in detail from the form shown in figure 5-4. Figure 5-9 shows the type of characteristic we observe. The high-current negative resistance regime is retraced each time the device is stressed. The same,

however, can not be said of the low-current positive resistance region: if the diode is driven deep enough (greater than approximately 11.15 mA for the device of figure 5-10) into the negative resistance region during a test, the current in the positive resistance region during the next test will decrease at all voltages. A three order of magnitude decrease is common, and the trends are as shown in figure 5-10. Here resistance, the magnetodiode voltage divided by the magnetodiode current VMD/IF, is graphed in order to make the range of the plots convenient. For current levels exceeding 28.53 mA (for the device of figure 5-9), thermal effects dominate, and a conductive molten silicon filament is likely to form between the two ohmic contacts [5.8]. The molten silicon when formed will mix with aluminum from the contacts to form a low resistance path between the n+ and p+ regions [5.9, 5.10]. Such a failure is shown in the photo of figure 5-11. It is therefore necessary to bias the magnetodiode below the 28.53 mA current value to exploit the high sensitivities mentioned in section 5.1.2.

Additional work needs to be carried out before we can firmly fit our magnetodiode data to the appropriate device model, but we can make a few preliminary comments at this point. Out of the ions present in the bubble film (Sm, Tm, Lu, Ga, and Fe), only Ga and Fe are likely to be present in the Si film. This conclusion is based on the observation that it is very difficult to introduce large ions into the silicon lattice: Gusev et al. were unsuccessful in trying to introduce Sm into silicon at 1240°C [5.11], and we therefore expect similar results for Tm and Lu as these ions are approximately the same size as Sm. Iron, on the other hand, is known to have a diffusion coefficient that is approximately five orders of magnitude greater than any of the commonly used silicon dopants (B, P, As, etc.) while Ga has a diffusion coefficient that is within an order of magnitude of the commonly used silicon dopants [5.12]. Both Fe and Ga introduce deep levels in the silicon band gap [5.13]. Fe introduces three deep donor levels: one is located 0.4 eV from the valence band, a second 0.14 eV from the conduction band, and a third 0.51 eV from the conduction band. Ga introduces a single deep acceptor at 0.072 eV from the valence band. Hence, we should not automatically expect a theory developed for a single deep-lying donor to adequately model the case where four possibly interacting deep levels are present.

The behavior of the low-current positive resistance part of the I-V characteristic can be explained by postulating the existence of traps within the Si₃N₄ spacer layer. Such a hypothesis is plausible and we refer the reader to [5.14,5.15,5.16] for the details. These traps are initially empty, and the occupancy of these traps is not greatly changed at low injection levels (low

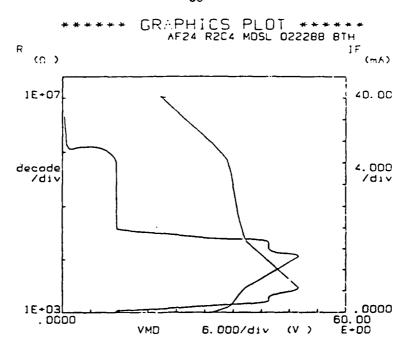


Figure 5-9: I-V characteristic for a silicon on garnet magnetodiode; a plot of the diode resistance (VMD/IF) is also given. The composition of the bubble film is (Sm Tm Lu)₃[Fe Ga]₅O₁₂.

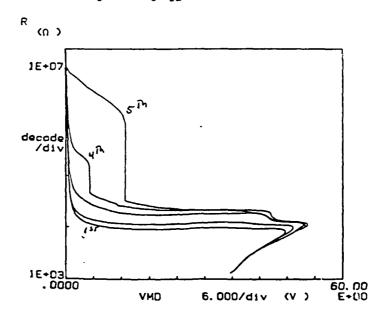


Figure 5-10: Magnetodiode resistance (VMD/IF) for a silicon on garnet magnetodiode vs. voltage across the device (AF24 R2C4 MDSL 021988) as a function of maximum forward current. The maximum forward currents for plots 1 through 5 are 11.15mA, 15.84mA, 19.65mA, 23.36mA, and 27.24mA, respectively. The composition of the bubble film is (Sm Tm Lu)₃[Fe Ga]₅O₁₂.

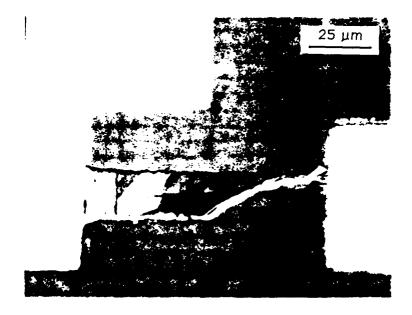


Figure 5-11: Al-Si short between the ohmic contacts of a magnetodiode (AF24 R1C4 MDSL 2-19-88/8:30P). The short appears as a narrow white streak. The composition of the bubble film is (Sm Tm Lu)₃[Fe Ga]₅O₁₂.

magnetodiode currents). At high injection levels (high magnetodiode currents), however, the occupancy will change significantly due to the presence of a large density of carriers that can tunnel to the Si_3N_4 deep levels from the silicon conduction band. We, in effect, have a gated diode structure in which the gating voltage (the charge injected into the Si_3N_4) depends on the injection level and past history of the device. This gating voltage decreases the device current at low injection levels since it reduces the free carrier density in the magnetodiode's base.

5.4 Summary

Magnetodiodes are important silicon on garnet devices because the fringing flux from a magnetic domain can modulate the diode's output current and/or voltage. This effect is most pronounced when the device is operated in one of the high-level double-injection regimes, and we also note that magnetodiodes can be of either the positive or negative resistance type. Negative resistance devices are preferred since these magnetodiodes have sensitivities exceeding 20 V/T if diode is biased such that one or more current filaments exist in the n- base of the device. Our silicon on garnet magnetodiodes can be biased in the negative resistance/filamentary mode of operation as reported in section 5.3.2. Operating points in this mode are stable and repeatable, but we have noticed some hysteresis effects in the pre-breakdown positive-resistance region. If the diode is driven too deep into the negative resistance mode, thermal effects will dominate, and

a conductive molten silicon filament is likely to form between the two ohmic contacts. This is a failure mode for the diode since the molten silicon will mix with aluminum from the contacts to form a permanent short between the n+ and p+ regions.

At present, the only sensitivity data we have for magnetodiodes is for diodes fabricated on silicon substrates. Section 5.2.2 reports that these devices have $\Delta I/\Delta B$ values of 2.5 x $10^{-4}\mu A$ per gauss per μm of diode width, and we think that this value underestimates the potential sensitivity of silicon on garnet magnetodiodes since the devices of section 5.2.2 are most likely not double injection ones.

5.5 References

- [5.1] H. P. Baltes and R. S. Popovic, "Integrated Semiconductor Magnetic Field Sensors," Proceedings of the IEEE, Vol. 74, No. 8, August, 1986, pp. 1107-1132.
- [5.2] A. Mohaghegh, S. Cristoloveanu and J. De Pontcharra, "Double- Injection Phenomena Under Magnetic Field in SOS Films: A New Generation of Magnetosensitive Microdevices," IEEE Transactions on Electron Devices, Vol. ED-28, No. 3, March 1981, pp. 237-242.
- [5.3] R. Baron and J.W. Mayer, in "Semiconductors and Semimetals," vol 6, New York: Academic Press, 1970, ch. 4, p208.
- [5.4] O. S. Lutes, P. S. Nussbaum, and O. S. Aadland, "Sensitivity Limits in SOS Magnetodiodes," IEEE Transactions on Electron Devices," Vol. ED-27, No. 11, November 1980, pp. 2156-2157.
- [5.5] S. Cristoloveanu, G. Kamarinos, P. Viktorovitch, J. Borel, and R. Staderini, "Characterization of Thin Silicon Films Based on Their Magnetosensitiveness," Proc. 7th Intern. Vac. Congr. & 3rd Intern. Conf. Solid Surfaces (Vienna 1977), pp. 1943-1946.
- [5.6] Allen M. Barnett, in "Semiconductors and Semimetals," vol. 6, New York: Academic Press, 1970, ch. 3, pp. 141-155.
- [5.7] E. I. Karakushan, V. Ya. Kovarskii, K. F. Komarovskikh, E. I. Gamolin, and V. I. Stafeev, "Magnetodiodes Made of Pigh-Resistivity Silicon," Soviet Physics -Semiconductors, Vol. 3, No. 11, May 1970, pp. 1453-1454.
- [5.8] D. H. Pontius, W. B. Smith, and P. P. Budenstein, "Filamentation in silicon-on-sapphire homogeneous thin films," J. Appl. Phys., Vol. 44, No. 1, January 1973, pp. 331-340.

- [5.9] D. W. Greve and L. V. Tran, "Polysilicon n+p-n+ Structures for Memory Redundancy," IEEE Transactions on Electron Devices, Vol. ED-29, No. 8, August 1982, pp. 1313-1318.
- [5.10] M. E. Lunnon, and D. W. Greve, "The microstructure of programmed n+pn+polycrystalline silicon antifuses," J. Appl. Phys., Vol. 54, No. 6, June 1983, pp. 3278-3281.
- [5.11] I. A. Gusev, L. I. Molkanov, and A. N. Murin, "Diffusion of Certain Rare Earth Elements into Germanium," Soviet Physics-Solid State, Vol. 6, No. 4, October 1964, pp. 980-981.
- [5.12] A. G. Milnes, "Deep Impurities in Semiconductors," John Wiley & Sons, 1973, pp. 29.
- [5.13] S. M. Sze, "Physics of Semiconductor Devices," Second Edition, John Wiley & Sons, 1981, pp. 21.
- [5.14] S. Fujita and A. Sasaki, "Dangling Bonds in Memory-Quality Silicon Nitride Films," J. Electrochem. Soc.: Solid-State Science and Technology, Vol. 132, No. 2, February 1985, pp. 398-402.
- [5.15] S. Fujita, H. Toyoshima, M. Nishihara, and A. Sasaki, "Variations of Trap States and Dangling Bonds in CVD Si₃N₄ Layer on Si Substrate by NH₃/SiH₄ Ratio," Journal of Electronic Materials, Vol. 11, No. 4, 1982, pp. 795-812.
- [5.16] S. Fujita, M. Nishihara, W. Hoi, and A. Sasaki, "Deep Trap States in Si₃N₄ Layer on Si Substrate," Japanese Journal of Applied Physics, Vol. 20, No. 5, May 1981, pp. 917-923.

Chapter 6 Silicon on Garnet MOSFET's

6.1 Introduction

In this chapter, we will present our results for MOSFET's that have been fabricated on magnetic bubble substrates. First, we present results for laser annealed devices that have been fabricated on bubble substrates coated with a single silicon dioxide spacer layer. Next, we present results for an improvement to this process: laser annealed devices that have been fabricated on bubble substrates coated with SiO₂ and Si₃N₄. The final results we report are for devices fabricated with a low temperature process on bubble substrates coated with a plasma SiO₂ spacer layer.

6.2 Laser annealed MOSFET's with a single layer spacer

The first silicon on garnet MOSFET's were fabricated on magnetic bubble substrates coated with a single SiO₂ spacer layer. This structure, shown in figure 6-1, has been previously described in detail [6.1]. Our discussion of this structure will focus on its fabrication and electrical characteristics.

6.2.1 Device fabrication

The substrates we start with are (111) GGG (Gd₃Ga₅O₁₂), and each substrate has a single [Y_{1.00}Sm_{0.39}Tm_{0.92}Ca_{0.69}](Ge_{0.70}Fe_{4.30})O₁₂ bubble film on it. A 1μm thick sputtered SiO₂ layer is the first film deposited on these substrates. This spacer layer isolates the silicon device layer from the bubble substrate. The device quality silicon layer is formed in a three part process: (1) 0.75 μm of silicon is deposited on the spacer in polycrystalline form at 625°C by low pressure chemical vapor deposition (LPCVD); (2) a 1μm SiO₂ cap layer is deposited on the polysilicon by sputtering, and (3) the grain size of the polysilicon is increased by laser recrystallization [6.2]. Isolated device islands are next defined, etched, and doped p-type by ion implantation. The n+ source/drain regions are also formed by ion implantation with the p-type channel being protected by photoresist during this step. We next grow a 0.1μm gate oxide layer

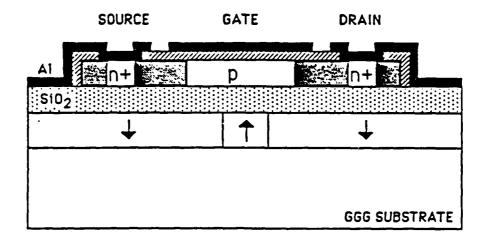


Figure 6-1: Cross section of a silicon on garnet MOSFET with a sputtered SiO₂ spacer layer. The spacer is $\sim 1\mu m$ thick.

from the polysilicon layer in a wet oxygen ambient at 850°C, open source/drain contacts, deposit aluminum, and pattern the aluminum layer to form the source, drain, and gate electrodes shown in figure 6-1.

6.2.2 Electrical Characteristics

A few devices fabricated with the process described in section 6.2.1 have I-V characteristic such as the one shown in figure 6-2. Electron mobilities for these devices are on the order of 3 cm²/V-sec. The remaining 95% have characteristics like the one shown in figure 6-3. In both the best and worst cases, gate leakage currents are orders of magnitude higher than those observed in high quality MOSFET's fabricated on silicon substrates. The case shown in figure 6-3 represents a total device failure since the gate currents are high enough to prevent the formation of an inversion layer under the MOSFET's gate. We believe that these leakage currents are caused by ionic contamination present in the gate oxide layer, and we further believe that this contamination originated in the sputtered SiO₂ and bubble films [6.1].

6.3 Laser annealed MOSFET's with a double layer spacer

In our second set of laser annealed MOSFET's, we used a double layer spacer to reduce contamination levels in the recrystallized silicon film and the oxide grown from it. This structure is shown in figure 6-4. The following discussion will concentrate on the fabrication and electrical characterization of MOSFET's fabricated on the oxide/nitride spacer system.

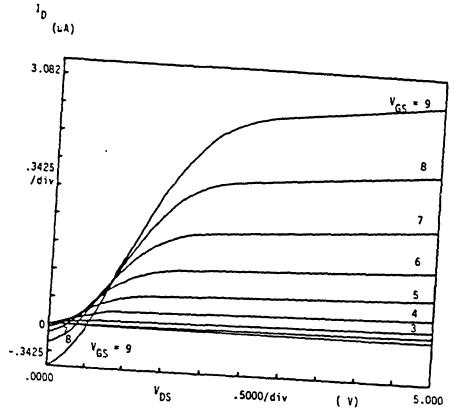


Figure 6-2: Drain characteristics for a silicon on garnet MOSFET with a non-zero gate leakage current. See figure 6-1 for a cross section of this device (wafer L10A).

8.3.1 Device fabrication

The substrates we start with are (111) GGG (Gd₃Ga₅O₁₂), and each substrate has a single [Sm_xTm_yLu_{3-(x+y)}](Fe₅₋₂Ga₂)O₁₂ bubble film on it. Two spacer layers are deposited on these bubble substrates: the first is a 0.41µm SiO₂ passivation layer, and the second is a 0.24µm Si₃N₄ barrier layer. Both of these films are deposited by low pressure chemical vapor deposition (LPCVD); the SiO₂ is deposited at 860°C/0.8-0.9 torr, and the Si₃N₄ is deposited at 800°C/0.7 torr. These films isolate the 0.55µm silicon device layer from the bubble substrate. The 0.55µ device quality silicon layer is formed in a two part process: (1) the silicon is deposited on the composite spacer in polycrystalline form at 625°C/0.4 torr by LPCVD, and (2) the grain size of the polysilicon is increased by laser recrystallization [6.2]. Device islands are next defined, etched, and doped n+ by ion implantation in the source/drain regions. We then grow a 0.1µm SiO₂ gate oxide layer from the large grain polysilicon film in a wet oxygen ambient at 850°C, open source/drain contacts, deposit aluminum and pattern the aluminum layer to form the source, drain, and gate electrodes. The completed structure is shown in figure 6-4.

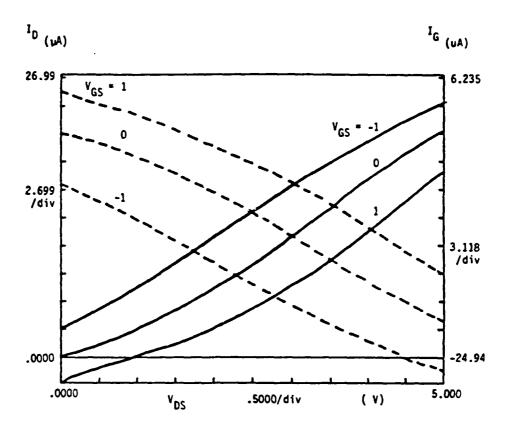


Figure 6-3: Drain characteristics for a silicon on garnet MOSFET with a catastrophic gate leakage current. See figure 6-1 for a cross section of this device (wafer L10A).

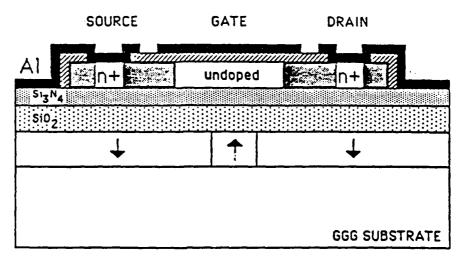


Figure 6-4: Cross section of a silicon on garnet MOSFET with a double spacer.

6.3.2 Electrical Characteristics

Most of the devices fabricated with the process described in section 6.3.1 have I-V characteristics like the one shown in figure 6-5. The characteristics are well behaved, and we

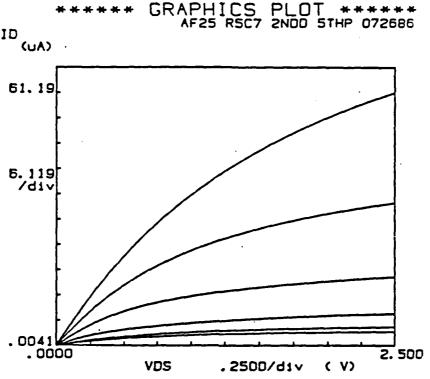


Figure 6-5: Drain characteristics for a device with the structure shown in figure 6-4; current is in μA, and voltage is in volts. The SiO₂ spacer layer is 0.41μm thick, and the Si₃N₄ film is 0.85μm thick (devices with 0.24μm of Si₃N₄ have similar drain characteristics). The composition of the magnetic bubble layer is Sm_xTm_yLu_{3-(x+y)}(Fe_{5-z}Ga_z)O₁₂. This MOSFET has a channel length/width ratio of 17μm/35μm.

note that gate leakage is not a problem for the test conditions used (the absence of negative drain current for small positive drain to source voltages confirms this point). This latter fact makes it possible for us to reliably measure the mobility of electrons in the channel of our n channel MOSFET's. We used the method suggested by Muller and Kamins [6.3]. Briefly stated, one plots the zero-bias channel conductance as a function of gate voltage and calculates the mobility from the slope of the resulting plot (figure 6-6(A)). Using this procedure we found, MOSFET's fabricated on bubble substrates coated with the oxide+nitride spacers have top gate electron mobilities on the order of 100-200 cm²/V-sec. We were also able to determine from this plot, and ones similar to it, that our MOSFET's had a back gate conductance: the value of the back gate conductance is just the value of I_d/V_{ds} near V_g =0 (the flat part of the curve). We

established that the top gate electron mobility is not affected by the presence of the back gate conductance by making a set of mobility measurements on silicon substrates coated with oxide+nitride spacer layers. First, we measured the electron mobility for a given device with the back gate on $(V_{bg}=0\ V)$. Next, we measured the electron mobility with the back gate turned off $(V_{bg}=-40\ V)$. The mobility with the back gate on was 175 cm²/V-sec, and the mobility with the back gate off was 177 cm²/V-sec. Within experimental error, these values are the same, and one can, therefore, model a silicon-on-garnet MOSFET with back gate conductance as shown in figure 6-6(B).

The superiority of the oxide+nitride spacer, over the oxide only spacer, is even more apparent when one views plots of the gate current I vs. gate voltage V with the source and drain grounded. Figure 6-7 shows three plots of Ig vs. Vg. The solid line plot is for a MOSFET fabricated on a bubble substrate coated with only a silicon dioxide spacer. The dashed line plot is for a MOSFET fabricated on a bubble substrate coated first with silicon dioxide and next with silicon nitride. Increasing the thickness of the Si_3N_4 film from $0.24\mu m$ to $0.85\mu m$ improves the gate breakdown voltage by nearly 1 volt; this can be seen by comparing the dashed line plot with the dotted line plot. The plot shown in figure 6-8 is for a MOSFET fabricated on a silicon substrate coated first with silicon dioxide and next with silicon nitride. This latter substrate served as a control or monitor wafer. The characteristics are noticeably sharper for the devices with the oxide + nitride spacer system. Now compare only the solid and dotted characteristics of figure 6-7. To make the comparison valid, the gate oxides of both devices are stressed such that the oxide electric fields are identical. We selected 25 V/µm for convenience. For the device represented by the solid characteristic shown in figure 6-7, this corresponds to a gate voltage of 1.25 V as its gate oxide is approximately 0.05 \mu m thick. For the device represented by the dotted characteristic of figure 6-7, this corresponds to a gate voltage of 2.5 V as its gate oxide is approximately $0.1\mu m$ thick. If we now take note of the gate areas (313 μm^2 for the device represented by the solid characteristic of figure 6-7 and 590 μm^2 for the device represented by the dotted characteristic of figure 6-7), we find: I per unit area of gate oxide is nearly 2.5 x 10⁵ times smaller for the MOSFET fabricated on the bubble substrate coated with the oxide+nitride spacer.

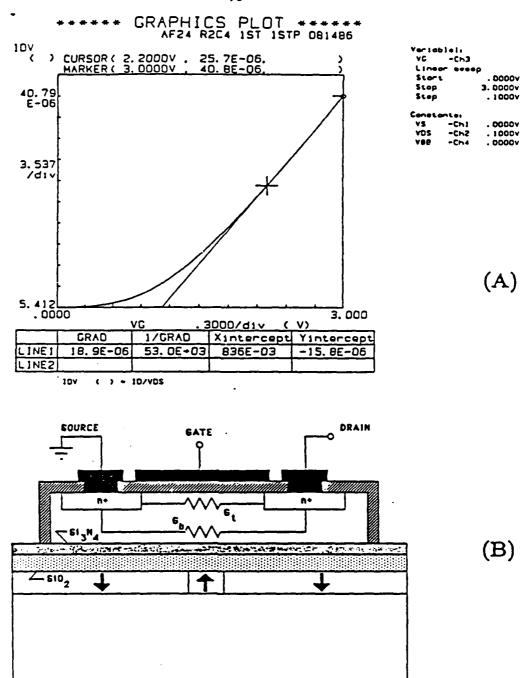


Figure 6-6: (A) Zero-bias channel conductance (amps/volt) as a function of gate voltage (volts); a potential of 0.1 V (zero bias for practical purposes) is applied between the source and drain. The SiO₂ spacer layer is 0.41 μm thick and the Si₃N₄ film is 0.24 μm thick. This MOSFET has a length/width ratio of 17μm/35μm. The composition of the magnetic bubble layer is Sm_xTm_yLu_{3-(x+y)}(Fe_{5-z}Ga_z)O₁₂. See figure 6-4 for the relevant cross section. (B) First order model of a silicon-on-garnet MOSFET with top (intended) and bottom (unintended) conduction channels.

GGG SUBSTRATE

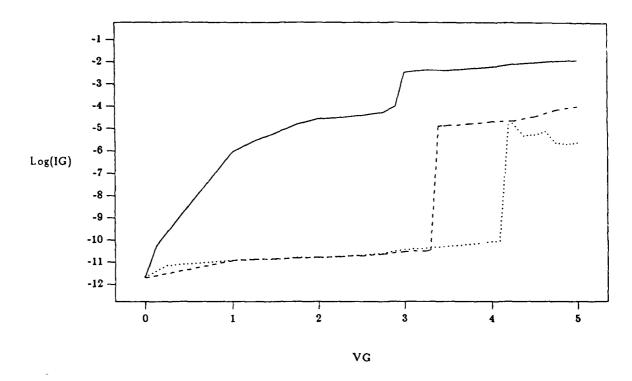


Figure 6-7: Plots of the gate leakage current I_g (in amps) vs. the gate voltage V_g (in volts) with the drain and source at ground potential $(V_{ds} = 0 \text{ V})$ for three sets of spacers: (1) the solid plot is for a MOSFET fabricated on a [Sm_{1.2}Tm_{0.1}Lu_{1.7}](Fe_{5-z}Ga_z)O₁₂ bubble substrate coated with a 1μm thick SiO, spacer (wafer AC44); (2) the dashed plot is for a MOSFET fabricated on a $[Sm_xTm_yLu_{3-(x+y)}](Fe_{5-z}Ga_z)O_{12}$ bubble substrate coated first with $0.41 \mu m$ of SiO₂ and next with $0.24 \mu m$ of Si₃N₄ (wafer AF24), and (3) the plot dotted is MOSFET for fabricated $[S \uparrow_x Tm_y Lu_{3-(x+y)}] (Fe_{5-z} Ga_z) O_{12}$ bubble substrate coated first with $0.41\mu \text{m}$ of SiO₂ and next with $0.85\mu \text{m}$ of Si₃N₄ (wafer AF25). The channel length/width ratios for these three cases are:(1) $12.5\mu m/25\mu m$, (2) $17\mu m/35\mu m$, and (3) $17\mu m/35\mu m$.

6.3.3 Conclusions

The data we have presented firmly establishes that high quality MOSFET's can be fabricated on magnetic bubble substrates. Electron mobilities are typically 100-200 cm²/V-sec, and most devices have gate breakdown voltages in the 3-4 V range. This 3-4 V value should not, however, be taken as an upper limit since these devices were not processed optimally: thermally induced stresses resulting from the laser recrystallization of large areas of polysilicon (each ~1.8cm x 1.8cm) caused significant cracking of the oxide+nitride spacer, and we speculate that this cracking may have allowed ions from the bubble film to contaminate the islands of

Ċ

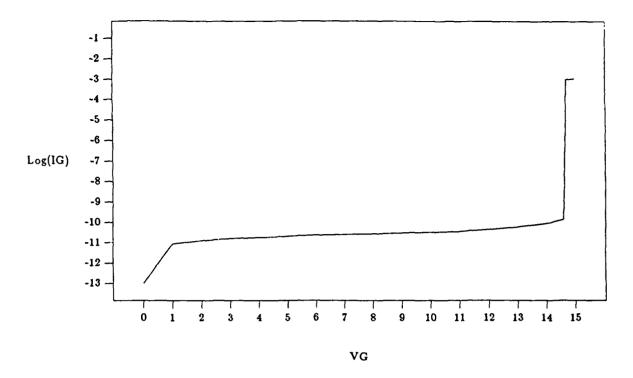


Figure 6-8: A plot of the gate leakage current I_g (in amps) vs. the gate voltage V_g (in volts) with the drain and source at ground potential ($V_{ds}=0$ V) for a MOSFET on a silicon substrate coated with $0.41\mu m$ of SiO_2 (first layer on the silicon substrate) and $0.24\mu m$ of Si_3N_4 (second layer on the silicon substrate 020586-2). The channel length/width ratio of the MOSFET is $17\mu m/35\mu m$.

recrystallized polysilicon. One can and should minimize the area of polysilicon recrystallized since smaller recrystallized areas have less tendency to crack than larger ones. We saw no cracking of the spacer in areas that were not recrystallized. The back gate channels that characterize our MOSFET's are the result of trapped positive charge present in the oxide plus nitride spacer layer [6.4, 6.5]. It is possible to suppress these back gate channels by heavily doping the silicon at the back interface.

6.4 Low temperature MOSFET's with a single layer spacer

Both sets of laser annealed MOSFET's (see sections 6.2 and 6.3) had contamination induced gate leakage currents; it is for this reason that we sought a process in which contaminants were less likely to diffuse from the bubble film into the silicon layer. Low temperature processes are therefore the most promising, and the one we adapted to the silicon on garnet material system was developed by Hseih et al. [6.6]. The 600°C maximum temperature of

this process is approximately 815°C lower than that of the laser based processes. In the next two subsections, we will discuss the fabrication and electrical characteristics of MOSFET's fabricated with this low temperature process.

6.4.1 Device fabrication

The substrates we start with are (111) GGG (Gd₃Ga₅O₁₂), and each substrate has a single $[Bi_{0.4}Dy_{0.7}Sm_{0.2}Lu_{1.2}Y_{0.5}](Fe_{4.45}Ga_{0.55})O_{12}$ or $[Bi_{0.3}Dy_{1.0}Sm_{0.2}Lu_{1.0}Y_{0.5}](Fe_{4.36}Ga_{0.64})O_{12}$ bubble film on it. The first layer deposited on these substrates is a 1μ m plasma SiO₂ film deposited at 300° C. It is this spacer layer that isolates the silicon device layer from the bubble substrate. The 0.1μ m device quality silicon layer is formed in a two part process: (1) the silicon is deposited on the spacer in amorphous form at 545° C/2 torr by low pressure chemical vapor deposition (LPCVD), and (2) it is converted to a polycrystalline film during a 72 hour/550°C vacuum anneal. Device islands are next defined, etched, and doped with arsenic. Following this, we deposit the gate material, a 0.1μ m thick layer of Semi-Insulating POly-Silicon (SIPOS). The SIPOS film is then oxidized for 24 hours at 600° C in a wet oxygen ambient. Contact windows to the n+ regions are opened in the oxidized SIPOS film; aluminum is deposited and etched to form the source, drain, and gate electrodes as shown in figure 6-9. The final step of the process is a 5 hour/ 300° C/0.7 torr hydrogen plasma passivation of the grain boundary trap states present in the polysilicon device layer.

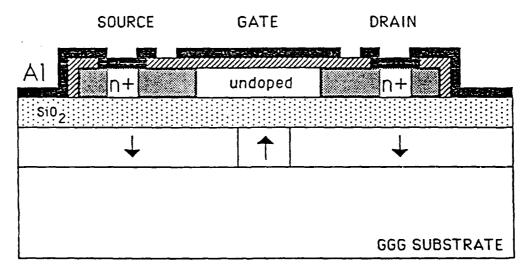


Figure 6-9: Cross section of a low temperature silicon on garnet MOSFET with a single SiO₂ spacer.

6.4.2 Electrical characteristics

Essentially all of the MOSFET's fabricated with the process described in section 6.4.1 have I-V characteristics like the one shown in figure 6-10. The characteristics are again well behaved,

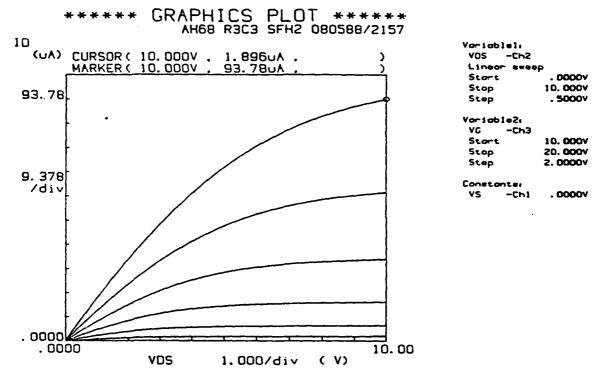


Figure 6-10: Drain characteristics for a low temperature silicon on garnet MOSFET with the structure shown in figure 6-9 after hydrogen passivation. The SiO_2 spacer is $0.1\mu m$ thick, and the channel length/width ratio is $7.9\mu m/75\mu m$.

and gate leakage is also not a problem for the test conditions used (the absence of negative drain current for small positive drain to source voltages confirms this point). It is therefore possible to apply the mobility extraction method described in section 6.3.2: we have found that our best low temperature silicon on garnet MOSFET's have channel electron mobilities on the order of 2.8 cm²/V-sec before hydrogen passivation and 8.0 cm²/V-sec after hydrogen passivation. More importantly, however, we found that gate breakdown voltages for devices with and without passivation exceed 20 V for both the silicon and bubble substrates. This represents at least a factor of five improvement with respect to the laser annealed MOSFET's with the double layer spacer system. We have also found that gate leakage currents before and after passivation are typically less than 250 μ A for gate voltages up to 20V; here the source and drain are held at 0V to insure a worst case test. Threshold voltages for the low temperature devices, V, is on the order of

7V (no passivation) to 9V (with hydrogen passivation). The laser annealed devices have V_t 's on the order of 0V (a typical device had $V_t = 0.4V$; see figure 6-6(A)).

The question of drift in thin-film transistors is an important one, and we did investigate the stability of our thin-film MOSFET's. In the experiment we conducted, we fixed the drain to source voltage at a value of 5-10V, applied a 15 V pulse to the gate, and observed the resulting drain current as a function of time. Figure 6-11(A) shows a plot from such an experiment for a device on a bubble substrate without hydrogen passivation (the drain to source voltage (VDS) was fixed at 10 V). There is a slight decay of drain current with time during the period in which the pulse is at a non-zero voltage, but this decay does not exceed 5.7% of the initial drain current. When this experiment was repeated on the same device after hydrogen passivation, we observed that the drain current increased as a function of time during the non-zero gate voltage interval; figure 6-11(B) shows the plot for this case. The 45.3% increase with respect to the initial drain current is much larger than that seen by Hseih et al. [6.6]. We compared our results for the bubble wafer to those determined for a silicon substrate and found the same trends: for devices on a silicon substrate, the drain current decay before hydrogen passivation was 4.6%, and after hydrogen passivation, the drain current increase was 17.0% (compare the plots in figure 6-12 with those of figure 6-11. The drain current decay seen in the devices without hydrogen passivation can be explained by postulating the trapping of charge in localized insulator states [6.6, 6.7]; however, the increase in drain current for the passivated devices requires a different explanation. Part of the answer may involve mobile ion charge in the oxidized SIPOS layer, but additional work needs to be done.

6.5 Summary

We have fabricated working silicon on garnet MOSFET's with three different processes. In the first process, we fabricated laser annealed MOSFET's on magnetic bubble wafers coated with a 1µm thick SiO₂ spacer layer. These first MOSFET's all had contamination induced gate leakage currents, and we note that the source of this contamination was the bubble substrate in large part. The electron mobilities for devices with the lowest leakage currents were on the order of 3 cm²/V-sec. With our second process, we fabricated laser annealed MOSFET's on magnetic bubble substrates coated with LPCVD SiO₂ (first layer on the bubble wafer) and Si₃N₄ (second layer on the bubble wafer). Devices with this double layer spacer had gate leakage currents that remained in the pA range for gate to source/drain voltages up to approximately 4.1V. Electron

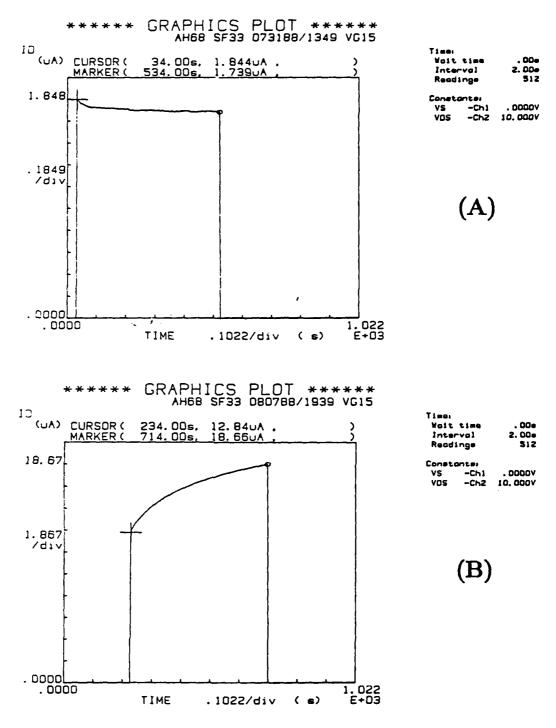


Figure 6-11: (A) A plot of the drain current I_d (in μA) vs. time (in seconds) for a low temperature silicon on garnet MOSFET before hydrogen passivation with the source at 0V, the gate at 15V, and drain at 10V. The channel length/width ratio of this device is 7.9μm/75μm, and we note that the composition of the bubble film is [Bi_{0.4}Dy_{0.7}Sm_{0.2}Lu_{1.2}Y_{0.5}](Fe_{4.45}Ga_{0.55})O₁₂. (B) Same as part (A) of this figure, but after hydrogen passivation.

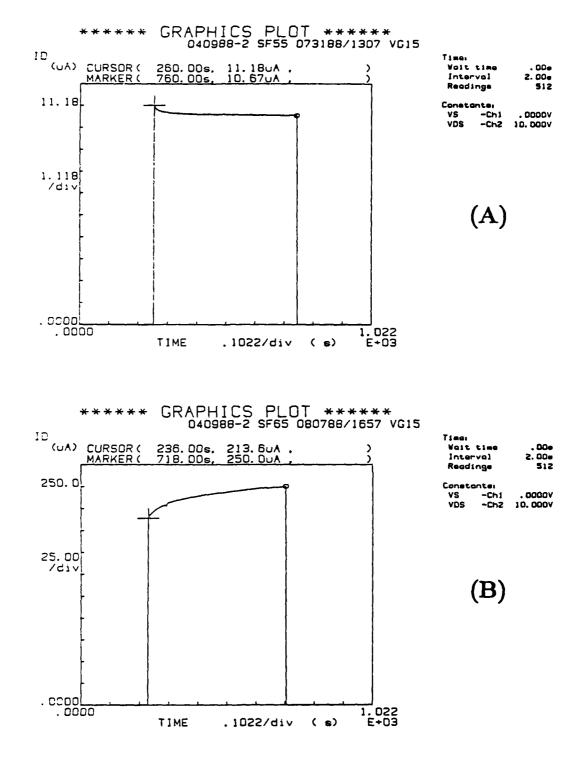


Figure 6-12: (A) A plot of the drain current I_d (in μ A) vs. time (in seconds) for a low temperature MOSFET fabricated on a silicon substrate coated with a 1μ m thick plasma SiO₂ spacer, before hydrogen passivation with the source at 0V, the gate at 15V, and drain at 10V. The channel length/width ratio of this device is 7.9μ m/75 μ m. (B) Same as part (A) of this figure, but after hydrogen passivation.

mobilities for these MOSFET's were typically in the 100-200 cm²/V-sec range. We can thus conclude that the nitride layer is acting somewhat like diffusion barrier: if were not, we would expect to see results similar to those we saw with our first process. Low temperature devices fabricated with our third process have gate breakdown voltages exceeding 20 V. Electron mobilities, on the other hand, tend to rather low, 2.8 cm²/V-sec before hydrogen passivation and 8.0 cm²/V-sec after. These later results are nonetheless important since they firmly show that silicon devices with low levels of contamination can be fabricated on magnetic garnets.

6.6 References

- [6.1] P. H. L. Rasky, "Silicon on Garnet MOSFET's: The Hybridization of Silicon and Magnetic Bubble Technologies," Masters Project Report, Carnegie Mellon University, December 1984.
- [6.2] R. A. Laff and G. L. Hutchins, "Laser Fabrication of Large-Area Arrays: Thin-Film Silicon Isolated Devices on Fused Silica Substrates," IEEE Transactions on Electron Devices, Vol. ED-21, 1974, pp. 743.
- [6.3] R. S. Muller and T. I. Kamins, "Device Electronics for Integrated Circuits," John Wiley & Sons, 1977, p. 362.
- [6.4] S. M. Sze (editor), "VLSI Technology," McGraw Hill, 1983, pp. 154-156.
- [6.5] B. G. Streetman, "Solid State Electronic Devices," second edition, Prentice-Hall, 1980, pp. 307-308.
- [6.6] B.-C. Hseih, M. K. Hatalis, and D. W. Greve, "Low Temperature Polycrystalline Silicon Thin-Film Transistors for Displays," IEEE Transactions on Electron Devices, Vol. ED-35, No. 11, 1988.
- [6.7] E. C. Freeman and F. C. Luo, "Traps at the Al₂O₃/CdSe Interface," J. Appl. Phys., Vol. 53, 1982, pp. 5294-5303.

Chapter 7

Conclusions

We have shown in this report that working silicon devices can be fabricated on magnetic bubble substrates. In particular, we have shown that silicon on garnet magnetodiodes can be integrated with ion-implanted contiguous-disk bubble propagation patterns to construct novel self-aligned magnetic-bubble sensors. Our magnetic field calculations for the design and placement of bubble domain sensors have clearly shown that diode base widths of a few micrometers are optimal for the detection of 2µm diameter bubble domains. Fabrication of these sensors has been attempted with a laser annealed silicon on garnet fabrication process, and we have discussed some of the problems which accompany such a process. Process induced coercivity increases can be avoided by limiting the maximum process temperature to 600°C. Higher temperatures can be used if steps are taken to prevent the loss of oxygen from the bubble film. The magnetodiodes we have fabricated on magnetic bubble substrates have current voltage characteristics that suggest that these devices may have magnetosensitivities exceeding 20 V/T. At present, however, the only sensitivity data we have for magnetodiodes is for diodes fabricated on silicon substrates; these devices have $\Delta I/\Delta B$ values of 2.5 μA per tesla per μm of diode width, and we think that this value underestimates the sensitivity of our silicon on garnet magnetodiodes since the former devices are most likely not operating in highest sensitivity mode, the negative resistance/filamentary double injection regime. Even if it does not underestimate the sensitivity of our silicon on garnet magnetodiodes, we can still demonstrate bubble detection as the sensor in connected in a differential fashion. In the worst case, we could use laser annealed or low temperature MOSFET's to amplify the detector's output to acceptable levels.

Simulation, Fabrication, and Testing of Logic Gates Designed for Deflecting and Non-deflecting Bubbles

A Project Report
Submitted to the Graduate School
In Partial Fulfillment of the Requirements
for the degree of
Master of Science
in
Electrical and Computer Engineering

by

Allen Bruce Cowen

Carnegie Mellon University Pittsburgh, PA 20 December 1988

Table of Contents

i

1. Introduction	2
1.1. Bubble Stability ⁵	3
1.2. Bubble Translation	6
1.3. Current Access Bubble Propagation	9
1.4. Previous Logic Gate Designs	10
1.4.1. Current Access Dual Conductor Logic Gates	10
1.4.1.1. Non-deflecting Bubbles	11
1.4.1.2. Deflecting Bubbles	13
2. Logic Element Design for Deflecting and Non-deflecting Bubbles	15
2.1. Computer Simulation	15
2.2. Device Design	17
3. Experimental Methods	21
3.1. Fabrication	21
3.2. Test	22
4. Results	26
4.1. Control Gate	28
4.2. AndOr Gate	34
4.3. ExclusiveOr Gate	38
5. Discussion	40
5.1. Fabrication	40
5.2. Design	41
5.3. Conclusion	42
Appendix A. Material Characterization	43
Annendix B. Riss Margins	46

List of Figures

Figure 1-1:	Coordinate system for specifying magnetization direction	4
Figure 1-2:	F, S ₀ , S ₂ vs. d/h (After Thiele ⁶)	6
Figure 1-3:	Variation in bubble size, d, vs. bias field, H _B , for film thickness, h/l	6
	(After Thiele ⁷)	
Figure 1-4:	Magnetic bubble wall structures: (a),(b) S=1 wall structure (c)	7
_	S=0 wall structure (after Eschenfelder ⁵)	
Figure 1-5:	Annihilation of Bloch lines (after Eschenfelder ⁵)	8
Figure 1-6:	Stability map showing state transitions (after Brown) ⁹	9
Figure 1-7:	Propagation in dual conductor current access devices: (a) field	11
1 .g d. c 1-1.	produced by perforation in conductor sheet (b) current sequence	••
T: 1 0.	used	10
Figure 1-8:	AndOr gate and the various possible routes for the input bubbles (after Wu ³)	12
Figure 1-9:	Control gate (after Smith ⁴)	13
Figure 2-1:	File created by simulator: indicates starting and stopping position	18
T: 0.0	of bubbles and the design of the gate	
Figure 2-2:	Bias field margin created by the simulator, indicates the landing positions of the bubbles and the range of the bias field and current	18
E: 0.0	density	
Figure 2-3:	New presentation of Fig. 2-2	19
Figure 2-4:	Multiple third level generators for continuous gate testing	20
Figure 3-1:	Process topography (not to scale, microns used for dimensions)	22
Figure 3-2:	Electronic equipment used in testing (after Smith)	24
Figure 3-3:	Test waveforms (after Smith) Control Gate	25
Figure 4-1: Figure 4-2:	Simulated margins for the four S=1 input bubbles	29 30
Figure 4-2:	Overall margin for the S=0 bubbles	31
Figure 4-4:	Simulated bias margins for S=1 and S=0 bubbles using an	32
1 18410 1-1.	increased mobility for gate in Fig. 4-1	02
Figure 4-5:	Experimental margins for the Control logic gate	32
Figure 4-6:	Simulated margins for the Control gate using measured material	33
	parameters	•
Figure 4-7:	AndOr Gate	34
Figure 4-8:	Simulated margins for the AndOr gate	35
Figure 4-9:	Experimental margins for the AndOr gate	36
Figure 4-10:		36

parameters Figure 4-11: Alternate design for the AndOr gate 37 Figure 4-12: Experimental margin for AndOr gate in Fig. 4-11 37 Figure 1-13: ExclusiveOr gate 38 Figure 4-14: Simulated margin for the Xor gate 39 Figure 4-15: Experimental margin for the Xor gate 39 Figure B-1: Gate 2: Control Gate 46 Figure B-2: Experimental margins for gate 2 46 Gate 3: Control Gate Figure B-3: 47 Figure B-4: Experimental margins for gate 3 47 Figure B-5: Gate 4: Control Gate 48 Figure B-6: Experimental margins for gate 4 48 Figure B-7: Gate 5: Control Gate 49 Figure B-8: Experimental margins for gate 5 49 Figure B-9: Gate 6: Control Gate **50** Figure B-10: Experimental margins for gate 6 50 Figure B-11: Gate 7: Control Gate 51 Figure B-12: Experimental margins for gate 7 51 Figure B-13: Gate 8: Control Gate **52** Figure B-14: Experimental margins for gate 8 52 Figure B-15: Gate 9: AndOr Gate **53** Figure B-16: Experimental margins for gate 9 53 Figure B-17: Gate 10: AndOr Gate 54 Figure B-18: Experimental margins for gate 10 54 Figure B-19: Gate 11: AndOr Gate 55 Figure B-20: Experimental margins for gate 11 **5**5 Figure B-21: Gate 13: AndOr Gate 56 Figure B-22: Experimental margins for gate 13 56 Figure B-23: Gate 15: AndOr Gate 57 Figure B-24: Experimental margins for gate 15 57 Figure B-25: Gate 16: AndOr Gate 58 Figure B-26: Experimental margins for gate 16 58 Figure B-27: Gate 17: ExclusiveOr Gate 59 Experimental margins for gate 17 Figure B-28: 59 Figure B-29: Gate 18: ExclusiveOr Gate 60 Figure B-30: Experimental margins for gate 18 60 Figure B-31: Gate 20: ExclusiveOr Gate 61 Figure B-32: Experimental margins for gate 20 61 Gate 21: Control Gate Figure B-33: 62 Figure B-34: Experimental margins for gate 21 62 Figure B-35: Gate 24: Control Gate 63

63

Figure B-36: Experimental margins for gate 24

List of Tables

Table 1-1:	Summary of bubble logic components (after Hwang ²)	12
Table 1-2:	Summary of experimental gate bias field margins for deflecting	14
	bubble logic gates operated at J1=2 mA/micron (after Smith4)	
Table 4-1:	Simulated and experimental device parameters	27
Table 5-1:	Summary of experimental gate field margins at J1=2ma/micron	42

Acknowledgements

I would like to extend my appreciation to my thesis advisor Mark H. Kryder for his guidance and support. I would also like to thank Stanley H. Charap and Zoltan Cendes for being on my committee.

This research could not have been attempted without the previous work done by Robert Smith, Dave Shenton, and J.C. Wu, all of whom helped me immensely. Thanks also should go to Mahedevan Ramesh for the growth and characterization of the films and to Pete Koeppe, Walt Eppler, Kathy Nitzberg, Shih-Cheng Cheng and Paul Raskey for their help with the experiments and for valuable discussions about the subject. Finally, I would like to give special thanks to Mike Alex for his help with the fabrication techniques and experiments.

Abstract

The objective of the work presented in this thesis was the design, fabrication, and successful testing of magnetic bubble logic gates that operate with bubbles that deflect from a field gradient and also with bubbles that do not deflect from the gradient. Bobeck's dual perforated conductor sheet current access technology was used to move the bubbles and the magnetostatic repulsion between the bubbles was used to produce the correct logic operations. Three types of gates have been designed to perform the Controlling, And, Or, and Exclusive-Or logical functions. The gates were designed to be tolerant of a wide range of forces between bubbles so that they will have wide drive current and bias field margins.

The devices are fabricated on two micron nominal bubble diameter films of composition $Y_{0.4}Sm_{0.2}Lu_{1.5}Bi_{0.7}Dy_{0.2}Ga_{0.9}Fe_{4.1}O_{12}$ uniformly implanted with 3.6×10^{14} oxygen ions per cm² at 110 KeV for hard bubble suppression. The thin film fabrication techniques produce .1 microns of sputtered SiO_2 spacer and three .25 micron thick sputtered aluminum layers separated by .26 micron thick hard-baked photoresist insulators. The minimum lithographic feature is 2.0 microns in the patterned aluminum layers.

The gates are tested at a 100KHz rate using the Faraday effect to observe the magnetic bubble domains optically. Outcomes are plotted as regions in two dimensional bias field versus drive current graphs. Overall bias field operating margins of 6%, 11%, and 3% of the nominal bias field for the Control, AndOr, and ExclusiveOr gates, respectively, are observed at drive currents of 2ma/micron in the bottom sheet and 3.4 ma/micron in the top current sheet. One failure was observed that seemed to limit the margin in most cases. At high fields the bubbles failed to switch paths even when forced by another bubble.

Chapter 1

Introduction

A magnetic bubble is defined as a cylindrical domain of reversed magnetization in a thin film of an appropriate magnetic material such as magnetic garnet. In order for the magnetization to be oriented perpendicular to the film plane, as it should if it is to sustain bubbles, the energy due to the uniaxial magnetic anisotropy of the magnetic material should be greater than the demagnetizing energy. The domain structure tends to minimize the free space fields outside the film. When no bias field is applied to the film, serpentine shaped domains will run throughout the film. Half of the domains will be oriented one way and the other half will be oriented oppositely. As a magnetic field is applied, one of the domains will shrink to the cylindrical domain of the magnetic bubble. Bubbles, which were first observed in 1960 by Kooy and Enz¹, range in size from 0.1 to 500 microns.

Magnetic bubbles have a number of desirable features leading to applications in memory storage. Among these are: they can be moved easily in low coercivity materials; they can be written and erased; and they can be detected optically or electronically with magneto-resistive detectors. Bubble memory devices are radiation hard, non-volatile as long as a bias field is applied, and contain no moving parts. Magnetic bubbles could be used to bridge a cost vs. speed gap that exists between magnetic recording and semiconductor memories. They could be used in applications where the user needs a low absolute cost but does not need a large capacity.

The use of bubbles as a means of performing logic also could have some advantages over semiconductor logic. Bubble logic could be placed on the memory chip to perform certain functions, such as searching and matching operations, that could help relieve an I/O bottleneck that exists between primary and secondary memory. J.P. Hwang showed that schemes of parallelism and pipelining could help make a faster memory².

The emphasis of the research presented in this thesis was to design logic gates to be used with deflecting and non-deflecting magnetic bubbles. If a large in-plane field is applied, bubbles propagate along the direction of the field gradient that is needed to move the bubbles; otherwise, bubbles deflect from the the direction of the gradient. J.P. Hwang and J.C. Wu designed and successfully tested a number of logic gates for use with non-deflecting bubbles^{2, 3}. However, the elimination of the large in-plane field would be desirable; thus, research on successful bubble logic gates for use with deflecting bubbles was performed by Robert Smith⁴. Furthermore, if logic functions were to be placed on the memory chip, it may be difficult to predict the behavior of the bubble as it enters the logic gates because the memory portion of the chip may produce stray in-plane fields. Therefore, the objective of the research presented here was the successful design of logic elements that operate independent of the bubble deflection angle as long as hard bubbles are not present.

The remainder of this chapter will present a brief introduction to bubble stability and translation including the effect the state of the bubble has on propagation. The method of propagation in current access devices and previous work in dual conductor magnetic bubble logic will also be discussed.

1.1. Bubble Stability⁵

A number of interactions occur between ions and magnetic moments in a bubble film. Two energies that result from such interactions are exchange and anisotropy, which are balanced against each other in a stable domain wall. The exchange energy density is $E_x = A(\frac{d\theta}{dy})^2$ and the anisotropy energy is $E_K = K_u \sin^2\theta$ where A is the exchange constant, θ is the orientation of the magnetization in reference to the normal to the film as shown in Fig. 1-1, and K_u is the uniaxial anisotropy parameter.

The equilibrium configuration of a bubble is found by minimizing the total energy change due to the presence of a bubble. That change can be expressed as the sum of the integral of the wall energy density over the wall area, E_W' , and the volume integrals of the magnetostatic and the applied magnetic field energy densities, E_M' and E_H' , respectively:

$$E_{T}^{\prime} = E_{M}^{\prime} + E_{W}^{\prime} + E_{H}^{\prime}. \tag{1.1}$$

For a circular bubble Thiele showed that $E_M' = -2\pi M_s^2 I(\frac{d}{h}) 2\pi h^3$ where d is the diameter

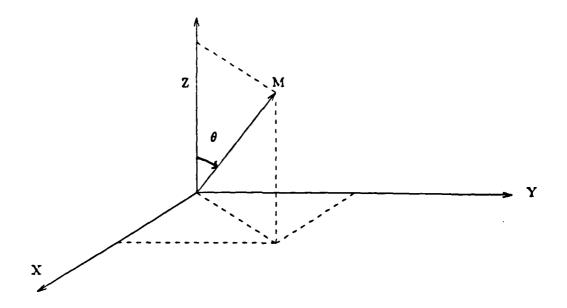


Figure 1-1: Coordinate system for specifying magnetization direction

of the bubble, h is the film thickness, M_s is the magnetization of the bubble film, and $I(\frac{d}{h})$ is a function tabulated by Thiele⁶. The wall energy is given by the following equation:

$$E_W' = \pi h^2 \sigma_w(\frac{d}{h}).$$

As the bubble expands E'_{M} will decrease and E'_{W} will increase. A new parameter, the "characteristic length", l, which is dependent on the film composition, is defined as the thickness where the magnetostatic energy balances the wall energy,

$$l = \frac{\sigma_w}{4\pi M_{\perp}^2} \tag{1.2}$$

where σ_{w} is the wall energy per cm² of the wall and is given by the following equation:

$$\sigma_w = 4(AK_w)^{\frac{1}{2}}.\tag{1.3}$$

An external field, H_B , is added to stabilize the bubble domain. The energy due to this field is $E_H' = 2M_e H_B \pi (\frac{d}{2})^2 h$.

Thiele⁶ drew the following conclusions about the equilibrium configuration of a magnetic bubble:

• The equilibrium diameter of a bubble can be determined by the equation

$$\frac{l}{h} + \frac{H_B}{4\pi M_s} \frac{d}{h} = F(\frac{d}{h}) \tag{1.4}$$

where $I(\frac{d}{h}) = \int_0^{d/h} F(x) dx$.

· Stability is determined by

$$S_2(\frac{d}{h}) < \frac{l}{h} < S_0(\frac{d}{h}) \tag{1.5}$$

where S₀ and S₂ are called the stability functions and have been tabulated⁶.

Equations (1.4) and (1.5) can be used to determine the bubble size and the collapse and stripe out fields. The functions F, S_0 , and S_2 are plotted in Fig. 1-2 and can be used to graphically determine the bubble size versus the bias field as illustrated by Eschenfelder⁵. For example, if $h{=}4l$ and a bias field is given, the diameter of the bubble may be found by plotting the value of $\frac{l}{h}$ on the ordinate of Fig. 1-2 and, then, drawing two lines. The first line is drawn with a slope equal to $\frac{H_B}{4\pi M_s}$ from the point just plotted. The second is drawn vertically from the point where the first line intersects the curve for F and the point of intersection of that line with the y-axis is an estimate of the bubble diameter. This is the graphical solution of Eq. (1.4). The limits for the bubble diameter and bias field can also be found through the use of Fig. 1-2⁵. A graph of the change in bubble size as the bias field is varied is shown in Fig. 1-3. Most films have a thickness of $h{=}9l$. The allowed variation in H_B is around 12.6% and the bubble will vary approximately 50% from the mid-bias value.

As mentioned previously, the bias field is necessary to sustain the bubble size and stability. If the field is increased or decreased, each segment of the wall will move inward or outward. This motion will stop when the bubble reaches its new equilibrium diameter, but there will not be any net translation. A net movement of the bubble will occur only when there is a gradient in the field across the bubble.

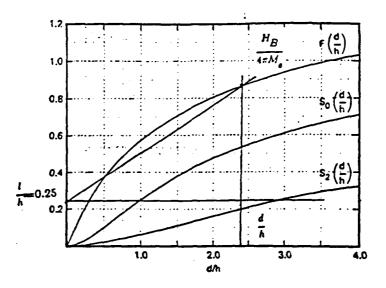


Figure 1-2: F, S₀, S₂ vs. d/h (After Thiele⁶)

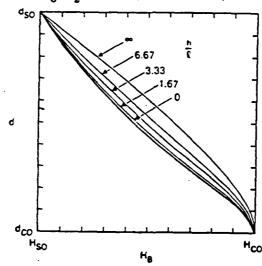


Figure 1-3: Variation in bubble size, d, vs. bias field, H_B, for film thickness, h/l (After Thiele⁷)

1.2. Bubble Translation

To cause a bubble to translate it is necessary that there be a gradient in the bias field. The bubble which seeks the position of lowest energy will move to the point where the magnetic field is the greatest because the energy is lowest where $-M\cdot H$ is lowest. The force, F^A , refers to the applied field, which is used to produce the field gradient as discussed in section 1.3. While F^A is used to translate a bubble, there is also a force which acts

transverse to the direction of propagation. This force is called the gyrotropic force, F^g, and is due to the makeup of the bubble wall. It will cause the bubble to deflect from the direction of the field gradient. Smith⁴ showed that the deflection angle could be approximated by the following equation:

$$\tan \varsigma = \frac{4S\mu_{\omega}}{\gamma d}.\tag{1.6}$$

 $\mu_{\rm w}$ is the wall mobility and S is the number of net wall magnetization revolutions as explained in the next paragraph.

There is a thin region around the circumference of the bubble domain called the bubble wall. In this region there is a gradual twist of magnetization due to the exchange between spins. A value called the state number is defined as the net number of revolutions of the magnetization along the center of the domain wall.

$$S = \int_0^{2\pi} \frac{d\phi}{2\pi} \tag{1.7}$$

If a bubble has a continuous 2π rotation around its wall as shown in Fig. 1-4a, the state number will have a magnitude equal to one. Bubbles may have negative state numbers,

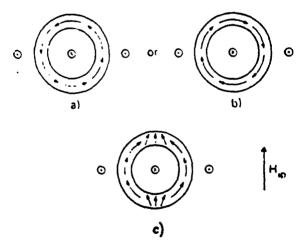


Figure 1-4: Magnetic bubble wall structures: (a),(b) S=1 wall structure (c) S=0 wall structure (after Eschenfelder⁵)

state numbers much larger than one, and state numbers between zero and one. The S number is important because it is related to the deflection angle of the bubble.

The transition region of tight, in-plane rotation of magnetization is called a "Bloch

line". The gyrotropic force is a force which propels the Bloch lines along the bubble wall with a speed proportional to the bubble velocity. It is dependent on the twists in the bubble $\frac{4\pi M_g hS}{\gamma}$ wall and can be defined as $\frac{4\pi M_g hS}{\gamma} \times V$. So, F_g is proportional to the state number; consequently, an S=0 bubble will not have a gyrotropic force acting on it and will not deflect from the normal direction of propagation. As S increases, the deflection angle increases. Bubbles with S>1 are called hard bubbles and are undesirable since bubble motion is harder to control and predict.

A surface layer of in-plane magnetization provides a mechanism for the annihilation of Bloch lines and, consequently, hard bubbles. The annihilation of a Bloch line is illustrated in Fig. 1-5. Pelt diagrams, 1-5a, are used to show how the wall spins rotate if the wall is

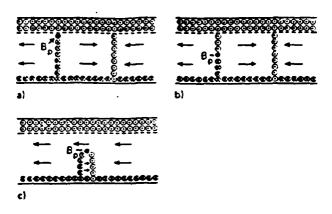


Figure 1-5: Annihilation of Bloch lines (after Eschenfelder⁵)

unwound. Ion implantation is used to form the surface layer of in-plane magnetization. If there are a pair of winding Bloch lines present in the bubble, a Bloch point will be nucleated where the oppositely oriented Bloch line meets the surface layer, 1-5a⁸. The Bloch point will move down the Bloch line and the Bloch line above the Bloch point will unwind, Fig. 1-5b. If the Bloch lines are pushed together as they are when a bubble is in motion, they would yield the configuration in Fig. 1-5c and the Bloch loop will shrink to oblivion. The bubble must reach a critical velocity in order to push the Bloch lines together. Beyond that velocity, S=1 bubbles are stable. An in-plane field can destroy the "umbrella" pattern of

magnetization shown in Fig. 1-5. Both states could be stable as long as the wall velocity is kept below the critical value and there is an in-plane field. The range of parameters for which S=1 and S=0 bubbles are simultaneously stable is shown in Fig. 1-6. Because S=0

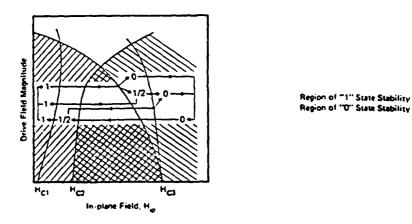


Figure 1-6: Stability map showing state transitions (after Brown)⁹ bubbles will not deflect, they are desirable for use in devices.

A large in-plane field can be used to change the bubble state from one to zero because the orientation of the magnetization in half of the S=1 bubble wall would be opposite to the field making the configuration energetically unfavorable. If the field is large enough, around 220 Oe., the magnetization in the wall will switch to that of an S=0 bubble to reduce the energy. However, the transition region in the bubble wall will have some energy that will keep the state from switching at low in-plane fields.

1.3. Current Access Bubble Propagation

There are a number of methods used to produce a bias field gradient needed to move a bubble. Previous work has been primarily focused on schemes using a rotating in-plane field. Examples of devices using a rotating field are permalloy patterned devices 10, 11, 12, 13 and contiguous disk devices 5, which utilize ion implantation. The method of propagation used in this research is called current access.

By placing perforations in a continuous conductor sheet, the current will be forced to

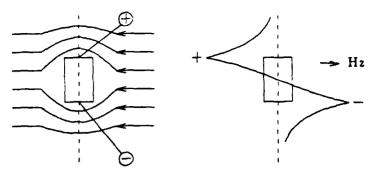
flow around the holes; thereby, creating a magnetic field perpendicular to the plane of the conductor sheets. Walsh and Charap were the first to introduce perforated sheet devices¹⁴. Their designs used one conductor sheet with perforations in the sheet designed similarly to TI bar patterns. Bobeck et. al.¹⁵ introduced a method in which two conductor sheets separated by an insulating layer are used. This configuration could be used to create a traveling potential well as shown in Fig. 1-7. Part (a) shows the current traveling around a perforation and the corresponding field produced. Part (b) shows holes in two conductor layers and the method of pulsing the conductors in order to put the bubble in the traveling potential well. The bubble will follow the plus signs because that will be the position of lowest energy for the bubble. The low inductance of the conductor sheets allows this type of device to be operated at a much higher frequency than devices using a rotating in-plane field.

1.4. Previous Logic Gate Designs

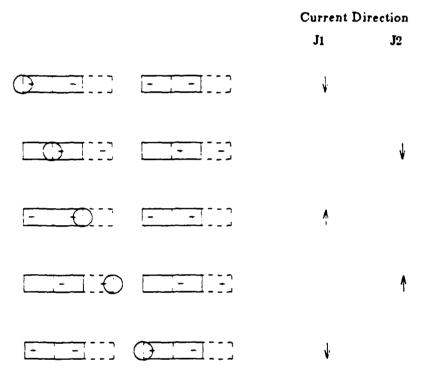
The capability of bubbles to perform logic has been known since the very early days of the technology. The presence or absence of a bubble indicates the true or false value of a bit. Logic operations are possible with bubbles due to the interaction that occurs between domains. With two propagation tracks, one easy and one hard, a bubble will follow the easy path if it is alone and it will follow the hard path if it is repelled by another bubble. Early work in magnetic bubble logic used permalloy elements to define the propagation paths 16, 17. Current access devices have recently been researched and some important results are presented here.

1.4.1. Current Access Dual Conductor Logic Gates

Gates using the current access dual conductor method of propagation have been designed at Carnegie Mellon University. The discussion of these gates can be divided into two sections: one section describing gates for use with non-deflecting bubbles and one section describing gates used for deflecting bubbles.



(a) Field produced



(b) Current sequence

Figure 1-7: Propagation in dual conductor current access devices: (a) field produced by perforation in conductor sheet (b) current sequence used

1.4.1.1. Non-deflecting Bubbles

J.P. Hwang² and J.C. Wu³ did work on the design and testing of gates for non-deflecting bubbles. The testing of these gates was done at 1MHz showing an order of magnitude increase in speed over permalloy devices. The AndOr gate is shown in Fig. 1-8. A list of gates designed and tested for S=0 bubbles is shown in Table 1-1. There is an 8.5%

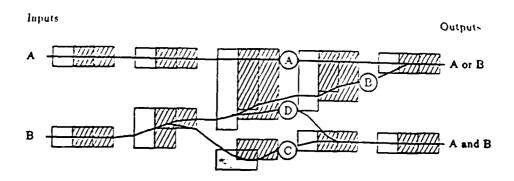


Figure 1-8: AndOr gate and the various possible routes for the input bubbles (after Wu³)

S=0 Bubble Logic Gates				
gate	Dimension	Bias Margin[%]		
Xor/And	16x12	12		
Switch	16x12	10.8		
And/Or	16x8	10.7		
Comparator	16x12	10.2		
Search	12x12	10		
Latch	16x12	10.6		
Bit-Pair Separator	16x12	8.5		
Merger	12x8	12		
Crossover	12x8	8.5		
Annihilator	8x8	15		
Splitter	12x8	9.5		

Table 1-1: Summary of bubble logic components (after Hwang²)

overlapped bias field margin for the devices. Some of the gates use a third level conductor to control, collapse, and stretch bubbles. An idler, which is a device that will allow a bubble to stay in basically the same location during multiple propagation cycles, is also used in some designs. All gates can tolerate deflecting bubbles except the Xor/And, Comparator, and Bit-Pair Separator gates; however, the bias margins will be reduced.

1.4.1.2. Deflecting Bubbles

Three gates have been designed and tested by Robert Smith for use with deflecting bubbles: the Control, AndOr, and Exclusive-Or (Xor) gates⁴. The Control gate, also referred to as the Switch gate, is very important in logic design because it can be used to perform the inversion operation. The gate takes two bubbles as inputs and uses the bubble-bubble interaction to direct the data bubble, as shown in Fig. 1-9. The top input is called

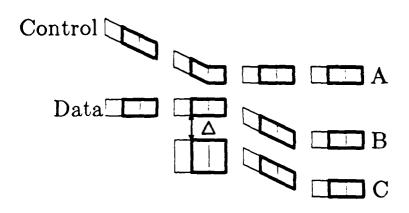


Figure 1-9: Control gate (after Smith4)

the control input because it controls the path of the data bubble. If there is a control bubble input, the data bubble will be forced into the lower path called the hard path and proceed to the C output. If there is not a control bubble, the data bubble will stay in the middle path, its easy path, and continue to the B output. Consequently, if a data bubble is always input, the B path output will be the opposite of the control input. A list of gates designed and tested for deflecting bubbles is shown in Table 1-2. The term, Δ , refers to the distance between the B and C paths. The width of the bias field margin is given by ΔH_B and $\Delta H_B[\%]$ is ΔH_B divided by the average field over which there is successful propagation. For instance, if the bubble will propagate from 200 to 250 Oe and the gate will work from 220 to 235 Oe, the % bias margin is $\frac{235-220}{(200+250)/2} \times 100\% = 6.67\%$. It was found that at high mobilities when only the data bubble is input, it will tend to deflect out of its path thus giving an incorrect C output. Delta was increased from 2 to 3 microns to limit the deflection from the path.

S=1 Bubble Logic Gates						
gate	Δ	$\Delta H_{\mathbf{B}}[Oe]$	ΔH _B [%]	Chip		
Control	2μ	11	4.6	f21#1v34		
	2.25	25	10.4	f21#1v34		
	2.5	27	11.3	f21#1v34		
	2.75	28	11.7	f21#1v34		
	3.00	25	2.4	f21#1v34		
	2.00	0	0	b1#3h61		
	2.5	8	3.3	b1#3h61		
	3.00	29	12.1	b1#3h61		
	3.50	28	11.7	b1#3h61		
	2.25	25	10.4	q2#4v21		
	3.00	20	8.3	q2#4v21		
AndOr	3.00	30	12.5	b1#3h61		
	3.50	29	12.1	f21#1v34		
Xor	2.50	22	9.2	f21#1v34		

Table 1-2: Summary of experimental gate bias field margins for deflecting bubble logic gates operated at J1=2 mA/micron (after Smith⁴)

Gates presented in the previous two sections were modified to help in the design of the gates for use with both deflecting and non-deflecting bubbles as will be seen in chapter four. Also, the simulator described in chapter two was used as a tool in the design of deflecting bubble gates and the fabrication and experimental methods presented in chapter three were developed and used by Smith, Hwang, and Wu. Bias margins for unique logic gates that operate using both deflecting and non-deflecting bubbles will be presented in the fourth chapter. In the fifth chapter, those results will be discussed along with the techniques used to obtain them.

Chapter 2

Logic Element Design for Deflecting and Non-deflecting Bubbles

Logic elements were designed using a computer simulator to help predict optimal conductor patterns. The same simulator had previously been used in the successful design of dual conductor current access logic gates for deflecting bubbles⁴. A brief discussion of the numerical methods used by the simulator and the user-interface is presented here along with the process used to transform the circuit design into actual physical masks.

2.1. Computer Simulation

A computer simulator was used in the design of the logic gates presented in this thesis. The code for the simulator was written by David Shenton and later modified extensively by Smith^{18, 4}. The simulator uses a number of empirically defined parameters to determine the bubble diameter, collapse field, and stripe out field. To keep the calculation time down, deformation of the bubble from circular is not modeled by the simulator. The bubble diameter and fields are found through a table look-up implementation of Eq. (1.4) and Eq. (1.5).

The simulator uses analytical equations derived to determine the bubble speed and the angle of deflection. Both are functions of the applied drive, ΔH^A , which is the sum of the drive from other bubbles and the drive from the current sheet. The velocity of the bubble is also dependent on the bubble diameter, d, the gyromagnetic ratio, γ , the wall mobility, μ_{w} , and ΔH^{CD} . The diameter is calculated during the propagation of the bubble since it is dependent on the applied drive field. Other parameters are entered as empirical constants. The drive from the gyrotropic force, ΔH^g , is inversely proportional to the bubble diameter; therefore, it produces a greater angle, ς , between ΔH^A and the direction of the field gradient as the bubble gets smaller.

As previously mentioned, the applied drive field is the sum of the drive from other bubbles and the drive from the current sheet,

$$\Delta H^A = \Delta H^S + \Delta H^B. \tag{2.1}$$

The force between bubbles, which are considered as non-overlapping magnetic charge distributions, is calculated as the derivative of the magnetostatic energy with respect to the bubble separation distance⁴. Maxwell's magnetostatic equations are used to solve for the drive due to the interaction of the bubbles:

$$\nabla \cdot H = -\nabla \cdot M \equiv \rho$$
$$\nabla \times H = -\nabla \times \nabla \phi = 0$$

where ρ is defined as the magnetic charge density and ϕ is defined as the external magnetostatic potential. The energy of a localized charge distribution $\rho_1(x)$ in an external potential $\phi(x)$ is

$$W = \int \rho_1(x)\phi(x)d^3x. \tag{2.2}$$

In the case where the external potential is from a second, non-overlapping charge distribution, the potential is

$$\phi(x) = \int \frac{\rho_2(x')}{|x - x'|} d^3x'. \tag{2.3}$$

and the energy, is by substituting (2.3) into (2.2),

$$W^{12} = \int \int \frac{\rho_1(x)\rho_2(x')}{|x-x'|} d^3x d^3x'. \tag{2.4}$$

The drive from a bubble is, therefore,

$$\Delta H_B \equiv \frac{F_B}{M_e h \pi d/2} = \frac{\pm \frac{\partial W^{(12)}}{\partial r_e}}{M_e h \pi d/2}$$

where r_e is the vector from the middle of one bubble to the middle of the other. An expansion of the energy in terms of the multipole moments of the two charge distributions and the spherical harmonics is used by the simulator.

The drive from the current sheet comes from the current sheet field, H_j^s, which produces a force

$$F_{i}^{s} = \int M_{j} \frac{\partial H_{j}^{s}}{\partial x_{i}} d^{3}r$$

where repeated indices are understood to be summed. The force can be manipulated to give

$$F^{\epsilon} = \frac{1}{2} M_s h \pi d \Delta H_z^{\epsilon}$$
 (2.5)

where

$$\Delta H_z^{\epsilon} \equiv -d\left[1 + \frac{r_o^2}{8} \left(\frac{\partial^2}{\partial x^2} + \frac{\partial^2}{\partial y^2}\right) + \cdots\right] \nabla H_z^{\epsilon} \Big|_{x=y=0}. \tag{2.6}$$

The simulator uses the first two terms, which are the perpendicular field, $\nabla \mathbf{H}_z$, and the two-dimensional Laplacian of that field.

Maxwell's electrostatic equations are used to find the current flowing in a conductor.

$$\mathbf{J} = \sigma \mathbf{E} = -\sigma \nabla \phi \tag{2.7}$$

$$\nabla^2 \phi = \frac{\rho}{\epsilon_0} = 0 \tag{2.8}$$

where ϕ is defined as the electric scalar potential. Laplace's equation, (2.8) is solved by the use of finite element methods⁴. The current density, J, is found by manipulating Eq. (2.7) and using the appropriate boundary conditions. From the current density, the perpendicular field can be found through the use of Biot-Savart's law.

$$\mathbf{H}(x) = \frac{1}{4\pi} \int \mathbf{J}(x') \times \frac{(x-x')}{|x-x'|^3} dV'.$$

The Laplacian can be found by taking the Laplacian of the trial functions used in the interpolation of the field.

2.2. Device Design

The computer simulator introduced in the previous section was used in the design of novel logic gates. Smith showed that the simulator, which uses menu driven routines for its input-output functions, could give accurate margins for logic gates⁴. The simulator was first written for use on the PERQ2 computer and, then, translated to the UNIX operating system. It is now run on a VAX 11/785 using a PC-AT for its graphics capabilities.

A logic gate is entered into the computer program by graphically entering the positions of the perforations in the conductors. The perforations are entered one layer at a time and after the gate entry is completed a mesh for each level is made and the potential throughout the conductor is found. Material parameters that match values found in existing garnets are entered into the computer. A list of the empirical parameters and some of their

sample values are shown in Table 4-1. Landing sites, which are used to indicate the landing positions of bubbles at the end of a simulation run, are entered next. They are indicated in Fig. 2-1 by the polygonal regions with labels used for identification placed in the middle of the regions. The position of the bubbles at the beginning of the simulation is marked and the ranges of the bias field and current density to be investigated are indicated. The propagation and interaction of the bubbles is simulated for different values of the bias field and current density.

Files are created which show the final positions of the bubbles and the bias field margins, as shown in Figs. 2-1 and 2-2. In Fig. 2-2 labels such as "B" or "a" are used to

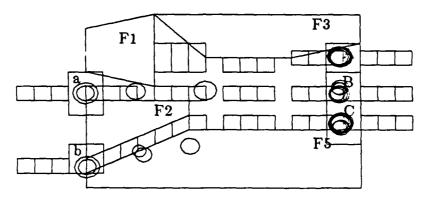


Figure 2-1: File created by simulator: indicates starting and stopping position of bubbles and the design of the gate
Bias Field (Oersteds)

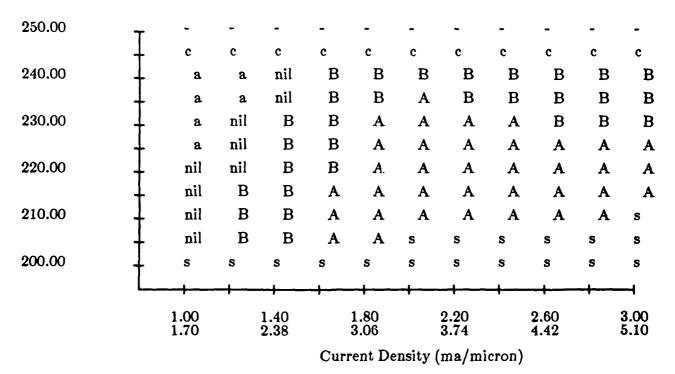


Figure 2-2: Bias field margin created by the simulator, indicates the landing positions of the bubbles and the range of the bias field and current density

indicate the landing positions of the bubbles designated in Fig. 2-1. By varying the parameters and the logic gate design, a good indication of the optimal design can be found. The file shown in Fig. 2-2 gives the output for just one bubble. To completely present the results for a single gate, it would take eight plots similar to Fig. 2-2. In order to save space, further results will be presented by a different method. The intersection of the working margins for all the input cases will be indicated by a solid line. Then, the main error mechanisms will be marked by roman numerals and explained in the text. This method is shown in Fig. 2-3 where the data shown in Fig. 2-2 is replotted. The regions where the incorrect B output was observed are marked by Π .

Dual a input S=0 bubble

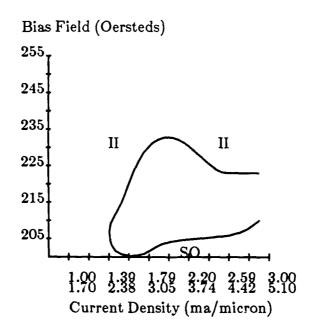


Figure 2-3: New presentation of Fig. 2-2

Once the gate is designed, a layout editor called Piglet is used to transfer the geometrical shapes from the designer's mind to a descriptive language that a computer can understand. Piglet is an internal Hewlett-Packard product which runs on an HP9836. It will translate the design into a descriptive language called IGS¹⁹, which is then translated to a lower level language called CIF(Caltech Intermediate Formref²⁰). The CIF format can be translated to a language that a Cambridge electron beam machine uses to convert patterns described in the low level language into appropriate shapes on a mask.

The circuit design consists of three conductor levels: two for propagation paths and logic gates and one for the generation of bubbles. The generators must provide three different input conditions, the two single input cases and the dual input case, as shown in Fig. 2-4. The overall design used here was very similar to that used by Robert Smith⁴ in the fabrication of devices designed for deflecting bubbles.

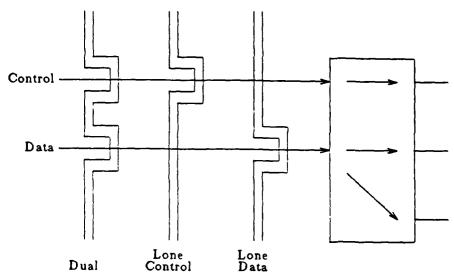


Figure 2-4: Multiple third level generators for continuous gate testing

Chapter 3

Experimental Methods

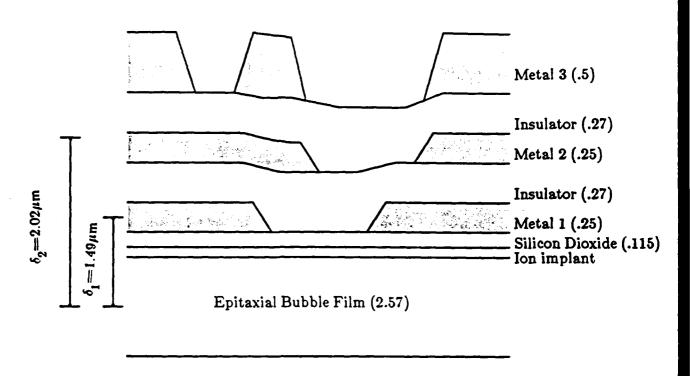
This chapter describes the experimental methods used in the fabrication and testing of the devices. The first section briefly describes the fabrication process along with some methods of characterizing the bubble film after growth. The second section describes the test procedure and equipment used.

3.1. Fabrication

There are four different masks denoted as first metal, via, second metal, and third metal needed in the fabrication of the device. These masks were patterned at Cornell with a Cambridge vector scanning electron beam system which writes shapes onto PMMA resist. The resist is subsequently developed and used as a mask in the etching of the underlying chrome.

Bubble films with a composition of $Y_{0.4} Sm_{0.2} Lu_{1.5} Bi_{0.7} Dy_{0.2} Ga_{0.9} Fe_{4.1} O_{12}$ were grown and characterized by Mahedevan Ramesh at Carnegie Mellon. The bubble film thickness, h, was measured with an optical interferometer²¹. The collapse field and the stripe width were measured through direct observation of domains using an optical microscope. These measured values were then used to calculate values of l and $4\pi M_8$ as illustrated in Appendix A. FMR measurements were made to determine the values of $H_{K'}$, γ , and α . The following parameters were estimated using the values of the parameters just mentioned: q, K_{u} , and μ_{w} as shown in Appendix A.

After growth and characterization of the garnet films, devices were fabricated that had a cross-section similar to that shown in Fig. 3-1. The first step in the fabrication was the uniform implantation of the bubble film with oxygen to suppress hard bubbles. A layer of



Garnet Substrate

Figure 3-1: Process topography (not to scale, microns used for dimensions)

SiO₂ was then sputtered for passivation followed by the deposition of the first conductor layer which consisted of AlCu. The metal layers are indicated by the shaded regions in Fig. 3-1. Conductor patterns were defined in photoresist which were then used as a mask for the chemical etching of AlCu. A second layer of photoresist was hard-baked and used as an insulator between the conductor layers. The process was repeated for the second conductor layer and its insulator. Finally, a third layer of AlCu was sputtered onto the substrate and etched in order to define the bubble generators.

3.2. Test

The observation of magnetic domains during testing was done by transmitting polarized light through the ferrimagnetic garnet material. The plane of polarization of the light was rotated, by the Faraday effect, as it passed through the material and the domains could be observed when the light passed through an analyzer. Previous experimenters have used a stroboscopic technique²² for the testing; however, for these gates only the output of a particular function was observed.

The experimental setup is shown in Fig. 3-2. A sample was inserted in the probe station and subsequently probed from above. Because light was reflected by the metal layers, domains could be observed from below the sample using an inverted microscope. This method of observation made it possible to probe the sample from above. The illumination source was a dye laser that was driven by ten nanosecond bursts of ultra-violet light which were produced by a pulsed nitrogen laser. An appropriate choice of dye produced wavelengths in the visible spectrum. The light then passed through an optical fiber. At the output of the fiber the light was polarized, reflected off a half-mirror, and focussed by an objective through the garnet substrate where the polarization plane of the, now, linearly polarized light was rotated. The light was reflected by the metal layer on top of the garnet and passed again through the substrate, objective, half-mirror, analyzer, and, finally, a 15x eyepiece that focused the images onto a television camera. The camera provided an image to a monitor in the custom built "sequencer" that controlled the experiment.

The sequencer controlled the bias field and the in-plane field as well as the current pulses that were sent to the conductor levels. The conductor levels had bonding pads that could be probed with micro-manipulators. These probes were connected to current transformers. The inputs to the current transformers came from a series of pulse generators. One pulse generator was used to control the current to the nucleators and the other four controlled the current through the conductors. There were two generators for each conductor; one produced a positive pulse and the other a negative pulse. A test run was executed by sending a generate pulse which would in turn create bubbles in the desired path or paths (see Fig. 2-4). A pulse generator then triggered the pulse sequence shown in Fig. 3-3 at a 100 KHz rate. The number of pulses sent, not more than 18, depended on the position of the input bubbles.

Margins were taken by setting the linear current density and, then, varying the bias field across the range that would accommodate bubbles in the bubble film. The current density was then increased and the bias field varied again. The linear current density is found by dividing the total current measured with the current probes by the full chip width of 400 microns. An in-plane field of 240 Oersteds was used to limit bubbles to S=0 when non-deflecting bubbles were desired.

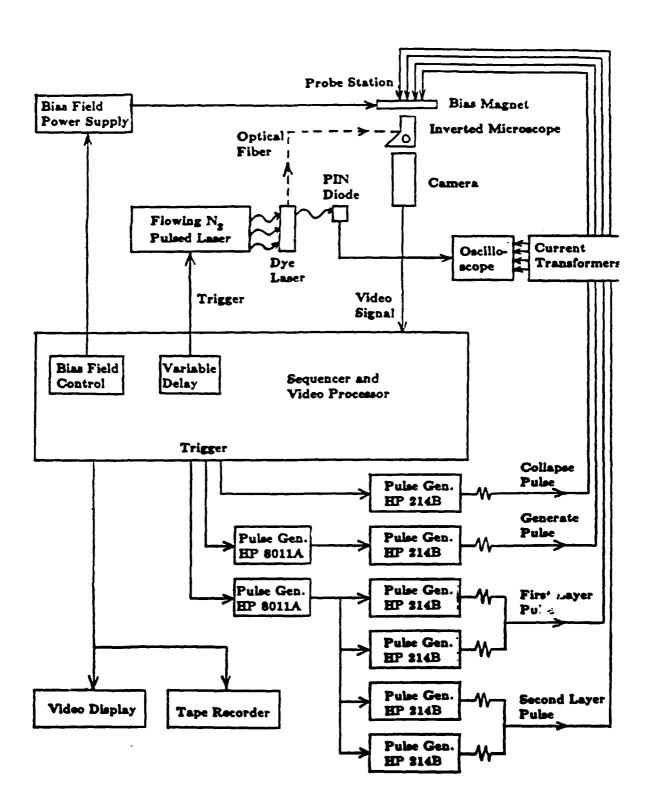


Figure 3-2: Electronic equipment used in testing (after Smith)

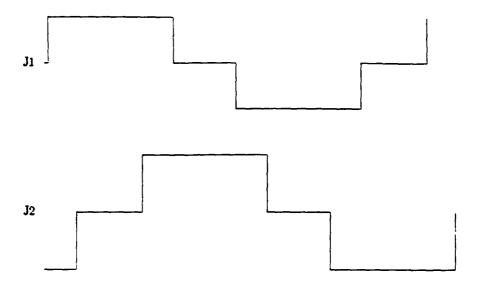


Figure 3-3: Test waveforms (after Smith)

Chapter 4

Results

Simulated and experimental bias margins for Control, AndOr, and ExclusiveOr gates will be presented in this chapter. The margins indicate resultant bubble positions for gate operation as the bias field (ordinate of plot) and the linear current density (abscissa of plot) are varied, as shown in Fig. 4-2. Simulated margins were found by dividing the current drive and the bias field ranges by 11 and testing at each step, thus creating 121 points on the margin. Experimental margins are found similarly. There are 6 sets of input conditions for these gates; they are the two single input cases and the dual input case for deflecting bubbles and for non-deflecting bubbles, respectively. Each two input gate requires eight margins to describe its behavior. For instance, for the Control gate there are the lone control S=0 and S=1, the lone data S=0 and S=1, the dual control S=0 and S=1, and the dual data S=0 and S=1 input conditions (e.g. Fig. 4-2). "Dual" means the control and data bubbles enter the gate simultaneously. Instead of presenting all eight margins for each gate, the results are condensed into two margins; one shows the overlap of the working margins for the S=0 input cases and one shows the overlap for the S=1 cases. The overall working margin is the overlap of these two margins. The line in the plots surrounds the overlapped working region. Erroneous outputs are indicated by marking regions with Roman numerals and referring to the regions in the text.

Four logic functions, the And, Or, Xor, and inversion functions have been investigated both through simulation and experimental methods. The effects of changes in mobility, coercivity, and the distance between paths were investigated to determine the optimal design. The values of those parameters and other parameters used in the simulations and the parameters measured on the chip are shown in Table 4-1. The simulations were done before testing to indicate a good design and after testing to try to match the experimental margins using the actual measured material parameters. The measured parameters are taken to be within ten percent of their actual value.

Parameters						
Parameter	Simulated(Control)	Simulated(And/Xor)	Experimental			
H _c ^{dyn}	.75	.75	xxx			
H _c stat	1.18	1.18	xxx			
$\delta_{f 1}[{f u}]_{f 1}$	1.46	1.46	1.49			
$\delta_{f 2}[{f u}]_{f 2}$	1.96	1.96	2.02			
J_2/J_1	1.7	1.7	1.7			
Frequency[kHz]	100	100	100			
Max. Dist.[μ]	.05	.05	xxx			
Overlap[%]	5	5	5			
$V_{\sf sat}[{ m cm/S}]$	1900	1900	xxx			
$\mu_{\mathbf{m}}[\mathbf{cm}/Oe\text{-}\mathbf{S}]$	318,varies	350	220			
$\delta_{_{f X}}[\mu]$	0	0	0			
$\delta_{_{f X}}[\mu]$	0	0	0			
$4\pi \mathrm{M_s[Oe]}$	445	445	423			
A[erg/cm]	2x10 ⁻⁷	2x10 ⁻⁷	1.5×10 ⁻⁷			
K _u [erg/cm ³]	3.4x10 ⁴	3.4x10 ⁴	3.615x10 ⁴			
$h[\mu]$	2.52	2.51	2.57			
a	.129	.129	.124			
H _{so} [Oe]	204	204	210			
H _{co} [Oe]	256	256	260			
γ[Oe ⁻¹ S ⁻¹]	1.49x10 ⁷	1.49x10 ⁷	1.3x10 ⁷			

Table 4-1: Simulated and experimental device parameters

Experiments and simulations used a frequency of 100 KHz and the ratio of the linear current densities was $\frac{J_2}{J_1}$ =1.7 where J_2 refers to the linear current in the conductor furthest from the bubble film. J_2 was made larger than J_1 because the second conductor was further

away and needed a larger current to produce a field equivalent to the field produced by current through the first conductor. The ratio of 1.7 was used because earlier researchers had used that ratio and found it to produce adequate results. The minimum lithographic feature is 2 microns leading to average gate dimensions of 16 microns by 32 microns. In the preliminary simulations the mobility was varied between 300 and $400\frac{Cm}{Oe\cdot S}$ and the coercivity was varied to determine a value that would produce propagation yet still be achievable through the fabrication techniques at Carnegie Mellon. The current density was varied from $1\frac{ma}{\mu m}$ to $3\frac{ma}{\mu m}$ in the simulations and from $1\frac{ma}{\mu m}$ to $2.5\frac{ma}{\mu m}$ in the experiments because too much heat had to be dissipated on the chip if the current were increased to greater than $2.5\frac{ma}{\mu m}$.

Since the gyrotropic force favors bubbles changing tracks in one direction perpendicular to the propagation and discourages changes in the opposite direction, gates using deflecting and non-deflecting bubbles for the most part must restrict any propagation at an angle opposing the favored direction. Gates previously designed for use with only S=0 bubbles use bubble-bubble interaction to repel bubbles in either an up or down angle from the field gradient to determine the correct output; therefore, they were undesirable as a starting point for the present designs. Robert Smith's gates⁴ designed for S=1 bubbles only allow deflection in one direction thus providing a good starting point for the present designs.

4.1. Control Gate

Smith's gates, briefly presented in the first chapter, used a variable distance, Δ , which represented the distance between the easy and hard paths for the data bubble in the control gate and was related to the potential energy needed to cross the barrier between the paths (see Fig. 1-9). It was determined that a Δ between 2.5 and 3 microns produced the optimal bias margins for his chips. If the distance were increased, the dual S=0 control bubble would have trouble forcing the dual S=0 data bubble into the hard path. If it were decreased, the lone S=1 data bubble would deflect into the hard path producing an incorrect C output for high bias fields and deflection angles.

Since the gates presented here must be designed to accommodate non-deflecting

bubbles, the distance, Δ , had to be reduced, else, the S=0 control bubble would not be able to push the S=0 data bubble into the hard path. Most designs use Δ =2 microns, which, of

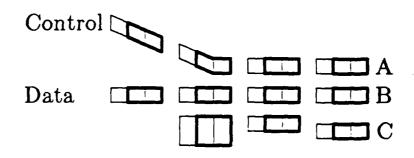


Figure 4-1: Control Gate

course, meant the gates would be limited in margin width by the lone S=1 data bubble case when the deflection angle was large. The size of the deflection angle is related to the mobility, the gyromagnetic ratio and the bubble diameter, as shown in Eq. (1.6). It is also inversely related to the coercivity of the bubble film.

Simulations showed the gate design in Fig. 4-1 to be optimal for the operation of the control function. The paths are closer together than in the gate shown in Fig 1-9 thus creating a longer area of interaction between dual input bubbles. This allows the S=0 control bubble more of a chance to push the S=0 data bubble into the hard path. Unfortunately, it also gives the lone S=1 data bubble more distance to deflect into the hard path. The larger 4x4 micron aperture is used to limit the force normal to the propagation direction so that the data bubble may be moved away from the control bubble. The four margins for the S=1 bubbles, shown in Fig. 4-2, and the overall margin for S=0 bubbles, shown in Fig. 4-3, indicate that the simulated overall working margin is around 12% of the average bias field for propagation using the simulation parameters in the first column of Table 4-1. If the mobility is increased causing the deflection angle to increase accordingly,

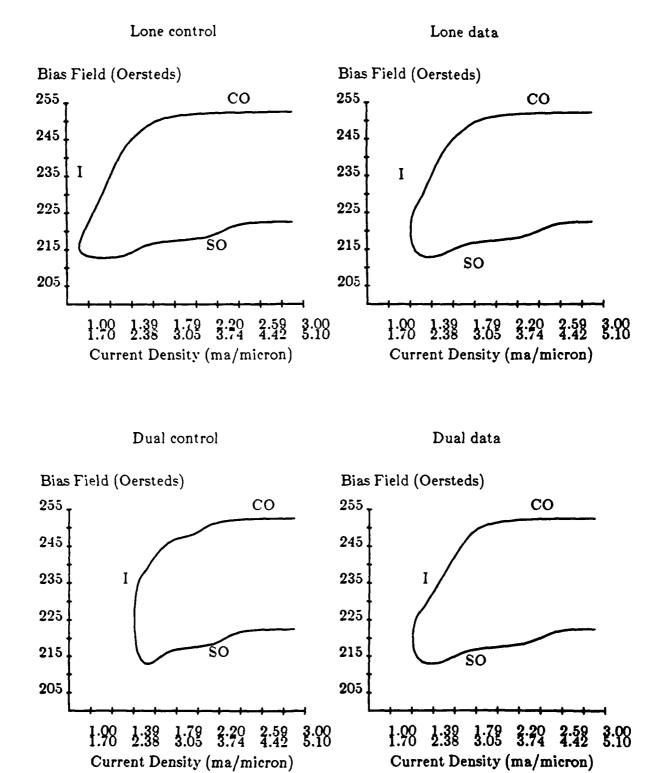


Figure 4-2: Simulated margins for the four S=1 input bubbles

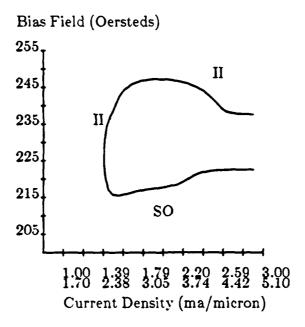


Figure 4-3: Overall margin for the S=0 bubbles the simulated overall margin for the S=1 bubble will decrease as shown in Fig. 4-4; this is due to the lone date bubble propagating out of its path.

The main error mechanisms shown by the simulations were the following: at low bias fields, the stripe out of the bubbles, SO; at low drive currents the loss of propagation or propagation out of the path, I; the incorrect B output for the data bubble when dual S=0 bubbles were input, II; at high mobilities, propagation of the dual S=1 data bubble out of the hard path, III; and at high bias fields the collapse of the bubbles, CO. The S=1 case was not limited by the error mechanism labeled with II because the combination of the bubble-bubble interaction with the gyrotropic force, which causes deflection, would virtually always repel the data bubble into the C path.

The experimental bias margin for this gate, shown in Fig. 4-5, has about half the predicted overall margin because the material parameters were not close enough to the desired parameters. It was difficult to determine if bubbles deviated from their path or lost propagation steps; however, the main error mechanism in this case was easily identified to be the incorrect B output for the dual input S=0 data bubble, II. Both the experimental

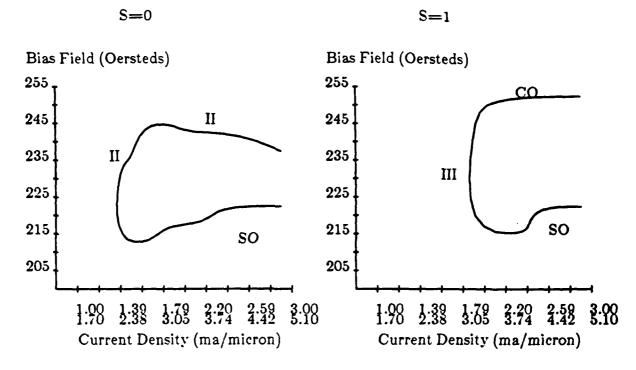


Figure 4-4: Simulated bias margins for S=1 and S=0 bubbles using an increased mobility for gate in Fig. 4-1

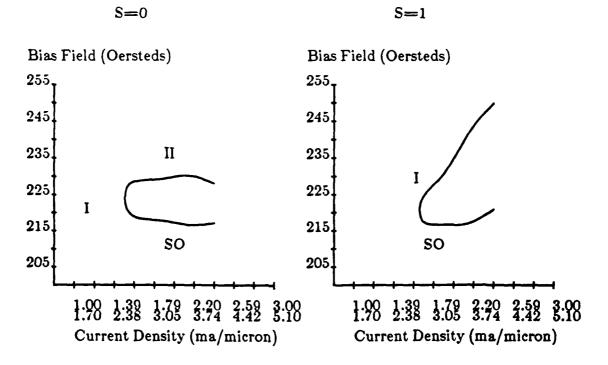


Figure 4-5: Experimental margins for the Control logic gate

and simulated margins were limited by this error mechanism. The simulated margins for the S=1 bubble also predicted the same error mechanism as was seen in the experiments. A few different designs for the Control gate other than the one shown in Fig. 4-1 were fabricated and tested; none gave a better bias margin. Gates with a greater distance, Δ , gave substantially smaller experimental margins as was suggested by the simulations. Also, one gate that was quite similar to the gate in Fig. 1-9 had less than a 1% working margin. These gates were all limited by the error mechanism, II, because the potential energy needed for a bubble to switch paths was larger than that needed in the gate shown in 4-1. Additional gates and margins may be examined in Appendix B.

Simulations were performed after the experimental data was taken to try and match the experimental results using the measured parameters, which are given in the third column of Table 4-1. These margins, shown in Fig. 4-6, had the same general shape as the

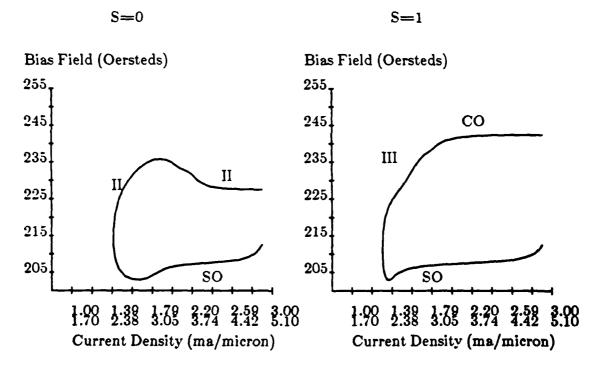


Figure 4-6: Simulated margins for the Control gate using measured material parameters

experimental margins. Also, the same limiting error mechanism, the incorrect output for the dual S=0 data bubble, II, was found for both the simulation and the experiment.

4.2. AndOr Gate

The AndOr gate is also very important in logic level design. As the name indicates the And function and the Or function can be performed using this gate. Again, it is a two input gate, shown in Fig. 4-7, with both inputs having the same easy path which leads to the Or output. The B input will follow its easy path unless there is also an A input; in which case, the B bubble will be forced into its hard path and propagate to the And output.

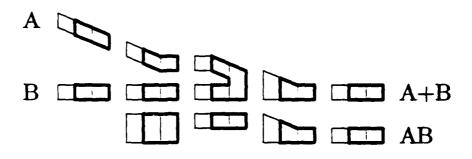


Figure 4-7: AndOr Gate

Because there are only two outputs the hard path may be moved to either the top or the bottom of the easy path with only a slight loss in the bias field margins. Similar to the Control gate design, the interaction between the paths is increased over gates designed for deflecting bubbles allowing the A bubble ample opportunity to push the B bubble into the hard path.

Simulations for this gate were done using a mobility of $350 \frac{Cm}{Sec-Oe}$ allowing for a medium size deflection angle. The simulated margins, shown in Fig. 4-8, were slightly less than found for the Control gate because of the higher mobility. Margins were limited at low drive currents by the loss of propagation for the dual B input S=0 bubble, I; at high bias fields and drive currents by the dual B input S=0 bubble staying in its easy path and forcing the A bubble out of its path, II; stripe out for low bias fields, SO; and collapse for high bias fields, CO. The experimental margins shown in Fig. 4-9 were very good because

S=0 S=1

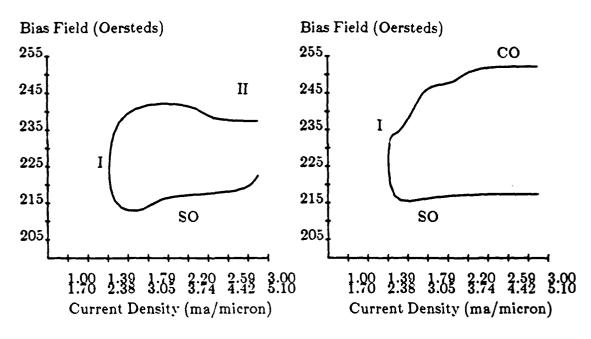


Figure 4-8: Simulated margins for the AndOr gate

the bubbles seek lower energy which is found under perforations in the conductors where the field produced by the current flowing around the holes is greatest. The perforations make up the bubble path; therefore, the bubbles prefer to stay in a path. The bubble under question is the non-deflecting dual B bubble, which exhibited two methods of staying in a path. The first was to take the hard path toward the correct output and the other was to continue in the easy path but lag the A bubble a cycle. The error mechanisms were similar to those predicted in the simulated margins.

Simulations were done to match the experimental margins using the measured parameters. These overall margins were very similar in working bias field width and error mechanisms as can be seen by comparing Fig. 4-9 to Fig. 4-10. The only major difference was at low currents the error mechanisms were different in that the simulator showed the A bubble being repelled out of its path instead of the B bubble just lagging behind the A bubble. Other gates were fabricated to test for better designs than the ones indicated by the simulator with one surprising result. The gate shown in Fig. 4-11 using $\Delta = 3$ microns showed a very good experimental margin, around 11%, shown in Fig. 4-12. This gate illustrates that the hard path may be placed opposite to the angle of gyrotropic deflection and still produce good results.

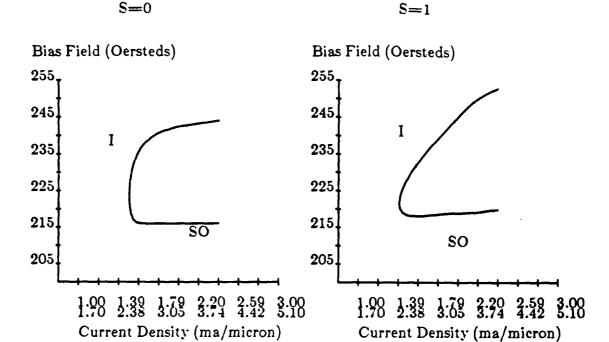


Figure 4-9: Experimental margins for the AndOr gate

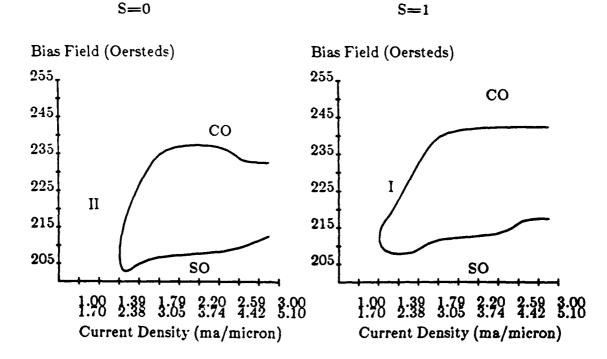


Figure 4-10: Simulated margins for the AndOr gate using measured material parameters

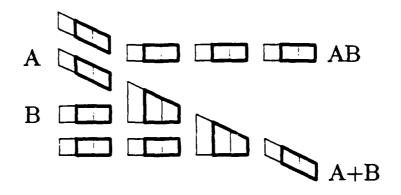


Figure 4-11: Alternate design for the AndOr gate

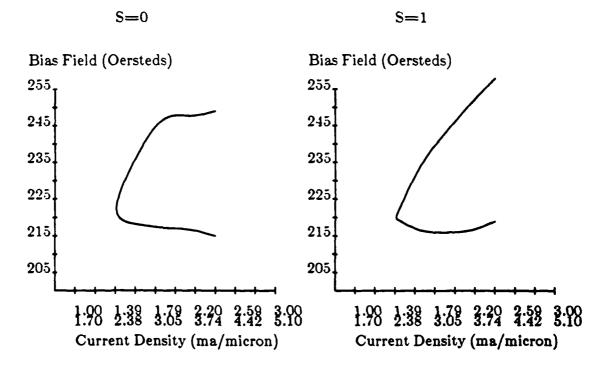


Figure 4-12: Experimental margin for AndOr gate in Fig. 4-11

4.3. ExclusiveOr Gate

The ExclusiveOr function is examined here because it can be accomplished using only bubble-bubble interaction to determine the correct paths. The design of an Xor gate for both deflecting and non-deflecting bubbles proved to be quite a bit more difficult than the design for the Control and AndOr gates for a couple reasons. The operation of the gate is similar to the other gates except that both bubbles have an easy path and a hard path. If one bubble is input, it will propagate along the middle path to the Xor output. If two bubbles are input, they will repel each other and take the outer paths to the And outputs. The design of this gate is more difficult because two bubbles have to be displaced from their easy paths instead of one. One of those bubbles will have to be repelled in a direction opposite to the angle of deflection. The optimal design, shown in Fig. 4-13, had a rather small margin of about 7% (see Fig. 4-14). Experimental margins proved to be about 4%

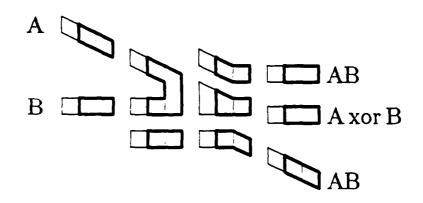


Figure 4-13: ExclusiveOr gate (see Fig. 4-15).

There were several limiting error mechanisms for this gate. In the simulations the dual B input S=0 bubble remained in its easy path at high bias fields, I; there was propagation out its path for the dual A input S=0 bubble at low drive currents, II; and the dual A input S=1 bubble stays in its easy path at high bias fields, III. The experimental margins were limited by the error, I, just mentioned.

S=0

S=1

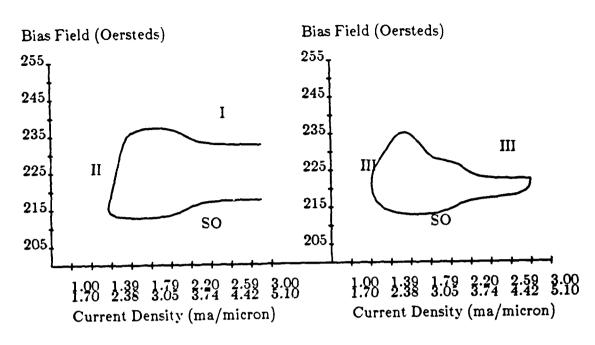


Figure 4-14: Simulated margin for the Xor gate

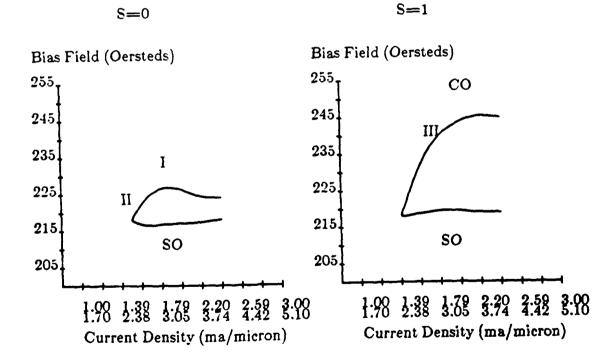


Figure 4-15: Experimental margin for the Xor gate

Chapter 5 Discussion

5.1. Fabrication

Devices presented in this thesis were the first devices using bubble films grown at Carnegie Mellon for use with current access technology. Previous devices fabricated for this sort of work used films that had measured parameters, and designs could be made to fit those values. Thus, the simulator described in Chapter two had a real test; in that, the gates were designed using expected parameters which were, of course, only approximations as is typical. The results, therefore, did not perfectly match the simulations, but when measured magnetic parameters were used in the simulations, a better match was obtained.

Bubble generators on two of the wafers produced bubbles while the field needed for nucleation, $H_{\rm N}=K_u-4\pi M_s$, on the other two was slightly larger than could be produced by the respective generators. Experimental margins were measured on one wafer. The coercivity on the wafer varied from place to place forcing some chips to operate only at high current densities; however, at some points the coercivity was lower allowing for very successful propagation of the bubbles in the film.

Another parameter that affected the bias margins was the mobility, approximately $\frac{Cm}{Sec \cdot Oe}$, which caused the deflection angle to be less than expected. While the bias margins found were acceptable, they were limited by the inability of one bubble to push another bubble out of its path. The force needed to push an S=0 bubble into its hard path is affected by a number of factors. The first and most prevalent is the magnetization in the bubble film. A lower magnetization in the bubble film would cause the force due to the bubble-bubble interaction to be less than desired as could be concluded from Eq. (2.4) where ρ is related to the divergence of the magnetization. Another factor may have been the

overetching of the perforations in the conductors. This would create a larger field due to the current sheet; thus making the area under the perforation have a lower energy. It would also allow bubbles to move farther apart and still stay in their path. Consequently, the bubble-bubble interaction force, which is inversely related to the distance between bubbles, would decrease.

5.2. Design

In the design of the gates there were tradeoffs between the design for deflecting bubbles and the design for non-deflecting bubbles. Designs for S=1 bubbles allowed for latitude in the distance, Δ . Because the gyrotropic force added to the force due to the bubble-bubble interaction, gates could, for the most part, only sustain deflection in one direction; in the case of deflection in the opposite direction those forces would counteract each other. Designs for S=0 bubbles allowed for hard paths to be above or below the easy paths because there was no gyrotropic force favoring deflection in one direction. Non-deflecting bubbles also allowed the designer the option of having paths combine. If two paths combine, S=1 bubbles entering the junction would leave following the lower path assuming downward deflecting bubbles. As can be seen in Fig. 1-8, a single B input S=1 bubble would leave the gate in the lower and incorrect path. Taking these factors into consideration, the gates presented in chapter 4 were designed and tested with the results summarized here.

The AndOr gate was the simplest to design because a bubble did not need to be repelled from its own unshared path. The experimental bias margins, around 10%, were usually limited by the successful propagation of the bubbles. This gate allowed for more latitude in the distance between paths, Δ .

In contrast, the Control gate was very dependent on the mobility and the distance, Δ . As Δ increased, it became difficult to get the correct output for the dual S=0 input; however, as Δ decreased, the single S=1 input would tend to deflect out of its path causing an incorrect output. The measured value for the mobility indicates that a smaller Δ would have given better overall margins than the measured 6% margins; but, a Δ =2 is still considered best for unknown material parameters.

The ExclusiveOr gate was much harder to design because both bubbles in the dual input case had to be pushed out of their preferred paths and one had to be pushed oppositely to its angle of deflection. Gates were found to have experimental working margins around 4%. In theory, they are limited by the inability of one of the dual input S=1 bubbles to force the other into a path opposite to the angle of deflection.

5.3. Conclusion

Table 5-1 shows some gates tested and their working margins at 2ma/micron. Hwang

Logic Gates				
gate	Δ	ΔH _B [Oe]	ΔH _B [%]	
Control	2μ	14	6.29	
	2.25	7	3.15	
	2.5	0	0	
AndOr	2	24	10.79	
	2.5	30	13.48	
Xor	2.5	7	3.15	

Table 5-1: Summary of experimental gate field margins at J1=2ma/micron

claimed his crossover, annihilator, latch, merger, and splitter gates would work with both S=0 and S=1 bubbles, creating a rather extensive library of working gates if the Control and AndOr gates in this thesis are included². It is difficult to say what the overlapping bias margin would be; but, there is a definite possibility of the combining of gates to create reliable and larger architectures.

Most devices would not have both S=0 and S=1 bubbles existing at the same time. If it is possible to determine that only one type of bubble exists in a device, larger bias margins could be found by using gate designs dedicated to only that type of bubble. Devices having bubbles with an intermediate state number between 0 and 1 (i.e. $S=\frac{1}{2}$) may prove to work better in gates designed for both types of bubbles because it is probable that bubbles with S=0 or S=1 may also exist in the device.

Appendix A Material Characterization

Materials used in this research were characterized only before processing took place; therefore, the actual post-processing parameters may be slightly different. The techniques used in the measurement of parameters were standard techniques that are regularly used. The thickness, h, at any point in the bubble film is found by measuring the number of interference fringes which pass through that point when the wavelength is varied from λ_1 to λ_2^{23} . The collapse field, H_{co} , and the stripewidth, W_s , were measured through the direct observation with an optical microscope of the domains in the bubble film. The stripewidth was averaged over a number of stripes in the film. The collapse field was found by measuring the field where isolated bubbles collapsed. The characteristic length, l, and the magnetization, $4\pi {\rm M_s}$, were found using the Fowlis method²³. Fowlis showed that upon knowing the stripewidth-to-thickness ratio, the thickness-to-characteristic length ratio could be determined. Thiele derived the equations for calculating the bias field-to-magnetization ratio as a function of the thickness-to-length ratio for bubble collapse. Therefore, once the values of W, and h were found the characteristic length could be found through table-lookup methods; as could the magnetization once the collapse field, l, and the thickness were known.

Ferromagnetic resonance techniques were used to find the gyromagnetic ratio, γ , the anisotropy field, H_K , and the damping parameter, α^{21} . The method used is described in PhD theses by C. Krafft and R. Smith⁴. Using these parameters along with those found in the first paragraph, the following equations can be used to find values for q, K_u , and μ_w :

$$K_{u} = \frac{H_{K}M_{s}}{2}$$

$$q = \frac{K_u}{2\pi M_e^2}$$

$$\mu_w = \frac{\gamma}{\alpha} \sqrt{\frac{A}{K_u}}$$

where the exchange constant, A, is estimated.

Appendix B Bias Margins

Various gates were used to assure the simulator did indicate the best overall design. The Experimental margins for those gates are shown here. Gates 1-8, 21, and 24 were designed to perform the Control function. Gates 9-16 and 17-20 were designed to perform the AndOr and ExclusiveOr operations, respectively. For the Control and the ExclusiveOr gate, the design that produced the best simulated margins also produced the best Experimental margins. Those gates are presented in chapter four. Gate 4 presented here is designed similarly to that in Fig. 1-9 and gates 5 and 7 have distances of 2.5 and 2.25 μ m, respectively, between the easy and hard paths.

Gates 9, 10, and 11 were all poorly laid out leading to uncharacteristically bad margins. An auxiliary path was placed too close to the gate allowing bubbles to switch paths into a path that wasn't actually in the gate design. While these gates may have had the best simulated margins, their design was close to that of gate 12 which was presented as the gate shown in Fig. 4-7, which produced a very good working margin.

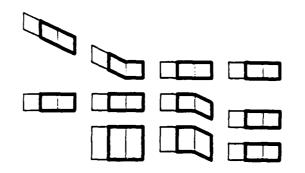


Figure B-1: Gate 2: Control Gate

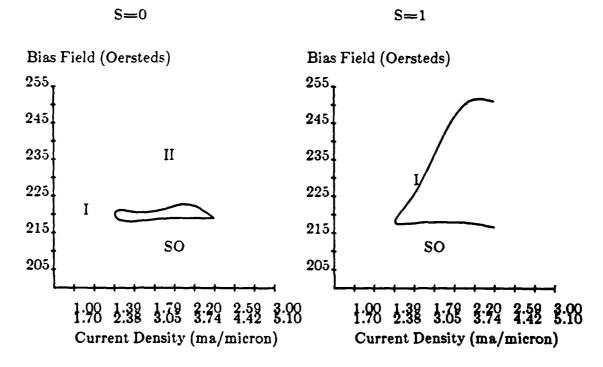


Figure B-2: Experimental margins for gate 2

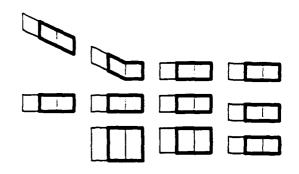


Figure B-3: Gate 3: Control Gate

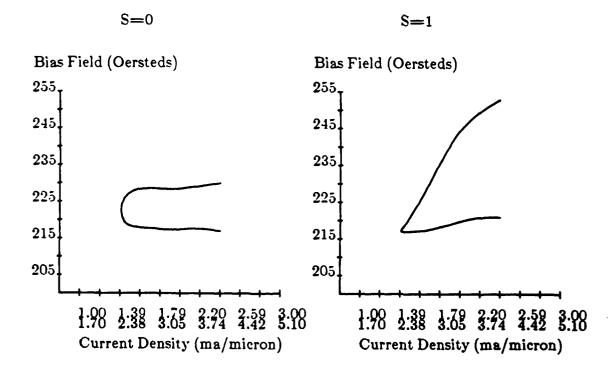


Figure B-4: Experimental margins for gate 3

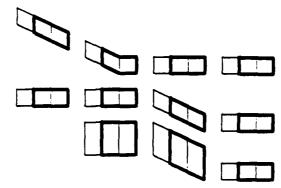


Figure B-5: Gate 4: Control Gate

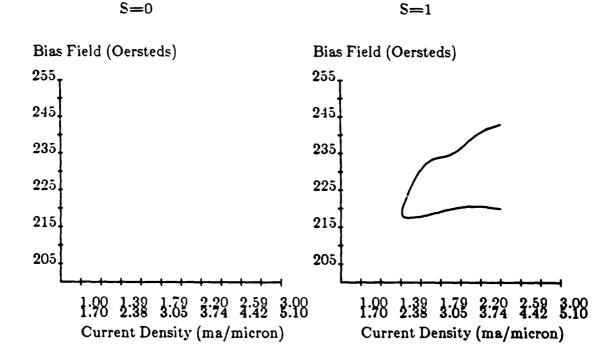


Figure B-6: Experimental margins for gate 4

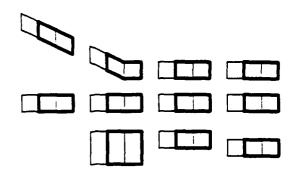


Figure B-7: Gate 5: Control Gate

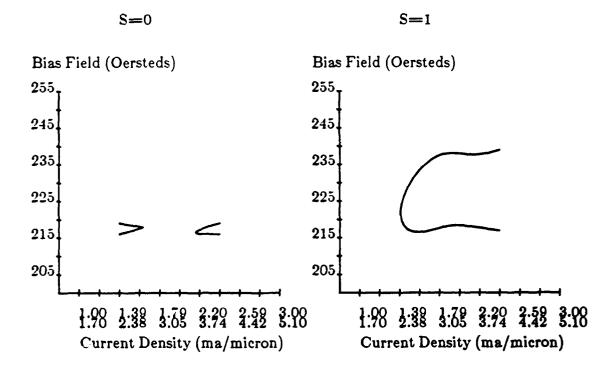


Figure B-8: Experimental margins for gate 5

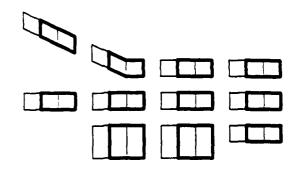


Figure B-9: Gate 6: Control Gate

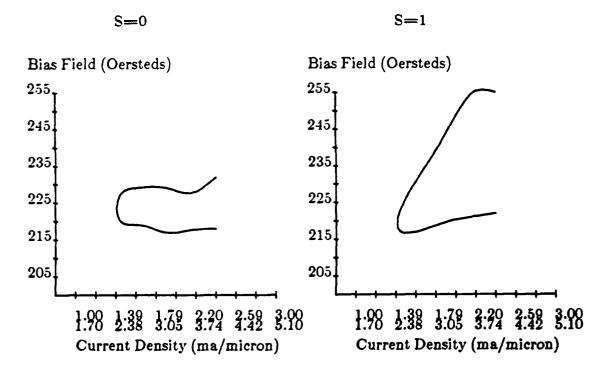


Figure B-10: Experimental margins for gate 6

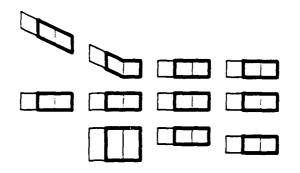


Figure B-11: Gate 7: Control Gate

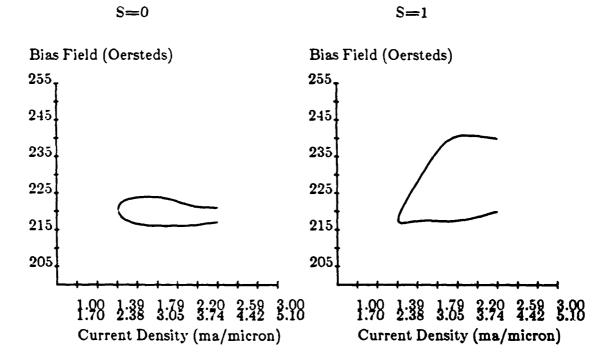


Figure B-12: Experimental margins for gate 7

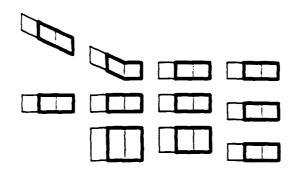


Figure B-13: Gate 8: Control Gate

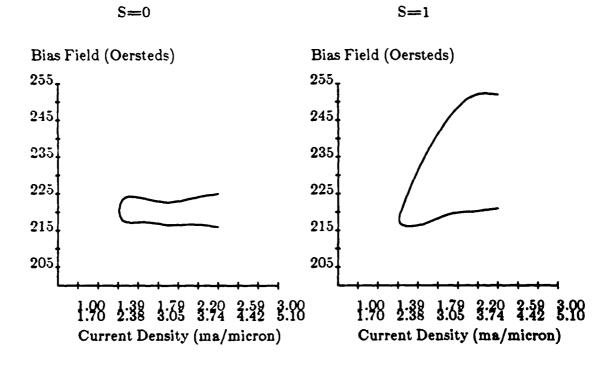


Figure B-14: Experimental margins for gate 8

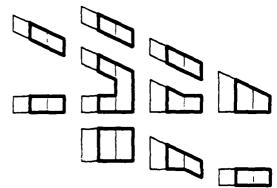


Figure B-15: Gate 9: AndOr Gate

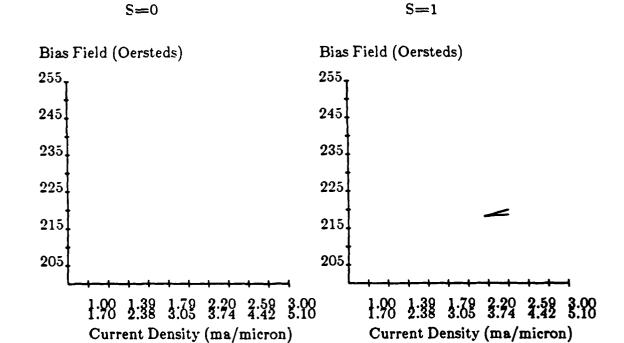


Figure B-16: Experimental margins for gate 9

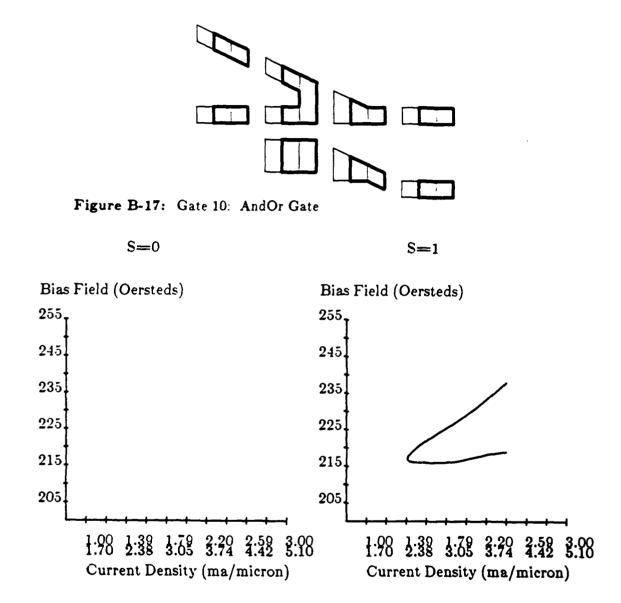


Figure B-18: Experimental margins for gate 10

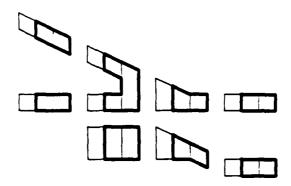


Figure B-19: Gate 11: AndOr Gate

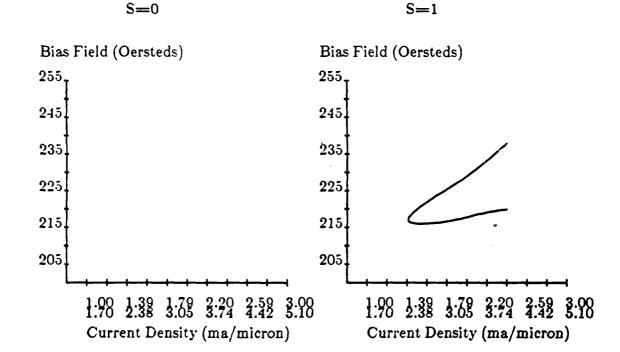


Figure B-20: Experimental margins for gate 11

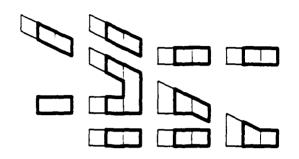


Figure B-21: Gate 13: AndOr Gate

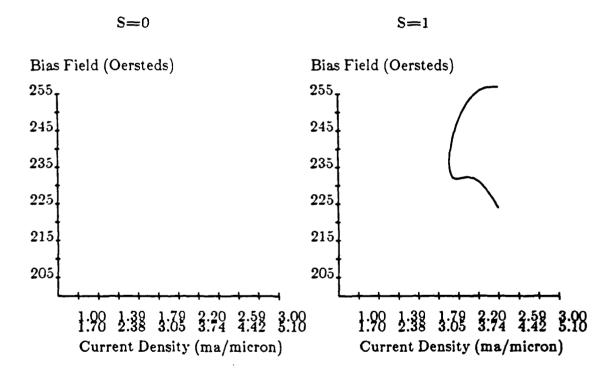


Figure B-22: Experimental margins for gate 13

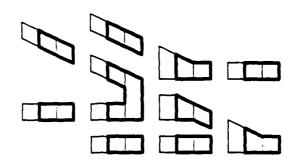


Figure B-23: Gate 15: AndOr Gate

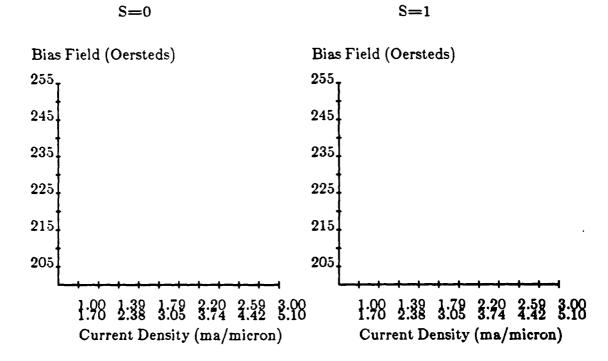


Figure B-24: Experimental margins for gate 15

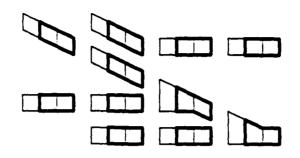


Figure B-25: Gate 16: AndOr Gate

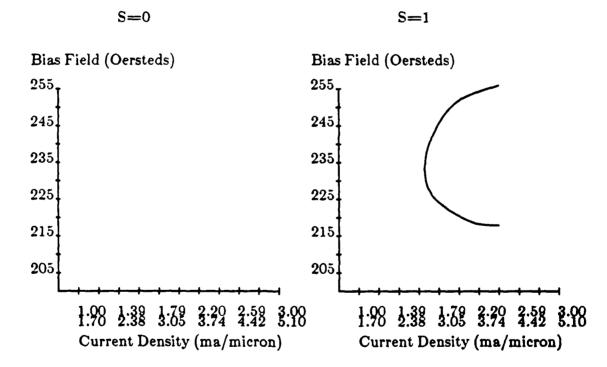
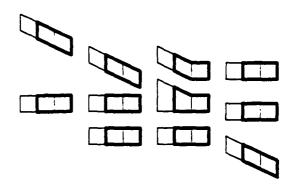


Figure B-26: Experimental margins for gate 16



S=1

Figure B-27: Gate 17: ExclusiveOr Gate

S=0

Bias Field (Oersteds) Bias Field (Oersteds) 255, 255, 245. 245. 235. 235. 225 225. 215. 215. 205 205. 1:70 1:38 1:79 2:20 2:59 3:00 1:70 2:38 3:05 3:74 4:42 5:10 1.00 1.39 1.79 2.20 2.59 3.00 1.70 2.38 3.05 3.74 4.42 5.10 Current Density (ma/micron) Current Density (ma/micron)

Figure B-28: Experimental margins for gate 17

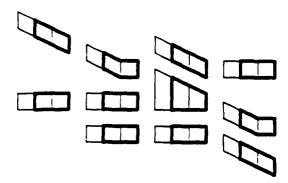


Figure B-29: Gate 18: ExclusiveOr Gate

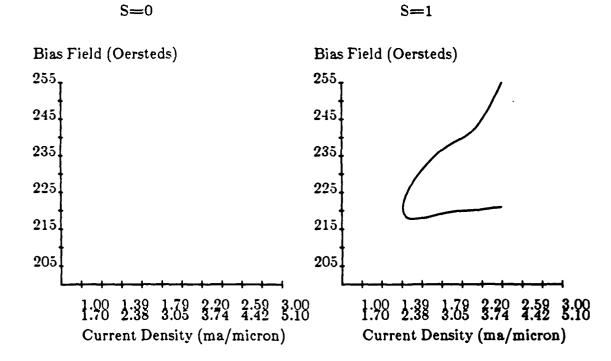
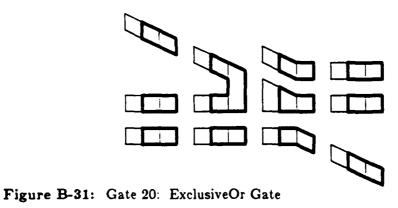


Figure B-30: Experimental margins for gate 18



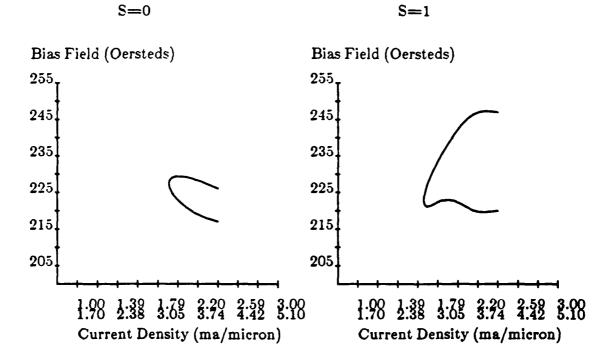


Figure B-32: Experimental margins for gate 20

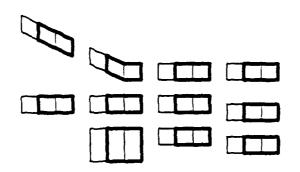


Figure B-33: Gate 21: Control Gate

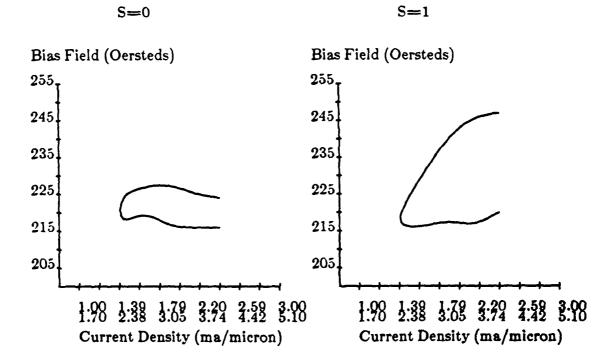


Figure B-34: Experimental margins for gate 21

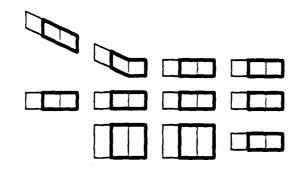


Figure B-35: Gate 24: Control Gate

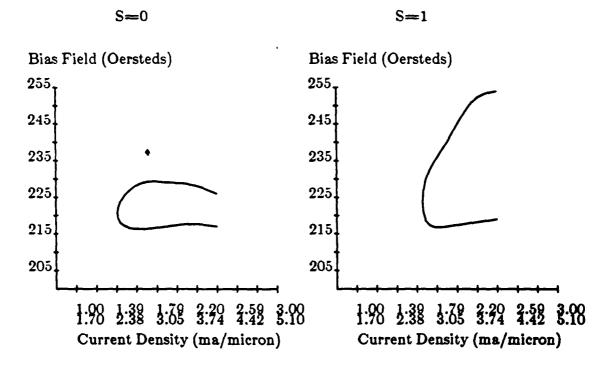


Figure B-36: Experimental margins for gate 24

References

- 1. C. Kooy, and U. Enz, "", Phillips Res. Repts., 1960.
- 2. Jyh-Ping Hwang, VLSI Intelligent Magnetic Bubble Memories, PhD dissertation, Carnegie-Mellon University, 1985.
- 3. Jiin-chuan Wu, Magnetic Bubble Logic Devices and Vertical Bloch Line Memory, PhD dissertation, Carnegie-Mellon University, 1986.
- 4. Robert L. Smith, Simulation, Design, Fabrication, and Operation of Magnetic Bubble Logic Gates, PhD dissertation, Carnegie-Mellon University, 1986.
- 5. Eschenfelder, A. H., Magnetic Bubble Technology, Springer-Verlag, Springer Series in Solid State Sciences, 1981.
- 6. A.A. Thiele, "The Theory of Cylindrical Magnetic Domains", Bell Syst. Tech. J., 1969, pp. 3287-3335.
- 7. A.A. Thiele, "", Bell Syst. Tech. J., 1971, pp. 725-773.
- 8. T.L. Hsu, "Control of Domain Wall States for Bubble Lattice Devices", AIP Conf. Proc., 1975, pp. 624-626.
- 9. B.R. Brown, "Wall State Stability during Translational Motion", AIP Conf. Proc., 1976, pp. 69-71.
- 10. A.J. Perneski, "Propagation of Cylindrical Magnetic Domains in Orthoferrites", IEEE Trans. Magn., 1976.
- 11. I.S. Gergis, P.K. George, and T. Kobayashi, "Gap Tolerant Bubble Propagation Circuit", IEEE Trans. Magn., 1976.
- 12. P.I. Bonyhard and J.L. Smith, "68 Kbit Capacity 16 micron Period Magnetic Bubble Memory Design with 2 micron Minimum Features", *IEEE Trans. Magn.*, 1976.
- 13. A.H. Bobeck and I. Danylchuk, "Characterization and Test Resultsfor a 272K Bubble Memory", IEEE Trans. Magn., 1977.
- 14. T. J. Walsh and S. H. Charap, "Novel Bubble Drive", AIP Conference Proceedings, Vol. 24, 1975, pp. 550-551.
- 15. A. H. Bobeck, S.L. Blank, A. D. Buthurus, F. J. Ciak, and W. Strauss, "Current-Access Magnetic Bubble Circuits", Bell Syst. Tech. J., Vol. 58, 1979, pp. 1453-1540.
- 16. R.M. Sandfort and E.R. Burke, "Logic Function for Magnetic Bubble Devices", IEEE Trans. Magn., 1971.
- 17. F.J. Nelson, "A Practical Magnetic-Bubble AND/OR Gate", IEEE Trans. Magn., 1975.
- 18. D. Shenton, S. H. Charap, H. David, and M. H. Kryder, "Simulation of Dual Conductor Current Access Magnetic Bubble Devices", *IEEE Transactions in Magnetics*, Vol. MAG-17, 1981, pp. 2677-9.

- 19. Piglet 2 Command Reference Guide, 1982, 1982.
- 20. C. Mead, L. Conway, Introduction to VLSI Systems, Addison-Wesley, 1980.
- 21. C.S. Krafft, Deuterium Implantation in Magnetic Garnets, PhD dissertation, Carnegie-Mellon University, July 1984.
- 22. F. B. Humphrey, "Transient Bubble Domain Configuration in Garnet Materials Observed Using High Speed Photography", *IEEE Transactions on Magnetics*, Vol. Mag-11, November 1975, pp. 1679-1684.
- 23. D.C. Fowlis and J.A. Copeland, "Rapid Method for Determining the Magnetization and Intrinsic Length of Magnetic Bubble Domain Materials", AIP Conference Proceedings, 1971, pp. 240-243.

Propagation
in One Micron
Ion-Implanted
Contiguous Disk
Bubble Memory Devices

A Project Report
Submitted to the Graduate School
In Partial Fulfillment of the Requirements
for the degree of
Master of Science
in
Electrical and Computer Engineering

by

Kathy R. Nitzberg

Carnegie Mellon University
Pittsburgh, PA
17 August 1988

Table of Contents

1.	Background	3
	1.1. Introduction	3
	1.2. Bubble Physics	4
	1.3. Bubble Materials	5
	1.4. Effects of Ion-Implantation in the Film	5
	1.5. Determination of Implant Conditions	10
	1.6. Bubble Memories	11
	1.7. Previous Work	11
2.	Experimental Methods	14
	2.1. Device Design	14
	2.2. Device Fabrication	15
	2.2.1. Computer-Aided Design of Device Layout	15
	2.2.2. Mask Fabrication	16
	2.2.3. Magnetic Garnet Films	16
	2.2.4. Wafer Processing	17
	2.3. Testing	19
	2.3.1. Testing Set-Up	19
	2.3.2. Performance Measurements	19
3.	Experimental Results	21
	3.1. Propagation Patterns	21
	3.1.1. Diamond Patterns	21
	3.1.2. Experimental Patterns	23
	3.1.3. Major Loop Propagation	24
	3.2. Implantation	24
	3.2.1. Bias Margins	26
	3.2.2. Bubble Position vs. In-Plane Field Direction	26
	3.2.3. Orientation Dependence of Bias Margins	29
4.	Discussion	82
	4.1. Minor Loop Propagation	32
	4.2. Major Loop Propagation	33
	4.3. Ion-Implantation	34
	4.3.1. Bias Margins	34
	4.3.2. Isotropic Propagation	35
5.	Conclusions	89
	5.1. Summary	39
	F.O. Suggestions for Future Work	90

List of Figures

Figure	1-1:	Magnetic Bubbles ⁵	3
Figure		Stripe domains ⁵	4
Figure		Stress relief in implanted films (after Kryder et al ⁷)	6
Figure		Magnetization directions in implanted film	6
Figure		Coordinate system	7
Figure		Qualitative representation of anisotropies induced by stresses around an	7
_		unimplanted disk4	
Figure	1-7:	Wall in high anisotropy area becomes charged as length is reduced ⁸	8
Figure		Charged wall around an unimplanted disk ⁴	8
Figure		Three Preferred Bubble Positions	8
Figure		•	g
Figure			11
Figure			12
Figure			12
Figure			13
Figure		· · · · · · · · · · · · · · · · · · ·	13
Figure		Propagation Patterns	14
Figure		Offset, or "snaked", modified triangular propagation patterns ¹	15
Figure		Major Loop	15
Figure		Flow chart of computer aided design process	16
Figure	2-5:	Wafer cross section	18
Figure	2- 6:	Testing set-up ⁴	20
Figure	3-1:	Representative Close Facked Minor Loop Diamond Track Bias Margin	22
Figure	3-2:	Propagation Margins for Diamond Tracks	22
Figure	3-3:	Most common positions for bubbles to stick in	23
Figure		Bubbles jumping in minor tracks	23
Figure		Propagation Margin - Experimental Pattern	25
Figure		Propagation Margin - Snaked Experimental Pattern	25
Figure		Major loop cusps where skipping occurred	26
Figure		Mis-oriented major loop track	26
Figure	3-V:	Side 1 good track bias margins as a function of implantation conditions for	27
F:	9 10.	wafers AH39 and AH31	_
Figure Figure		•	27
Figure		·	28
r igure	A-17;	Bubble position vs. in-plane field direction for low dose implantation (1.25x10 ¹⁶ ions/cm ²)	28
Figure	9.13.	· ·	29
* igaic	0 -10.	(1.5x10 ¹⁶ ions/cm ²)	48
Figure	3-14:	Bubble position vs. in-plane field direction for highest dose implantation	30

$(1.75 \times 10^{16} ions/cm^2)$ Figure 3-15: Bias margins for low dose (1.25x10¹⁶ions/cm²) 30 Bias margin for intermediate dose (1.5x10¹⁶ions/cm²) Figure 3-16: 31 Figure 3-17: Bias margin for high dose (1.75x10¹⁶ions/cm²) 31 Figure 4-1: Stripeout distance between tracks 32 Figure 4-2: Skipping failure 33 Cusps on top of major loop Figure 4-3: 34 Bubble position and bias margin for low dose implant (1.25x10¹⁶ions/cm²) Figure 4-4: 36 position Figure 4-5: Bubble andbias margin for intermediate 37 $implant(1.5x10^{16}ions/cm^2)$ Figure 4-6: Bubble position and bias margin for high implant dose (1.75x10¹⁶ions/cm²) 38

List of Tables

Table 2-1:	Magnetic properities of sample AH39	17
Table 2-2:	Implantation Conditions	18
Table 2-3:	Summary of process	18

Abstract

Propagation in one micron ion-implanted contiguous disk bubble memories has been studied. Major and minor loop propagation structures were fabricated with a range of implantation doses. Testing was performed with a polarized-light optical microscope and computer controlled drive and bias fields.

Propagation patterns were studied to determine optimal track designs in both minor and major loop structures. The primary minor loop propagation pattern studied was a diamond shaped contiguous disk pattern. An original track design, proposed by John Wullert¹, was also tested. The traditional diamond patterns performed better and had wider bias margins. Track designs for a non-rectangular major loop are discussed and design criteria identified.

Propagation characteristics, as measured by bias margins and degree of anisotropic propagation, have been studied as a function of implantation dose. An optimum implantation dose of 1.5×10^{16} ions/cm² has been identified which provides wide bias margins on tracks of different orientations. This dose exhibits the three-fold symmetry common in ion-implanted devices². Lower dose implants exhibit nearly isotropic propagation while the highest dose exhibits a different symmetry. Samples fabricated with higher implantation doses showed more anisotropic propagation due to the greater stress in the film.

Introduction

Magnetic bubble memory devices offer high density, non-volatile digital storage which is portable, resistant to harsh environments, and unlike other forms of magnetic recording contain no moving parts. Because of their electrical and mechanical durability, bubble memories are used in applications requiring high reliability, maintenance-free operation such as electronic switching systems, factory automation, avionics and space.

Bubbles research is moving towards fabrication of submicron, ion-implanted, contiguous disk bubble devices. Ion-implanted devices are a way of achieving higher density devices than present generation permalloy devices³. Propagation in submicron structures has been studied and isotropic propagation structures fabricated at Carnegie Mellon⁴ along with a study of one micron devices fabricated at Bell Labs¹. This project continues the study of isotropic propagation and novel propagation structures in one micron bubble devices.

The first chapter of this thesis explains the physics behind magnetic bubbles. It describes, in detail, the mechanisms of ion-implantation and briefly discusses some previous work in ion-implanted devices. The second chapter describes design and fabrication procedures, along with the experimental set-up and testing procedures. The third chapter presents the results including propagation margins and results from varying implantation dose. The fourth chapter discusses the results with emphasis on the effects of implantation dose on device operation. The fifth chapter contains a summary of the project and suggestions for future work.

Chapter 1 Background

1.1. Introduction

Bubble memories are a form of digital magnetic memory where the existence or absence of a magnetic bubble represents a one or a zero. Magnetic bubbles are small regions of magnetization in a magnetic thin film with the direction of magnetization opposite the direction of magnetization in the rest of the film, shown in Fig. 1-1. The magnetic properties of the film are modified, through deposition of magnetic materials or ion-implantation of the film, to control the position of the bubbles. Conductors are deposited to implement other functions, such as generation and detection, necessary for a complete device. Packaged devices include a permanent magnet surrounding the device to provide the external field necessary for the maintenance of the bubbles. In the absence of power the bubbles will remain in their positions as long as the permanent magnet remains.

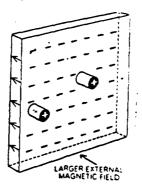


Figure 1-1: Magnetic Bubbles⁵

Ion-implanted, contiguous disk devices offer a order of magnitude improvement in density over permalloy devices now in production³. The principle advantage of contiguous disk devices is the relative coarseness of the lithography required to form them. In addition, ion-implanted circuits operate at a lower drive field than permalloy, so packages can be driven with less power dissipation and decreased temperature rise.

1.2. Bubble Physics

Magnetic bubbles are cylindrical domains of magnetization directed opposite to the magnetization of the surrounding material. For a material to be able to support bubbles, the uniaxial anisotropy energy must overcome the demagnetizing energy so that the moments point perpendicular to the plane of the film. In a bubble film, the anisotropy energy and the demagnetizing energy are represented by the equations:

Uniaxial Anisotropy Energy:

$$E_{A} = K_{u} \sin^{2}\theta \tag{1.1}$$

Demagnetizing Energy:

$$E_D = -2\pi M_s^2 \sin^2 \theta \tag{1.2}$$

The ratio of the anisotropy energy to the demagnetizing energy is called Q and is an indicator of the tendency of the material to support bubbles. Q must be greater than one for a material to support bubbles.

$$Q = \frac{K_u}{2\pi M_*^2} > 1 \tag{1.3}$$

An applied field oriented perpendicular to the film surface is called the bias field in bubble devices. As the bias field is increased, the domains oriented in the same direction as the bias field grow at the expense of the oppositely oriented domains, shown in Fig. 1-2. The unfavored stripes narrow until they shrink into cylindrically shaped domains called bubbles shown in Fig. 1-1. The bubbles continue to shrink as the bias field is increased, until a critical field is reached at which point the bubbles collapse and the film is uniformly magnetized in the direction of the bias field.

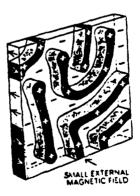


Figure 1-2: Stripe domains⁵

1.3. Bubble Materials

The primary criteria for a material to support bubbles is Q must be greater than one. Two other criteria for devices are small bubble size and high mobility. Bubble size limits density and mobility limits operating frequency, both of which are important in developing useful memory devices. The material found to exhibit the necessary properties were synthetic garnets (RE₃Fe₅O₁₂ where RE stands for rare earth elements). The properties of the garnets can be tailored by changing the relative composition of the rare earth elements.

1.4. Effects of Ion-Implantation in the Film

Magnetostriction is the phenomenon by which the shape of a material is altered by the direction of the magnetization within it. In the inverse process, a stress in the material will cause a change in the magnetic anisotropy and therefore a change in the direction of magnetization. The energy associated with inverse magnetostriction is a function of the direction of magnetization along with the direction and magnitude of stress. The equation which describes this relationship is:

$$E_{\sigma} = -3/2\lambda_{100}\sigma[\alpha_1^2\gamma_1^2 + \alpha_2^2\gamma_2^2 + \alpha_3^2\gamma_3^2]$$
 (1.4)

$$-3\lambda_{111}\sigma[\alpha_{1}\alpha_{2}\gamma_{1}\gamma_{2}+\alpha_{2}\alpha_{3}\gamma_{2}\gamma_{3}+\alpha_{3}\alpha_{1}\gamma_{3}\gamma_{1}]$$

where the γ_i are the direction cosines of a tension σ in the material and the α_i are the direction cosines of the magnetization, both with respect to the crystal axes of the film, and λ_{100} and λ_{111} are the magnetostriction coefficients.

Ion-implantation into a garnet film tends to expand the film perpendicular to the surface. Parallel expansion is prevented by the thick substrate, as shown in Fig. 1-3. This causes the material to be under a compressive stress in the plane of the film. In terms of magnetostriction, this can be equivalently viewed as a tension perpendicular to the plane of the film. The inverse magnetostrictive energy far from an implantation boundary in a (111) oriented garnet film can be rewritten as:

$$E_{111} = -3/2\lambda_{111}\sigma_{o}\cos^{2}\theta \tag{1.5}$$

where σ_0 is defined as a positive tension perpendicular to the film and θ is the angle the magnetization makes with the film normal. Since bubble films are grown such that $\lambda_{111} < 0$, the energy will be minimized when $\theta = 90^{\circ}$, which is when the magnetization direction is in the plane of

the film. The result is that in the implanted areas the direction of magnetization lies in the plane of the film while in the unimplanted regions the direction of magnetization remains perpendicular to the plane of the film as shown in Fig. 1-4. Under the influence of a bias field the magnetization in the implanted region will tip out of the plane of the film.

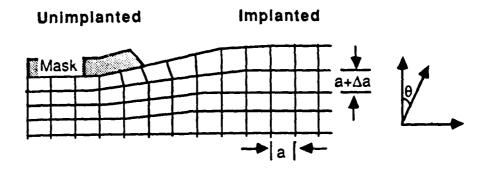


Figure 1-3: Stress relief in implanted films (after Kryder et al⁷)

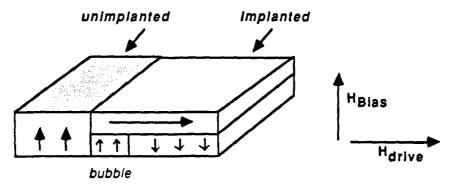


Figure 1-4: Magnetization directions in implanted film

At the interface of the implanted and unimplanted regions, boundary conditions must be satisfied. The magnetostrictive anisotropies at the implantation pattern boundary are described in the following equation⁷:

$$E = -3/2\lambda_{111} \{ [(\sigma_z - \sigma_z) + \Delta(\sigma_y - \sigma_z)/6] \cos^2 \theta$$

$$+ [(\sigma_y - \sigma_z)(1 - \Delta/3)] \sin^2 \theta \sin^2 \phi$$

$$+ [(\sigma_y - \sigma_z)\sqrt{2} \Delta/6] \sin(2\theta) \sin(\phi + 3\psi) \}$$
(1.6)

where θ is the polar angle of the magnetization from the film normal, ϕ is the azimuthal angle of the magnetization from the [11-2] direction, ψ is the angle between the [11-2] direction and the pattern edge, σ_i is the stress along the i^{th} direction and λ_{111} and λ_{100} are the magnetostriction coefficients of

the garnet film. Δ is defined as $(\lambda_{111}^{-1}-\lambda_{100}^{-1})/\lambda_{111}^{-1}$. The terms proportional to the shear stress (σ_{xz}) are small and have been disregarded⁸. The coordinate system used is shown in Fig. 1-5.

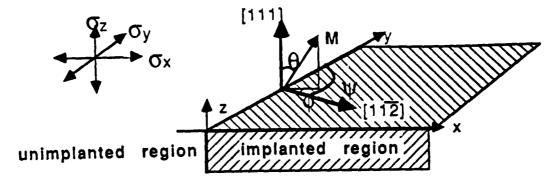


Figure 1-5: Coordinate system

The first term is the negative uniaxial anisotropy which causes the magnetization to lie in the plane far from the boundary. The second term is a uniaxial anisotropy parallel to the implant boundary, providing an easy axis parallel to the boundary on the outside of an unimplanted disk, shown in a of Fig. 1-6. The third term is a unidirectional anisotropy which varies with orientation of the boundary, shown in b of Fig. 1-6. The term behaves as an effective field whose orientation around a disk varies as 3ψ . From this term arises anisotropic propagation, to be described later.

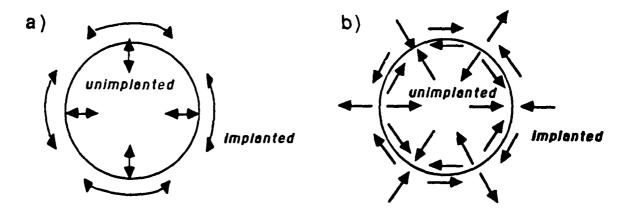


Figure 1-6: Qualitative representation of anisotropies induced by stresses around an unimplanted disk⁴

Charged walls form on the boundary between the implanted and unimplanted regions when the in-plane magnetization of the implanted region tries to orient around the unimplanted region. Stress relief perpendicular to the boundary contributes to the formation of the charged walls by providing an easy axis parallel to the boundary edge. Without this easy axis, closure domains would form instead of charged walls⁹. Generally in a sample having uniform anisotropy, a wall would be

oriented parallel to the easy axis ($\beta=0$) to avoid the formation of poles, shown in Fig. 1-7. Because the wall energy is proportional to the anisotropy constant, a wall in a high anisotropy region, such as the region near the implant boundary, will bend to decrease the anisotropy energy at the expense of forming surface poles on the wall. Thus a wall at the edge of an ion-implanted region becomes charged to minimize the length of the wall in the high anisotropy region at the boundary, as shown in Fig. 1-8.

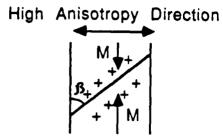


Figure 1-7: Wall in high anisotropy area becomes charged as length is reduced⁸

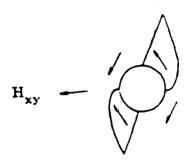


Figure 1-8: Charged wall around an unimplanted disk⁴

When an in-plane field is applied and rotated, the charged walls move, carrying the bubbles along. Propagation in ion-implanted patterns is complicated by the three fold symmetries of the implanted garnet. Both the cubic crystalline anisotropy and the magnetostrictive anisotropies at the boundary edge add terms to this three fold anisotropy. Due to these symmetries certain in-plane directions of the magnetization are more favorable than others which leads to three preferred bubble positions on an unimplanted disk, shown in Fig. 1-9. At low drive fields the bubble will lead or lag the rotating field to stay near these positions.

The preferred bubble positions cause an orientation dependence of the bias margins. The bias margin is a figure of merit for bubble devices, indicating the region of proper device performance. If both the bias field and drive field are within the curve, the bubbles will propagate. Fig. 1-10 shows a typical bias margin exhibiting this orientation dependence. Tracks parallel to one of the easy stripeout directions will have good bias field margins. Tracks perpendicular to these "good" tracks

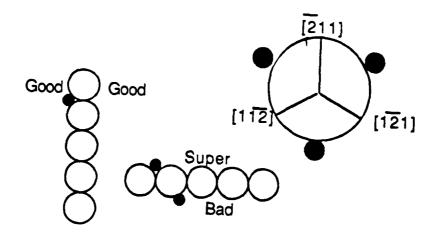


Figure 1-9: Three Preferred Bubble Positions

show different results. The side of the tracks with the peak pointed along one of the easy directions will exhibit significantly reduced margins ("bad" tracks) while the tracks on the opposite side will exhibit better margins ("super" tracks).

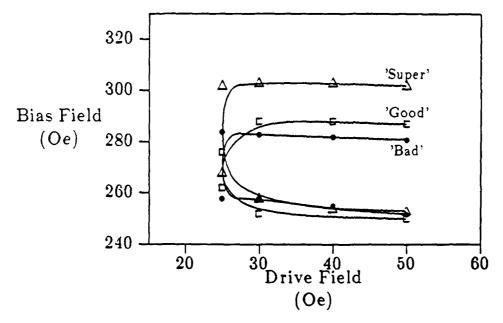


Figure 1-10: Propagation Margins from Conventional Films²

The difficulty in designing ion-implanted devices comes from trying to orient the three fold symmetry of the charged walls onto a four fold major-minor loop arrangement. Kryder and Saunders⁷ and independently Hubert⁹ have suggested that isotropic propagation could be achieved by

adjusting the magnetostriction coefficients λ_{111} and λ_{100} . According to Eqn. (1.6), bubbles grown in films with nearly isotropic magnetostriction ($\lambda_{111} \sim \lambda_{100}$) should have isotropic propagation margins.

1.5. Determination of Implant Conditions

As described above, ion-implantation is the process by which the perpendicular anisotropy of the film is overcome so the magnetization direction lies in the plane of the film. The implantation conditions must be optimized to get proper device performance. The adjustable implantation parameters are ion species, dose and acceleration energy.

Smaller diameter bubble devices require greater changes in anisotropy from the implantation because of their higher anisotropy. When heavier ions such as neon and oxygen are used the strain saturates at approximately $1.5\%^{10}$. To overcome saturation, lighter ions such as hydrogen are used in small diameter bubble devices. Deuterium has the same advantages as hydrogen but the required dosage is cut in half, reducing implantation time.

The proper dose of ions for best device performance is generally determined by empirical methods⁴. The dose determines the magnitude of the strain in the film and therefore influences both the width of the propagation margins and the degree of anisotropic propagation in the film.

The depth of ion penetration into the film is determined by the acceleration energy. The depth distribution of ions into the film is roughly Gaussian and characterized by a mean projected range R_p and a projected standard deviation ΔR_p . Tabulations of these values according to ion species are used to determine the energy required for a desired depth¹¹. An estimate of the desired thickness of the implanted layer, obtained by considering magnetic flux matching of a charged wall and the underlying bubble⁴, indicates Δh should be approximately 0.3 - 0.5d, where d is the diameter of the bubble. A thicker layer provides longer and stronger charged walls, which can lead to interference between charged walls of adjacent tracks and decreased track density.

The distribution of ions roughly correlates to the damage and strain of the lattice and the anisotropy change in the implanted layer. Since a single implant gives roughly a Gaussian profile, multiple implants (generally double or triple) at different energies and doses, are used to make the profile more uniform. The shallower (second) implant should be about one-half to one-third the dose of the first implant to produce a relatively uniform implant profile. Saunders ¹² suggests for films where $\Delta \neq 0$, the implant should peak slightly near the surface to increase the effect of the reduced stress-relief anisotropy.

1.6. Bubble Memories

In addition to propagation, other functions are necessary to have a complete memory device. A typical bubble chip organization is shown in Fig. 1-11. A string of current pulses representing the information to be stored is applied to the generator which converts the pulses into bubbles. The absence or presence of a bubble represents the original digital information. The bubbles move around the major loop to the storage area where they are stored in long loops called minor loops. Bubbles remain in the minor loops until a current pulse is applied to the transfer gates to transfer them back to the major loop. The bubbles then move around the major loop to the detector which reconverts the presence or absence of a bubble to an electrical pulse. There are many different organizational schemes for bubbles, but all have the same components.

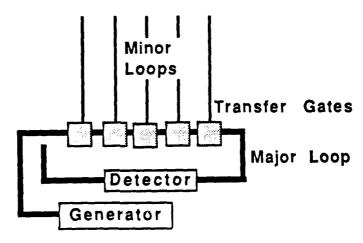


Figure 1-11: Typical bubble device organization

1.7. Previous Work

A study of one micron diameter bubble devices, fabricated at Bell Labs, was done at Carnegie Mellon by John Wullert¹ in 1986. This section outlines some of Wullert's analysis of propagation structures.

After testing disk, snake and triangle patterns, Wullert proposed the modified triangle pattern shown in Fig. 1-12 as a minor loop propagation pattern. This design corrects the low bias failure he observed, illustrated in Fig. 1-13, where the bubbles would stripe-up the slope into the next cusp. The stripe-up failure did not occur when the bubble was pressed against the flat side of a triangular propagation pattern. The proposed pattern has the flat edges of a triangle for the bubbles to rest on in the cusps. Other features include rounded edges to extend the high bias margin, since collapse usually occurred at the peaks of the triangles, and round end loops for increased transfer margins.

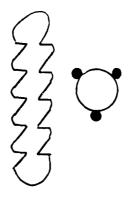


Figure 1-12: Modified triangular propagation patterns¹

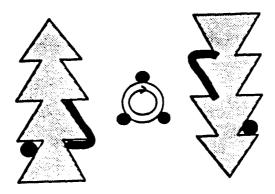


Figure 1-13: Low bias failure mode1

Design of the major loop is complicated by the three-fold symmetry effects in ion-implanted devices. As mentioned earlier, the bias margins of propagation tracks depend on the orientation of the track with respect to the crystal lattice. If the major loop is a simple rectangular loop at some point the bubbles would be oriented along weak "bad" tracks², as shown in Fig. 1-14.

Wullert identified three problem areas in a non-rectangular major loop, shown in Fig. 1-15. Wullert found bubbles skipped cusps in turns sharper than 90° in addition to skipping on sides parallel to the minor loops. He also noted decreased margins on backwards turns, where the track is aligned along a "bad" direction for some part of the turn.

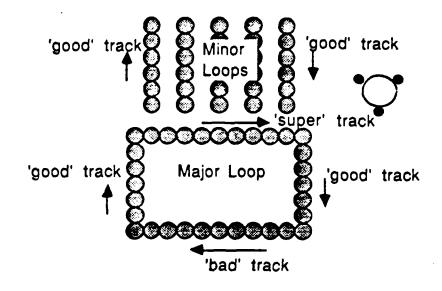


Figure 1-14: Rectangular major loop

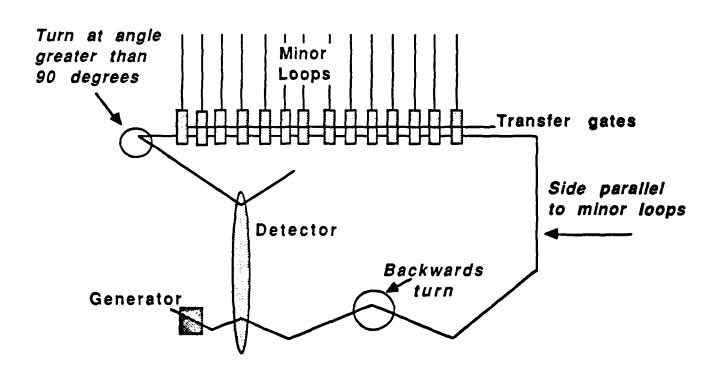


Figure 1-15: Major loop problem areas(after Wullert1)

Chapter 2 Experimental Methods

This project involves the design and fabrication of ion-implanted, contiguous disk propagation tracks. This chapter describes the design criteria, the computer-aided design process, the fabrication process and the testing methods used.

2.1. Device Design

The primary minor loop propagation pattern used in this project is similar to the original contiguous disk patterns as described by Lin et.al.¹³, but the peaks are sharper so the disks resemble diamonds as shown in Fig. 2-1.

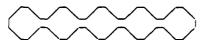


Figure 2-1: Propagation Patterns

The propagation pattern proposed by Wullert¹, described in Section 1.7 was also used in this project. Along with his original design, an offset or "snaked" version of the proposed pattern was tested. The two sides of the pattern were offset as shown in Fig. 2-2 so two bubbles would not sit directly across the small implanted region when in the cusps. Snake patterns are used to minimize bubble interaction and increase track density.

In this project a non-rectangular major loop, shown in Fig. 2-3, which avoided the problem areas identified by Wullert, was used. Instead of a rectangle, the loop is made up of tracks at 30° and 60° to the weak side. The minor loops are aligned as "good" tracks and the major loop is a combination of "good" and "super" tracks. As recommended by Wullert, the turn away from the horizontal top is kept at 90°. There are no sides parallel to the minor loops and backwards turns, as

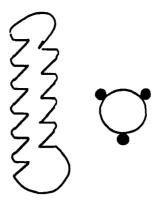


Figure 2-2: Offset, or "snaked", modified triangular propagation patterns¹ shown in Fig. 1-15, are also avoided. One disadvantage of the angled major loop structure is the large area enclosed by the loop.

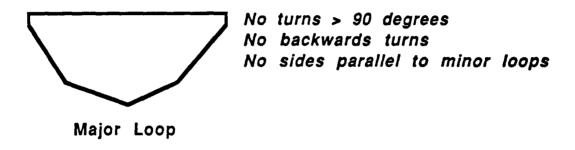


Figure 2-3: Major Loop

2.2. Device Fabrication

The first part of this section describes the tools used to design and fabricate the masks for the photolithographic steps. Once the masks were made, the remainder of the fabrication was done in the clean room at Carnegie Mellon. A more detailed description of the wafer processing and device fabrication can be found in Appendix A.

2.2.1. Computer-Aided Design of Device Layout

The chip layout design was done on a Hewlett Packard 9836 computer using the Piglet graphic design editor. Piglet is an internal HP product which is used to translate device design into a high level descriptive language called IGS. The Piglet data files are transferred on to a VAX and translated into CIF (Caltech Intermediate Form) and then translated into DIP, a compiler for the Cambridge Source Pattern Data Language. The patterns described in DIP are converted into

appropriate shapes on the mask by vector scanning of an electron beam using a Cambridge electron beam pattern generator located at the National Nanofabrication Facility at Cornell University. A flow chart of the mask design process is shown in Fig. 2-4.

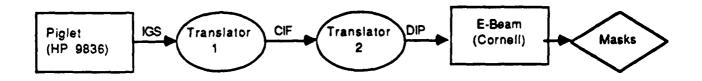


Figure 2-4: Flow chart of computer aided design process

2.2.2. Mask Fabrication

Three masks were fabricated for this project, two of which had submicron dimensions. The first mask was the ion-implantation mask, used to pattern the photoresist which blocks the propagation tracks from implantation. The second mask was the conductor pattern for the bubble generator and transfer gates. The minimum linewidth on both these masks is approximately one micron. The pattern generator can resolve smaller dimensions, but the linewidth used was limited by the photolithography equipment. The third mask was used to open vias for etching alignment marks and for building up the conductor material on the bonding pads.

2.2.3. Magnetic Garnet Films

The composition of the garnet film is roughly:

$$\mathrm{Bi_{0.4}Dy_{0.7}Sm_{0.2}Lu_{1.2}Y_{0.5}Fe_{4.45}Ga_{0.55}}$$

Bi (Bismuth) provides the necessary anisotropy and helps visibility due its high Faraday rotation. Dy (Dysprosium) aids in developing garnets with nearly isotropic magnetostriction constants, since for both Bi and Dy $\lambda_{100} < \lambda_{111}$ while for most other rare earth garnets $\lambda_{100} > \lambda_{111}^4$. Sm (Samarium) and Dy give the garnet a large negative magnetostriction λ_{111} , which is required for the magnetization direction to change through implantation 14.

The films were epitaxially grown on gadolinium gallium garnet (GGG) substrates. GGG is a non-magnetic garnet with an intermediate lattice spacing, allowing a good match for the grown epitaxial garnet films¹⁵. The films were all grown from the same melt, though different growth rates and temperatures were used. The parameters of a typical film are shown in Table 2-1. The films used in this study have nearly isotropic magnetostriction constants $(\lambda_{111} \sim \lambda_{100})$.

Magnetic Properties of Typical Film				
Thickness	th	1.23 µm		
Stripe Width	\$W	2.55 μm		
Collapse Field	H _{co}	313 G		
Characteristic Length	1	0.1124 μm		
Magnetization	$4\pi { m M_s}$	559 G		
Anisotropy Field	$\mathbf{H}_{\mathbf{k}}$	1959 G		
Bubble Diameter	ď	1.01 µm		
Magnetostriction Coefficient	λ ₁₁₁	-3.7x10 ⁻⁶		
	λ ₁₀₀	-2.5x10 ⁻⁶		

Table 2-1: Magnetic properities of sample AH39

2.2.4. Wafer Processing

First a thin prespacer of SiO₂ was deposited to protect the bubble film during subsequent processing. Next, the ion implant mask of AZ 4110 resist was deposited and patterned photolithographically. Each wafer was divided into four regions and each region was implanted using different doses (Table 2-2) to study the effects of ion-implantation conditions on propagation performance. Double implantation of singly-ionized deuterium molecules (D₂⁺) was used. With the implant resist patterns still on the wafers, alignment marks were etched into selected areas by phosphoric acid. The photoresist implantation mask patterns were then removed. Next, an Al layer was deposited to serve as a mirror for the magneto-optical observation of the bubbles. For isolation, a SiO₂ layer was rf sputtered on top of the mirror. Then the conductors were deposited by DC magnetron sputtering. Photoresist was patterned for the conductor layers and baked. The hardbaked photoresist served as a mask as the patterned conductors were etched in a phosphoric acid solution. Additional insulator and conductor layers were deposited for other devices on the wafers. The process is summarized in Table 2-3. A cross section of a finished wafer is shown in Fig. 2-5.

Implantation Conditions				
Quadrant	Energy	Dose		
	(KeV)	(ions/cm ²)		
I	66	1.00x10 ¹⁶		
	3 6	6.70x10 ¹⁵		
II	6 6	1.25x10 ¹⁶		
	3 6	8.30x10 ¹⁵		
ш	66	1.50x10 ¹⁶		
	3 6	1.00x10 ¹⁶		
IV.	66	1.75x10 ¹⁶		
	36	1.20x10 ¹⁶		

Table 2-2: Implantation Conditions

Processing Parameters				
Purpose of Step	Material	Process	Thickness	
Bubble Layer Growth	Garnet	epitaxial	1 micron	
Spacer	SiO ₂	RF Sputter	1000 angstrom	
Ion-Implant Mask	AZ 4110 Resist	Contact Printing	1 micron	
Ion Implantation	Deuterium	Implantation	.27 micron	
Mirror Layer	AlCu	DC Sputter	250-300 angstroms	
Insulator	SiO ₂	RF Sputter	1000 angstroms	
Conductor Deposition	AlCu	DC Sputter	4500-5000 angstroms	
Conductor Patterning	AZ 1350B-SF Resist	Contact Printing		

Table 2-3: Summary of process

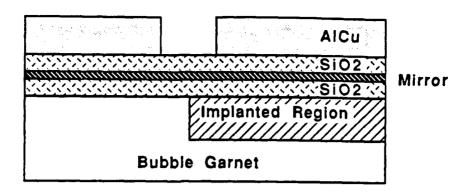


Figure 2-5: Wafer cross section

2.3. Testing

This section describes the computer-based test system, Kilotest, and the types of testing done.

2.3.1. Testing Set-Up

The sample is mounted in a bias-drive field coil arrangement which is controlled by a computer-based test system called Kilotest. Through Kilotest, the magnitude of the in-plane drive field as well as the magnitude and phase of the current pulses for the active functions can be controlled while the perpendicular bias field is adjusted manually or automatically. The drive field phase and magnitude can also be adjusted manually. The bias-drive field coil arrangement is placed on the stage of a Leitz polarized-light optical microscope. Light from a mercury arc-lamp is polarized before shining through the objective onto the sample. The sample is viewed in reflection, with another polarizing element in the path set to provide maximum Kerr magneto-optic effect contrast. The resulting image is projected into a camera and fed to a monitor for viewing. The microscope set-up is shown in Fig. 2-6.

2.3.2. Performance Measurements

All the bias margins were measured quasi-statically, with a rotating field frequency of one Hertz, to easily observe failure modes. The term bias margin is used to refer both to the plot of bias fields vs. drive fields, where points within the curves denote the operating region, and the bias range for a given value of drive field. In the latter case, when a percentage is given, it is the total bias field range divided by the mid-range value.

Bubble positions around an unimplanted disk were measured as a function of the direction of the in-plane drive field. The bubble position was measured on a circle with radials marked at 5

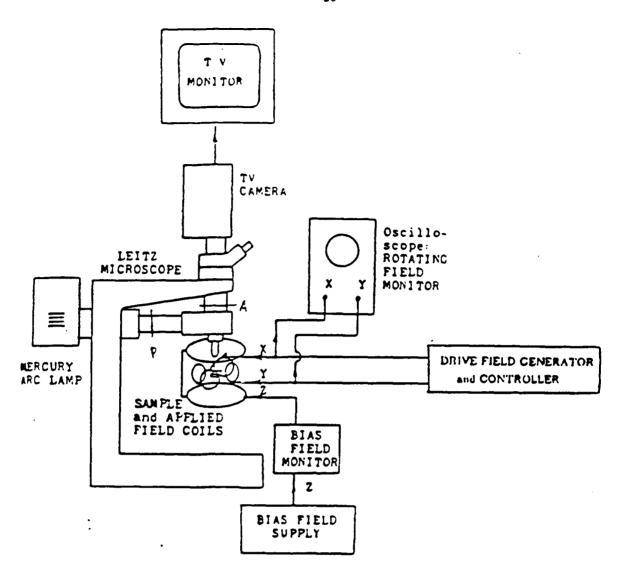


Figure 2-6: Testing set-up4

degree increments, as viewed on the video monitor. The drive field angle was measured by a similar circle taped on the screen of the oscilloscope monitoring the x,y in-plane field. To make the measurements, the drive field was manually rotated to the desired angle, usually in 10° increments. The bubble position was read off the video monitor. The smallest magnitude drive field for which the bubble would rotate completely around the disk was used.

Chapter 3 Experimental Results

This chapter presents the results from characterization of the wafers. The goal of the project was to fabricate one micron propagation tracks, test the designs and determine design improvements. The first section describes the results of testing propagation in the minor and major loops. The second part describes bias margins and propagation characteristics as a function of ion-implantation dose.

3.1. Propagation Patterns

Measurements were made on the diamond shaped contiguous disk patterns, Wullert's proposed patterns and the major loop.

3.1.1. Diamond Patterns

The diamond patterns were tested at three track orientations, "good", "super" and "bad", as defined in Chapter 1. The names "good", "super" and "bad" are used to describe the orientation of the track in terms of traditional, anisotropic devices, not the results of the device operation; often the results disagreed with the name. "Good" tracks were measured both in close packed minor loops and in more loosely packed tracks positioned around the principal chip area. "Super" and "bad" tracks were measured only on the more loosely packed tracks.

Propagation worked well on the traditional diamond shaped patterns. Margins of 10% were obtained on the closely packed minor loops, shown in Fig. 3-1. Wider margins were obtained on other tracks positioned on the outside of the chip, which had larger spacing between tracks. Also on the same device, 50 Oe drive field margins of 15.3% on a "super" track, 13.7% on a "good" track and 12.7% on a "bad" track were measured. These margins are shown in Fig. 3-2.

At all drive field strengths, the primary low bias failure mode was stripeout between neighboring tracks, where the bubble would stretch into a stripe domain, interfering with

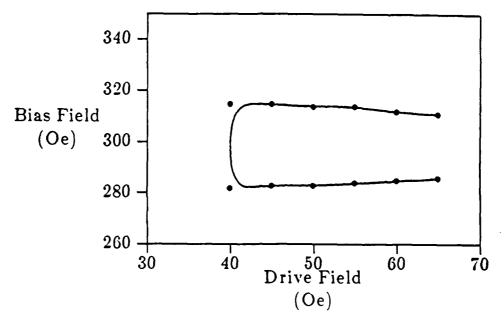


Figure 3-1: Representative Close Packed Minor Loop Diamond Track Bias Margin

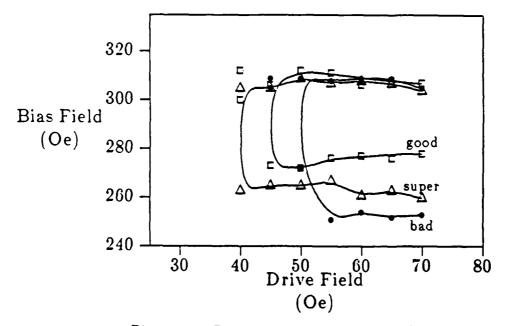


Figure 3-2: Propagation Margins for Diamond Tracks

propagation on adjacent tracks. Sometimes the stripe would contract back into a bubble but not always on the same track on which it started. A secondary failure was bubbles sticking in the cusps; the bubbles would usually remain in the first cusp from the end of the loop, as shown in Fig. 3-3. A secondary failure mode at higher drive fields was skipping. The first cusps were the most likely

cusps to be skipped, as the bubble went around the end of the track. At mid and high drive fields some jumping was observed between tracks, where the bubble would jump to another track, without forming a stripe domain. The bubbles usually jumped to the left, with the tracks oriented as shown in Fig. 3-4. For a couple of samples, the bubbles were observed jumping back and forth between two tracks.

On all tracks and at all drive fields the primary high bias failure mode was collapse, with skidding a secondary failure. In the high bias skidding failure mode, the bubbles would skip many cusps along the track.

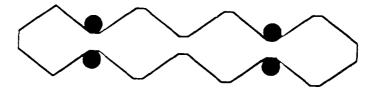


Figure 3-3: Most common positions for bubbles to stick in

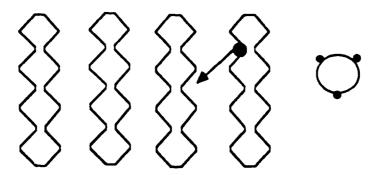


Figure 3-4: Bubbles jumping in minor tracks

3.1.2. Experimental Patterns

The results of Wullert's experimental patterns were not as promising as expected. As shown in Fig. 3-5, the minimum drive field was 50 Oe and the maximum bias margin was 8.9% with a 50 Oe drive field. Although 9% is a suitable value, the overall margin is small compared to that of the disk pattern. There is also a high drive field cutoff caused by spontaneous nucleation on the track.

At low bias fields, the main failure mode was bubbles jumping between tracks. Also at low

bias the bubbles were difficult to propagate out of the cusps. The low bias failure of striping up into the next cusp, as described in Section 1.7, was replaced with different failure modes. The original high bias failure of low collapse fields was improved but not corrected. Collapse still occurred at a low value of the bias field. While the edges are rounded, they are not rounded more than the disk patterns.

The snaked experimental pattern had a higher maximum margin which for a drive field value of 60 Oe was 12.2 % as shown in Fig. 3-6. The increase in margin was caused by a decrease in the low bias limits because the snake pattern did not exhibit any jumping between tracks. The pattern has a small overall margin, partially due to the increase in the minimum drive field. The main failure mode at low bias and low drive field was bubbles sticking in the cusps as the drive field rotated.

3.1.3. Major Loop Propagation

Bias margins of the major loop were not taken because there was no region for which the entire loop functioned properly. A description of problem areas and failure modes should give insight into future designs.

The primary problem, occurring at most values of bias and drive fields, was spontaneous nucleation along the top of the major loop which was positioned as a "super" track. Skipping of cusps, especially around turns, was another problem. The cusps most likely to be skipped are shown in Fig. 3-7. These cusps had smaller peak/cusp ratios than the regular tracks. The edge shown in Fig. 3-8 was positioned along a "super" track because the generator was positioned along it. The edge was not aligned properly as seen by the position of the bubbles when the drive field stopped rotating. Had the track had been aligned properly, the bubbles would have stopped in the cusps. Rather, they were shifted as shown in the Fig. 3-8.

3.2. Implantation

Various measurements were taken as a function of implantation dose. Bias margins at 50 Oe drive field indicate the ability of the material to propagate bubbles over a large bias field range. 50 Oe was chosen because it is a value of drive field which gave optimal results for most devices. The shape of the plot of bubble position as a function of in-plane field direction shows the propagation symmetries in the film. The full bias margins as a function of track orientation presents device operation along different track orientations.

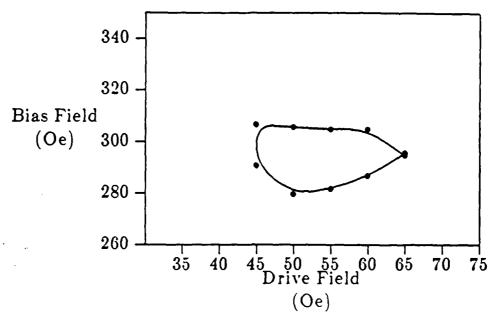


Figure 3-5: Propagation Margin - Experimental Pattern

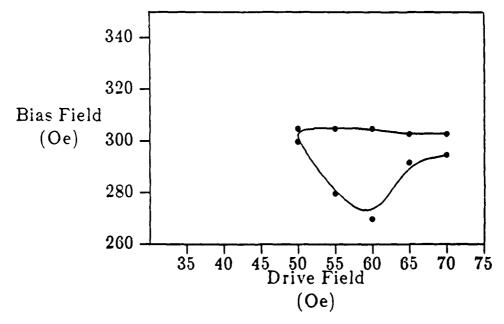


Figure 3-6: Propagation Margin - Snaked Experimental Pattern

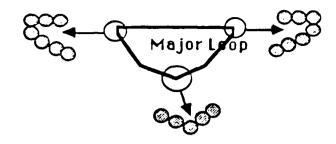


Figure 3-7: Major loop cusps where skipping occurred

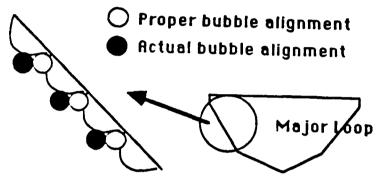


Figure 3-8: Mis-oriented major loop track

3.2.1. Bias Margins

The widths of the propagation bias margins for "super", "good" and "bad" tracks at a 50 Oe drive field were measured for each implant dose. The margin width plotted by increasing implantation dose for one side of a "good" track is shown in Fig. 3-9. Although the widest margin for wafer AH31 appears to be at a dose of $1.75 \times 10^{16} \text{ ions/cm}^2$, the best overall margin, taking into account all track orientations, is found at a dose of $1.5 \times 10^{16} \text{ions/cm}^2$ for both wafers. At a higher dose, wafer AH31 would not propagate bubbles on both sides of the "good" track. Figures 3-10 and 3-11 show the "super" and "bad" track dependences on implantation dose. At high implantation dose the margins on the "super" tracks decreased sharply while on the "bad" tracks they improved.

8.2.2. Bubble Position vs. In-Plane Field Direction

Bubble positions around an unimplanted disk were measured as the drive field was rotated. Figures 3-12 and 3-13 show the bubble position in relation to the angle of the drive field. The straight lines drawn in the figures are for comparison and indicate perfect synchronization between the bubble and the drive field. As seen in the figures, the degree to which the bubble follows the

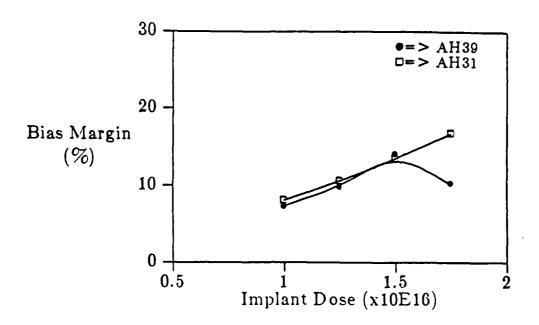


Figure 3-9: Side 1 good track bias margins as a function of implantation conditions for wafers AH39 and AH31

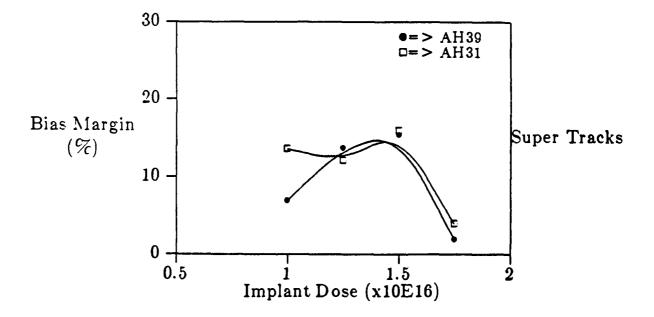


Figure 3-10: Super track bias margins as a function of implantation conditions drive field depends on the implantation dose. The bubble follows the in-plane field closer in the samples with low dose (Fig. 3-12) than the higher dose samples (Fig. 3-13). Figure 3-14 shows the bubble positions for the highest implantation dose used in this project. A change in symmetry appears to occur between the dose levels of Fig. 3-13 and Fig. 3-14, as seen by the different number of peaks in the two figures.

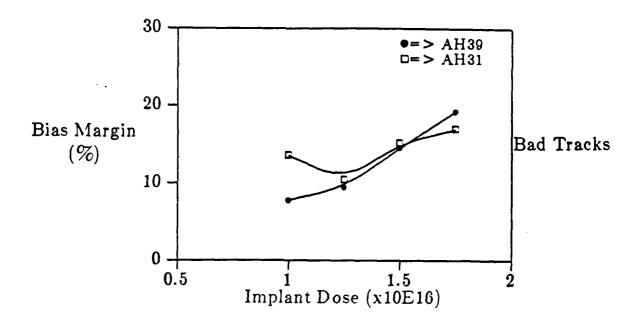
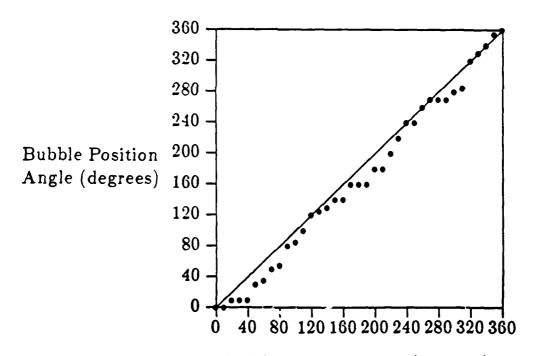


Figure 3-11: Bad track bias margins as a function of implantation conditions



In-Plane Field Angle (degrees)
Figure 3-12: Bubble position vs. in-plane field direction for low dose

implantation (1.25x10¹⁶ions/cm²)

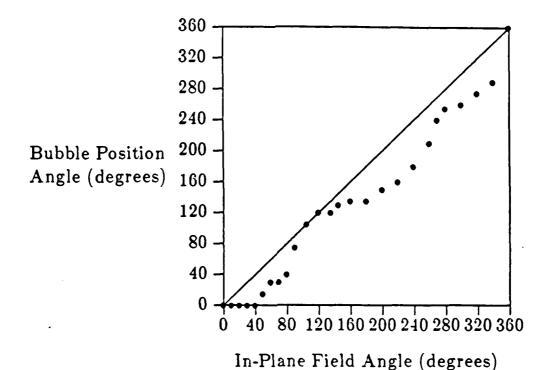
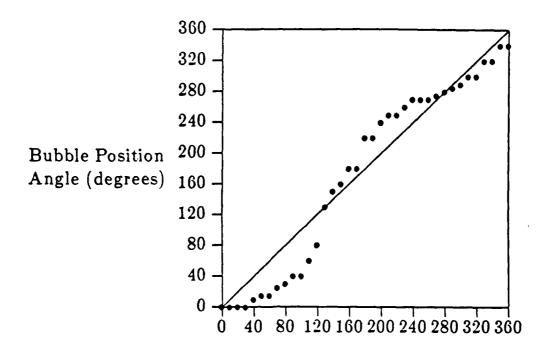


Figure 3-13: Bubble position vs. in-plane field direction for higher dose implantation (1.5x10¹⁶ions/cm²)

3.2.3. Orientation Dependence of Bias Margins

Bias margins for the different track orientations were measured for each implantation dose. Figures 3-15, 3-16 and 3-17 show the bias margins for increasing implantation dose. The more similar the bias margins, the less dependent propagation is on track orientation. Equal margins on all tracks would indicate isotropic propagation, eliminating the need for unusual major loop structures. The low dose margin, shown in Fig. 3-15, exhibits isotropic propagation around the tracks. The middle dose, shown in Fig. 3-16, shows a three fold symmetry. There are three distinctive bias margins, dependent on track orientation. All tracks on this sample show an improved margin from the lower dose sample, except for the increased minimum drive of the tracks oriented as "bad" tracks. The high dose margins in Fig. 3-17 show a different symmetry, where two orientations have good margins while the third has a greatly decreased margin.



In-Plane Field Angle (degrees)

Figure 3-14: Bubble position vs. in-plane field direction for highest dose implantation (1.75x10¹⁶ions/cm²)

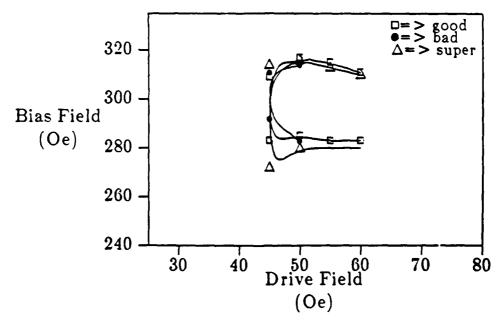


Figure 3-15: Bias margins for low dose (1.25x10¹⁶ions/cm²)

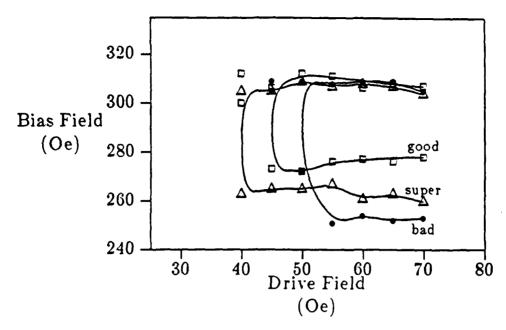


Figure 3-16: Bias margin for intermediate dose (1.5x10¹⁶ions/cm²)

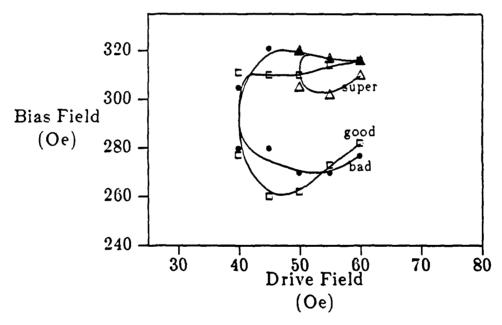


Figure 8-17: Bias margin for high dose (1.75x10¹⁶ions/cm²)

Chapter 4 Discussion

This chapter explains the results presented in the previous chapter. First the failure modes of the propagation structures will be discussed, then the implantation results.

4.1. Minor Loop Propagation

The close packed minor loops have higher low bias limits than the less densely packed tracks positioned around the device, due to charged wall interaction between tracks, which increases with the density of the tracks. In addition to failures caused by the density of the tracks, "good" tracks, used in the minor loops, often stripeout at a higher value of bias field than "super" or "bad" tracks because the stripeout direction of a "good" track is into the cusp of the adjacent "good" track. Meanwhile the stripeout direction of a "bad" track is toward the peak of the "super" track, but then it bends toward the cusp because of the strong attractive wall in the cusp. The stripeout distance is smaller and the stripeout bias field is higher for "good" tracks as shown in Fig. 4-1.

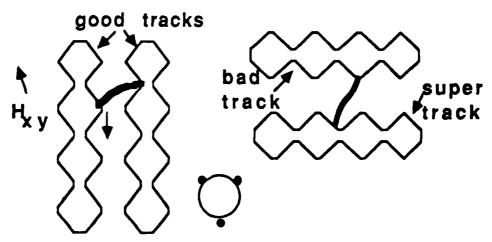


Figure 4-1: Stripeout distance between tracks

Common on densely packed tracks, especially at higher drive fields, were bubbles jumping between tracks, due to the interaction of the long charged walls. The charged walls may have been

too long, explaining the degree of interaction between tracks which was observed. The strength and depth of the charged walls are determined by the acceleration energy of the implanted ions. Since no variation of acceleration energy was done, the effects of varying the length and depth of the charged walls were not studied.

At low drive fields, the secondary low bias failure, after stripeout, was bubbles remaining in the cusps. At low drive field the charged wall does not move smoothly and can leave the bubbles in the cusps. The first cusp was often where this failure would occur. In addition to sticking in the first cusp, the bubbles would often skip the first cusp at low bias. At low bias and low drive the charged wall can become very long when the in-plane drive fields points in the easy stripeout direction. This causes the bubble to skip the first cusp, depicted in Fig. 4-2. Another skipping failure was quite different. In some devices and orientations the bubble would skip many cusps in the middle as well as the ends of the track. Skidding through many cusps happens when the affinity of the cusp is not strong enough to hold the bubble against the pushing of the repulsive charged wall.

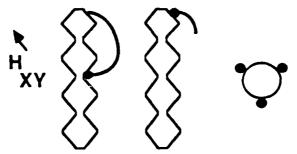


Figure 4-2: Skipping failure

The high bias failure was usually collapse, though occasionally skidding was the cause of failure. The collapse field of a skidding bubble is lower than other bubbles since it is under the influence of a repulsive charged wall instead of an attractive one⁴. The collapse fields on all tracks at all orientations were similar, which is a result of using films with nearly isotropic magnetostriction constants.

4.2. Major Loop Propagation

It is believed that many of the major loop failure modes observed can be avoided with careful design of the cusp depth and position.

The first problem was spontaneous nucleation along the top of the major loop. The top of the loop is positioned as a "super" track, making it most susceptible to spontaneous nucleation because the charged walls are the strongest there. The cusps along the top were also very sharp, as shown in

Fig. 4-3, due to the raised peaks for improved transfer margins. The sharp cusps could have increased the degree of spontaneous nucleation. Shallow cusps, on the other hand, are more likely to exhibit skipping, especially as the charged wall goes around the turn. Proper design of the cusps on the major loop should eliminate both skipping and spontaneous nucleation.

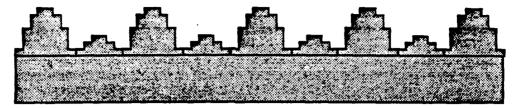


Figure 4-3: Cusps on top of major loop

4.3. Ion-Implantation

Here, the same accelerating energy of D_2^+ ions was used for all experiments, while the implantation doses were varied. Therefore, the depth of the implanted level was constant for all samples while the stress relief $(\sigma_y - \sigma_x)$ varied. The stress influences propagation through the magnetostrictive energy terms.

4.3.1. Bias Margins

The largest overall bias margins were seen in the devices implanted with a dose of 1.5×10^{16} ions/cm² even though a dose of 1.25×10^{16} ions/cm² gave isotropic propagation. The magnitude of the uniaxial anisotropy, the anisotropy responsible for the 'easy' axis along the boundary, is proportional to the stress relief $(\sigma_y - \sigma_x)$ by the term from equation(1.6):

$$E_{uniaz} = [(\sigma_y - \sigma_z)(1 - \Delta/3)]\sin^2\theta \sin^2\phi$$
 (4.1)

If the implant dose is too small, the uniaxial anisotropy along the pattern boundary will also be small. The lowest implant doses were the devices which exhibited skipping the most, which as explained above, occurs when the affinity of the cusps is not strong enough to hold the bubble in the cusp.

4.3.2. Isotropic Propagation

Both the magnetocrystalline and magnetostrictive anisotropies add to the three fold propagation observed. The three fold energy terms, taking into account both anisotropies are:

$$E_{3-fold} = \sqrt{2}/3K_1 \sin^3\theta \cos\theta \cos(3\phi)$$

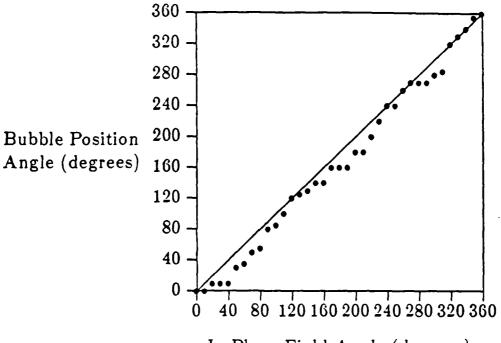
$$+ [(\sigma_y - \sigma_z)\sqrt{2} \Delta/6] \sin(2\theta) \sin(\phi + 3\psi)$$

$$(4.2)$$

Hubert⁹ estimated that the magnetostrictive effects dominate over the magnetocrystalline effects by a factor of approximately 10. Considering only the magnetostrictive effects, it can be seen for materials where Δ =0, the three fold term will disappear. The films used in this study have Δ ~3, which means the term will not disappear completely. In that case, the magnitude of the three fold term depends on the magnitude of the stress in the film $(\sigma_v$ - σ_x).

The low dose samples had nearly isotropic propagation as shown by the data in Fig. 4-4. This is explained by the low value of stress in the film. When the stress was increased as a result of increased ion dose, both the bubble position and bias margins displayed anisotropic propagation, as shown in Fig. 4-5.

The most interesting and most difficult results to explain are those from the regions implanted with the highest implant dose, $1.75 \times 10^{16} \mathrm{ions/cm^2}$. As seen in Fig. 4-6, the symmetry in the bubble position vs. drive field is different than the three-fold symmetry seen in the other samples. The bias margins also display a different symmetry.



In-Plane Field Angle (degrees)

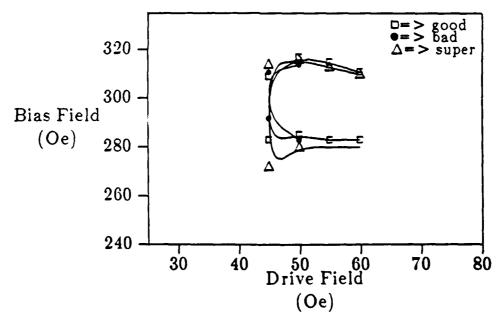
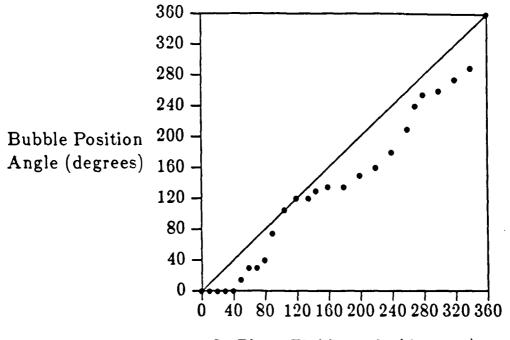


Figure 4-4: Bubble position and bias margin for low dose implant (1.25x10¹⁶ions/cm²)



In-Plane Field Angle (degrees)

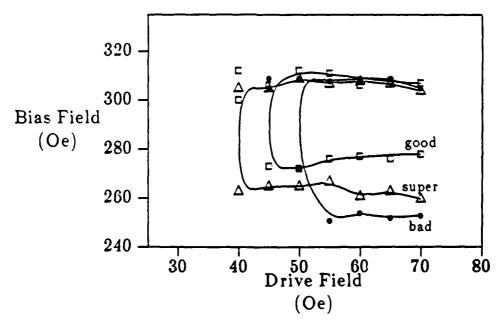
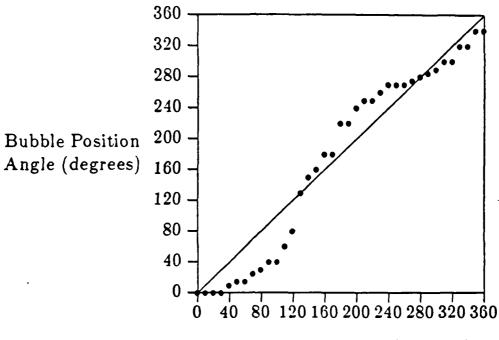


Figure 4-5: Bubble position and bias margin for intermediate dose implant(1.5x10¹⁶ions/cm²)



In-Plane Field Angle (degrees)

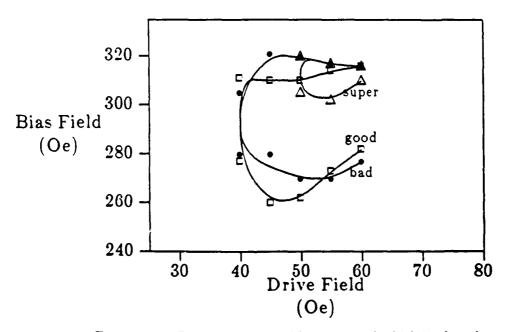


Figure 4-6: Bubble position and bias margin for high implant dose (1.75x10¹⁶ions/cm²)

Chapter 5 Conclusions

5.1. Summary

A one micron diameter, ion-implanted, contiguous disk magnetic bubble memory device has been designed and fabricated on garnet films with nearly isotropic magnetostriction constants. An optimum implantation dose of $1.5 \times 10^{16} ions/cm^2$ has been identified. Good propagation has been achieved on tracks of "good", "bad" and "super" orientations.

The symmetries and bias margins of the tracks have been studied as a function of implant dose. Devices implanted with low doses of ions had the most isotropic propagation but with reduced bias margins in all directions. Higher doses display greater anisotropies in propagation, but all tracks had wider margins. Too high a dose changed the symmetry in the film, but wide margins were still obtained from two directions of tracks. The optimal dose achieved large propagation margins in all directions.

The importance of careful design of cusp depth and position was noted, especially in design of the major loop. Use of nearly isotropic films would allow rectangular major loops which should alleviate some design difficulties.

5.2. Suggestions for Future Work

Explaining the change in symmetry for high implant dose presents an interesting area for continuing research.

The devices were fabricated with generators and transfer gates which were not tested. Work on the active functions could continue.

A half micron bubble device would be the next step in working towards small diameter, high density devices. Given similar films, with nearly isotropic magnetostriction constants, the major loop could be designed as a rectangular track.

Appendix A Device Processing

This appendix contains a detailed description of the process used in fabricating the wafers for this project.

Prespacer Deposition:

First, a thin prespacer of SiO₂ was deposited on the clean wafers by RF sputtering. This layer protects the epitaxial bubble film and prevents desorption of the deuterium during subsequent processing¹⁶.

Ion-Implantation Level:

The wafer was dehydrated in a 200°C oven for roughly one hour to promote adhesion of the photoresist to the SiO₂ layer. After cooling to room temperature, the wafer was mounted on a spinner chuck, 4-5 drops of HMDS (an adhesion promoter) were deposited on the surface and the wafer was spun at 5000 rpm for 30 seconds. A few drops of AZ 4110 photoresist were then deposited and the wafer was again spun at 5000 rpm for 30 seconds, yielding a layer of resist approximately one micron thick. The resist was prebaked at 90°C for 30 minutes.

The ion-implantation mask was patterned using a Karl Suess contact printer. At a power density of 4.5mw/cm^2 , exposure times were typically around 2 minutes with a UV filter. The exposed resist was developed in 4 parts water to one part AZ 400 developer for 60 seconds, and rinsed thoroughly in deionized (DI) water.

The wafer was divided into four regions and the different regions were implanted using the double doses shown in Table 2-2 of singly-ionized deuterium molecules $(D_2^{\ +})$.

Alignment Mark Etch:

With the implant resist patterns still on the wafers, alignment marks were etched into selected areas. To do this, AZ 1350 J photoresist was spun onto the wafer at 5000 rpm for 30 seconds and prebaked at 90°C for 30 minutes. Using a power density of 4.8 mw/cm² and no filter on the Karl Suess contact printer, an exposure time of roughly one minute was required to expose the via mask. The AZ 1350 J resist was developed for 60 seconds in a 3.5/1 ratio of water and AZ 351 developer. The mask left the alignment mark patterns exposed while the device areas were protected beneath the thick layer of photoresist. After the resist was hard baked for 30 minutes at 120°C, the wafer was placed in a buffered hydrofluoric acid solution for five minutes. The acid etched away the SiO₂ prespacer in the region

exposed by the alignment mark mask. After rinsing, the wafer was submerged in hot (90°C) phosphoric acid for three minutes. Implanted garnet etches faster than unimplanted garnet, so the patterned implanted marks were etched into the substrate for alignment of other layers. The wafers were soaked in acetone and ultrasonically agitated for several minutes to remove the resist, including the implantation mask. After drying, they were soaked in RT-2 stripping solution for a few minutes to remove any remaining resist, rinsed well with DI water, and dried once again.

Mirror Deposition:

A 250-300 angstrom thick AlCu layer was deposited by DC Magnetron sputtering to serve as a mirror for magneto-optical observation of the bubbles. For isolation, a 1000 angstrom thick SiO₂ layer was RF sputtered on top of the mirror. Later samples did not have a mirror level to prevent shorting between levels.

Conductor Layer:

The conductors were deposited by DC magnetron sputtering on a Leybold-Heraeus Z-400 sputtering system. For typical 1μ m bubble devices, 4500-5000 angstroms of Al were deposited.

The conductors were patterned using AZ-1350B-SF photoresist exposed on the Suess contact printer. The resist was spun on at 5000 rpm and then prebaked at 90°C. They were exposed for approximately 7 seconds with a power level of 5 mW/cm² and developed in a 3.5/1 solution of DI water and AZ 351 developer for one minute at 19-20°C. The temperature of the developer was kept constant as it was found to be critical to the development time. Following development and a DI rinse, they were hard baked for 15 minutes at 120°C.

Patterned AlCu conductors were etched in a solution consisting of phosphoric acid, acetic acid, water and nitric acid (PAWN). The etch solution was at room temperature and the sample was midly agitated during the etch process. Etching 5000 Angstroms took approximately 9 minutes. After etching, the samples were rinsed with DI water.

References

- 1. J.R. Wullert II, "Analysis and Design of Ion-Implanted Contiguous Disk Bubble Memory Devices", Master's thesis, Carnegie Mellon University, May 1986.
- 2. R. Wolfe and T.J. Nelson, "Crystal Symmetry Effects in Ion-Implanted Propagation Patterns for Magnetic Bubbles", *IEEE Transactions on Magnetics*, Vol. MAG-15, , 1979, pp. 1323.
- 3. Ryo Suzuki, "Recent Development in Magnetic Bubble Memory", Proceedings of the IEEE, Vol. 74, November 1986, pp. 1582-1590.
- 4. Soonchul Jo, Propagation in Submicron Ion Implanted Magnetic Bubble Computer Memory Devices, PhD dissertation, Carnegie Mellon University, 1987.
- 5. Andrew H. Bobeck and H.E.D. Scovil, "Magnetic Bubbles", Scientific American, Vol. 224, June 1971, pp. 78-90.
- 6. Sushin Chikazumi and Stanley H. Charap, Physics of Magnetism, Robert E. Krieger Publishing Company, Malabar, Florida, 1984.
- 7. M.H. Kryder and D.A. Saunders, "The Effects of Stress Relaxation and Anisotropic Magnetostriction on Charged Walls in Iom-Implanted Garnets", IEEE Transactions on Magnetics, Vol. MAG-19, September 1983, pp. 1817-1822.
- 8. Douglas A. Saunders, Stress-induced Magnetic Anisotropies in Ion-implanted, Contiguousdisk, Magnetic Bubble Devices, PhD dissertation, Carnegie Mellon University, September 1987.
- 9. A. Hubert, "The Role of Cubic Magnetostrictive Anistropy in Ion-Implanted Garnets for Magnetic Bubble Devices", unpublished.
- 10. Charles Krafft, Deuterium Implantation in Magnetic Garnets, PhD dissertation, Carnegie Mellon University, September 1984.
- 11. J. Linhard, M. Scharff, and H. E. Schiott, "", Mat. Gye. Medd. Dan. Vid. Selsk., Vol. 33, No. 14, 1963.
- 12. D.A. Saunders and M.H. Kryder, "Stresses and magnetoelastic anisotropies at implantation edges in ion-implanted garnet films", *Journal of Applied Physics*, Vol. 57, No. 1, April 1985, pp. 4061-4063.
- 13. Yeong S. Lin, George S. Almasi and George E. Keefe, "Contiguous-Disk Bubble Domain Devices", IEEE Transactions on Magnetics, Vol. Mag-13, November 1977, pp. 1744-1764.
- 14. P. Gerard, "Implantation of Bubble Garnets", Thin Solid Films, Vol. 114, 1984.
- 15. Eschenfelder, A. H., Magnetic Bubble Technology, Springer-Verlag, Springer Series in Solid State Sciences, 1981.
- 16. C.S. Krafft, M.H. Kryder and J.O. Artman, "Annealing Behavior of Deuterium Implanted Garnet Films", *IEEE Transactions on Magnetics*, Vol. Mag-20, No. 5, September 1983, pp. 1111-1113.

Simulation of Gates for Ion-Implanted Magnetic Bubble Devices

A Dissertation
Submitted to the Graduate School
In Partial Fulfillment of the Requirements

for the degree of

Doctor of Philosophy
in
Electrical and Computer Engineering

by

Michael Alex

Carnegie-Mellon University Pittsburgh, Pennsylvania October, 1988

Abstract

A computer simulator has been constructed which can be used to model the operation of current-activated gates used in ion-implanted magnetic bubble devices. parameters for the simulator include the geometry of the implanted patterns, magnetic characteristics of the bubble film, implanted layer thickness, conductor geometry, amplitude and phase of currents in conductors, and the frequency and amplitude of the The fields acting upon the bubble include those from the conductors. implanted/unimplanted boundaries and charged walls. The length and strength of the charged walls of the model are a function of the drive field strength, as are their positions, which are computed with a model similar to that described by Calhoun.¹ Once all the forces that act upon the bubble are computed, the resultant bubble wall motion is computed using the Hayashi method.² In this way, operation of various gates for ion-implanted devices has been analyzed, including a trapping transfer gate and a dual conductor block replicate gate. A novel true swap gate for ion-implanted bubble devices was also devised and simulated. Furthermore, simulation of propagation on ionimplanted patterns has been performed and predicted failure modes are the same as those observed in experimental devices. The simulated bias margins of both propagation and gate operation are seen to correspond well with experimentally obtained margins.

^[1] B. A. Calhoun, IEEE Trans. Magn., MAG-18 (6), 1395 (1982)

^[2] N. Hayashi and K. Abe, Japan. J. Appl. Phys., 14 (11), 1705 (1975)

Acknowledgments

The author would like to thank Dr. Jiin-Chuan Wu of Jet Propulsion Laboratories for his technical assistance and useful discussions throughout the course of this research, and Professor Floyd B. Humphrey of Boston University for the use of his equipment. Experimental data provided by Dr. Ryo Suzuki of Hitachi Central Research Laboratories was also helpful. Special thanks go to Dr. Douglas Saunders and Dr. Soonchul Jo who patiently explained the mechanism of charged wall formation and motion to the author. Discussions with Dr. Alfred Thiele were always interesting, sometimes voluntary, and occasionally helpful. Sincere gratitude is extended to the thesis committee, Professors James Hoburg, Lloyd Bauer and Stanley Charap, who were burdened with the honor of having to read the pages that follow - all of them. The constructive comments of Professor Charap were particularly helpful, much appreciated, and incisive. Of course, this work would never have been initiated and completed without the patience of Professor Mark H. Kryder.

This research was supported by the Air Force Office of Scientific Research under grant 84-0341, the National Science Foundation under grant ECS-8307261, and the National Nanofabrication Facility at Cornell University under grant ECS-8200312.

Table of Contents

1.	Introduction	1
	1.1. Magnetic Bubble Devices	1
	1.2. Magnetic Bubbles	1
	1.3. Current Access Devices	3
	1.4. Permalloy Bubble Memory Device Organization	4
	1.5. Permalloy Devices	6
	1.6. Contiguous Disc Devices	8
	1.7. Hybrid Devices	10
	1.8. Gates For Ion-Implanted Devices	13
	1.8.1. The Trapping Transfer Gate	14
	1.8.1.1. Transfer-In	15
	1.8.1.2. Transfer-Out	17
	1.8.2. The Block Replicate Gate	17
	1.9. The Dual Gate	19
	1.9.1. The Pseudo-Swap Function	21
	1.9.2. The Block Replicate Function	22
	1.10. Summary	24
2.	Theoretical Background	27
	2.1. Energies in Magnetic Bubble Films	27
	2.1.1. Introduction	27
	2.1.2. Anisotropy Requirements for Bubble Stability	28
	2.2. The Inverse Magnetostrictive Effect	29
	2.3. Crystalline Anisotropy	30
	2.4. Magnetization in Implanted Layers	31
	2.5. Stress Relaxation and Charged Wall Formation at Implanted Edges	35
	2.6. Domain Walls and Their Motion	41
	2.6.1. Introduction	41
	2.6.2. Wall Energy and Wall Width	41
	2.6.3. Wall Dynamics	45
	2.6.4. The Effects of Finite Wall Thickness on Wall Motion	48
	2.6.5. Bubble Motion	50
	2.7. Bubble Domain Stability	53
	2.7.1. Mathematical Analysis of Domain Stability	53
	2.7.2. Stable Bubble Diameter	61
	2.7.3. Bubble Collapse and Stripeout Fields	63
	2.8. Fields in Ion-Implanted Devices	63
	2.8.1. Introduction	63
	282 The Edge Affinity Field	64

	2.8.3. Charged Wall Model	68
	2.8.4. The Charged Wall Field	69
	2.8.5. Charged Wall Motion	71
	2.9. Spontaneous Bubble Nucleation	74
	2.9.1. Nucleation Model	75
	2.10. Summary	77
3.	Simulation of Bubble Devices	81
	3.1. The Hayashi Method	81
	3.1.1. Numerical Methods	85
	3.2. Simulator Overview	90
	3.2.1. Introduction	90
	3.2.2. Simulator Programs	91
	3.2.2.1. Charged Wall and Bubble Motion	91
	3.2.2.2. Propagation Pattern Geometry	92
	3.2.2.3. Conductor Geometry	93
	3.2.2.4. Domain Wall Motion Calculation	94
	3.3. Summary	95
4.	Transfer Gate Simulation	97
	4.1. Bubble Propagation	97
	4.2. Trapping Transfer Gate Simulation	102
	4.3. Transfer-In Simulation	105
	4.3.1. Trapping Current Amplitude	105
	4.3.2. Trapping Current Phases	108
	4.4. Transfer-Out Simulation	118
	4.4.1. Trapping Current Amplitude	118
	4.4.2. Trapping Current Phases	121
	4.5. Summary	129
5.	Replicate Gate Simulation	131
	5.1. Bubble Propagation	131
	5.2. Block Replication Simulation	134
	5.2.1. Replicate Current Margins	135
	5.2.2. Replicate Current Phase Margins	143
	5.2.2.1. High Coercivity Failure	155
	5.2.2.2. Replicate-In Mode	155
	5.3. The Dual Gate	161
	5.3.1. Introduction	161
	5.3.2. The Replication Process	161
	5.3.3. The Pseudo-Swap Function	163
	5.4. Summary	168
6.	New Swap Gate Design and Simulation	171
	6.1. Introduction	171
	6.2. Swap Gate Design	172
	6.2.1. Gate Geometry	172
	6.2.2. New Swap Gate Operation	172
	6.3. Swap Gate Simulation	175
	6.3.1. The Simulated Swap Process	175

6.3.2. Simulated Gate Current Margins	177
6.3.3. Single Bubble Swap Gate Operation	179
6.3.3.1. Transfer-In	180
6.3.3.2. Transfer-Out	180
6.4. Summary	185
7. Conclusions	189
7.1. Contributions of This Thesis	189
7.2. Future Work	191
7.2.1. Simulator Improvement	191
7.2.2. New Gate Design	192
Bibliography	193

List of Figures

Figure 1-1:	Schematic diagram of the organization of a 68 Kbit bubble chip. ¹	5
Figure 1-2:	Bubble propagation in an asymmetric chevron permalloy bubble device as a function of the direction of the drive field, H _{ip} .	7
Figure 1-3:	Replicate (a) and swap (b) gates for permalloy bubble devices. Their operation is explained in the text.	8
Figure 1-4:	Bubble propagation on ion-implanted bubble device as a function of the direction of the drive field, H _{xv} .	10
Figure 1-5:	Comparision of the bubble size and device cell in (a) T-bar, (b) asymmetric chevron, and (c) contiguous disc devices. ⁵ The minimum lithographic feature is W.	11
Figure 1-6:	A portion of a hybrid bubble device in which the major line consists of permalloy. The minor loops are higher density ion-implanted tracks and interface to the major line by having portions that also consist of permalloy, requiring bubbles to traverse an implanted/unimplanted boundary during propagation. The shaded portion depicted is the ion implanted area of the device. Arrows indicate potential barriers, IP (implanted to permalloy) and PI (permalloy to implanted) that bubbles must surmount at the implanted/unimplanted interface.	13
Figure 1-7:	Schematic illustration of the potential barrier that exists at an implanted/unimplanted boundary. A bubble must surmount this barrier as it traverses the boundary.	14
Figure 1-8:	Trapping transfer gate design by Bell Laboratories. Sense of the drive field H _{xy} , is given along with the three easy-stripeout directions. Gate operation in both transfer-in and transfer-out mode is explained fully below.	15
Figure 1-9:	Implementation of the transfer-in function using the trapping transfer gate of Fig. 1-8. In (a), the bubble is seen rotating counterclockwise with the drive field. As the field approaches 180 degrees as in (b), the hairpin is activated, trapping the bubble. The current is turned off in (c) when the field is near 360 (0) degrees, allowing the bubble to attach to the charged wall on the minor loop end. The bubble then propagates away on the minor loop in (d).	16

Figure 1-10:	Implementation of the transfer-out function using the trapping transfer gate of Fig. 1-8. As the drive field approaches 0 degrees the bubble approaches the hairpin and the conductor is pulsed, as depicted in (a) and (b). The bubble is trapped by the hairpin and the next attractive passing charged wall is formed on the major loop as the field is near 180 degrees, at which time the current is turned off, allowing the bubble to propagate along the major track with this wall as in (d).	18
Figure 1-11:	A block replicate gate for ion-implanted devices. Conductor 1 (shaded) is the stretching conductor; conductor 2 (hatched) is used for chopping domains elongated by conductor 1.	19
Figure 1-12:	Operation sequence of the block replicate gate of Fig. 1-11. In (a) the bubble is propagating on the end of the minor loop, and when it gets near the tip of the loop (the field is near 0 degrees here), stretch current I_s is activated and the bubble stripes out, (b). Upon completion of stripeout, I_s is terminated and chopping current I_c is used to cut the stripe in half, (c). The two stripes shrink into bubble domains and the replication process is complete, (d).	20
Figure 1-13:	Design of a block replicate and pseudo-swap gate. 13, 14 Coined a "dual gate", its modes of operation are explained in detail below.	21
Figure 1-14:	Implementation of the pseudo-swap function using the dual gate. Initially, Conductor 2 is pulsed in order to annihilate any data extant in the minor loops. In (a) we see that a bubble has been collapsed by pulse I_2 . When the drive field is near 0 degrees, current I_1 is pulsed, stretching out the major loop data, (b). Upon stripeout of the domain, which has now reached the minor loop, I_1 is terminated and current I_2 is used to chop the domain in half, effecting a "replicate-in" process, (c) and (d).	23
Figure 1-15:	Relative annihilation, stretching, and chopping current phases required for implementation of the pseudo-swap function depicted in Fig. 1-14.	24
Figure 1-16:	Implementation of the block replicate function using the dual gate. The block replicate function as performed by this gate is identical to the process described for the gate of Fig. 1-12, except for slight variations in conductor geometry. Refer to Fig. 1-12 for details of its operation.	25
Figure 1-17:	Relative stretching and chopping current phases required for implementation of the block-replicate function depicted in Fig. 1-16.	26
Figure 2-1:	Coordinate system used for calculating domain energy.	29
Figure 2-2:	Charged wall formation due to in-plane magnetization anisotropy parallel to the unimplanted propagation pattern edges. The applied drive field is denoted as H	31

Figure 2-3:	Critical curve used to find stable directions of M in the implanted layer.	34
Figure 2-4:	Exaggerated view of an implanted/unimplanted boundary illustrating the effects of implantation on lattice expansion.	36
Figure 2-5:	Coordinate system used for calculating magnetostrictive anisotropies of Eqn. (2.13).	38
Figure 2-6:	Schematic illustration of the magnetostrictive anisotropies of Eqn. (2.13) responsible for charged wall formation and position.	40
Figure 2-7:	A cross-sectional view of a bubble domain in a thin platelet depicting the rotation of spins through the bubble wall.	41
Figure 2-8:	A section of a domain Bloch wall showing the wall width and the orientation of the spins as a function of position through the wall. After Eschenfelder. 1	43
Figure 2-9:	Configuration of spins in the center of a Bloch wall. After Eschenfelder. 1	44
Figure 2-10:	The effect of the stray field on spins in the wall.	49
Figure 2-11:		51
Figure 2-12	Coordinate system describing domain and coordinate system used in calculating domain stability.	54
Figure 2-13	Graphical determination of bubble stability. After Thiele. 15	60
Figure 2-14		62
Figure 2-15		62
Figure 2-16	,	64
Figure 2-17	B	
_	·	65
Figure 2-18	· · · · · · · · · · · · · · · · · · ·	66
Figure 2-19	: Perpendicular field, averaged through the film thickness, of the implanted/unimplanted edge of Fig. 2-18. Here, $\theta = 85$ degrees, $4\pi M_s$ of the material is 600 G, $h = 0.4\mu m$ and $h_1 = 1.2\mu m$	67
Figure 2-20	·	70
Figure 2-21	•	72
Figure 2-22		75
Figure 2-23	·	76
Figure 2-24	· · · · · · · · · · · · · · · · · · ·	78
Figure 2-25		79

	depicted in Fig. 2-24. The conductors each have $w = 3\mu m$ and are separated by $g = 2\mu m$. Each conductor carries a	
Figure 3-1:	current of 1mA; field values shown are for $z=1.55\mu\text{m}$. Representation of the bubble domain wall in the laboratory and local frames. The wall point $P(\xi)$ is specified by a parameter ξ which is the wall length $O_{\mathbf{w}}P$ divided by the	82
E: 2 0	total wall length L.	00
Figure 3-2:	Wall displacement at wall point P(I) in the R-S frame.	88
Figure 3-3: Figure 4-1:	The calculation of the demagnetizing field on a wall point. Typical bubble propagation simulation. The three easy	98 90
rigure 4-1:	stripe-out directions and drive field rotation sense are also shown. Bubble positions plotted every 160 nsec, except in cusps where positions are plotted every 5μ sec. Simulation drive field frequency was 125 kHz.	
Figure 4-2:	Simulated bias field margins of bubble propagation in the minor loops of the A.T.&T. trapping transfer gate denoted by the filled circles. Published margins of Nelson et al. are given by the open boxes. ⁸ Simulations performed using the parameters of Table 4-1.	101
Figure 4-3:	Field contours of the charged walls used in the simulator described herein. On the left hand side of the minor loop are the perpendicular field contours, plotted in 2 Oe increments, for the charged wall assumed to exist at a drive field of 40 Oe, as explained in the text. The right hand side charged wall field contours are assumed to occur when the drive field amplitude is 80 Oe. For intermediate drive field values, the charged wall field is found by interpolating between the two extremes depicted here.	102
Figure 4-4:	The three types of propagation failure observed during simulation. On the left-hand side is seen bubble stripe-out along the pattern edge. The middle depicts bubble collapse in the cusp, and on the right-hand side is seen bubble lag, explained in detail in the text.	103
Figure 4-5:	A.T.&T. trapping transfer gate and grid used to compute fields and bubble wall positions. 1 grid unit equals $0.25\mu m$ here.	104
Figure 4-6:	Simulated transfer-in current vs bias field margins for the trapping transfer gate. Successful transfer denoted by open circles, failure is shown by the crosses. Here, the current pulse was initiated at $\theta = 160.0$ degrees and was terminated at $\theta = 358.0$ degrees.	106
Figure 4-7:	_ ~ ~	107
Figure 4-8:	VI	108
	margins for the transfer-in process. Simulation parameters are given in Table 4-1.	
Figure 4-9:	Simulated bias field vs transfer current turn-on angle, θ_{t1}	109

	margins of transfer-in for an isotropic material. These simulations were performed using the same parameters used	
	to obtain Fig. 4-8.	
Figure 4-10:	Simulated bias field vs transfer current turn-on angle, θ_{t1}	109
	margins for the transfer-in process.	
Figure 4-11:	Simulated bias field vs transfer current turn-on angle, θ_{t1} margins of transfer-in for an isotropic material. These simulations were performed using the same parameters used to obtain Fig. 4-8.	110
Figure 4-12:	Simulated bias field vs transfer-in current turn-off angle, θ_{t2}	111
Figure 4-13:	margins for an anisotropic material. Measured bias field vs transfer-in current leading edge angle margins for the trapping transfer gate as given by Nelson et al. ⁸	111
Figure 4-14:	Measured bias field vs transfer-in current trailing edge angle margins for the trapping transfer gate as given by Nelson et al. ⁸	112
Figure 4-15:	The transfer-in process shown as a function of time.	115
Figure 4-18:	Perpendicular magnetic field contours of the trapping transfer gate for a current of 1 mA flowing through the conductor. Each number denotes the contour value in Oe/mA, with the positive contours being a potential minimum for the bubble.	117
Figure 4-17:	Transfer-in failure due to low bias and low trapping current.	119
Figure 4-18:	Simulated bias field vs transfer-out current margins for the trapping transfer gate. Here, the current pulse was initiated at $\theta = 2.0$ degrees and was terminated at $\theta = 160.0$ degrees. Open circles denote good transfer and crosses denote failure.	120
Figure 4-19:	Measured bias field vs transfer-out current margins for the trapping transfer gate as given by Nelson et al. ⁸	120
Figure 4-20:	Simulated bias field vs transfer-out current leading edge phase, θ_{tl} margins for the trapping transfer gate. Here, the current pulse was terminated at $\theta = 160.0$ degrees with an	122
Figure 4-21:	amplitude of 35 mA for a typical anisotropic material. Transfer-out margins of Fig. 4-20 for an ideal isotropic material.	123
Figure 4-22:	Simulated bias field vs transfer-out current trailing edge phase, θ_{t2} margins for the trapping transfer gate. Here, the	124
	current pulse was initiated at $\theta = 2.0$ degrees with an amplitude of 35 mA in a typical anisotropic material.	
Figure 4-23:	•	124
Figure 4-24:		125
Figure 4-25:	-	125
9~ 3-20.	TATOMORION AIMS TIME AS ALMINIOS AND ARTICLES ASSESSED.	

	angle margins for the trapping transfer gate as given by Nelson et al. ⁸	
Figure 4-26:	The transfer-out process.	127
Figure 4-27:	The transfer-out process illustrating how the bubble can be "pulled" back into the gate area even though the bubble is a few bubble diameters beyond the conductor notch. The current pulse was activated at $\theta = 65$ degrees here.	128
Figure 4-28:		130
Figure 5-1:	Experimental and simulated propagation margins for the minor loops of the block-replicate gate of Urai et al. ⁹ Parameters used in obtaining the simulated margins are given in Table 5-1. The heavy black line is the published experimental data of Urai et al. and the diamonds denote successful simulated margins. Simulated stripeout and bubble collapse are given by the minus signs (-) and dots, respectively.	132
Figure 5-2:	Simulated bias field margins for bubble propagation with the wall coercivity as a parameter. Margins degrade from the low bias end as the coercivity is increased from 1.0 Oe (Light line) to 3.0 Oe (Dark line). When $H_c = 3.5$ Oe, the high bias margins fall drastically. (Dashed line.)	134
Figure 5-3:	Block replicate gate design and grid used to compute fields and bubble wall positions. 1 grid unit equals 0.25 \mu m here.	136
Figure 5-4:	Simulated bias field vs stretching current margins for the gate depicted in Fig. 5-3, depicted by the open circles. $I_c = 100$	137
	mA. The experimental margins of Urai et al. ⁹ are shown as open boxes.	
Figure 5-5:	Simulated bias field vs chopping current margins for the gate depicted in Fig. 5-3. $I_s = 80 \text{ mA}$.	137
Figure 5-8:	The block replicate process shown as a function of time.	139
Figure 5-7:	Failure mode in the block replicate process due to insufficient stretching current.	142
	Failure mode in the block replicate process due to insufficient chopping current.	144
Figure 5-9:	margins for the gate depicted in Fig. 5-3. $I_s = 80$ mA, $I_c = 100$ mA.	145
Figure 5-10:	margins for the gate depicted in Fig. 5-3, shown by the open circles. Experimental margins of Urai et al. given by open boxes. The stretching current turn-off angle, denoted by the arrow, was 27 degrees here.	146
Figure 5-11:	between termination of the stretching current pulse and beginning of the chopping current pulse.	148
Figure 5-12:	Failure mode in the block replicate process due to late stretching current pulse leading edge.	151

Figure 5-13:	Normalized perpendicular magnetic field contours due to a current of 1 mA. in the stretching conductor. The fields are	152
Figure 5-14:	averaged over the height of the bubble film thickness. Failure mode in the block replicate process due to late	154
5 .	stretching current pulse falling edge.	
Figure 5-15:	Failure in the block replicate process due to short chopping pulse.	156
Figure 5-16:	Successful replication even though short stretching pulse duration prevented the expanding stripehead from reaching the major loop cusp prior to activation of the chopping conductor.	157
Figure 5-17:	Effect of coercivity on minimum stretching current required for successful replication in the gate Fig. 5-3. Squares denote current margin at a bias field of 346 Oe, circles give margin at 320 Oe bias field. $I_c = 100$ mA for both sets of data.	158
Figure 5-18:		159
Figure 5-19:	Operation of the block replicate gate in the replicate-in mode.	160
Figure 5-20:		161
Figure 5-21:	Simulated replication process as performed by the dual gate. 13, 14 Parameters used in the simulation given in Table 5-2.	164
Figure 5-22:	Annihilation, stretching, and chopping current phases required for implementation of the simulated pseudo-swap function depicted in Fig. 5-23.	166
Figure 5-23:		169
Figure 6-1:	New swap gate design for ion-implanted devices. The shaded conductor is a pair of parallel stretching hairpin conductors. The hatched second level conductor is used to shift elongated domains to the nearest implanted pattern.	173
Figure 6-2:	Swap operation as performed by the gate depicted in Fig. 6-1. Bubbles at positions A and B are simultaneously transferred to positions A' and B' respectively.	174
Figure 6-3:	Actual simulation of the swap function as performed by the simulator described in this thesis. Nominal simulation parameters are given in Table 6-1.	176
Figure 6-4:	Simulated bias field vs Conductor 1 current I_1 margins for the swap gate described in this disclosure. Conductor 2 current I_2	178
Figure 6-5:	= 65 mA here; other parameters are given in Table 6-1.	178
	- OF HIS HOLD, OTHER PERMITORIS MIS BITCH IN AMOIS O'A.	

Figure 6-6:	Actual simulation of the transfer-in function as performed by the simulator described in this thesis. Nominal simulation parameters are given in Table 6-1, except that $I_2 = 0$ here.	181
Figure 6-7:	Error in the transfer-in process due to long current pulse delay.	183
Figure 6-8:	Actual simulation of the transfer-out function as performed by the simulator described in this thesis. Nominal simulation parameters are given in Table 6-1, but $I_2 = 0$ here.	186
Figure 6-9:	Error in the transfer-out process due to long I, current pulse.	188

List of Tables

Table 2-1:	Comparison between Thiele's computed force and stability functions and approximated force and stability functions for $d/h = 1.0$. Approximated values of $F(d/h)$ and $S_0(d/h)$ were	61
	computed from equations (2.55) and (2.56) respectively, 25 and the approximated value of $S_2(d/h)$ was computed using	
	equation $(2.57)^{26}$.	
Table 4-1:	Nominal trapping gate simulation parameters.	99
Table 5-1:	Nominal replicate gate simulation parameters.	133
Table 5-2:	Parameters used to simulate the block replicate function as performed by the dual gate of Fig. 5-20.	163
Table 5-3:	Parameters used to simulate the pseudo-swap function as performed by the dual gate of Fig. 5-20.	167
Table 6-1:	Nominal swap gate simulation parameters.	179

Chapter 1

Introduction

1.1. Magnetic Bubble Devices

Magnetic bubble devices, used in magnetic bubble memory storage systems, are solid state devices that take advantage of the non-volatility typical of magnetic storage devices (tapes, discs, etc.) as well as the non-mechanical access inherent in semiconductor memories (DRAMS, etc.). Their non-volatility, small size, lack of moving parts and radiation hardness favors their use in hostile environments where vibration, power interruption, and moisture prevent the use of mechanical storage devices such as discs and tape drives. Being solid state devices, they utilize the same well-known fabrication procedures used in typical semiconductor devices and as a result are easy to produce, are relatively inexpensive compared to certain types of mechanically accessed storage media and have high densities.

In this section, bubble devices are introduced following a brief explanation of what is exactly meant by a bubble. The essential components of a bubble memory device as well as the different types of bubble devices that have been invented and their differences will be presented. Devices being used at the time of this writing and future devices will be described and it will be shown that this thesis work is most important in the design and simulation of next-generation bubble devices.

1.2. Magnetic Bubbles

Being the key component of the bubble device, here a very cursory description of bubbles is given. In the following chapter, the magnetic and material characteristics of bubbles will be presented in mathematical detail.

Bubbles are magnetic domains whose magnetization is oriented antiparallel to the

magnetization in an otherwise saturated thin platelet which, for practical reasons, has a thickness comparable to the bubble domain diameter. In order to have a magnetic configuration of this type, the material must have certain characteristics. First and foremost is the requirement that the magnetization lie perpendicular to the plane of Fortunately, the rare earth iron garnet system has just these the thin film. characteristics. Although other types of materials have been shown to support the formation of bubbles, the rare earth iron garnet system has been most widely used. Having the general formula {RE₃}[Fe₂](Fe₃) O₁₂, this ferrimagnetic cubic crystalline material has three magnetic sublattices. The magnetizations on the two Fe sublattices are antiparallel to each other and may provide some of the net room temperatu e magnetization. Antiparallel to the net Fe sublattice magnetization is the RE sublattice magnetization. Depending upon the type(s) of rare earth element(s) substituted into this lattice, the net magnetization desired may be chosen by the device designer. In addition, the Fe sites may also be diluted by other elements in order to vary other magnetic parameters, such as bubble size, magnetostriction coefficients, mobility, K₁₁, etc. 1

Having a material with perpendicular uniaxial anisotropy is not enough to qualify the material for use in bubble devices. If we look at the magnetic configuration of a virgin bubble film, we would see that half the area of the film is magnetized parallel to the film normal (typically the [111] direction) and one half the area is magnetized antiparallel to the film normal. A film in this state is referred to as demagnetized and is in the lowest magnetic energy configuration in the absence of applied fields. The uniaxial symmetry of this state is broken by the application of a magnetic field with a component normal to the film plane. Domains oriented parallel to the applied field component will grow and increase in area at the expense of domains oriented Given an applied field of sufficient amplitude, the antiparallel to the field. antiparallel domains will shrink in size to become domains having the shape of rightcircular cylinders, which are termed "bubbles". Above a critical field value, all of the antiparallel domains (bubbles) will collapse and the platelet will be saturated in the same direction as the applied field. In the Theory chapter, the magnetic field range of bubble stability, typically used to characterize the "quality" of a bubble device, will be calculated in terms of the film thickness and magnetic parameters of the film.

Bubbles, once formed and stabilized by an external applied field as described above, may be moved in the plane of the bubble film by using field gradients. For now, let us not be concerned with how these gradients are applied to the device in order to induce bubble motion. It will suffice to say that bubbles, logical "1's", may be propagated along with the absence of bubbles, logical "O's", in a periodic fashion along propagation tracks that also physically define stable bit positions. Bubbles, once propagated to a specific chip region may be replicated and their presence (absence) converted to an electrical pulse (no pulse) in order to be read by peripheral circuitry as a digital "1" ("0"). Here, we have alluded to all the essential ingredients required for a memory device. The first requirement was bubble formation and stabilization by using an external field. In any memory device data must be written into the memory. The second requirement was bubble propagation. The ability to move bubbles allows selective readout of specific data that one is interested in reading. Finally, it was mentioned that bubbles may be replicated and read out. The ability to read data without losing it or having to rewrite it back into the memory is a highly desired feature. The way all of these functions are implemented is a function of the method used to propagate bubbles and as such they will be described independently when the different schemes used for propagating bubbles are introduced.

1.3. Current Access Devices

Magnetic bubbles were first propagated in orthoferrites through the use of control conductors placed on the surface of the bubble film.² It was obvious to early researchers that field gradients created by pulsed conductors were a logical way to control bubble domain motion. These early devices used current loops and meandering conductors in conjunction with etched grooves or ferrite patterns on the film surface to propagate bubbles.

Since the early current access devices utilized narrow conductors as a means of creating drive fields, power dissipation/bit was relatively high. In addition, to avoid having a bubble accessed (that was not meant to be accessed) by a conductor line in proximity meant that the bit density of these devices was low. Even though high data rates could be obtained, the large number of electrical contacts made fabrication difficult. In addition, it was usually required that the bubble and the propagation

pattern maintain rather precise geometrical constraints for proper device operation. These constraints were relaxed somewhat by current-access schemes in which drive field gradients were produced by coarsely patterning a planar conducting sheet deposited onto the bubble film.^{3, 4}

Research on devices utilizing current as a means of bubble propagation (henceforth referred to as as current access devices) was superseded by research on field access devices. In field access devices, a globally rotating field in the plane of the bubble film causes bubbles to propagate, with the assistance of permalloy or ion-implanted structures on the film surface. The in-plane field responsible for propagation, known as the drive field, is provided by a pair of orthogonal coils wrapped around the chip. Since this thesis is concerned only with field access devices, the discussion of current-access bubble propagation schemes will not be pursued to any further extent.

1.4. Permalloy Bubble Memory Device Organization

In this section, typical bubble memory device organization will be presented. This is because one may better appreciate the problems associated with improving the characteristics of a device or system in order to conceive an improved or new system if one has a good grasp of the workings of the present system. It will also point out to the less initiated reader that beyond high density, successful implementation of bubble replication and bubble transfer is critical for a useful bubble device.

The organization of a 68 Kbit bubble memory chip is depicted in Fig. 1-1.¹ Although present day chips have higher capacities, their organization is identical to the major/minor loop organization of the device shown and thus it will be suitable to use this example to illustrate the relevant features of today's devices. First, it will help to define some bubble device terminology. In a typical bubble device, the storage area of the device usually consists of long, parallel tracks that define bit positions and act as propagation elements. These tracks are commonly referred to as the storage or minor loops. In the chip shown in the figure, there are a total of 131 minor loops that consist of 523 bits each; actually there are 65 odd block loops and 66 even block loops. Odd numbered bits are stored in the odd block loops and even numbered bits are stored in the even block loops. Thus, this device stores 523 records; each record is 131

bits long with each minor loop storing one bit of one record. Data is transferred into or out of the minor loops along separate propagation paths called *major* loops. Major loop data are spaced *two* bits apart, and if the even block major line is L_1 bits long then the odd block major line will be L_1+1 bits long so that data can be interleaved and read or written on every rotating field cycle.

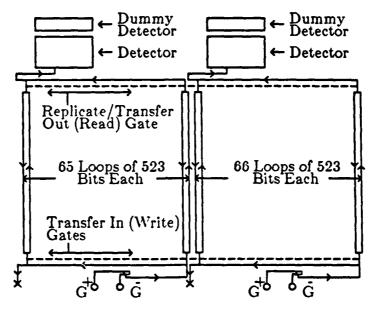


Figure 1-1: Schematic diagram of the organization of a 68 Kbit bubble chip. 1

When writing to the chip, the generators, G, are pulsed, creating bubbles where required. The bubbles are written serially as they are being propagated along the major loop as shown in the bottom of the figure. Not seen in the figure is the geometry of the transfer in or write gate. In the region of this gate the major and minor loops are in close proximity and a current carrying conductor can be pulsed which "pops" the bubbles from the major loop into the minor loops. Thus, all 131 bits of one record are written into the minor loops in parallel. After a full record (131 bits) is written, the generators can begin writing more data into the major loops as the previously written record data shuttles or idles about the bit positions of the minor loops, each bit of the record moving one bit position with each rotating field cycle. To read a record, the chosen record is propagated to the "top" of the minor

loops into the vicinity of the replicate or transfer out gate. Again, this gate is the interface between the minor loops and a second major loop, this major loop leading to a detector which converts the bubble magnetization to an electrical signal. When the record is in position on the top of the minor loops, a replicate conductor is pulsed which replicates the bubbles by essentially splitting them in two; one of the pair of bubbles "pops" out to the major loop while the other one stays in the minor loops. The record on the major loop is propagated through the detector and discarded, while the record which was copied is idling in the minor loops. Thus, the data is read out non-destructively, a desirable feature to have in memory devices.

1.5. Permalloy Devices

At the time of this writing all commercially available bubble devices are of this type. In permalloy devices, bubbles are attracted to a magnetically soft patterned overlay, such as NiFe (permalloy) on top of the bubble film. As the rotating drive field polarizes the propagation elements, bubbles follow the attractive poles and are driven to the next attractive pole due to the perpendicular field gradient as seen in Fig. 1-2.

One desirable feature of these devices is the ability to replicate data from the minor loops as it is being transferred into the major loops. This is seen in Fig. 1-3(a), where the small arrows indicate directions of bubble propagation and the sense of the drive field H_{xv} is also shown. The major loop in (a) is at the top of the figure running horizontally and the minor loops are at the bottom oriented vertically; thus we are looking at the interface between the major and minor loops. As a bubble propagating along Path 1 reaches the pick-axe shaped permalloy element it stripes out along the edge of the element due to the poles induced there by the rotating drive field, as seen in the figure. Then the control conductor loop is pulsed, chopping the stripe in half. Since the drive field is still rotating, one bubble remains in the minor loop, moving along Path 2 and the replicated bubble moves along Path 3 to the major line. The data has been replicated to be read out, and it also remains in the storage area of the This is referred to as Non Destructive Read Out or NDRO, and is a desireable feature for devices of practical interest, as mentioned previously. If the control conductor is not pulsed, no data replication occurs and the bubble simply circulates around the minor loop along Path 2.

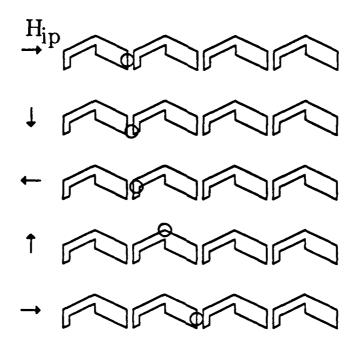


Figure 1-2: Bubble propagation in an asymmetric chevron permalloy bubble device as a function of the direction of the drive field, H_{ip}.

Furthermore, in (b) of the same figure, we see a typical gate used for swapping data between the minor and major loops of permalloy devices. Here, the major loop is at the bottom of the figure, and as in the replicate gate above, the major and minor loop is bridged by a conductor. A bubble at position "C" in the major loop will move to position "D" in two rotating field cycles in the absence of any applied current to the conductor. Likewise, a bubble in the minor loop starting at position "A" will circulate to "B" under the same conditions. Both bubbles will traverse the positions labeled "1, 2, 3, 4" etc. in their respective loops in sequence as the drive field rotates. Now upon applying a current to the conductor, a bubble beginning at "C" is frustrated from moving along the path "1, 2, 3, 4" etc. and will travel along the path "2c, 3c, 4c, 1c" etc. up to position "B". Likewise, the bubble in the minor loop at position "A" will move along the path "4a, 1a, 2a, 3a" etc to position "D" in the major loop. The net result is that the data at "A" and "C" are swapped with each other.

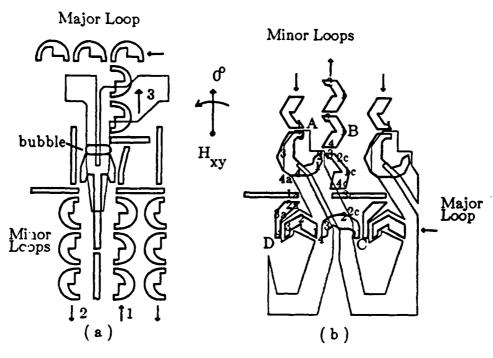


Figure 1-3: Replicate (a) and swap (b) gates for permalloy bubble devices. Their operation is explained in the text.

1.6. Contiguous Disc Devices

One type of field access device utilizes ion-implantation to create a bubble propagation structure. This type of device is known as a contiguous disc or ion-implanted device. It is fabricated as follows: An epitaxial film with magnetic anisotropy perpendicular to the film plane is masked with photoresist, gold, etc. The wafer is then ion-implanted. After implantation, the stress induced in the implanted areas causes the magnetization there to lie in the plane of the film while the magnetization under the masked patterns remains perpendicular to the film plane. Under the application of an in-plane field, the in-plane magnetization is oriented in the same direction as the in-plane field. However, at the implanted/unimplanted boundary, the magnetization diverges, causing the formation of charged walls, one positive (converging) and the other negative (diverging). As the in-plane field is rotated, the in-plane magnetization and charged walls also rotate; bubbles coupled to the charged walls will then also rotate along with the drive field. Judicious selection

of the ion-implanted mask geometry will allow formation of a bubble propagation structure.

In Fig. 1-4 we illustrate schematically bubble motion on an ion-implanted propagation structure as a function of the drive field direction. When the drive field H_{xv} is oriented along direction 1 as indicated in the lower half of Fig. 1-4, bubbles on the upper portion of the propagation pattern will be positioned at the points denoted by the number 1; bubbles on the lower portion of the pattern will be in the cusps that are labelled 6-3. As the drive field rotates in clockwise sense to position 2, the the upper bubbles also move on the propagation pattern to points labelled as 2 while the bubbles in the cusps remain stationary. Now as the field rotates through 3, 4, 5, and 6, bubbles on the upper half of the propagation pattern cannot move and remain in the cusps denoted by labels 3-6. On the other hand bubbles on the lower half of the pattern move one pattern period during this portion of the field cycle to an adjacent cusp. The salient features of this propagation scheme are as follows: One complete drive field rotation (360 degrees) will move a bubble one bit period and for a reasonable portion of the field cycle (at least 180 degrees) bubbles remain stationary in the cusps. Bubble propagation is dictated by the formation and propagation of charged walls that form on the propagation pattern. Due to the complex nature of charged wall formation and propagation, to be discussed in more detail later, bubble propagation on ion-implanted structures is complex and not readily computed.

The major advantage of ion-implanted devices over permalloy devices is the increase in areal density obtainable for a given lithography constraint in ion-implanted devices. This is clearly seen in Fig. 1-5⁵ in which (a) permalloy T-bar, (b) permalloy asymmetric chevron, and (c) ion-implanted contiguous disk devices are all drawn to the same relative scale. We see that for a given lithographic restraint (the minimum feature that can be resolved), W, the T-bar device has a device cell that occupies an area of 18W x 18W and the corresponding bubble size is 4W. The asymmetric chevron, which is the propagation pattern utilized in present day (1988) commercially available bubble devices, allows the bubble size to be reduced to 1.5W and the cell size occupies an area of 8W x 9W. Finally, in (c) it is seen that in ion-implanted devices the cell size can be as small as 2.5W x 3W and that the bubble size is less than the minimum resolvable lithographic feature by a factor of two.

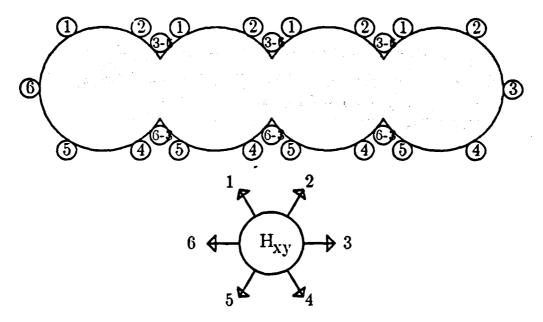
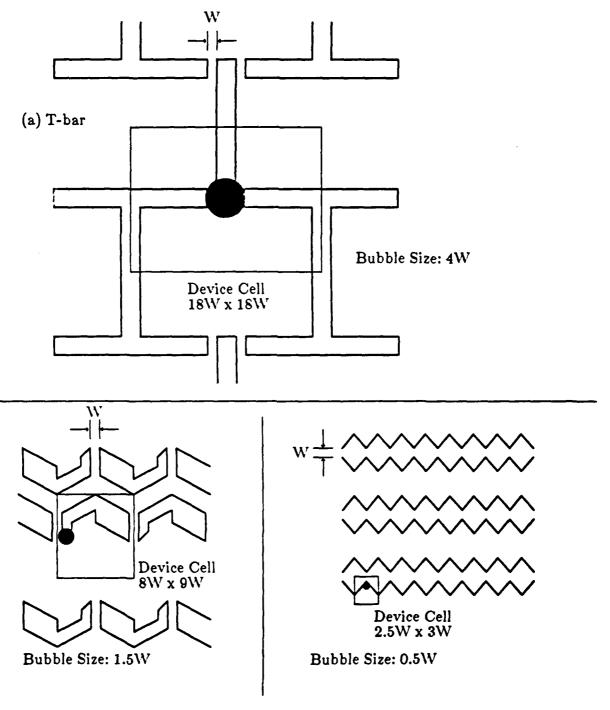


Figure 1-4: Bubble propagation on ion-implanted bubble device as a function of the direction of the drive field, H_{xv}.

1.7. Hybrid Devices

From the above discussion regarding the density advantage of ion-implanted devices over permalloy devices one can easily see how ion-implanted devices are preferred to permalloy devices. However, bubble behavior in ion-implanted devices is different than that in permalloy devices. For now let us only discuss briefly these major differences as they will be analyzed in detail in a later section.

One of the major impediments preventing ion-implanted devices from supplanting permalloy devices is the fact that to date there is not a gate with sufficient operating margin that will non-destructively replicate data in ion-implanted devices. As discussed in the section on permalloy devices, it was seen that due to the nature of the propagation elements in these devices that bubbles to be replicated stripe out passively, facilitating the replicate process. In this type of replication process, only one conductor level is required. During propagation in ion-implanted devices, bubbles are typically confined to the vicinity of the propagation pattern edge and do not stripe



(b) Asymmetric chevron

(c) Contiguous disk

Figure 1-5: Comparision of the bubble size and device cell in (a) T-bar, (b) asymmetric chevron, and (c) contiguous disc devices.⁵ The minimum lithographic feature is W.

out spontaneously. Thus, to implement replication, a conductor is required for striping out the bubble and another is needed to chop the stripe in half, creating two bubbles. The need for two conductors increases the fabrication complexity of the device as well as the complexity of the bubble chip control circuitry, since now two active functions must be performed by the chip controller, requiring another external power supply.

To circumvent this problem while taking advantage of the higher density of ion-implanted devices, the hybrid device was proposed. In this device, of which a portion is seen in Fig. 1-6, the minor loops consist mainly of high density ion-implanted loops (the shaded area on the right hand side of the figure) while the major loop consists of permalloy. A small section of the minor loop is also made of permalloy, requiring the bubbles propagating on these loops to periodically cross an implanted/unimplanted interface. Passive stretching in this device is still performed by a permalloy element and stripe chopping is done by a single conductor, making this device compatible with the controller for all-permalloy devices.

Although the hybrid device enables the replicate function to be implemented in very much the same fashion as the less dense all-permalloy devices while at the same time allowing the highest bit density possible, it does suffer from a number of handicaps that are inherent in this technology. Obviously, fabrication complexity is increased, since both an implantation mask level and a permalloy deposition and patterning level must be employed in its manufacture. Beyond this, however, are the problems that arise due to the differences in bubble characteristics in permalloy and implanted devices. For example, in a given material, the bias field range of bubble stability may be much different before and after ion-implantation due to the effects ion-implantation has on the physical and magnetic properties of the material, both of which will be explained in detail in the chapter on Theory. This is illustrated schematically in Fig. 1-7 where it is seen that for a bubble to traverse an implanted/unimplanted boundary there is an energy barrier that must be surmounted. Furthermore, an additional permalloy pattern in the vicinity of this boundary makes the potential that affects the bubble there even more complex. The potential barrier is not symmetric as indicated in Fig. 1-6, where the arrows indicate that bubbles must

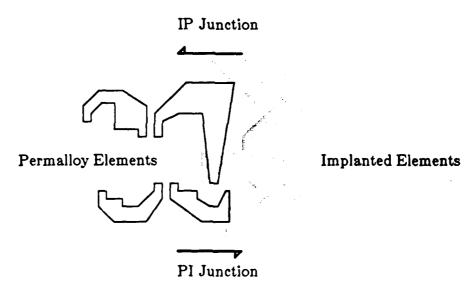


Figure 1-6: A portion of a hybrid bubble device in which the major line consists of permalloy. The minor loops are higher density ion-implanted tracks and interface to the major line by having portions that also consist of permalloy, requiring bubbles to traverse an implanted/unimplanted boundary during propagation. The shaded portion depicted is the ion implanted area of the device. Arrows indicate potential barriers, IP (implanted to permalloy) and PI (permalloy to implanted) that bubbles must surmount at the implanted/unimplanted interface.

cross both an implanted to permalloy barrier (IP junction) and a permalloy to implanted barrier (PI junction). Needless to say, bubble propagation across these barriers is unreliable and highly dependent on the fabrication processes and geometries of the elements in the vicinity of the junctions.⁷

1.8. Gates For Ion-Implanted Devices

It is obvious that in order to utilize any type of data storage scheme, the data to be stored must be written and read without loss of data integrity in the read and/or write process. In addition, the ability to access data should not come at the expense of inordinate amounts of chip area, processing complexity, etc. While the hybrid permalloy/ion-implanted structure was seen as a means by which the inherent high density of ion-implanted devices could be complemented with the passive bubble stretching properties of permalloy in order to implement the block replicate function,

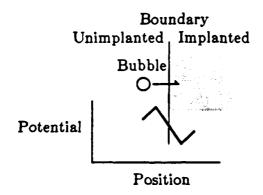


Figure 1-7: Schematic illustration of the potential barrier that exists at an implanted/unimplanted boundary. A bubble must surmount this barrier as it traverses the boundary.

there are problems associated with this structure as has been shown in the previous section and this device is more complicated to fabricate than other devices. In fact, there are indications that some bubble manufacturing concerns that were exploring the hybrid technology have encountered problems so severe that they have chosen instead to pursue fully ion-implanted technology. Even if the hybrid technology is successfully employed in the next generation of bubble devices it is only a matter of time before they are superseded by all-implanted chips. Thus, various types of transfer, replicate, and swap gates need to be implemented for ion-implanted devices. Several of the gates which were investigated in this study are presented and their operation described briefly.

1.8.1. The Trapping Transfer Gate

A transfer gate that was proposed by workers at Bell Laboratories is depicted in Fig. 1-8.8 In this figure we see a bubble on the end of a minor loop; the major loop in the lower half of the figure is bridged to the minor loop end by a hairpin conductor, shown shaded in the figure. Also given in the figure is the sense of the rotating drive field, H_{xy} , and the orientation of the three easy-stripeout directions. We will next show how this gate may be used to transfer a bubble from the minor loop to the major loop (transfer-out) or from the major loop to the minor loop (transfer-in). Since bubble transfer in this device is implemented by trapping the bubble by means of a current through the hairpin conductor for a portion of the rotating field cycle, this gate is referred to as a trapping transfer gate.

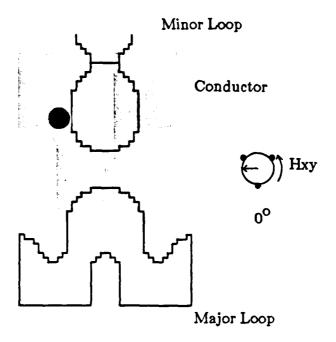


Figure 1-8: Trapping transfer gate design by Bell Laboratories. Sense of the drive field H_{xy}, is given along with the three easy-stripeout directions. Gate operation in both transfer-in and transfer-out mode is explained fully below.

1.8.1.1. Transfer-In

Here will be shown how the trapping transfer gate of Fig. 1-8 is used to transfer bubbles from the major loop into the minor loops. Referring to Fig. 1-9(a), we see that bubbles propagate along the convex portions of the major loop in the same sense as the drive field, that is, the bubble shown is moving counterclockwise towards the center of the hairpin conductor. As the drive field H_{xy} , approaches 180 degrees as seen in Fig. 1-9(b), the conductor is pulsed with current I. Now, if the field continues rotating as a current I of sufficient amplitude is applied, the bubble will be trapped in the center of the hairpin as the charged wall to which the bubble is attached continues rotating along the major loop with the drive field. As the field approaches 360 (0) degrees, an attractive charged wall forms at the bottom of the minor loop. Upon turning off the current through the hairpin, the bubble can be "captured" by this wall as depicted in Fig. 1-9(c). As the field continues rotating, the bubble which is now in the minor loop, propagates away from the gate area as seen in (d) of the figure.

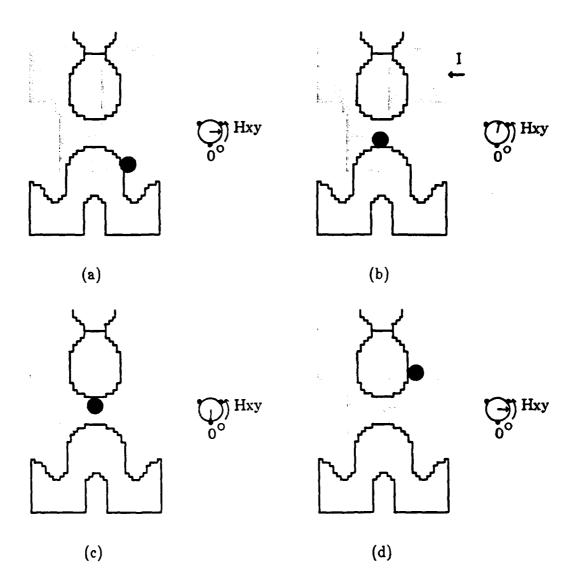


Figure 1-9: Implementation of the transfer-in function using the trapping transfer gate of Fig. 1-8. In (a), the bubble is seen rotating counterclockwise with the drive field. As the field approaches 180 degrees as in (b), the hairpin is activated, trapping the bubble. The current is turned off in (c) when the field is near 360 (0) degrees, allowing the bubble to attach to the charged wall on the minor loop end. The bubble then propagates away on the minor loop in (d).

Introduction 17

1.8.1.2. Transfer-Out

As the name implies, this process is just the reverse of transfer-in. Referring to Fig. 1-10(a), a bubble that is stored in the minor loop is seen circulating on the end of the minor loop near the gate. As the bubble approaches the gate, which it will do when the drive field is near 0 degrees, the conductor is pulsed with current I as seen in part (b) of the figure. As in the transfer-in process, the current is applied so that the bubble becomes trapped as the drive field continues rotating. When the field is near 180 degrees, as shown in (c), the nearest attractive charged wall is on the tip of the major loop to which the bubble becomes attached when the current is turned off. The bubble is now in-phase with the charged wall and drive field and may be propagated out along the major loop for detection (d).

1.8.2. The Block Replicate Gate

The block replicate gate for ion-implanted devices as described here was presented simultaneously by a number of independent authors with only minor differences in the gate design. 9, 10, 11, 12 For now, these differences will be overlooked since they are not relevant to the general features of gate operation.

The basic gate design is shown in Fig. 1-11. It consists of two overlapping conductors that lie orthogonal to each other; their point of intersection lies in the gap between the major and minor loop as seen in the figure. "Conductor 1", shaded in the figure is a stretching conductor and the hatched conductor denoted as "Conductor 2" is used for chopping stripe domains. The conductors are electrically isolated from each other and are enabled independently as seen in the following description of gate operation. Note that Figure 1 11 also gives the sense of the drive field as well as the three easy-stripeout directions.

Operation of the gate depicted in Fig. 1-11 is illustrated in Fig. 1-12. In Fig. 1-12(a) a bubble is seen propagating on the minor loop tip as the drive field is approaching 0 degrees. The stretching current I_s is activated causing bubble elongation along the hairpin channel length (Fig. 1-12(b)). Following bubble stretching I_s is terminated and the chopping current I_c is activated (Fig. 1-12(c)), cutting the stripe in half. The two stripes contract and become bubbles; one bubble remains in the minor loop and the new bubble is now in the major line to be read out.

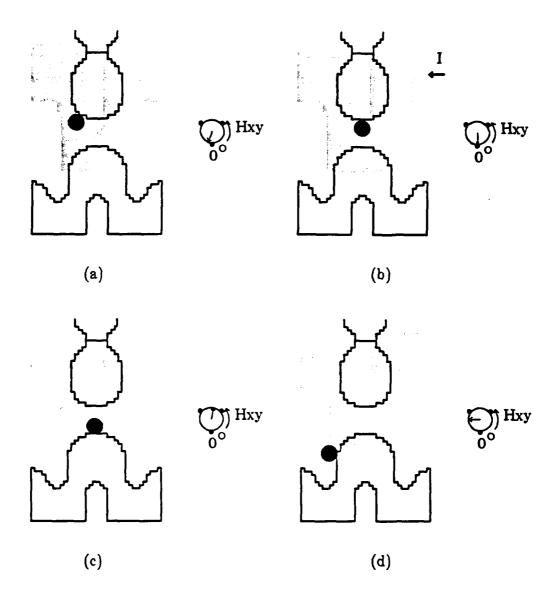


Figure 1-10: Implementation of the transfer-out function using the trapping transfer gate of Fig. 1-8. As the drive field approaches 0 degrees the bubble approaches the hairpin and the conductor is pulsed, as depicted in (a) and (b). The bubble is trapped by the hairpin and the next attractive passing charged wall is formed on the major loop as the field is near 180 degrees, at which time the current is turned off, allowing the bubble to propagate along the major track with this wall as in (d).

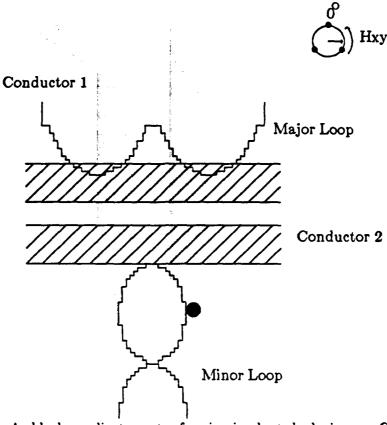


Figure 1-11: A block replicate gate for ion-implanted devices. Conductor 1 (shaded) is the stretching conductor; conductor 2 (hatched) is used for chopping domains elongated by conductor 1.

1.9. The Dual Gate

The dual gate was proposed by Sato et al. and its configuration is given in Fig. 1-13.^{13, 14} It consists of two hairpin conductors that overlap the minor loop end and the cusp on a major loop. The conductors are electrically isolated from each other and are activated independently. In the figure the first level conductor is shaded and denoted as "Conductor 1"; the second level conductor is shown as "Conductor 2". The rotation sense of the drive field is also given in the figure along with the three easy-stripeout directions. The gate gets its name from the fact that it is used to implement two distinct functions: block replicate and pseudo-swap (annihilate and replicate-in). Both of these functions will be explained in detail.

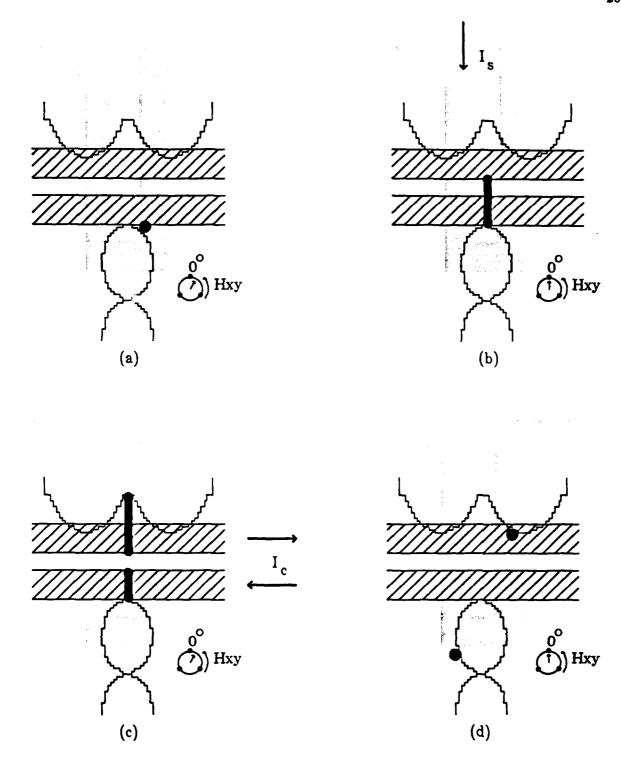


Figure 1-12: Operation sequence of the block replicate gate of Fig. 1-11. In (a) the bubble is propagating on the end of the minor loop, and when it gets near the tip of the loop (the field is near 0 degrees here), stretch current I_s is activated and the bubble stripes out, (b). Upon completion of stripeout, I_s is terminated and chopping current I_c is used to cut the stripe in half, (c). The two stripes shrink into bubble domains and the replication process is complete, (d).

The Dual Gate

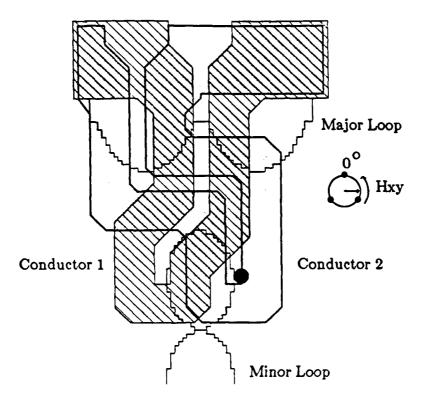


Figure 1-13: Design of a block replicate and pseudo-swap gate. Coined a "dual gate", its modes of operation are explained in detail below.

1.9.1. The Pseudo-Swap Function

The "pseudo-swap" function does not actually swap or exchange data between the major and minor loops as it does as implemented in permalloy technology. It merely deletes existing data in the minor loops before replacing that data with new data from the major loop. From the following description of its operation, the reader will see that it is more like an "erase before write" gate.

From Fig. 1-14(a) it is seen that if bubbles are circulating about the minor loops as well as propagating along the major line, when the drive field is at approximately 270 degrees the major loop bubbles are in the cusps and the minor loop bubbles may be situated on the right-hand-side of the minor loop tip as shown. The major loop bubble is black and the minor loop bubble is depicted as the open circle here. When the current through Conductor 2, I₂, is pulsed in a sense such that the magnetic field in the center of the channel of Conductor 2 raises the bias field there, the bubble on the minor loop tip will collapse, as indicated in the figure. This annihilation pulse is

depicted in Fig. 1-15 as the chopper current pulse commencing at θ_{a1} and ending at θ_{a2} . The pulse length required for collapsing the bubble is short compared with the period of the rotating field, so the bubble motion during this time period is small. When the field is near 0 degrees, current I_1 through Conductor 1 is pulsed, stretching the bubble which has been residing in the major loop cusp. This point in field phase is denoted as θ_{s1} in Fig. 1-15, and is shown in Fig. 1-14(b), where I_1 is denoted by the dashed arrow. Note that the polarity of I_1 is opposite that of I_2 . In (c) of the figure, it is seen that the stripe domain has reached the minor loop along the channel of Conductor 1 and more importantly, the middle of the stripe is now positioned perpendicular to the channel of Conductor 2. At this point in time, the current which is stretching the domain is terminated and followed by I_2 in a sense that results in chopping the stripe in half, as shown. The portion of the stripe on the minor loop contracts back into a bubble in the absence of any applied currents and is then propagated away by a charged wall on the minor loop as seen in (d) of the figure.

1.9.2. The Block Replicate Function

The block replicate function is similar to the aforementioned pseudo-swap function, except that there is no annihilation of minor loop data prior to bubble stretching and chopping. Furthermore, in this case, data is replicated out of the minor loop and into the major loop. Looking at this operation in more detail we see in Fig. 1-16(a) that as the bubble to be replicated is circulating around the minor loop end as the field approaches 0 degrees, current I_1 in Conductor 1 is activated, stretching the bubble upwards toward the major loop as depicted in (b). When the bubble stretches along the channel of Conductor 1 and has bridged the major and minor loops, I_1 is terminated and the bubble is chopped due to the cutting current I_2 in Conductor 2 as seen in (c) of the figure. Due to nearby attractive charged walls, the cut stripes, which quickly shrink into bubbles, propagate out of the gate area in phase with the drive field. The relative stretching and chopping current phases are depicted in Fig. 1-17 and with the exception of the annihilation pulse needed for the "pseudo-swap" function, they are identical to the pulses used to implement "pseudo-swap".

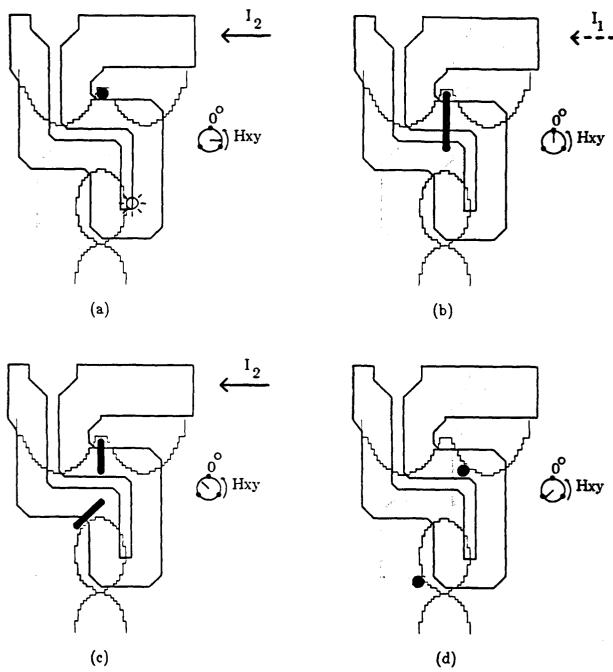


Figure 1-14: Implementation of the pseudo-swap function using the dual gate. Initially, Conductor 2 is pulsed in order to annihilate any data extant in the minor loops. In (a) we see that a bubble has been collapsed by pulse I₂. When the drive field is near 0 degrees, current I₁ is pulsed, stretching out the major loop data, (b). Upon stripeout of the domain, which has now reached the minor loop, I₁ is terminated and current I₂ is used to chop the domain in half, effecting a "replicate-in" process, (c) and (d).

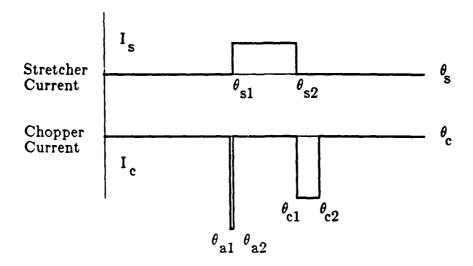


Figure 1-15: Relative annihilation, stretching, and chopping current phases required for implementation of the pseudo-swap function depicted in Fig. 1-14.

1.10. Summary

Here, we have tried to briefly introduce to the reader the method used to replicate data in present-day permalloy devices. An all-permalloy major/minor loop chip can be designed to take advantage of the fact that bubbles will spontaneously elongate due to poles on permalloy patterns, and upon stretching these bubbles can be chopped for reading. However, to take advantage of the inherent density of ion-implanted devices and avoid the additional fabrication complexity and marginal performance of hybrid devices, there is a need for implementation of the replicate function in all-implanted devices. To our knowledge, feasible implementation will require the use of two conductor levels: one for stretching the bubble and the other for chopping the elongated domain. As a result, simulation of the replication process was deemed to be an important means to this end.

In the following chapter, background and theory pertinent to the understanding of magnetic bubbles will be given. The effect of ion-implantation on magnetic bubble material will be described in detail since we shall see that bubble behaviour in implanted devices is strongly affected by this process as compared to un-implanted

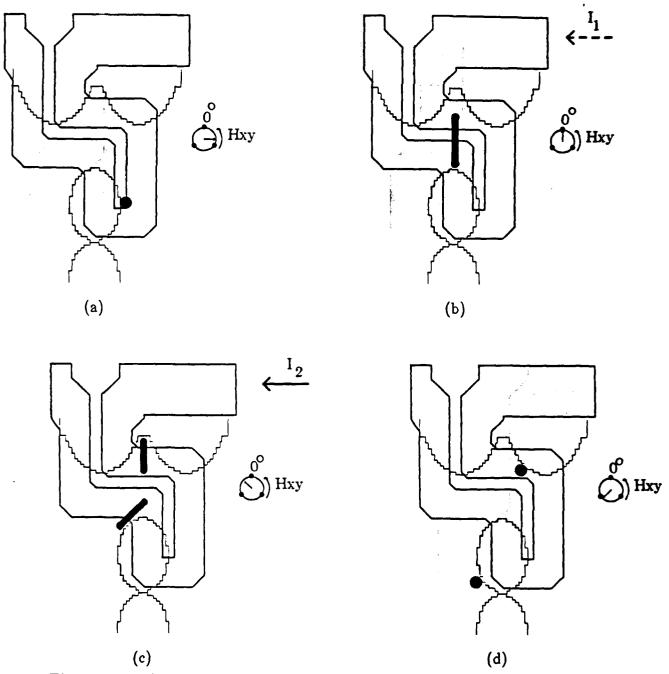


Figure 1-16: Implementation of the block replicate function using the dual gate.

The block replicate function as performed by this gate is identical to the process described for the gate of Fig. 1-12, except for slight variations in conductor geometry. Refer to Fig. 1-12 for details of its operation.

devices. Finally, the assorted fields that may play roles in determining domain behaviour in implanted devices are described and the methods used to calculate the magnitude of these fields formulated.

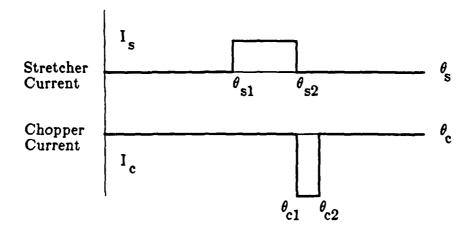


Figure 1-17: Relative stretching and chopping current phases required for implementation of the block-replicate function depicted in Fig. 1-16.

Chapter 2

Theoretical Background

2.1. Energies in Magnetic Bubble Films

2.1.1. Introduction

In this chapter, we develop the theoretical framework that will be required in order to model bubble domain behavior in ion-implanted devices. First and foremost is the anisotropy that appears in ion-implanted layers and its effect on bubble motion in these types of devices. We will briefly introduce the roles of anisotropic magnetostriction and magnetocrystalline anisotropy in implanted films and how they are responsible for the 3-fold symmetric behavior observed in these films.

As was described in the Introduction, proper implementation of the replicate function in ion-implanted devices requires that the bubble stripe out prior to chopping. The theory of bubble stability as formulated by Thiele¹⁵ is introduced since this allows one to calculate the field threshold at which a stable bubble domain will expand into a stripe. Since the field required for domain stretching is proportional to the current needed in patterned conductors on the bubble film surface, this critical field is an important parameter in device design, particularly in devices with small bubble diameters in which the current densities are near the limits of electromigration.¹⁶

Since bubbles in ion-implanted devices are under the influence of fields from the implanted/unimplanted interface that defines the propagation patterns, the method used for computing these fields is described. The field computed, depicted in the Introduction in Fig. 1-7, is plotted for a straight boundary to illustrate the magnitude of this effect commonly referred to as the edge affinity. Following this, the model

used to account for the field of the charged wall, and its motion around propagation patterns will be described. Finally, the phenomenon known as spontaneous bubble nucleation will be described and a model introduced to account for this error mode.

2.1.2. Anisotropy Requirements for Bubble Stability

Bubble materials are typically grown with an easy axis of anisotropy perpendicular to the film plane, i.e. the magnetization M is perpendicular to the film surface and parallel to the [111] crystal direction as seen in Fig. 2-1. Due to the aspect ratio of the film (its thickness compared to its planar dimensions) there is a demagnetizing energy penalty that must be paid for this magnetic configuration. The demagnetizing energy reduces the uniaxial anisotropy as given by the equation:

$$E = (K_u - 2\pi M_s^2) \sin^2 \theta , \qquad (2.1)$$

where K_u is the uniaxial anisotropy constant of the material, M_s is the saturation magnetization of the material and θ is the angle between M and the film normal. Note that if K_u is less than the $2\pi M^2$, which is the demagnetizing energy for a thin film, it is energetically favorable for M to lie in the film plane. The ratio of the anisotropy energy to the demagnetizing energy is defined as the quality factor:

$$Q = \frac{K_u}{2\pi M_s^2} \ . \tag{2.2}$$

Clearly, Q must be greater than one for stability of perpendicularly oriented domains.

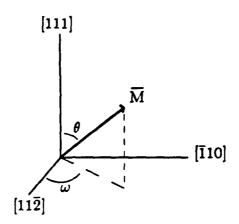


Figure 2-1: Coordinate system used for calculating domain energy.

2.2. The Inverse Magnetostrictive Effect

As mentioned in the Introduction, ion-implanted devices utilize the magnetostrictive effect to alter the magnetic properties of the upper surface of the bubble layer in order to define a propagation structure. For now, let us look at the effect ion-implantation has on the film far from an implanted/unimplanted boundary. (The effect in the vicinity of pattern edges will be discussed in detail shortly.) Our purpose in this section is to explain the anisotropic behavior observed in ion-implanted bubble devices which, it will be seen, has major impact on device performance and results in design restrictions that must be considered when designing and studying bubble device elements, such as propagation patterns.

When a film is ion-implanted, a strain is induced which results in lattice expansion perpendicular to the film plane. Since the film is confined by the thick substrate it is grown upon, no expansion occurs in the film plane, giving rise to a state of planar compression. Through the inverse magnetostrictive effect the magnetostrictive energy is given by:

$$E = -\frac{3}{2}\sigma_p \lambda_{111} \sin^2 \theta = -K_i \sin^2 \theta , \qquad (2.3)$$

where $\sigma_{\rm p}$ is the planar stress, λ_{111} is the magnetostriction constant along the [111] direction and θ is the angle between M and the [111] direction. In typical garnet compositions, λ_{111} is negative and $\sigma_{\rm p}$ due to ion-implantation is also negative (the film is in a state of compression) resulting in an easy axis in the film plane which reduces the uniaxial perpendicular anisotropy. Thus, for appropriate values of λ_{111} and $\sigma_{\rm p}$, M may be induced to lie in the film plane.

2.3. Crystalline Anisotropy

Since the garnets are crystals, there is magnetocrystalline energy which must be accounted for in analyzing the total magnetic energy of the system. To first order, the cubic crystalline anisotropy energy density is given as:

$$E_{1} = K_{1} \left(\alpha_{1}^{2} \alpha_{2}^{2} + \alpha_{2}^{2} \alpha_{3}^{2} + \alpha_{3}^{2} \alpha_{1}^{2} \right) , \qquad (2.4)$$

where the α 's are the direction cosines of M with respect to the crystal axes. For positive K_1 there are three easy <100> axes. For negative K_1 , typical of ion-implanted bubble device materials, there are four easy <111> axes.

Using the coordinate system of Fig. 2-1, Eqn. (2.4) may be rewritten as:

$$E_1 = K_1 \left(\frac{1}{4} \sin^4 \theta + \frac{1}{3} \cos^2 \theta + \frac{\sqrt{2}}{3} \sin^3 \theta \cos \theta \cos 3\omega \right) . \tag{2.5}$$

2.4. Magnetization in Implanted Layers

As mentioned above, the ion-implanted bubble device derives its propagation force from the motion of charged walls in the implanted layer which can be rotated under the influence of a rotating in-plane field. Bubbles coupled to the charged walls then propagate along with the rotating charged walls. Charged wall formation is due to the in-plane anisotropy induced by ion-implantion which causes the magnetization of the ion-implanted layer, termed the drive layer, to lie in the plane of the film. The charged walls form where the in-plane magnetization diverges, as is depicted in Fig. 2-2. Here, our purpose is twofold: 1) to show the reader that charged wall behavior is dictated by the anisotropic magnetic characteristics of the drive layer and, 2) to calculate the effect of these anisotropies. Once again utilizing the coordinate

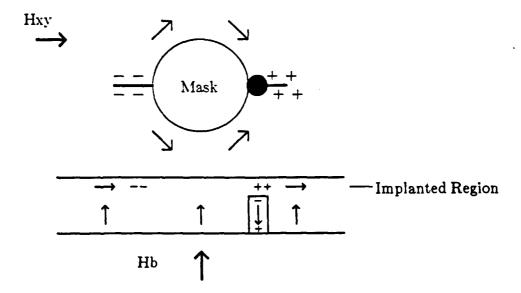


Figure 2-2: Charged wall formation due to in-plane magnetization anisotropy parallel to the unimplanted propagation pattern edges. The applied drive field is denoted as H_{xy} .

system depicted in Fig. 2-1 we may write the total magnetic energy of a domain in the

implanted region by summing the previously discussed energy terms as shown in the following equation:

$$\begin{split} E &= -MH_x \sin\theta \cos\omega - MH_y \sin\theta \sin\omega - MH_z \cos\theta \\ &- (K_u - K_i - 2\pi M^2) \cos^2\theta \\ &+ K_1 (\frac{1}{4} \sin^4\theta + \frac{1}{3} \cos^2\theta + \frac{\sqrt{2}}{3} \sin^3\theta \cos\theta \cos3\omega) \ , \end{split} \tag{2.6}$$

where the first three terms are due to the applied field interaction energy, the fourth term is the net perpendicular uniaxial anisotropy (the growth induced uniaxial anisotropy, K_u , minus both the stress-induced in-plane anisotropy, K_i , and the demagnetizing energy, $2\pi M^2$) and the last term is due to the aforementioned magnetocrystalline anisotropy. The externally applied fields H_x , H_y , and H_z are directed along the $\begin{bmatrix} 1 & 1 & 2 \end{bmatrix}$, $\begin{bmatrix} \overline{\Gamma} & 1 & 0 \end{bmatrix}$, and $\begin{bmatrix} 1 & 1 & 1 \end{bmatrix}$ axes of Fig. 2-1 respectively.

In order to calculate the stable equilibrium magnetization configuration of the drive layer, the total energy must satisfy the following equations:

$$\frac{\partial E}{\partial \theta} \; = \; 0 \; \; \text{and} \; \; \frac{\partial^2 E}{\partial \theta^2} \; > \; 0 \; \; , \label{eq:energy_energy}$$

$$\frac{\partial E}{\partial \omega} = 0$$
 and $\frac{\partial^2 E}{\partial \omega^2} > 0$. (2.7)

Fortunately, the analysis is facilitated due to the fact that the applied bias field, H_g , forces variations of θ with respect to ω to be small.¹⁷ Computations show that θ in typical materials varies from 73 to 78 degrees and can be treated as a constant. Thus, only the variations of energy with respect to ω need be considered here. Calculating the first and second derivatives:

$$\frac{\partial E}{\partial \omega} = M H_x \sin \omega \sin \theta - M H_y \sin \theta \cos \omega - \sqrt{2} K_1 \sin^3 \theta \cos \theta \sin 3\omega ,$$

and

$$\frac{\partial^2 E}{\partial \omega^2} = MH_x \cos \omega \sin \theta + MH_y \sin \theta \sin \omega - 3\sqrt{2}K_1 \sin^3 \theta \cos \theta \cos 3\omega. \tag{2.8}$$

If we define

$$H_{K1} = 3\sqrt{2}K_1 \sin^3\theta \cos\theta/M , \qquad (2.9)$$

as the magnetocrystalline anisotropy field, through trigonometric manipulation we get the following equations:

$$\begin{split} h_x &= H_x/H_{K1} = -\{2\cos2\omega + \cos4\omega\}/3 \ , \\ \text{and} \\ h_y &= H_y/H_{K1} = -\{-2\sin2\omega + \sin4\omega\}/3 \ , \end{split} \tag{2.10}$$

which are parametric representations of what is termed the critical curve. The critical curve in the h_x - h_y plane is the solution to Eqn. (2.7), which represents the critical stability of the magnetization in the plane. (Recall that θ is held constant here.) Due to the cubic anisotropy introduced by the magneto-crystalline energy contribution to the total energy (the 3ω dependence), the critical curve is an astroid with three vertices as depicted in Fig. 2-3. The three-fold nature of the curve is indicative of the three easy magnetization directions in the film plane. The utility

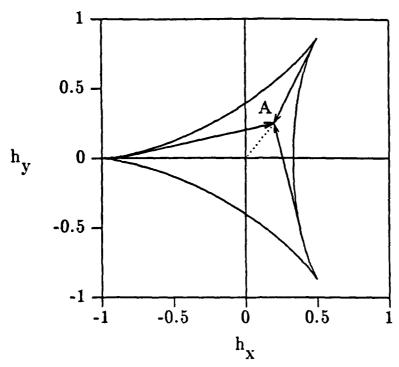


Figure 2-3: Critical curve used to find stable directions of M in the implanted layer.

of the critical curve is due to the fact that for a given applied field, (h_x, h_y) , the stable magnetization directions can be readily found using this curve. Referring to Fig. 2-3 in which an applied field is denoted by the dotted line from the origin $(h_x = h_y = 0)$ to point A, the stable magnetization directions are then found by drawing tangents from the critical curve to the field point as shown in the figure, in which it is seen that for field values of magnitude h < 1/3, there are 3 stable directions of M, the most stable being the one whose direction is closest to that of the applied field. For h > 1, there is only one direction of M that is energetically favorable. For the special case of 1 > h > 1/3, there is either only one stable direction when the applied field lies outside the curve or two if the field point lies within the curve, the degeneracy in the latter case being removed by the angular orientation of the applied field.

The usefulness of the critical curve in explaining the behavior of domains in implanted films can not be over emphasized. Additionally, since charged walls

generally form at the interface or boundary between two stable domains, the same type of curve can also be used to explain charged wall behavior. ¹⁷ In the same fashion that the critical curve can be used to compute stable orientations of M, Saunders constructed a critical curve for charged walls which will be described in the next section. It must be remembered that the preceeding calculations and critical curve formulation for ascertaining stable orientations of M are applicable far from an unimplanted boundary. This restriction will be removed in the following section after the effects of stress induced magnetic anisotropies in the vicinity of implanted/unimplanted pattern edges are described.

2.5. Stress Relaxation and Charged Wall Formation at Implanted Edges

It was shown in the previous section that through the inverse magnetostrictive effect the magnetization of an implanted region can be induced to lie in the plane of the film provided that the ion-implantion induced anisotropy is greater than the net uniaxial anisotropy, i.e.:

$$|K_i| > |K_u - 2\pi M_s^2| . {(2.11)}$$

To review briefly, due to the confining nature of the substrate, the implanted film can only expand perpendicular to the film plane. The reader is referred to Fig. 2-4, which shows an exaggerated cross-sectional view of an implanted/unimplanted infinite half-space in a material with unstrained lattice constant a. Far from the edge (for large values of x), the lattice is free to expand in the direction of the plane normal by Δa , but is confined to lattice constant a in the (x,y) plane. For large x, the planar stress, σ_{n} is given by the equation:

$$\sigma_p = \frac{-E\Delta a}{a(1+\nu)} \,, \tag{2.12}$$

where E is Young's modulus of the material and ν is Poisson's ratio. At the

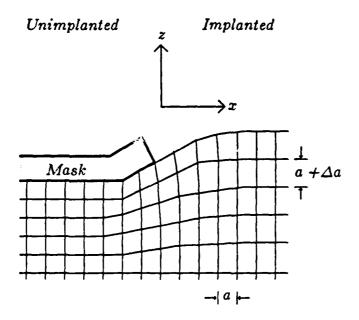


Figure 2-4: Exaggerated view of an implanted/unimplanted boundary illustrating the effects of implantation on lattice expansion.

boundary (x = 0), the stress is partially relieved due to the implanted region straining perpendicular to the boundary and expanding into the unimplanted region. It is not difficult to imagine that by analogy to the situation far from the edge where lattice expansion perpendicular to the plane of the film results in an easy axis parallel to the film plane, that stress relief perpendicular to the implanted/unimplanted boundary may result in an easy axis parallel to the boundary. This is, in reality, the mechanism for creating uniaxial anisotropy parallel to implanted edges in implanted devices, and is essential for the formation of charged walls. ^{19, 20, 21}

Saunders calculated in detail the magnetostrictive anisotropies at an implanted/unimplanted boundary like the one seen in Fig. 2-5 and found the magnetostrictive energy to be: 18

$$\begin{split} E &= -\frac{3}{2} \lambda_{111} \left\{ \left[(\sigma_z - \sigma_x) - \Delta \left(\sigma_y - \sigma_x \right) / 6 \right] \cos^2 \theta \right. \\ &+ \left[(\sigma_y - \sigma_x) (1 - \Delta / 3) \right] \sin^2 \theta \sin^2 \omega \\ &+ \left[(\sigma_y - \sigma_x) \sqrt{2} \; \Delta / 6 \right] \sin 2\theta \sin (\omega + 3\psi) \\ &+ \left[(\sigma_y - \sigma_x) \sqrt{2} \; \Delta / 6 \right] \sin 2\theta \cos \omega \\ &- \left[\sigma_{xz} \sqrt{2} \Delta / 3 \right] \sin^2 \theta \sin (2\omega + 3\psi) \right\} \\ &= - K_i \left\{ \left[S_3 - S_2 \left(\Delta / 6 \right) \right] \cos^2 \theta \right. \\ &+ \left[S_2 \left(1 - \Delta / 3 \right) \right] \sin^2 \theta \sin^2 \omega \\ &+ \left[S_2 \left(\sqrt{2} \; \Delta / 6 \right) \right] \sin 2\theta \sin (\omega + 3\psi) \\ &+ \left[S_{13} \left(1 - 2\Delta / 3 \right) \right] \sin 2\theta \cos \omega \\ &- \left[S_{13} \sqrt{2} \Delta / 3 \right] \sin^2 \theta \sin (2\omega + 3\psi) \right\} \end{split} \tag{2.13}$$

where θ is the polar angle of the magnetization from the film normal, ω is the azimuthal angle of the magnetization from the edge normal (the x-axis), ψ is the angle

between the $[1 \ 1 \ 2]$ direction and the implantation edge (the y-axis), $S_2 = (\sigma_y - \sigma_x)/\sigma_p$, $S_3 = (\sigma_z - \sigma_x)/\sigma_p$, $S_{13} = (\sigma_{xz}/\sigma_p)$, $\Delta = (\lambda_{111} - \lambda_{100})/\lambda_{111}$, σ_p is the planar stress far from the edge, λ_{111} and λ_{100} are the magnetostriction coefficients of the cubic garnet film and $K_i = 3/2$ λ_{111} σ_p as previously defined. Fortuitously, Eqn. (2.13) is divided into five different terms so that analysis is simplified. The reader should note that each term is either proportional to a differential stress or a shear stress, resulting in the use of normalized shear or differential stresses, S_i or S_{ii} .

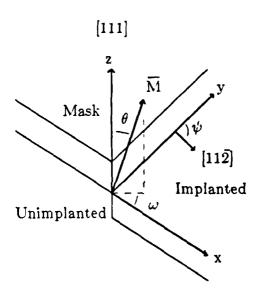


Figure 2-5: Coordinate system used for calculating magnetostrictive anisotropies of Eqn. (2.13).

Proceeding with the analysis of Eqn. (2.13), it is noted that each term except for the first has an ω dependence. In fact, the first term of the equation is responsible for the ion-implantation induced in-plane anisotropy far from the implantation edge that was described above. Far from any edges, $\sigma_{\rm x}=\sigma_{\rm y}=\sigma_{\rm p}$, and $\sigma_{\rm z}=\sigma_{\rm xz}=0$. The second term is easily seen to be a uniaxial anisotropy with its easy axis parallel to the implanted edge. This is qualitatively illustrated in Fig. 2-6(a). It is this anisotropy

term that is most responsible for the formation of charged walls, not demagnetizing effects of the boundary as once believed. Note also that this term is independent of ψ , that is, it is not a function of the orientation of the boundary. The third term of the equation describes a unidirectional anisotropy which is a function of position around the edge of the boundary, and is illustrated in Fig. 2-6(b). This term is responsible for the preferred stable locations of charged walls around an unimplanted disc, and is the reason for the energy barrier charged walls must surmount as a rotating field is used to circulate them about a disc, resulting in discontinuous charged wall motion. The fourth and fifth terms are due to shearing stresses at the boundary, are extremely localized, and as such do not contribute significantly to charged wall motion or formation in the devices under discussion here. 18 Hence, they may be omitted from Looking at Fig. 2-6(a), and the corresponding energy term further consideration. associated with this qualitative schematic of the uniaxial magnetization anisotropy, it is seen, in the absence of any other anisotropies, that charged walls formed by this anisotropy component should propagate smoothly around an unimplanted disc under the effect of a rotating in-plane field. (The uniaxial nature of the anisotropy is indicated by the double ended arrows in this figure.) Unfortunately, the easy axes of Fig. 2-6(a) become easy directions due to the effective 3 fold unidirectional offset fields resulting from the third term of Eqn. (2.13) which is illustrated in Fig. 2-6(b). The single ended arrows indicate the unidirectional nature of this anisotropy term, resulting in the preserence of one uniaxial direction over the other. Note that this term has the same angular dependence as the crystalline anisotropy term of Eqn. (2.5), which was responsible for the 3-fold symmetry of the critical curve derived and discussed in the previous section. In fact, it was initially believed that the anisotropic propagation of bubbles in ion-imp anted devices was due to the crystalline anisotropy, until Hubert showed that anisotropic magnetostriction was the dominant factor in explaining the observed 3-fold symmetric characteristics of these devices.²² It is seen in the figure that the unidirectional term is responsible for causing the formation of alternating positions of magnetization convergence and divergence, each position being 60 degrees apart.

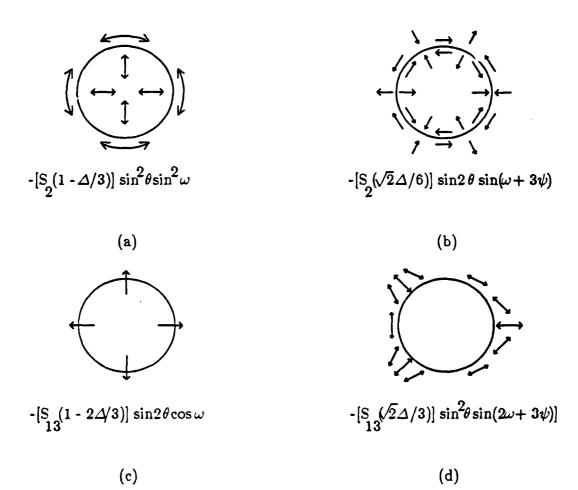


Figure 2-6: Schematic illustration of the magnetostrictive anisotropies of Eqn. (2.13) responsible for charged wall formation and position.

2.6. Domain Walls and Their Motion

2.6.1. Introduction

As previously described, bubbles are domains of reversed magnetization in an otherwise saturated platelet. The magnetization of the platelet is oriented perpendicular to the film plane due to the uniaxial anisotropy, K_u . Between the two antiparallel regions of magnetization there is a transition region of finite width, called the domain wall, through which the magnetization changes direction, as seen in Fig. 2-7. In this figure is seen the cross-section of a bubble domain in a thin platelet which is stabilized by the presence of an external bias field.

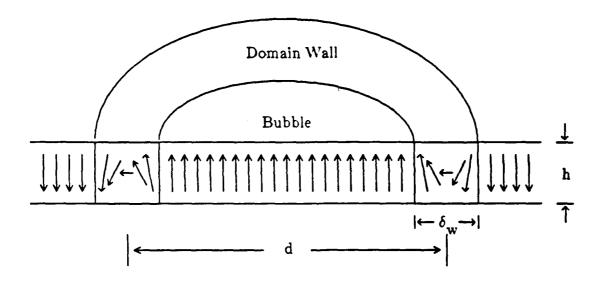


Figure 2-7: A cross-sectional view of a bubble domain in a thin platelet depicting the rotation of spins through the bubble wall.

2.6.2. Wall Energy and Wall Width

In order to calculate the wall width, $\delta_{\rm w}$, and other relevant wall parameters, it will be advantageous to analyze the planar wall segment depicted in Fig. 2-8. The easy axis is parallel to the z axis and the spins are confined to rotate in the z-z plane as shown. If θ is the angle between M and the easy axis, then the anisotropy energy density is $E_{\rm K} = K_{\rm u} \sin^2 \theta$. Now, in a magnetic material, the exchange energy, $E_{\rm x}$, is

responsible for keeping adjacent spins parallel and preventing abrupt changes in magnetization. For the configuration shown, the exchange energy density is given as $E_{\chi} = A(d\theta/dy)^2$, where A is the exchange constant. Note that as the wall width increases, the anisotropy energy increases due to the fact that there are more spins that are not parallel to the easy axis, but the exchange energy decreases since $(d\theta/dy)^2$ decreases. On the other hand as the wall width decreases, the exchange energy increases as the anisotropy energy is decreased. At any point in the wall, there will be equilibrium between the two opposing torques due to the exchange and anisotropy energy components. Equating the two torques, $-dE_{\chi}/d\theta = -dE_{K}/d\theta$ yields:

$$\frac{d^2\theta}{dy^2} = \frac{K_u}{A} \sin\theta \cos\theta , \qquad (2.14)$$

whose solution

$$\tan \frac{\theta}{2} = exp[y(K_u/A)^{1/2}],$$
(2.15)

is seen plotted in Fig. 2-8.

The wall width, $\delta_{\rm w}$, is defined as the distance between the points where the line tangent at the wall midpoint intersects $\theta = 0$ and π as seen in the figure, which is found to be

$$\delta_w = \pi (\frac{A}{K_u})^{1/2} \ . \tag{2.16}$$

It is seen that as the exchange energy increases, the wall width increases while an

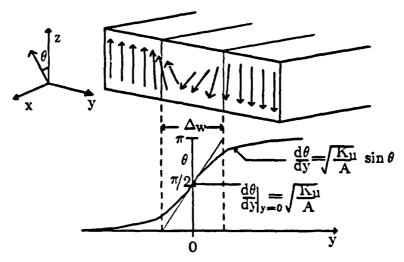


Figure 2-8: A section of a domain Bloch wall showing the wall width and the orientation of the spins as a function of position through the wall. After Eschenfelder. 1

increase in anisotropy decreases the wall width. The total wall energy density (ergs/cm²) is calculated by integrating the energy density components over the entire wall width, that is:

$$\sigma_w = \int_{-\infty}^{+\infty} (E_K + E_X) dy = 4(AK_u)^{1/2} . \tag{2.17}$$

In Fig. 2-8 we may define the position of the center plane of the Bloch wall as being at y=0 and then for y<<0 M is oriented in the +z direction and for y>>0 M is parallel to -z. A schematic of this situation as seen by looking down the -z axis is given in Fig. 2-9. Also shown in this figure is a polar coordinate system used to describe the orientation of the moments in the wall. For the wall shown, the moments with $\theta=\pi/2$ are depicted as arrows directed along the line $y=y_0$. Here, let us for now assume that the wall is infinite in the x-z plane and that ϕ is independent of z,

constraints that will be removed in the next section. Also seen in labeled wall segment B of Fig. 2-9 is a region of the wall that contains a Vertical Bloch Line, which is actually a wall within the previously described Bloch wall. The Bloch Line segment is located at $x = x_0$ and ϕ does not change along z.

Slonczewski¹ showed that if ϕ is a function of x as in the Bloch Line segment B, and for applied fields H_x and H_y that the wall energy given in equation (2.17) is modified in the form

$$\sigma = \sigma_w + \frac{2A\delta_w}{\pi} \left(\frac{\partial \phi}{\partial x}\right)^{1/2} + 4\delta_w M_e^2 \sin^2 \phi - \delta_w M_e (H_x \cos \phi + H_y \sin \phi)$$
 (2.18)

where δ_{w} is given in Eqn. (2.16) and σ_{w} is as computed in Eqn. (2.17). In equation (2.18), the exchange energy due to variations of M along x have been included, as well as the demagnetizing energy that arises from the x component of M from the neighboring Bloch wall regions that converge into the Bloch Line region.

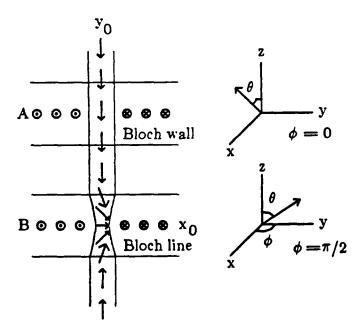


Figure 2-9: Configuration of spins in the center of a Bloch wall. After Eschenfelder. 1

2.6.3. Wall Dynamics

Referring to segment A of Fig. 2-9, it is seen for a fixed wall configuration that a uniform rotation in θ corresponds to a translation of y_0 , that is:

$$\dot{y}_o = -\dot{\theta} \frac{dy}{d\theta} \,, \tag{2.19}$$

and for the Bloch Line segment B that a rotation of ϕ corresponds to a translation of x_0 yielding

$$\dot{x}_o = -\dot{\phi} \frac{dx}{d\phi} \,, \tag{2.20}$$

and from Eqn. (2.14) which describes the wall shape it is seen that

$$\dot{y}_o = -\dot{\theta}\sqrt{\frac{A}{K_u}}\frac{1}{\sin\theta} = -\frac{1}{\sin\theta}\frac{\delta_w}{\pi}\dot{\theta} , \qquad (2.21)$$

and for the Bloch line segment B

$$\dot{x}_o = -\frac{1}{\sin\phi} \frac{\delta_{BL}}{\pi} \dot{\phi},\tag{2.22}$$

where, by analogy to the Bloch wall width, $\delta_{\rm BL}$ is the Bloch Line width. The Bloch Line width is calculated to be²³

$$\delta_{BL} = (A/2\pi M_s^2)^{1/2}. (2.23)$$

It is to be noted that the Bloch Line width increases as the exchange energy is increased, just as the Bloch wall width does. However, where in the Bloch wall width calculation the anisotropy causes a decrease in the wall width, here the Bloch Line width decreases due to the demagnetizing energy in the wall.

From the Landau-Lifshitz-Gilbert equation the domain wall position coordinates y_o = q and ϕ at the wall center can be described by the following two equations of motion:

$$\dot{\phi} = -\frac{\gamma}{2M_e} \frac{\delta\sigma}{\delta q} - \frac{\alpha\pi}{\delta_w} \dot{q} , \qquad (2.24)$$

and

$$\dot{q} = \frac{\gamma}{2M_s} \frac{\delta\sigma}{\delta\phi} + \frac{\alpha\delta_w}{\pi} \dot{\phi} , \qquad (2.25)$$

where α is the Gilbert damping parameter and γ is the gyromagnetic ratio. If $H_x = H_y = 0$ and $H_z = H_A$ it is found that for an infinitely thick wall segment that Eqn. (2.18) becomes¹

$$\frac{\delta\sigma}{\delta q} = -2M_{\rm s}H_{A} \ , \tag{2.26}$$

and

$$\frac{\delta\sigma}{\delta\phi} = 4\delta_w M_{\theta}^2 \sin 2\phi \ . \tag{2.27}$$

Inserting these terms into equations (2.24) and (2.25) respectively yields the following:

$$\dot{\phi} = \gamma H_A - \frac{\alpha \pi}{\delta_w} \dot{y}_o \tag{2.28}$$

and

$$\frac{\dot{y}_o}{\delta_w} = 2M_e \gamma \sin 2\phi + \alpha \frac{\dot{\phi}}{\pi} . \tag{2.29}$$

From Eqn. (2.28) it is seen that the applied field H_A induces a rotation in ϕ , which in turn produces a demagnetizing field responsible for y_o . In steady state ($\dot{\phi} = 0$), equations (2.28) and (2.29) become:

$$\dot{y}_o = \frac{\delta_w \gamma}{\alpha \pi} H_A \tag{2.30}$$

and

$$\sin 2\phi_o = \frac{H_A}{2\pi\alpha M_e} \ . \tag{2.31}$$

From Eqn. (2.31) the simple situation under discussion breaks down when H_A exceeds $2\pi\alpha M_s$, corresponding to a critical velocity

$$V_{w} = \dot{y}_{o} = 2\pi\alpha M_{e} \tag{2.32}$$

where V_w is called the Walker breakdown velocity. Eqn. (2.30) states that prior to breakdown, i.e. for $\dot{y}_o < V_w$, the wall velocity is linearly proportional to the applied field, H_A . The constant of proportionality, termed the wall mobility, μ_w is seen to be:

$$\mu_w = \frac{\delta_w \gamma}{\pi \alpha} \,. \tag{2.33}$$

In an actual material, there is a threshold field below which no wall motion is seen to occur. This is termed the coercive field, H_c , and is due to fluctuations in material parameters, wall pinning sites, etc. Thus,

$$V = \mu_w (H_A - H_c) \quad for \quad H_A > H_c \ ,$$

$$V = 0 \ , \quad \text{else}. \tag{2.34}$$

2.6.4. The Effects of Finite Wall Thickness on Wall Motion

The preceeding analyses and discussions pertaining to Bloch walls, their internal structure, and dynamics have been for walls that are infinitely thick in extent, allowing the dependence of ϕ on z to be neglected. However, in the more realistic case, as in a thin film that typifies practical bubble materials, for example, the divergence of M at the film surfaces will give rise to stray fields that will cause

variations of ϕ through the film thickness. Assuming the magnetization configuration depicted in segment A of Fig. 2-9 in a thin film with -h/2 < z < +h/2, the stray field in the wall is approximately²³

$$H_{v} = -4M_{s}[ln(h+2z) - ln(h-2z)]. \tag{2.35}$$

The effect of this field is to twist the wall magnetization near the film surfaces so that ϕ is $-\pi/2$ at one surface and $+\pi/2$ at the other. Only near the film center is $H_y = 0$ and $\phi = 0$ as in the infinitely thick film case. The effect of the stray field on spins on the wall is schematically depicted in Fig. 2-10.

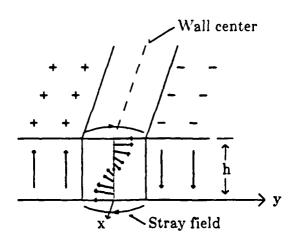


Figure 2-10: The effect of the stray field on spins in the wall.

When an external field is applied parallel to the z axis for the purpose of inducing wall motion, the spins in the wall are forced to precess about the z axis due to the induced torque. However, at the surfaces of the film, the spins are essentially fixed by the stray fields. For the purpose of understanding how these stray fields affect device behavior, it will suffice to explain the resulting wall motion under the influence of the applied field without delving into spin motion calculations which are treated in detail elsewhere.²³ As in the thick film case, there is a region in which the wall velocity is

linearly proportional to the applied field as seen in Fig. 2-11 for the case in which it is assumed $H_c=0$. At the applied field value of H_o , the maximum velocity attained is $V_p=\dot{q}$ where the wall velocity is

$$V_{p} = \dot{q} = \frac{24\gamma A}{h \left(K_{y}\right)^{1/2}} \,. \tag{2.36}$$

The maximum velocity is due to the formation of a particular spin configuration called a *Horizontal Bloch Line*, or HBL, in the wall. When the applied field exceeds H_o , the subsequent motion of the HBL within the domain wall (termed punch-through) causes the wall velocity to suddenly decrease to a value of

$$V_o = \dot{q} = \frac{7.1\gamma A}{h (K_o)^{1/2}} , \qquad (2.37)$$

in which case the velocity remains constant, independent of the value of the applied field. The effect HBL formation and motion has on wall motion is depicted in Fig. 2-11, where the Walker velocity, $V_{\rm w}$, is also shown. It is seen that the major effect of finite film thickness is the reduction in breakdown velocity; the wall mobility is the same here as in the thick film case. The alert reader will also note that in Fig. 2-11 we have neglected the effect of coercivity.

2.6.5. Bubble Motion

A uniform bias field, while stabilizing a bubble domain against stripout, will not cause net bubble motion in the plane of the bubble film. However, a bias field gradient will cause bubble translation very much in the same manner as an applied field may cause planar wall displacement as was seen earlier. Thiele showed that there is a simple equation of motion for a bubble which is analogous to Eqn. (2.34) which describes the motion of a planar wall, that is for a bubble of diameter d^{24}

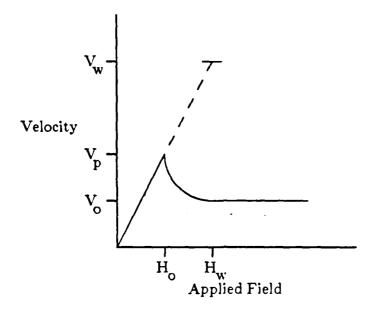


Figure 2-11: Wall velocity as a function of applied field in a film of thickness h. The effect of finite H_c has been neglected here.

$$V = -\mu_B (\Delta H_B - \frac{8}{\pi} H_c), \qquad (2.38)$$

where

$$\mu_B = \frac{\mu_w}{2} \,, \quad \Delta H_B = d \, \frac{d \, H_B}{dy} \,. \label{eq:muB}$$

From this equation it is seen that the bubble mobility is one half the wall mobility and the bias field gradient across the bubble diameter provides the driving force. Furthermore, we see that the bubble coercivity is greater than the wall coercivity by a factor of $8/\pi$.

In actual translation experiments, bubbles may be observed to move in directions that are not parallel to the field gradient direction. This deflection is due to a gyrotropic force that arises from the rotation of spins in the bubble wall as was depicted in Fig. 2-7. These forces have been neglected in the calculation used to derive Eqn. (2.38). When gyrotropic forces are taken into account and in the absence of coercivity Eqn. (2.38) is modified in the form¹

$$V = -\frac{\mu_w}{2} \Delta H_B - \frac{4\mu_w H_B \times V}{\gamma d |H_B|}.$$
 (2.39)

From this equation we see that a bubble moving in a gradient will be deflected in the direction of $V \times H_{R}$.

It should be pointed out that the gyrotropic forces causing the bubble deflection described by Eqn. (2.39) arise from the magnetization rotation in the region that defines the wall of the bubble. Depending on the specific configuration of spins in the wall, the deflection angle will vary. The propensity for bubbles to deflect has led to the proposal of various novel bubble devices and bubble logic gates, which are beyond the scope of this thesis. However, it is important to note that bubbles may have a number of different wall magnetization spin configurations or states that are simultaneously stable. Furthermore, the wall states have dynamic properties that vary as a function of bubble drive and velocity, which compounds the problem. In a specific device or propagation scheme bubbles with different states may deflect, resulting in propagation errors if the propagator does not have enough tolerance to handle variations in bubble position as a function of time, drive field, etc. Needless to say, these effects may be undesireable in typical bubble devices.

Fortunately, there are a number of methods by which bubble states may essentially be fixed, yielding a device whose bubbles all behave in similar fashion. One of these methods requires the application of a large magnetic field in the plane of the bubble film. This in-plane field forces the surface magnetization of the bubble to remain fixed in a constant direction and allows any dynamic wall effects to be

dissipated while the bubble is propagating. The result is uniform bubble behavior. Unfortunately, the in-plane field required in this technique may be greater than the drive field used in field-access devices; therefore it is only a practical method in current-access propagation schemes. On the other hand, a surface layer of in-plane magnetization is a well-known inhibitor of static and dynamic anomalous bubble behavior and is used routinely in bubble device production. Since the devices that are the subject of this thesis are of the ion-implanted variety, we focus our attention on "well-behaved" bubbles, unless where specifically noted.

2.7. Bubble Domain Stability

Thiele calculated in detail stability criteria for bubble domains in thin platelets. As a result of his calculations, which are briefly reviewed and summarized here, one may compute the stable bubble domain diameter as a function of applied fields and film thicknesses. The range of stable bubble diameters is found to be bounded by the collapse diameter d_{co} , and the stripe-out diameter d_{so} , both of which were also calculated by Thiele. Most importantly, the operating bias range of domain stability was found as a function of the film thickness and material parameters. This is relevant to bubble devices in general since it gives an estimate of the range of fields over which a bubble domain remains stable and circular. In particular, for the devices discussed in this thesis in which successful operation of the device depends upon controlled bubble stripe-out, as in the block replicate gate, the analysis allows one to calculate the bias field reduction required to induce bubble stripe-out.

2.7.1. Mathematical Analysis of Domain Stability

In this section the analysis of bubble domain stability as formulated by Thiele is presented. The stable diameter of an isolated bubble domain is calculated, as well as the diameters of collapse, d_{co} and stripe-out, d_{so} . Approximation formulae are given for the magnetostatic force and stability functions, which, as given by Thiele, are cumbersome and complex. It is shown that the approximation formulae are in good agreement with Thiele's results. Finally, the bias field margins for stable device operation are computed.

At the center of the domain is placed a cylindrical (r,θ,z) coordinate system, as shown in Fig. 2-12.¹⁵ The z-axis is perpendicular to the plane of the infinite plate, of uniform thickness h, in which the domain resides. The magnetization, M, is confined to be parallel to the z-axis. The domain wall is assumed to have a wall energy density, σ_w , which is independent of the orientation or curvature of the wall and the wall is assumed to have negligible thickness.

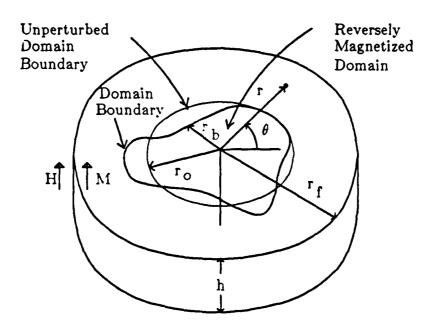


Figure 2-12: Coordinate system describing domain and coordinate system used in calculating domain stability.

The domain radius, r_b , may be expanded in terms of the Fourier coefficients, r_n and θ_n , as follows:

$$r_b(\theta) = \sum_{n=0}^{\infty} r_n \cos[n(\theta - \theta_n)]$$
 (2.40)

where n is known as the "rotational periodicity". By imposing the condition

$$|r_0| >> \sum_{n=1}^{\infty} n|r_n| \tag{2.41}$$

it is assured that the domain is near circular and that the function $r_b(\theta)$ is smooth and single valued.

In order to describe variations in domain size and shape from a circular domain of radius $r_b(\theta) = r_0$, the domain radius function given by Eqn. (2.40) may be expanded in terms of finite variations of r_n and θ_n , Δr_n and $\Delta \theta_n$ respectively, as:

$$r_b(\theta) = r_o + \Delta r_b + \sum_{n=1}^{\infty} \Delta r_n \cos[n(\theta - \theta_n - \Delta \theta_n)]. \tag{2.42}$$

In order to ascertain the domain size and stability, the first and second variations of the total domain energy with respect to the Fourier coefficients must be computed. The total domain energy is

$$E_{_{\rm T}} = E_{_{\rm W}} + E_{_{\rm H}} + E_{_{\rm M}}, \tag{2.43}$$

where $E_{_{\mathrm{W}}}$ is the wall energy, $E_{_{\mathrm{H}}}$ is the applied field interaction energy, and $E_{_{\mathrm{M}}}$ is the internal magnetostatic energy.

The wall energy is the product of the wall energy density, σ_w , and the wall area a and is given by

$$E_{w} = \int_{a} \sigma_{w} da = h\sigma_{w} \int_{0}^{2\pi} \left(r_{b}^{2}(\theta) + \left[\frac{\partial r_{b}(\theta)}{\partial \theta} \right]^{2} \right)^{1/2} d\theta. \tag{2.44}$$

The applied field energy due to a spatially uniform magnetic field, H, oriented in the positive z direction is:

$$E_{\rm H} = -\int_{\rm V} \mathbf{M} \cdot \mathbf{H} \, dV = -\int_{-\infty}^{\infty} \int_{0}^{2\pi} \int_{0}^{\infty} M_{z} \, H \, r \, dr \, d\theta \, dz, \qquad (2.45)$$

and the internal magnetostatic energy is:

$$E_{\rm M} = \frac{1}{2} \int_{V} \int_{V'} \frac{\nabla \cdot \mathbf{M} \nabla' \cdot \mathbf{M}'}{|\mathbf{r} - \mathbf{r}'|} dV dV. \tag{2.46}$$

The first and second variations of the total domain energy with respect to the finite variations, Δr_n and $\Delta \theta_n$, determine the domain stability and equilibrium conditions. The variation in total energy is:

$$\Delta E_{\mathrm{T}} = \sum_{n=0}^{\infty} \left[\left(\frac{\partial E_{\mathrm{T}}}{\partial r_{n}} \right)_{0} \Delta r_{n} + \left(\frac{\partial E_{\mathrm{T}}}{\partial \theta_{n}} \right)_{0} \Delta \theta_{n} \right]$$

$$+\frac{1}{2}\sum_{n=0}^{\infty}\sum_{m=0}^{\infty}\left[\left(\frac{\partial^{2}E_{T}}{\partial r_{n}\ \partial r_{m}}\right)_{o}\Delta r_{n}\Delta r_{m}+2\left(\frac{\partial^{2}E_{T}}{\partial r_{n}\ \partial \theta_{m}}\right)_{o}\Delta r_{n}\Delta \theta_{m}$$

$$+\left(\frac{\partial^{2} E_{T}}{\partial \theta_{n} \partial \theta_{m}}\right)_{\circ} \triangle \theta_{n} \triangle \theta_{m} + O_{3}, \tag{2.47}$$

where, for brevity, Δr_n and $\Delta \theta_n$ are given as r_n and θ_n , the o subscript implies evaluation of the derivatives in the circular domain state, $r_b(\theta) = r_o$, and terms of order three and higher are lumped together in the term O_3 . The first partial derivatives of the energy, $-(\partial E_T/\partial r_n)_o$ and $-(\partial E_T/\partial \theta_n)_o$, are the generalized forces of the system while the second partial derivatives form the stiffness matrix of the system. Domain size and stability is completely characterized by knowledge of the forces and stiffness matrix elements. Thiele meticulously calculated the energy variation in detail; only the results are presented here.

The normalized form of the energy variation is:

$$\frac{\Delta E_{T}}{2(4\pi M_{s}^{2})(\pi h^{3})} = \left[\frac{l}{h} + \frac{d}{h} \frac{H}{4\pi M_{s}} - F(d/h)\right] \frac{\Delta r_{o}}{h} - \left[\frac{l}{h} - S_{o}(d/h)\right] \frac{d}{h} \left(\frac{\Delta r_{o}}{h}\right)^{2} + \frac{1}{2} \sum_{n=2}^{\infty} (n^{2} - 1) \left[\frac{l}{h} - S_{n}(d/h)\right] \frac{d}{h} \left(\frac{\Delta r_{n}}{h}\right)^{2} + O_{3}, \qquad (2.48)$$

where $l = \sigma_w/4\pi M_s$ is defined as the characteristic length, and F(d/h) and $S_n(d/h)$ are called the force and stability functions, respectively. To find the equilibrium bubble diameter, the coefficient of the first order variation, the negative of the normalized radial force, is set equal to zero, yielding:

$$\frac{l}{h} + \frac{H_b}{4\pi M_s} \frac{d}{h} = F\left(\frac{d}{h}\right) . \tag{2.49}$$

The domain is stable with respect to an arbitrary variation in shape when all of the coefficients of the Δr_n^2 terms are positive, i.e.,

$$\frac{l}{h} - S_o\left(\frac{d}{h}\right) < 0 \tag{2.50}$$

and

$$\frac{l}{h} - S_n\left(\frac{d}{h}\right) > 0 \text{ for } n \geq 2 . \tag{2.51}$$

Since the stability functions have the property

$$S_{n+1} \left(\frac{d}{h}\right) < S_n \left(\frac{d}{h}\right) , \qquad (2.52)$$

the domains are stable for

$$S_2\left(\frac{d}{h}\right) < \frac{l}{h} < S_o\left(\frac{d}{h}\right) . \tag{2.53}$$

If S_2 (d/h) is larger than l/h the bubble stripes out and if S_o (d/h) is smaller than l/h the bubble collapses.

Thiele calculated the force and stability functions, F(d/h) and $S_n(d/h)$ respectively, in laborious detail by expressing them in terms of elliptic integrals. Confronted with, as described in their own words "the intractability of the Thiele formulation", Callen and Josephs found that F(d/h) could be approximated as²⁵

$$F(d/h) = \frac{d/h}{1 + (3/4)(d/h)} , \qquad (2.54)$$

which, for values of d/h pertinent for the devices under discussion here (0.5 < d/h < 2.0), is found to be in good agreement with Thiele's "exact" computed results, which will be shown shortly. Since $S_0(d/h)$ is given by

$$S_0(x) = F(x) - x \frac{\partial F(x)}{\partial x} , \qquad (2.55)$$

it is found by substituting Eqn. (2.54) into Eqn. (2.55) that

$$S_0(d/h) = \frac{3}{4}F^2(d/h). \tag{2.56}$$

Fortuitously, it has been shown that $S_2(d/h)_1^p$ may also be approximated with very good accuracy in the form:²⁶

$$S_2(d/h) = \frac{1}{3}F^3(d/h)$$
. (2.57)

The functions, F(d/h), $S_0(d/h)$, $S_2(d/h)$ versus d/h are plotted in Fig. 2-13. In addition, in Table 2-1 are compared the approximated force and stability functions computed using eqs. (2.54), (2.56) and (2.57) with Thiele's "exact" computed values for a value of d/h = 1.0, which is typically used for the devices under discussion here. In the table it is seen that the force and stability functions may be reasonably approximated by simple analytic expressions. Fig. 2-13 also shows how the bubble diameter in the presence of the external magnetic field can be determined graphically as a function of the characteristic length and thickness of the film. First, the value of l/h (.25) for the film is plotted on the ordinate. Then two lines are drawn from this point, one horizontal and the other with a slope equal to $H_b/4\pi M_s$ where H_b denotes the external bias field. From Eqn. (2.49) it can be seen that the equilibrium bubble size is determined by the intersection of the second straight line with the curve for F. In the case shown in Fig. 2-13, when $H_b/4\pi M_s$ is greater than 0.329 (the slope of the tangent to curve F), there is no intersection with the curve F, i.e., no bubble can exist at such a field.

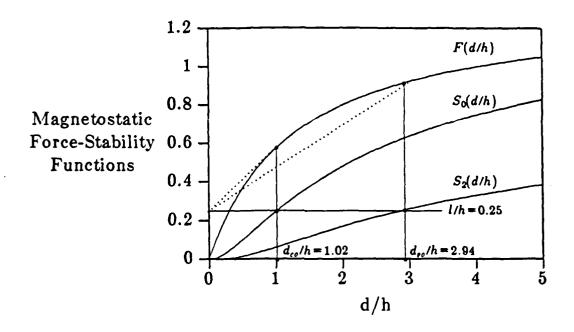


Figure 2-13: Graphical determination of bubble stability. After Thiele. 15

Therefore, this is the bubble collapse field, H_{co} of the film. When the applied field is smaller than H_{co} , there are two intersections with curve F. However, not all of the solutions are stable. From the stability criteria [Eqn. (2.53)], it is clear that only the solutions are stable which are located between the two intersections obtained from the horizontal line drawn from the point indicating l/h value on the ordinate. The smaller diameter limit represents the collapse diameter d_{co} and the larger limit the stripeout diameter d_{so} . The corresponding applied fields shown in the figure as H_b^{co} and H_b^{so} are then the collapse field and the stripeout field, respectively.

Parameter	Thiele's Value 15	Approximated Value
F(d/h)	0.5794	0.5714 ²⁵
$S_0(d/h)$	0.2552	0.2449 ²⁵
$S_2(d/h)$	0.0603	0.0623 ²⁶

Table 2-1: Comparison between Thiele's computed force and stability functions and approximated force and stability functions for d/h = 1.0. Approximated values of F(d/h) and $S_0(d/h)$ were computed from equations (2.55) and (2.56) respectively, 25 and the approximated value of $S_2(d/h)$ was computed using equation (2.57) 26 .

2.7.2. Stable Bubble Diameter

The bubble diameter variation with respect to the film thickness can be obtained as follows. First, Fig. 2-13 is used to obtain d_{co}/h and d_{co}/h values as a function of l/h by drawing a straight line from the point (l/h) on the ordinate as was explained earlier since these values are defined by

$$\frac{l}{h} = S_o\left(\frac{d_{co}}{h}\right) = S_2\left(\frac{d_{so}}{h}\right) . \tag{2.58}$$

This relationship is depicted in Fig. 2-14. A more useful result is obtained by transposing the parameters in this figure and plotting the normalized stripout and collapse diameters versus the normalized film thickness, where all normalization is done with respect to l, the material characteristic length. The result is given in Fig. 2-15.

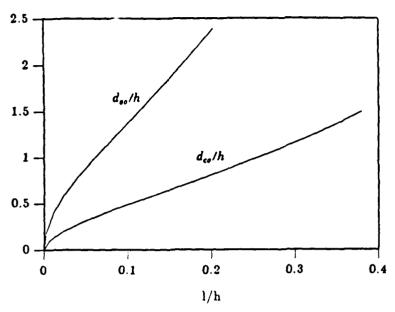


Figure 2-14: Bubble diameter variations with respect to the film thickness.

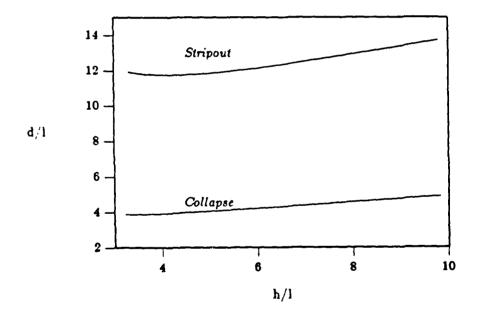


Figure 2-15: Extremes of bubble size as a function of h/l.

2.7.3. Bubble Collapse and Stripeout Fields

The collapse and stripeout fields $H_b^{co}/4\pi M_s$ and $H_b^{so}/4\pi M_s$ may be obtained from Eqn. (2.49) and Eqn. (2.58):

$$\frac{H_b^{co}}{4\pi M_s} = \frac{F\left(\frac{d_{co}}{h}\right) - \frac{l}{h}}{d_{co}/h} = \frac{F\left(\frac{d_{co}}{h}\right) - S_o\left(\frac{d_{co}}{h}\right)}{d_{co}/h}, \qquad (2.59)$$

and

$$\frac{H_b^{so}}{4\pi M_s} = \frac{F\left(\frac{d_{so}}{h}\right) - \frac{l}{h}}{d_{so}/h} = \frac{F\left(\frac{d_{so}}{h}\right) - S_2\left(\frac{d_{so}}{h}\right)}{d_{so}/h} . \tag{2.60}$$

These relationships are plotted in Fig. 2-16 for various h/l.

It is seen that both collapse fields and stripeout fields decrease steadily as the height of the bubble decreases. The bias field margin width defined by the difference of the collapse field and the stripeout field also decreases as the bubble height decreases. It is expected from the plots that the bubble will have a bias margin width of about $0.11 \times 4\pi M_s$ when the bubble height is 91.

2.8. Fields in Ion-Implanted Devices

2.8.1. Introduction

In this section, we shall describe the different fields that play roles in determining the behavior of bubbles in ion-implanted devices and also the methods by which these fields were calculated. Here, we focus only on two important effects found usually in ion-implanted devices only: the field due to the implanted/unimplanted boundary and the field from the charged wall.

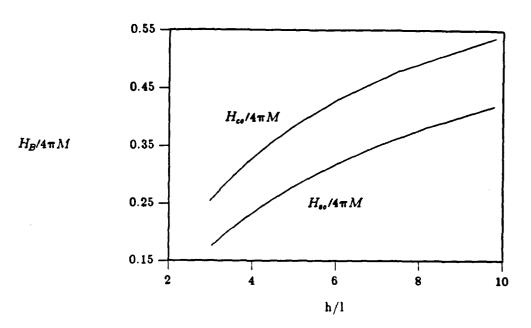


Figure 2-16: H_B margins vs. h/l.

2.8.2. The Edge Affinity Field

It is well known that bubbles couple strongly to an implanted/unimplanted boundary.²⁷ This is due to the stray field created by the thickness difference between the implanted and unimplanted regions. Bubbles prefer to reside in the thicker unimplanted area, but the field produced at the boundary prevents bubbles from crossing from the thinner implanted area into this region. As a result, bubbles in the implanted region adhere strongly to the unimplanted pattern edge. The demagnetizing field due to the thickness step is modeled by an equivalent current. It can be shown⁴ that the stray field of a bubble and a loop current are identical if the bubble is replaced by a loop current with amplitude $I = 2 M_g h$, where the units are mA, gauss, and μ m, respectively. Similarly, for a cylindrical hole in a garnet film, the amplitude of the equivalent loop current is $I = M_g h$. For the case of partially etched holes, i.e., craters, the amplitude is $I = M_g h$, where Δh is the etched thickness. This concept of equivalent loop current can be extended to the pattern used in contiguous disk devices, since the pattern is generally a continuous chain of circular Ω bles.

By extending the concept of equivalent currents, the calculation of the

demagnetizing field is quite straight forward. The contiguous disk pattern is replaced by a current "loop" with the same shape as the unimplanted disk pattern. The z-component of the demagnetizing field, H_z , at point P, is given by:

$$H_{z} = \int_{C} \frac{I \, d\mathbf{l} \times \mathbf{r}}{\mathbf{r}^{3}} \bullet \mathbf{i}_{z}, \tag{2.61}$$

where I is the equivalent current, dl is the length vector of a small segment of the current loop, r is the vector pointing from dl to point P, r is the length of r, i_2 is the unit vector in the z axis, and C is the path of the current loop. In evaluating Eqn. (2.61), the contour C is broken up into small line segments; the integration is then carried out segment by segment.

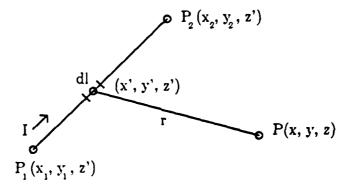


Figure 2-17: A line segment of a current loop.

Consider a line segment between $P_1(x_1, y_1, z')$ and $P_2(x_2, y_2, z')$ with current flowing from P_1 to P_2 , as shown in Fig. 2-17. For a small current element dl at (x', y', z'), we have

$$dl = d\ell_x i_x + d\ell_y i_y$$
, and $r = (x-x')i_x + (y-y')i_y + (z-z')i_z$, (2.62)

where $d\ell_x$ and $d\ell_y$ are the component of dl in x and y axis, respectively. Inserting Eqn. (2.62) into Eqn. (2.61), the z-field averaged over the film thickness, $H_z(x, y, z)$, at point P due to the current in the line segment is given by:

$$H_{z}(x, y, z) = \frac{I}{z_{0} - z_{1}} \int_{L} \int_{z_{1}}^{z_{2}} \frac{(y-y') d\ell_{x} - (x-x') d\ell_{y}}{\left[(x-x')^{2} + (y-y')^{2} + (z-z')^{2}\right]^{3/2}} dz'$$

$$= \frac{I}{z_{2} - z_{1}} \int_{L} \frac{(y - y') d\ell_{x} - (x - x') d\ell_{y}}{(x - x')^{2} + (y - y')^{2}} \left[\frac{z_{2}}{[(x - x')^{2} + (y - y')^{2} + z_{2}^{2}]^{1/2}} - \frac{z_{1}}{[(x - x')^{2} + (y - y')^{2} + z_{1}^{2}]^{1/2}} \right], \qquad (2.63)$$

where L is the line segment between P_1 and P_2 , and the unimplanted film is between z_1 and z_2 along the z axis. Divide the line segment, L, into N equal small divisions, then $d\ell_x := (x_2 - x_1)/N$, $d\ell_y = (y_2 - y_1)/N$. Simpson's rule is used to evaluate Eqn. (2.63) numerically. The total z-field at point P is the summation of the contributions from all the line segments of the current loop.

There are analytic solutions to Eqn. (2.61) for a number of simple implanted/unimplanted edge geometries. One of the most commonly studied and informative is the straight edge, a cross-section of which is seen in Fig. 2-18. The film is magnetized in the +z direction, θ is the inclination angle of the edge with respect to the x axis, and the half-width of the sloped region is denoted as a.

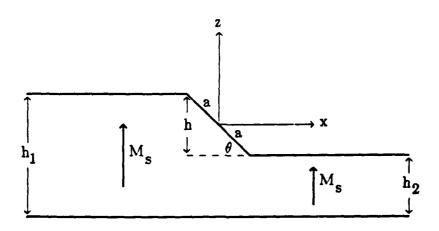


Figure 2-18: Cross-sectional view of implanted/unimplanted boundary.

The perpendicular field from the edge discontinuity depicted in Fig. 2-18 is shown in Fig. 2-19. We see that away from the implanted edge, the average field approaches $4\pi M_s$ of the bulk material, but there is an abrupt discontinuity in the field centered about the boundary. This is the force felt by bubbles in hybrid devices as the bubbles propagate between implanted/unimplanted regions in these devices, and we can see that it can not be neglected.

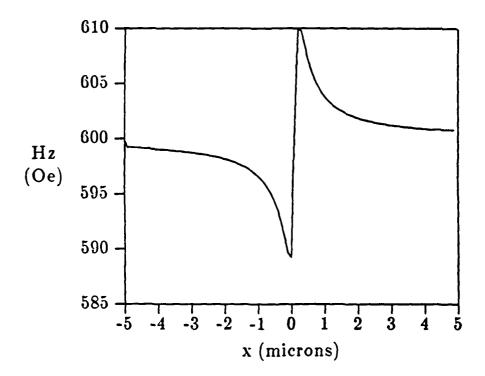


Figure 2-19: Perpendicular field, averaged through the film thickness, of the implanted/unimplanted edge of Fig. 2-18. Here, $\theta=85$ degrees, $4\pi M_s$ or the macerial is 600 G, h = 0.4 μ m and h₁ = 1.2 μ m

2.8.3. Charged Wall Model

In contiguous disc devices, the bubble driving force is produced by charged walls formed at the edge of unimplanted propagation patterns. The charged walls, to which bubbles strongly couple, are rotated by a rotating drive field along the propagation pattern edges, providing a driving force for bubbles in the implanted region.

It is well known that the magnetization distribution in ion-implanted layers is dominated by the stress-induced uniaxial anisotropy, particularly in the vicinity of the implanted/unimplanted boundary. ^{18, 28, 19, 29, 21, 30} This anisotropy, being parallel to the boundary, is responsible for charged wall formation. Since the form of this anisotropy is known, it may be used to deduce the structure of the charged wall without resorting to a laborious and time consuming calculation that will not enhance the accuracy of the result. ^{31, 20}

As mentioned above, the dominant stress-induced anisotropy near the implanted/unimplanted boundary is strong and parallel to the boundary. As a result of this uniaxial anisotropy, the magnetization distribution near the boundary is aligned parallel to the boundary. At preferred positions, depending upon the boundary orientation with respect to the crystalline axes and the drive field direction, this magnetization will align itself in one of the two preferred anisotropy directions. By rotating the drive field, the magnetization can be made to switch or rotate to the other stable direction. Charged walls, formed where this magnetization diverges, rotate and switch their stable positions as the magnetization rotates or switches. It is well known that the typical bias and drive fields used in implanted devices result in an extremely localized charged wall at the unimplanted boundary edge. 22, 32 As a result of this, and our own experimental observations, we chose to model the charged wall as a localized region of converging (or diverging) magnetization at the unimplanted boundary, which will be explained in detail in the succeeding section, in which the charged wall field is calculated. While this may lead to errors in propagation margins and other functions highly dependent on charged wall structure at lower bias and drive fields, we shall show that for current activated functions such as transfer or block replicate, the salient features of gate performance are maintained irrespective of assumed charged wall structure.

2.8.4. The Charged Wall Field

The charged wall may be modelled as a region of converging or diverging magnetization (depending on its polarity) which occupies a finite volume in the implanted region. The divergence of the magnetization creates a net charge concentration, that is, the charged wall. The stray field from a charged wall is obtained by directly integrating the stray field from the charge in the charged wall. A charged wall has a finite width, length and thickness. Without loss of generality, we can assume that the charged wall length is along the y-axis, extending from 0 to y_2 ; the width is between x_1 and x_2 , and the thickness is between 0 and x_1 , as shown in Fig. 2-20. The garnet film is parallel to the xy plane, and located between x_1 and x_2 . The x component of the stray field due to the charged wall at point x, averaged over the thickness of the film is given by:

$$H(x,y) = \frac{\rho}{z_2 - z_1} \int_{x_1}^{x_2} \int_{0}^{y_2} \int_{z_1}^{z_2} \frac{z}{[(x-x')^2 + (y-y')^2 + z^2]^{3/2}} dz dy' dx', \quad (2.64)$$

where ρ is the charge density. After carrying out the first two integrations, Eqn. (2.64) becomes:

$$H(x,y) = \frac{\rho}{z_2 - z_1} \int_{x_1}^{x_2} \ln \left[\frac{\left[(x-x')^2 + (y-y_\varrho)^2 + z_\varrho^2 \right]^{1/2} + (y-y_\varrho)}{\left[(x-x')^2 + y^2 + z_\varrho^2 \right]^{1/2} + y} - \frac{\left[(x-x')^2 + y^2 + z_\varrho^2 \right]^{1/2} + y}{\left[(x-x')^2 + (y-y_\varrho)^2 + z_\varrho^2 \right]^{1/2} + (y-y_\varrho)} \right] dx'. \quad (2.65)$$

Equation (2.65) is evaluated numerically.

The charge density ρ of Eqns. (2.64) and (2.65) is assumed to be constant in these equations. For the actual calculations of the fields due to the charged walls in this thesis, Eqn. (2.64) was modified in the form:

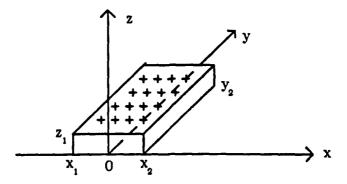


Figure 2-20: Model for the charged wall.

$$H(x,y) = \frac{1}{z_2 - z_1} \int_{x_1}^{x_2} \int_{0}^{y_2} \int_{z_1}^{z_2} \frac{\rho(x,y) z}{\left[(x-x')^{\ell} + (y-y')^{\ell} + z^{\ell} \right]^{3/2}} dz dy' dx', \quad (2.66)$$

where $\rho(x,y)$ is the spatial distribution of the charge density which is given as $\rho(x,y)$ = $\rho_0 f(x)g(y)$ where $\rho_0 = 2M_s/1.3$. Two different sets of f(x) and g(y) were used to describe two different length charged walls. The general forms of f(x) and g(y) are:

$$f(x) = \frac{x + 0.75}{0.45}, \quad -0.75 < x < -0.3$$

$$= 1, \quad -0.3 < x < 0.3$$

$$= \frac{0.75 - x}{0.45}, \quad 0.3 < x < 0.75$$
(2.67)

and,

$$g(y) = 1, 0 < y < 1$$

$$= \frac{y_2 - y}{y_2 - 1}, 1 < y < y_2$$

$$= 0, y < 0 \text{ or } y > y_2$$
(2.68)

where both x and y are measured in microns.

In the simulations, for drive fields of 40 Oe, the value of y_2 , the charged wall length, is assumed to be 4μ m. When the drive field is set to 80 Oe, the value of y_2 is assumed to be 2μ m. For drive fields between 40 Oe and 80 Oe, the charged wall field value used in the simulations is found by linearly interpolating between these two drive field extremes. Plots of the fields produced by the charged walls described by this heuristic model will be given in the following chapter.

From experimental measurements, 33, 34, 35, 31 the charged wall potential well depth at the edge of the unimplanted disk decreases by about 20% when the in-plane field is increased from 20 Oe to 100 Oe. For the same amount of increase in in-plane field, the charged wall length decreases more rapidly; almost 100% reduction in length is seen. When the in-plane field is pointing into the cusp of the contiguous disk pattern, a strong charged wall is formed in the cusp whose potential well depth is about 2 times that of the charged wall not in the cusp. The potential well depth also varies with the charged wall direction around the disk pattern. Excluding the cusp positions, a 20% variation in well depth is measured around the disk pattern. The charged wall position vs rotating in-plane field direction is calculated based on Calhoun's model which is given directly below 36.

2.8.5. Charged Wall Motion

As a starting point for describing bubble motion in ion-implanted bubble devices, it is not unreasonable to begin with trying to predict bubble motion on the most basic propagation element, the unimplanted disc. Typical ion-implanted minor and major loops are constructed simply by joining these discs in series, hence the reason for the name "contiguous disc devices". If the motion of a bubble on such a simple element can be predicted with reasonable accuracy, then one has a good foundation for extending the scheme to more complex propagation structures.

In his work, Calhoun calculated the motion of a bubble driven by a charged wall circulating about an unimplanted disc.³⁶ A schematic of the situation is depicted in

Fig. 2-21. Through the use of his method, one may calculate the position of the bubble/charged wall system as a function of the drive field and also calculate the phase lag (or lead) of the bubble/charged wall with respect to the drive field. Although he only accounted for the magnetocrystalline anisotropy in his calculations, Calhouns' method of analysis is easily extended to include the aforementioned three-fold magnetostrictive anisotropy, due to its similar form to the magnetocrystalline anisotropy.

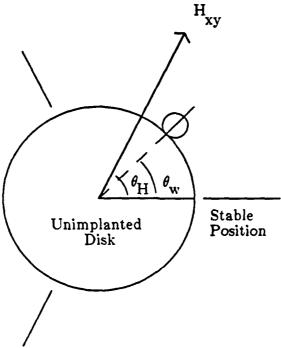


Figure 2-21: Geometry used to calculate motion of bubble coupled to unimplanted disc.

Several assumptions are used to simplify the analysis. It is assumed that the bubble and charged wall are rigidly coupled and that all the damping of the moving charged wall/bubble system is due to the bubble. Experiments have borne out the latter assumption to be correct.³⁷

The damping force of the bubble may be approximated as³⁸

$$F_{d} = \pi dM_{s}t_{s}(R/\mu_{w})d\theta/dt, \qquad (2.69)$$

where μ_w is the wall mobility of the storage layer, t_s is the storage layer thickness, M_s is the magnetization of the storage layer, R is the radius of the bubble trajectory and d is the bubble diameter.

The bubble/charged wall is driven around the disc by the applied field, H_{xy} . To first order, we may approximate the charged wall as a sheet of length L, height t_d , the thickness of the ion-implanted drive layer, having a uniform charge density $\rho = 2M_d \cos \alpha$, where α is the angle between the wall normal and M_d , the drive layer magnetization. Then, the tangential force due to H_{xy} driving the wall F_H may be given by:

$$F_{H} = (2M_{d}t_{d} L \cos\alpha) H_{xy} \sin(\theta_{H} - \theta_{w})$$
 (2.70)

where $\theta_{\rm H}$ is the angle of the applied field and $\theta_{\rm w}$ is the angular position of the wall and bubble.

In ion-implanted devices of the type described here, as has been shown, crystalline and stress- induced anisotropies play major roles in affecting charged wall behavior. The major component, the stress-induced anisotropy, has the same angular dependence as the crystalline anisotropy and is proportional to $\sin 3\theta_w$. The form of these anisotropies gives rise to the three "easy" and "hard" directions of these devices; the charged wall will prefer to reside at $\theta = 0^\circ$, 120° or 240° . The restoring force is then given as:

$$F_r = (2M_d t_d L \cos \alpha)(H_{eff}/3) \sin 3\theta_w, \qquad (2.71)$$

where H_{eff}, the effective anisotropy field due to crystal symmetry and stress relaxation is:

$$H_{eff} = 9\sqrt{2}[(1/3)K_1 + (\lambda_{111} - \lambda_{100})(\sigma_p - \sigma_p)]H_B/(Q_d - 1)4\pi M^2$$
 (2.72)

where Q_d is the quality factor of the implanted layer, H_B is the applied bias field, the λ 's are the appropriate magnetostriction constants and σ_n and σ_p are the stress components normal and parallel to the implanted edge respectively. Note that for equal magnetostriction constants there is no contribution to the anisotropy field due to magnetostriction, and that H_{eff} can be forced equal to zero by judicious selection of material parameters such as the λ 's and K_1 .

By equating the driving force with the restoring and damping force, $F_d + F_r = F_H$, we get the following first order non-linear differential equation:

$$v d\theta/d\omega t + 1/3 \sin 3\theta = h \sin(\omega t - \theta), \qquad (2.73)$$

where h =
$$H_{xy}/H_{eff}$$
, v = $R\omega/\mu_e$, $\theta_H = \omega t$ and $\mu_e = \mu(2M_d t_d L \cos \alpha)/\pi dM_s t_s$.

A computer program was written to solve the equation of motion given by Eqn. (2.73) by the Runge-Kutta method.³⁹ Two useful results obtained are 1), the position of the charged wall/bubble as a function of the in-plane field position, and 2), the phase lag between the drive field and the charged wall/bubble. In addition, the effects of drive field magnitude, stress and magnetostriction constants, operating frequency and dynamic bubble parameters on bubble circulation may be modelled.

In Fig. 2-22 is seen the bubble position as a function of drive field position around an unimplanted disc for $H_{eff} = 37$ Oe, f = 100 kHz, and h = 1.75.

The computed bubble motion presented in this section will be compared to experimental results in the following chapter.

Of course, in real devices, the propagation structure is more complex than that of an unimplanted disc. However, a contiguous disc propagation pattern can be constructed by piecing together arcs from circles of various radii and matching "boundary conditions" where the arcs intersect.

2.9. Spontaneous Bubble Nucleation

One type of failure mode seen in bubble devices is known as spontaneous nucleation. This failure results in a bubble self-nucleating or forming where a bubble should not exist; this usually occurs at low bias fields. In bubble devices, during the "write" operation, the bias field is locally reduced by a pulsed hairpin conductor, resulting in bubble nucleation. It is easy to see how the use of conductors for other bubble device functions, such as replication or transfer can result in unwanted bubble nucleation, resulting in an error.

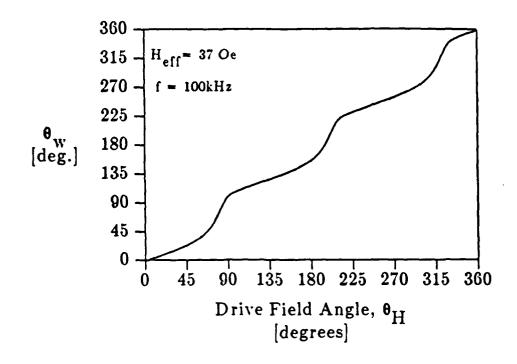


Figure 2-22: Bubble position as a function of drive field position around an unimplanted disc for two different values of the normalized drive field, h.

2.9.1. Nucleation Model

Since nucleation of a bubble is essentially a magnetization reversal of 180 degrees, it may be modelled by a Stoner-Wohlfarth equation and will occur when the local field exceeds the effective anisotropy field. One might think that in a thin film with perpendicular uniaxial anisotropy the vertical field produced by a conductor must exceed the effective anisotropy field of the film in order to induce magnetization reversal. However, Nelson et. al. showed that high fields are required only at the surface of the bubble film and that in-plane field components also contribute to the initial surface reversal. They also showed that ion-implanted films were more easily reversed than unimplanted films. ⁴⁰ Furthermore, Almasi et. al. showed that bubbles are much more readily nucleated with the assistance of charged walls than without them. ⁴¹ In fact, their studies showed that the charged wall may contribute a field on the order of $0.5 \times 4\pi M$ to the nucleation process. That is, bubble nucleation will occur when the vector sum of the bias field, the drive field, the conductor fields, the

charged wall field and the edge affinity field exceed the critical curve. This is given as:

$$(H_{dx} + H_{cx} + H_{ex})^{2/3} + (H_b + H_{ez} + H_{cz} + H_{wz})^{2/3} = (H_k - 4\pi M)^{2/3},$$
(2.74)

where H_{dx} is the x component of the drive field, H_{cx} is the x component of the conductor field, H_{ex} is the x component of the edge affinity field, H_{b} is the bias field, H_{ez} is the z component of the edge affinity field, H_{wz} is the z component of the charged wall field and H_{cz} is the z component of the conductor field. The critical curve defined by this equation is seen in Fig. 2-23 where the value of $Q = H_k/4\pi M = 2.7$.

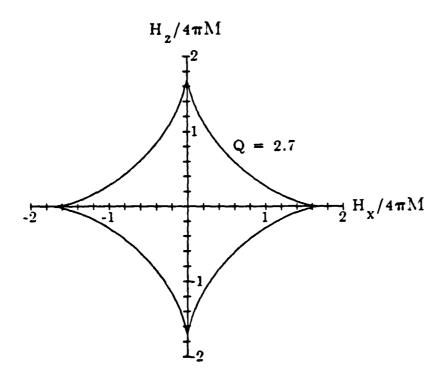


Figure 2-23: Critical curve for determining bubble nucleation threshold. The quality factor of the film is 2.7 here.

In the work under discussion here, we assume that bubble nucleation occurs at the top of the bubble storage film near the implanted/unimplanted interface. Therefore, for the conductor-induced field values of equation (2.74), H_{cz} and H_{cx} , the values used in the actual simulator calculation are those computed at the bubble film surface. Since the field values fall off quickly as a function of distance from the film surface,

the vector sum of the conductor fields is maximum here and this would be the most likely place for nucleation to occur. In addition, this is also where the charged wall field strength is maximum. The contribution of the edge affinity field must also be accounted for, although this is typically on the order of tens of oersteds and conductor fields may be an order of magnitude higher than this with the charged wall field contribution being on the order of $0.5x4\pi M$.

For the purpose of illustration, in Fig. 2-25 we plot the perpendicular and in-plane magnetic fields due to a current-carrying pair of parallel conductors, whose geometry are depicted in Fig. 2-24. This conductor configuration is typical of bubble stretcher designs as we shall see. Both conductors are 3μ m wide and are separated by a distance of 2μ m. The conductors, lying in the x-y plane each carry 1 mA (in opposite directions), and from symmetry we see that there is no y field produced. The field values in Fig. 2-25 are those at a surface assumed to be 1.55 μ m from the midplane of the two conductors. In an actual device, the spacer might be a combination of insulators as well as other conductors used in the fabrication of the gate. We assumed in our simulations that bubble nucleation will occur where the H_x and H_z field contributions to the nucleation threshold defined by Eqn. (2.74) are maximum.

2.10. Summary

In this chapter the various fields that are needed to describe bubble domain behaviour in ion-implanted magnetic bubble devices have been described and formulated. In addition, the reader has been provided with the background required to understand general bubble domain and magnetic domain behaviour in response to applied fields. In the chapter to follow, the method used to model magnetic bubble domain motion in response to the aforementioned fields will be presented. Once this has been accomplished, we may proceed to use these results to construct a simulator which will be shown to accurately predict and describe bubble domain behavior during the transfer and replicate processes in ion-implanted devices. Once agreement between simulated and experimental gate operation is verified, then the simulator can be used to simulate new gate designs.

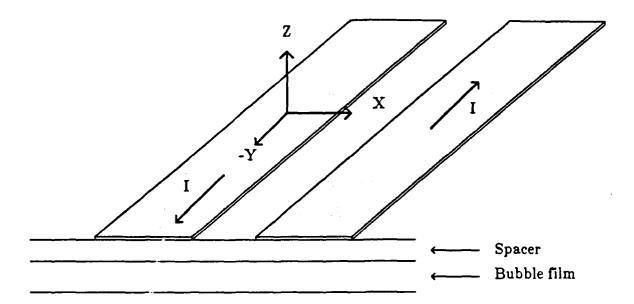


Figure 2-24: A pair of current-carrying conductors, typical of the bubble stretcher used in the replicate gate studied in this report. The conductors are of infinite length, of width w, separated by distance g, and assumed to be infinitesimally thin.

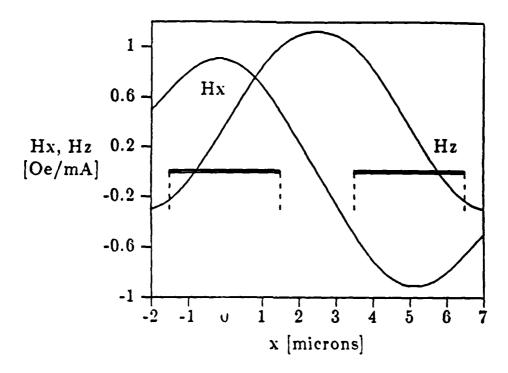


Figure 2-25: In-plane and perpendicular magnetic fields due to the pair of parallel current-carrying conductors in the x-y plane depicted in Fig. 2-24. The conductors each have $w = 3\mu m$ and are separated by $g = 2\mu m$. Each conductor carries a current of 1mA; field values shown are for $z = 1.55\mu m$.

Chapter 3 Simulation of Bubble Devices

The previous chapter introduced the various fields (and their sources) that play roles in dictating domain behavior in ion-implanted devices. In this section, the method formulated by Hayashi^{42, 43, 44} to compute domain wall motion is presented and described in detail. Although this scheme is rather complex, we shall see that the Hayashi method can be used to simulate very complex domain behavior such as stretching and chopping, two very important processes for the gates described herein. Finally, the general attributes of the bubble gate simulator are tersely described. Here, we restrict discussion to the features and input parameters of the assorted programs that comprise the simulator. The purpose of this brief overview is to indicate to the reader the utility of the simulator, its flexibility, and the parameters that may be varied during its use. The use of the simulator in predicting bubble behaviour in current-activated gates and its utility in exploring new gate designs is left as the topic of the chapters to follow.

3.1. The Hayashi Method

Unlike other bubble motion models that require the bubble shape to remain circular, the method of Hayashi 42 , 43 , 44 can model bubble domain deformation while only requiring a modest amount of computing time; in addition, bubble stripe out and collapse, the two most common failure mechanisms in bubble devices can be modelled by this method. It was this method that was used to model the devices described in this thesis. In this model, the bubble domain wall consists of N wall sections that are evenly spaced. N typically varies from 18 to 72 depending on the bubble or stripe circumference. The total effective field acting on the center of each wall section is computed and the section moves in response to the field.

Figure 3-1 shows a Cartesian coordinate system (X, Y, Z) fixed to the crystal with the Z-axis parallel to the film normal and is used as the laboratory frame. The direction of the magnetization M at any point (X, Y, Z) within the crystal is represented by the polar angle θ measured from the Z-axis and the azimuthal angle ϕ_a measured from the X-axis, both of which are assumed not to vary along the Z-axis. The angle θ is assumed to be π within the bubble domain and 0 outside. The locus, c, of points where θ equals to $\pi/2$ is used to represent the wall shape. In order to describe the wall structure and hence the wall shape we also use a local frame (called the R-S frame) with its origin on a wall point P. The R-axis is parallel to the outward normal of the curve c, and the S-axis is normal to the R-axis (tangential to c). Figure 3-1 also shows the R-S frame and the azimuth of the magnetization vector on the curve c, $\phi_a = \phi_w + \phi_n$, where ϕ_n denotes the angle between the R-axis and the X-axis, and ϕ_w denotes the azimuthal angle of the magnetization vector measured from the R-axis.

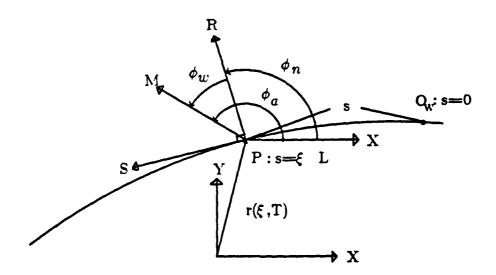


Figure 3-1: Representation of the bubble domain wall in the laboratory and local frames. The wall point $P(\xi)$ is specified by a parameter ξ which is the wall length O_wP divided by the total wall length L.

The motion of the domain wall is caused by rotation of the magnetization in the domain wall as described by the Landau-Lifshitz-Gilbert equation:

$$\dot{M} = -\gamma M \times H_{eff} + \alpha \frac{M \times \dot{M}}{|M|}.$$
 (3.1)

In the local coordinate system the following components are obtained:

$$\dot{\theta} = -\frac{|\gamma|}{M_{\rm g}} \frac{1}{\sin \theta} \frac{\delta \epsilon}{\delta \phi_{\rm g}} - \alpha \dot{\phi}_{\rm g} \sin \theta , \qquad (3.2)$$

$$\dot{\phi}_{a} \sin\theta = \frac{|\gamma|}{M_{a}} \frac{\delta\epsilon}{\delta\theta} + \alpha \dot{\theta} , \qquad (3.3)$$

where $\delta\epsilon/\delta\phi_{\rm a}$ and $\delta\epsilon/\delta\theta$ denote the functional derivatives of the magnetic energy density $\epsilon(\theta, \phi_{\rm a})$ with respect to $\phi_{\rm a}$ and θ , respectively. To solve Eqs. (3.2) and (3.3) directly would consume enormous computation time because it is a two-dimensional problem. However, Hayashi derived one-dimensional equations for the wall by assuming that the structure of the moving domain wall can be approximated by that of a stationary wall. With this assumption the angular velocity θ can be converted to the translational velocity in the direction of the wall normal, $V_{\rm g}$ of the wall as follows:

$$V_{R} = \dot{\theta} / \left(\frac{\partial \theta}{\partial R}\right)_{S}. \tag{3.4}$$

Equations (3.2) and (3.3) are transformed into:

$$\frac{V_R}{4\pi M_s \mu} = f_R + \frac{\ell}{2q\alpha} \frac{\dot{\phi}_a}{4\pi M_s \mu} , \qquad (3.5)$$

$$\frac{\ell}{2q\alpha} \frac{\dot{\phi}_{a}}{4\pi M_{a}\mu} = -\frac{1}{1+\alpha^{2}} (f_{R} - \alpha^{2} f_{s}) , \qquad (3.6)$$

where M_s is the saturation magnetization, $\mu(=|\gamma|\ell/\pi\alpha)$ is the wall mobility, $\ell=\sigma_w/4\pi M_s$ is the characteristic length, q is the quality factor, α is the damping factor, and the normalized effective radial and tangential forces f_R and f_s respectively are given by the following equations:

$$f_{\rm R} = -\frac{\ell}{2\rho_{\rm O}} - \frac{\ell}{4q} \frac{\partial \sin 2\phi_{\rm W}}{\partial S} + \frac{H_{\rm D} - H_{\rm A}}{4\pi M_{\rm S}}, \qquad (3.7)$$

$$f_{s} = \frac{1}{2\alpha} \left(\sin 2\phi_{w} + \frac{\ell^{2}}{2\theta} \frac{\partial^{2}\phi_{a}}{\partial S^{2}} \right), \tag{3.8}$$

where ρ_0 denotes the radius of the curve c, H_A and H_D denote the Z components of the applied field and the demagnetizing field originating from surface pole density averaged over the film thickness, respectively. The effective forces f_R and f_S are evaluated at each wall point (R = S = 0).

For a soft bubble with an applied in-plane field large enough to freeze the azimuthal angle of the magnetization in the domain wall, i.e., $\dot{\phi}_{a}=0$, the normalized effective force, f_{R} , is given by:

$$f_{\rm R} = -\frac{\ell}{2\rho_{\rm 0}} + \frac{H_{\rm D}}{4\pi M_{\rm s}} - \frac{H_{\rm A}}{4\pi M_{\rm s}}.$$
 (3.9)

The first term on the right hand side of Eqn. (3.9) is the equivalent force of wall pressure which tends to decrease the bubble diameter. The second term, due to the demagnetizing field, tends to increase the bubble diameter and the third term, the applied field, tends to decrease the bubble diameter. The effective force expressed by Eqn. (3.9) must be modified to account for the coercivity and wall saturation velocity. The net effective force, f_R^{**} , is given by:

$$f_{R}^{\bullet} = \begin{cases} f_{R} - \frac{H_{c}}{4\pi M_{s}} \operatorname{sign}(f_{R}), & \text{if } |f_{R}| > H_{c}/4\pi M_{s} \\ 0 & \text{otherwise,} \end{cases}$$
(3.10)

$$f_{\rm R}^{**} = \begin{cases} \sin(f_{\rm R}^*) \frac{v_{\rm S}}{4\pi M_{\rm S} \mu}, & \text{if } |f_{\rm R}| > v_{\rm S}/4\pi M_{\rm S} \mu \\ f_{\rm R}^* & \text{otherwise,} \end{cases}$$
(3.11)

where H_c is the coercivity, v_s is the saturation velocity, μ is the wall mobility, and f_R

and $f_{\rm R}^{-\frac{1}{2}}$ are the effective forces before and after subtracting the coercive force, respectively.

3.1.1. Numerical Methods

The bubble domain wall c is represented by a set of N wall points, P(1) to P(N). Each wall point P(I) has its own value of the magnetization azimuth angle $\phi_a(I)$. Since the azimuth angle $\phi_n(I)$ of the outward wall normal at P(I) can be obtained from the wall shape, the magnetization azimuth angle $\phi_w(I)$ can also be obtained if $\phi_a(I)$ is known. Thus Eqs. (3.5) and (3.6) can be solved directly from the current wall shape and wall structure represented by the position of each wall point P(I) and the value of $\phi_a(I)$. This style of solution (to be called the explicit solution later) has two severe drawbacks: (1) Because each wall point is made to move in the direction of the wall normal alone, iterative calculations may lead to an uneven distribution of the wall points over the bubble wall c. (2) For the calculation to proceed stably, a time step is required with difference ΔT far smaller than required for the accuracy of the calculation. Methods of calculation which overcome these difficulties are presented below.

To keep the displacement uniform, a parametric representation is employed for the wall shape at time T by using a parameter ξ (called the normalized distance parameter) equal to the ratio of s to the total wall length L, where s is the wall length between a reference point O_w on c and the wall point $P(\xi)$ to be represented (See Fig. 3-1). Then the velocity $V(\xi,T)$ of $P(\xi)$ at time T is given by:

$$V(\xi(T), T) = \frac{dr(\xi(T), T)}{dT} = \left(\frac{\partial r(\xi, T)}{\partial T}\right)_{\xi} + \left(\frac{\partial r(\xi, T)}{\partial \xi}\right)_{T} \frac{d\xi}{dT}, \quad (3.12)$$

where $\mathbf{r}(\xi,T)$ is a vector drawn from the origin of the laboratory frame to $\mathbf{P}(\xi)$. Since the derivative $(\partial r/\partial \xi)_T$ is equal to the unit tangential vector of the wall c at $\mathbf{P}(\xi)$ multiplied by L, we have the normal and tangential components of the velocity \mathbf{V} as $\mathbf{V}_R(\xi,T) = (\partial r/\partial T)_\xi$ and $\mathbf{V}_S(\xi,T) = (\partial r/\partial T)_\xi$ and $\mathbf{V}_S(\xi,T) = (\partial r/\partial T)_\xi$ and $\mathbf{V}_S(\xi,T) = (\partial r/\partial T)_\xi$ are the unit outward normal vector and t is the unit tangential vector. The wall motion described by Eqs. (3.5) and (3.6) is such that $\mathbf{V}_R(\xi,T)$ is the one obtained

from Eqn. (3.5) and that $V_s(\xi, T)$ is zero. Therefore we obtain the following equations equivalent to Eqs. (3.5) and (3.6):

$$\Delta R(\xi, T) = V_R(\xi, T) \Delta T, \qquad (3.13)$$

$$\Delta S(\xi, T) = -L d\xi/dT$$

$$= \left\{ L\xi \int_0^1 \frac{V_R(\xi, T)}{\rho_0(\xi)} d\xi - L \int_0^{\xi} \frac{V_R(\xi, T)}{\rho_0(\xi)} d\xi \right\} \Delta T, \qquad (3.14)$$

where ΔR and ΔS are the displacements in the R and S directions, respectively, and $\rho_0(\xi)$ is the radius of the curve c at $P(\xi)$. The displacement vector given by the components ΔR and ΔS in Eqs. (3.13) and (3.14) equals $(\partial r/\partial T)_{\xi}\Delta T$, and hence represents wall motion with the normalized distance parameter ξ unaltered at each wall point.

In the actual calculation the equations of wall motion, i.e., Eqs. (3.5) and (3.6) which are differential equations containing time T and the local coordinate S as independent variables, must be replaced by appropriate difference equations with respect to time difference ΔT and spatial difference δs . Generally ΔT is bounded by an upper limit beyond which the numerical process becomes unstable. We shall show an *implicit* solution that has a much larger upper bound of ΔT than that of the explicit solution.

The $V_{\rm R}$ -equation (Eqn. (3.5)) can be expressed in the following form at a wall point specified by the normalized distance parameter s_0/L :

$$\frac{V_{\rm R}(s_0)}{4\pi {\rm M_s}\mu} = p(s_0) - \frac{\ell}{2\rho_0} \,, \tag{3.15}$$

where $p(s_0)$ denotes the sum of the effective force terms other than the wall force. In the R-S frame with the origin at the wall point under consideration, the wall shape in the neighborhood of the origin at time T can be expressed as $R(S, T) = -S^2/(2\rho_0)$. Therefore Eqn. (3.15) can be rewritten at the wall point under consideration as:

$$\frac{\partial R(S,T)}{\partial T}\Big|_{S=0} = 2\pi M_s \mu \ell \frac{\partial^2 R(S,T)}{\partial S^2}\Big|_{S=0} + 4\pi M_s \mu p(s_0). \tag{3.16}$$

The partial derivatives in Eqn. (3.16) can be expressed in the following difference equation form:

$$\frac{\partial R(S,T)}{\partial T}\Big|_{S=0} = \frac{R(0,T+\Delta T)}{\Delta T},$$
(3.17)

and

$$\frac{\partial^2 R(S,T)}{\partial S^2}\Big|_{S=0} = \frac{R(\delta s, T+\Delta T) - 2R(0, T+\Delta T) + R(-\delta s, T+\Delta T)}{\delta s^2}, \quad (3.18)$$

where wall points P(1) to P(N) are placed at equal distance $\delta s(=L(T)/N)$ on the curve c. Positions $R(0, T+\Delta T)$ and $R(\pm \delta s, T+\Delta T)$ denote the ordinates of the wall points P(I) and P(I±1), respectively, at time $T+\Delta T$ in the R-S frame placed at P(I) defined at time T and are related with the normal displacements $\Delta R(I, T)$ and $\Delta R(I\pm 1, T)$ as follows (see Fig. 3-2):

$$R(0, T+\Delta T) = \Delta R(I, T),$$

and

$$R(\pm \delta s, T + \Delta T) + \frac{\delta s^2}{2 \rho_0} = \Delta R(I \pm 1, T) + O(\delta s^4).$$
 (3.19)

From Eqs. (3.16) to (3.19) we obtain a set of equations which implicitly determine the displacement $\Delta R(I)$ of P(I) when $p(s_0) - \ell/(2\rho_0)$ is given at time T:

$$-\Delta R(I+1, T) + (2 + 1/\lambda) \Delta R(I, T) - \Delta R(I-1, T)$$

$$= \frac{2 \delta s^2 f(s_0)}{\ell} \qquad (I = 1, 2, 3, \dots, N), \qquad (3.20)$$

where λ equals $2\pi M_s \mu \ell \Delta T/\delta s^2$ and $f(s_0)$ denotes the right-hand side of Eqn. (3.15). Note that the matrix formed by Eqn. (3.20) is essentially band diagonal so that both the memory requirements and the computation time of solving Eqn. (3.20) are proportional to N and not N^2 .

Most of the computation time is spent in computing the right-hand side of Eqn.

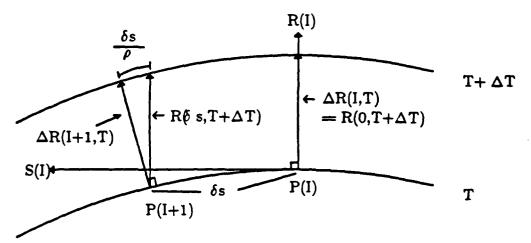


Figure 3-2: Wall displacement at wall point P(I) in the R-S frame.

(3.7), in particular the demagnetizing field H_D and the applied field H_A . The demagnetizing field is the sum of self and mutual demagnetizing fields, the latter being due to bubble-bubble interaction. The applied field is the sum of the uniform bias field, the field from the charged wall, the field due to the edge affinity of the unimplanted boundary and fields due to stretching and/or chopping conductors. The method used for computing H_D is described in the following section. Computation of the various terms that comprise H_A were described in the previous chapter.

The average demagnetizing field on the domain wall P is obtained by summing the field due to all the surface charges and averaging it over the thickness of the film. Actually the magnetic potential at point P is calculated. Assuming the z-axis is normal to the film plane, the average demagnetizing field at point P is:

$$H_{d} = \frac{1}{h} \int_{0}^{h} 2M_{s} \left[\int_{S^{-}} \frac{i_{z} \cdot i_{p}}{p^{2}} dS - \int_{S^{+}} \frac{i_{z} \cdot i_{p}}{p^{2}} dS \right] dz, \qquad (3.21)$$

where:

- S⁺ is the surface with positive magnetic charge,
- S' is the surface with negative magnetic charge,

- p is the vector pointing from any surface pole to P,
- i, is the unit vector along the z-axis,
- in is the unit vector along the direction of p,
- p is the length of the vector p,
- h is the thickness of the film, and
- $4\pi M_e$ is the saturation magnetization.

Since $\int_{S} \mathbf{i}_{z} \cdot \mathbf{i}_{p} dS/p^{2} = 2\pi$, Eqn. (3.21) becomes:

$$H_{d} = 4\pi M_{s} - \frac{4M_{s}}{h} \int_{0}^{h} \int_{S^{+}} \frac{i_{z} \cdot i_{p}}{p^{2}} dS dz, \qquad (3.22)$$

where S^+ is taken to be the surface area of the bubble. Using cylindrical coordinates with the z axis normal to the plane, the surface integral in Eqn. (3.22) can be expressed as:

$$H_{d} = 4\pi M_{s} - \frac{4M_{s}}{h} \int_{0}^{h} \int_{0}^{\pi} \int_{0}^{r} \frac{z}{(\rho^{2} + z^{2})^{3/2}} \rho \, d\rho \, d\phi \, dz, \qquad (3.23)$$

where r is the vector pointing from point P to any other point on the bubble domain wall, r is the length of r and is a function of ϕ , and ϕ is the angle of the vector r measured from the tangent of the bubble at point P, as shown in Fig. 3-3(a). If there is only one bubble, H_d is the self-demagnetizing field which can be reduced to:

$$H_{d} = 4\pi M_{s} + \frac{4M_{s}}{h} \int_{0}^{\pi} \left[(r^{2} + h^{2})^{1/2} - (r + h) \right] d\phi.$$
 (3.24)

If there is more than one bubble, each additional bubble introduces an additional volume integral term in Eqn. (3.23) due to bubble-bubble interaction. The integral in Eqn. (3.24) must be carried out numerically. The integration is equivalent to finding the area under the curve shown in Fig. 3-3(b). Note that the value of the integrand is always zero at $\phi=0$ and $\phi=\pi$, because r=0 at these two points. The shape of the curve is arbitrarily drawn. Because the bubble domain is represented by N wall

points, we can only know the value of the integrand at the N ϕ 's corresponding to the N wall points. Simpson's rule is used to calculate the area of each segment, such as the one between ϕ_{i-1} and ϕ_i , shown in Fig. 3-3(b). The value of the mid-point needed in Simpson's rule is obtained by finding the value of r corresponding to $(\phi_{i-1}+\phi_i)/2$. This method is chosen because it requires little computation time and the error is acceptable. The use of other more complicated schemes to integrate Eqn. (3.24) is ruled out because by using Simpson's rule, the computation of H_D accounts for 80% of the CPU time during simulation. Using a more complicated scheme would at least double or triple the computation time but the improvement in accuracy would be small.

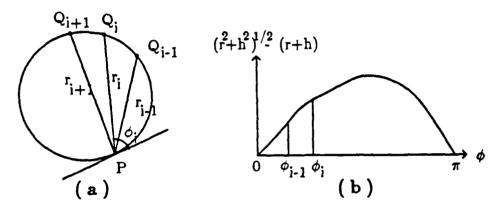


Figure 3-3: The calculation of the demagnetizing field on a wall point.

3.2. Simulator Overview

3.2.1. Introduction

In the devices under study here, we recall that magnetic bubble domains are under the influence of not only the static bias field, but are also affected by fields from the charged walls that propagate them. Furthermore, pulsed conductors used to implement functions such as transfer or replicate will of course affect domain wall behavior. Finally, the edge affinity of the implanted/unimplanted boundary will be shown to be of significance, and this effect should also be accounted for in trying to describe bubble behavior. If the fields due to the aforementioned effects can be computed as a function of time, then the bubble motion that results from these

dynamic fields can be calculated. In short, there are two problems to be solved here:

1) field calculation and, 2) resulting domain wall motion due to these fields. The advantages of this "separation" are obvious. If, for example, one would like to simulate the effects of conductor geometry changes in an active bubble gate while leaving the ion-implanted propagation track geometry unchanged, then the only fields that need be recomputed for each geometry variation are the fields from the conductor. This saves time for the device designer and allows one to study the effects of varying parameters truly independently.

3.2.2 Simulator Programs

The simulator consists of several programs that are used to compute various fields that in turn are used to compute bubble motion. All the programs are listed and their functions described here. As stated above, the specific calculations performed by the various programs have been already introduced. The purpose of this terse summary is to give the reader a functional overview of the simulator and its capabilities.

3.2.2.1. Charged Wall and Bubble Motion

In field access propagation schemes, bubbles move under the influence of a rotating in-plane drive field. Typically, one full drive field rotation results in a bubble advancing one bit position along a propagation track. Since all the bubbles in a device feel this global drive field, all bubbles move in unison; this holds true for ion-implanted as well as for permalloy devices. As we have seen in the ion-implanted devices, the drive field rotates a charged wall which in turn drives the bubble coupled to it. Due to the nature of the charged wall and its formation, there is not a linear correspondence between the drive field rotation and the subsequent charged wall motion. This anisotropy was described earlier and attributed to the anisotropic magnetostriction of the bubble material. As a result of this anisotropy, around an unimplanted disc the charged wall has three stable positions.

One of the most pronounced effects of this three-fold anisotropy is the behavior of a bubble propagating around an unimplanted propagation pattern. At various phases of the drive field cycle, the bubble will be moving at different velocities. Since the drive field rotates with constant frequency, the bubble can either lag or lead the drive

field in phase. Furthermore, the magnitude of the phase difference between the drive field position and bubble position is a function of the drive field amplitude.

A method devised by Calhoun was presented earlier which allows one to calculate the bubble/charged wall position as a function of the drive field and other relevant parameters, such as mobility, anisotropy, etc., and a typical charged wall/bubble position vs. drive field position relationship was seen in Fig. 2-22. In the simulator under discussion here, the charged wall position as a function of drive field position is computed prior to simulation and stored in a table. For constant material parameters, this table need not be modified for gate design variations. During the simulation as the drive field rotates, the charged wall position is simply "looked up" in the table instead of computed, which speeds up the simulation. On the other hand, for a change in material parameters such as the anisotropy for example, the new charged wall/drive field relationship is easily computed and a new "look up" table is then used for the simulation.

3.2.2.2. Propagation Pattern Geometry

Since the method used for calculating the relationship between the drive field and the charged wall is based on a very simple element, an unimplanted disc, modifications must be made to extend this scheme to more practical structures, such as the propagation patterns used in actual ion-implanted devices. Fortunately, this is easily done since the propagation patterns used in ion-implanted devices are typically formed by connecting circular discs in series, hence the alternative name "contiguous disc devices". The charged wall/drive field relationship computed above is assumed to hold on the arcs of the interconnected discs that comprise the propagation patterns. The simulator updates the charged wall positions on the various pattern segments as the drive field rotates at a specified frequency.

When the ion-implanted pattern geometries are input to the simulator, in addition to defining charged wall positions used later during an actual simulation, there is another calculation performed that is pertinent to the operation of ion-implanted devices, namely, the calculation of the fields due to the implanted/unimplanted boundary discontinuity. These "edge affinity" fields play an important role in bubble behavior in these devices and are responsible for keeping the bubble rather tightly

bound to the propagation pattern edge. In order to compute these field strengths, in addition to knowing the propagation pattern geometry the user must specify M_s, the magnetization of the material, and the implant depth.

3.2.2.3. Conductor Geometry

In some of the current-activated functions of contiguous disc devices, there are operations that require the use of two patterned conductors that have to be excited independently. Therefore, there is a need to be able to input different conductor pattern geometries, compute the fields that these conductors produce and then excite these conductors at various times with respect to the rotating drive field. Of course in the most general case, the currents that flow through the conductors may also be of varying amplitudes and polarities. Given the aforementioned restrictions, the simulator was designed to be able to pulse two isolated conductors independently at any phase of the rotating field cycle. The general features of this method are described in the following paragraph.

In the most complex gate that we will be discussing, the block-replicate gate, there are two overlapping conductors on top of the bubble film separated by an insulator. Specifically, there is a conductor which stripes out the bubble and another conductor which is used to chop the stripe in half. One conductor (the stretcher) reduces the local bias field and the other (the chopper) increases the local bias field. Obviously, the polarity of these fields, their phases, and their magnitudes will be different. So, in order to generalize the simulator input for maximum flexibility, the following is done: First, the conductor patterns are digitized and input in separate files, each conductor having its own separation from the bubble film. Then, the magnetic fields from each conductor are computed utilizing a current density normalized to 1 mA/µm and stored in their respective data files. Finally, when one of the conductors is pulsed during an actual simulation, the appropriate conductor field value is extracted from the data file and multiplied by the actual current value. This field value is then used to compute domain wall motion. The employment of this technique dispenses with the need to compute the field during the actual simulation, and reduces the field computation to a simple multiplication. It further allows the user to specify independently when the various conductors should be turned off and on with respect to the rotating field cycle. Finally, it allows variations in ion-implanted pattern geometry, magnetic material characteristics and even conductor current amplitude and phase to be made without having to recompute the conductor fields.

3.2.2.4. Domain Wall Motion Calculation

Once all the fields that may act upon the domain are computed, subsequent motion of the domain is calculated by the Hayashi method, which was described earlier. The Hayashi method was chosen to model domain wall motion since this method, in which the domain wall is assumed to consist of N evenly spaced planar wall segments, is not restricted to bubble shapes that remain circular. Furthermore, N can vary depending upon the process being simulated: for a circular bubble low N can speed up computation time with little loss of accuracy and in the case of bubble stripeout N can be increased for enhanced accuracy. In the simulations presented here, N varied from 18 for a circular bubble to 60 for an elongated domain.

Simulations of gate operation are performed after all fields are computed and stored in their respective files. Material parameters such as the magnetization of the bubble film $4\pi M$, the characteristic length l, the wall coercivity H_c , the wall mobility μ_w , the saturation velocity v_s , the stripe width w_s , and the bubble film thickness t are required in order to compute bubble motion and a complete set of parameters would include the current densities through the conductors, the turn-on and turn-off phases of these currents, the frequency of the drive field, the strength of the bias field and the initial bubble position and initial angular orientation of the drive field. The positions of the N bubble wall segments are computed in increments of 1 nsec as the simulation proceeds. By monitoring the circumference of the bubble, flags indicate bubble collapse or stripeout errors, terminating the simulation if either of these failures should occur.

For the simulator described in this thesis, computations were performed on a VAX-11/780 computer, although programs were also capable of running on an HP9836 computer. A typical simulation would require on the order of several thousand steps. On the HP9836 this would require several hours of CPU time; on the VAX-11780 a complete simulation would be performed in roughly 50 minutes of CPU time.

3.3. Summary

The method used to compute domain wall motion has been described in detail herein. Following this, the simulator that was used to calculate and predict gate operation was briefly introduced as were the programs that comprise the simulator. The two chapters that follow give the simulated operation margins and failure modes of two current-activated gates for contiguous disc devices; these simulated margins are compared to experimental margins wherever possible, and we show that the simulator does indeed model domain behaviour accurately, proving its utility as a tool for modelling new gate designs.

Chapter 4 Transfer Gate Simulation

In this chapter, we present results of the simulation of a bubble transfer gate that was introduced by Nelson et al.⁸ and whose operation was described in the Introduction. As we recall, this gate was designed to operate in two distinct but similar modes: bubble transfer from the major to minor loops (transfer-in) and bubble transfer from the minor to major loop (transfer-out). Since this gate only requires one conductor level and does not stretch or chop the domain to be transferred, it is a good starting point for introducing the operation of the simulator and ascertaining its accuracy with only a modicum of effort. Once we show how well the simulator can predict operating margins and failure modes faithfully for such a simple gate design, we will extend its utility to more complex gates in the next chapter, such as the blockreplicate gate. Transfer gate margins that were simulated include bias field us transfer current amplitude and bias field vs transfer current phases. Wherever possible, simulated margins are compared with experimental margins. Furthermore, we give margins obtained by simulation assuming that the bubble material is completely isotropic and compare these results to simulated anisotropic and experimental margins. Finally, in order to learn more about some of the transfer failure modes and the transfer operation in general we also show simulated bubble domain wall motion as a function of time during the transfer process.

4.1. Bubble Propagation

In this study, before active functions were simulated, bubble propagation margins were first obtained since all gate functions require that the bubble first successfully propagate into the gate before any currents are applied. This simulation of propagation margins is also a good "confidence check" with the experimental data.

In order to simulate propagation margins, a bubble was initially placed at a specific location on the minor loop and the drive field was specified to rotate a designated number of field cycles; the designated number of field cycles was high enough to propagate the bubble around the minor loop end and into and out of cusps. Simulator results of typical successful propagation are shown in Fig. 4-1. Also seen in the figure are the three easy bubble stripe-out positions and the sense of the drive field. The initial bubble position was on the right-hand-side of the second disk of the minor loop and its trajectory as it rotated around the minor loop tip counter-clockwise is also depicted. At a simulated drive field frequency of 125kHz, one full drive field rotation requires 8 \(\mu\)sec. The bubble position was plotted at 160 nsec intervals, except when the bubble was idling in the cusps; then its position was plotted every 5 \(\mu\)sec. The effect of the three-fold anisotropy is clear as it is seen that the bubble spends more time near the easy stripe-out directions and quickly propagates through the hard directions.

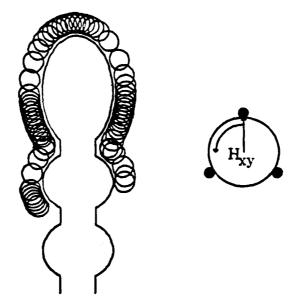


Figure 4-1: Typical bubble propagation simulation. The three easy stripe-out directions and drive field rotation sense are also shown. Bubble positions plotted every 160 nsec, except in cusps where positions are plotted every 5µsec. Simulation drive field frequency was 125 kHz.

Table 4-1: Nominal trapping gate simulation parameters.

Magnetization	$4\pi { m M_s}$	851 G
Anisotropy field	H _k	1861 Oe
Characteristic length	1	0.105 μm
Bubble film thickness	t	1.28 μm
Stripe width	w	1.1 μm
Wall Coercivity	H _c	2.0 Oe
Bubble mobility	$\mu_{\mathbf{w}}$	300 cm/sec-Oe
Saturation velocity	v _s	3800 cm/sec
Operating frequency	ı	100 kHz
Drive Field	H _{xy}	65 Oe
Transfer-In Pulse Amplitude	I _{in}	35 mA.
Transfer-Out Pulse Amplitude	Iout	35 mA.
I _{in} Pulse Leading Edge	θ_{i1}	160 Degrees
I _{in} Pulse Falling Edge	θ_{i2}	360 Degrees
Iout Pulse Leading Edge	θ_{o1}	2.0 Degrees
Iout Pulse Falling Edge	02	160 Degrees
Conductor thickness	t _s	0.6 µm
Implantation depth	t _d	0.40 μm

Since we studied operation of the A.T.&T. trapping transfer gate, we also tried to predict bubble propagation margins in the minor loops of this device, and the results are seen in Fig. 4-2 where the simulated margins are depicted by the dark circles and measured margins as given by Nelson et al., are given by the square open boxes. Both the simulated and experimental margins are given for a drive field frequency of 100kHz. The margins are offset by a constant field value, most likely due to the difference between the unknown experimental implanted layer thickness and the

assumed value of $0.4\mu m$ used for the simulations. Furthermore, we assumed in our simulations that $4\pi M$ of the implanted layer was equal to $4\pi M$ of the bubble layer. Studies have shown that $4\pi M$ may be reduced substantially due to ion-implantation which would result in a reduction in the charged wall strength. A reduction in charged wall strength would result in the upper bias margin of Fig. 4-2 being reduced, making the simulated margins correspond better with the experimental margins. We should point out once again that given our very simplistic charged wall model and the fact that there are no assumed adjustable parameters in our model the correspondence between theory and experiment is quite good. Parameters used in the simulations are given in Table 4-1.

It would be instructive at this point to illustrate the effect of the charged wall here by plotting the fields produced by the wall. The charged wall field was described by Eqn. (2.66), using the spatial charge functions described by Eqns. (2.67) and (2.68). Using the parameters of Table 4-1, the "short" and "long" charged wall perpendicular field contours are seen plotted in Fig. 4-3. In this figure the minor loop is also depicted for reference. Perpendicular contours are plotted in increments of 2 Oe starting from 2 Oe. On the left hand side of the pattern the "long" charged wall, assumed to occur at drive fields of 40 Oe as described earlier, is depicted. The maximum contour value plotted has a field value of 26 Oe. On the right hand side of the minor loop the "short" charged wall is given; the maximum contour value here is 22 Oe.

Three major propagation failure modes were observed: bubble collapse, bubble stripe-out and bubble "lag". Bubble "lag" is defined as the failure that occurs when a bubble gets stuck in a cusp and can not be pulled out of the cusp by the rotating drive field. Bubble collapse usually occurred at one of two places on the minor loop at two different drive field phases. It occurred in the cusps during the portion of the field cycle that the bubble is held stationary in the cusps and is subject to the influence of a passing negative charged wall, and it occurred at the extreme edges or tips of the pattern edge where the edge affinity is low. In the center of Fig. 4-4 is seen the simulator result obtained for bubble collapse in the cusp. The bubble is seen to propagate successfully into the cusp, but it collapsed afterwards due to the negative

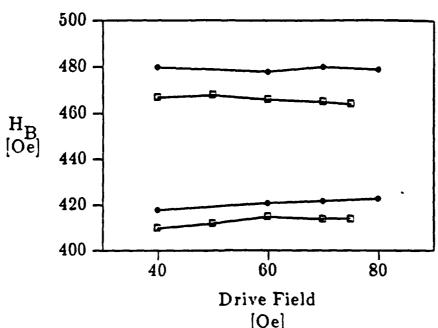


Figure 4-2: Simulated bias field margins of bubble propagation in the minor loops of the A.T.&T. trapping transfer gate denoted by the filled circles.

Published margins of Nelson et al. are given by the open boxes.

Simulations performed using the parameters of Table 4-1.

charged wall formed there as the drive field rotated. Both of these collapse failure modes (collapse on loop tips and collapse in cusps) were seen in the devices tested in the laboratory. Stripe-out was observed to occur at low bias fields where the bubble would stripe-out along one of the easy stripe-out directions under the influence of the strong positive charged wall there or along the unimplanted pattern edge where the edge affinity was high. This is depicted on the left-hand side of Fig. 4-4. Bubble lag would occur in the left-hand side minor loop cusps as seen in the right-hand side of Fig. 4-4. Note that the bubble, starting on the right side of the minor loop and propagating counter-clockwise, could successfully negotiate the cusp on the right hand side of the pattern, but failed to propagate out of the cusp on the left-hand-side. This is due to the fact that for the right-hand side cusps, the bubble in the cusp couples to the charged wall which is moving smoothly and relatively slowly due to the proximity of the easy stripe-out direction as it leaves the cusp. However, on the left-hand-side of the track, the bubble residing in the cusp must couple to a charged wall which is racing through a hard direction towards the nearest stripe-out position, which

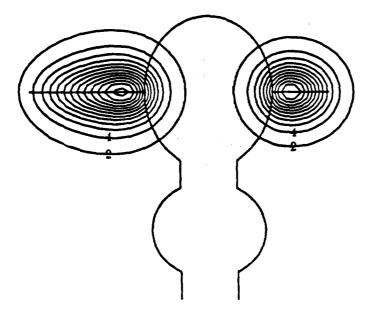


Figure 4-3: Field contours of the charged walls used in the simulator described herein. On the left hand side of the minor loop are the perpendicular field contours, plotted in 2 Oe increments, for the charged wall assumed to exist at a drive field of 40 Oe, as explained in the text. The right hand side charged wall field contours are assumed to occur when the drive field amplitude is 80 Oe. For intermediate drive field values, the charged wall field is found by interpolating between the two extremes depicted here.

is essentially in the next cusp, a full pattern period away. If the bubble can not catch up and keep up with the charged wall at this time, it will simply fall back to the cusp, being held there stably by the edge affinity. Observation of this type of failure with the simulator was not anticipated, but has been seen frequently in our experimental devices.

4.2. Trapping Transfer Gate Simulation

One of the first gates that was simulated was the bi-directional trapping transfer gate that was introduced by Nelson, et al.⁸ and described in detail in a previous section of this thesis. For convenience, we have reproduced the geometry of the gate in Fig. 4-5 as well as the rotation sense of the drive field and the position of the three easy bubble stripe-out directions. Furthermore, this figure also includes the grid utilized to discretize the conductor and ion-implanted patterns in order to calculate

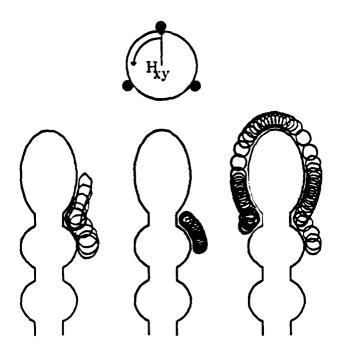


Figure 4-4: The three types of propagation failure observed during simulation. On the left-hand side is seen bubble stripe-out along the pattern edge. The middle depicts bubble collapse in the cusp, and on the right-hand side is seen bubble lag, explained in detail in the text.

the fields used in the simulation. In Fig. 4-5, 1μ m is equal to 4 grid units; fields were therefore computed every 0.25μ m in the x-y plane.

Assuming all relevant fields have been previously computed, a simulation would be initiated as follows: For transfer-out, the bubble center would be positioned at X=27, Y=33 and θ , the angle of the drive field H_{xy} , would be specified as 270 degrees. (These values are arbitrary, but judicious selection of the initial bubble position helps minimize simulation run time.) As the simulation proceeds, the new bubble wall positions are computed and updated. For transfer-in, the bubble might be placed at X=9, Y=65 and θ might be set to 90 degrees. Of course for both transfer-in and transfer-out the amplitude of the transfer current I_t , as well as the leading and falling edges of this current, θ_{t1} and θ_{t2} respectively, must also be specified. Nominal parameter values used in the characterization of the transfer gate are given in Table 4-1, unless noted otherwise.

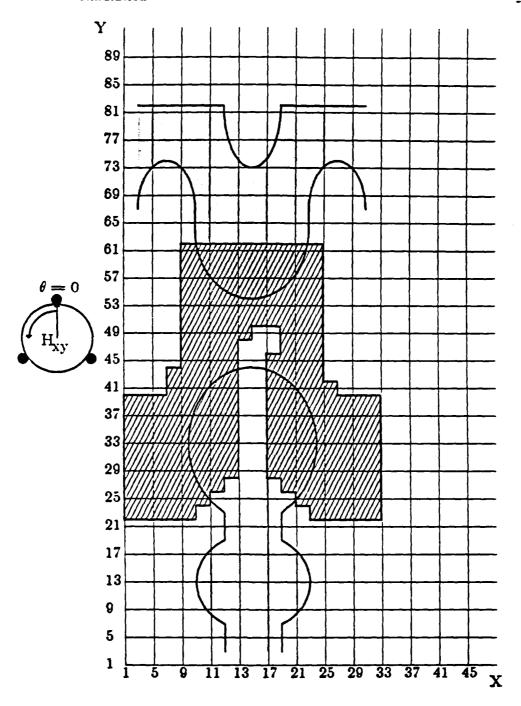


Figure 4-5: A.T.&T. trapping transfer gate and grid used to compute fields and bubble wall positions. 1 grid unit equals $0.25\mu m$ here.

4.3. Transfer-In Simulation

In the transfer-in process, bubbles circulating on convex portions of the major loop near the trapping conductor are uncoupled from the charged walls that propagate them by current through the conductor. In other words a propagating bubble is prevented from rotating when it gets trapped in the potetial well of a current carrying conductor. Since the drive field still rotates as the bubble sits idly in the potential well the charged walls still rotate, from which the bubble becomes uncoupled. From Fig. 4-5 we note that major loop bubbles are in the vicinity of the conductor at roughly $\theta = 180$ degrees. Through application of the current as the drive field rotates near 180 degrees, we see that the bubble, held fixed in the small notch of the conductor due to the attractive potential well there, will be in the vicinity of an attractive charged wall on the minor loop tip near the easy stripeout position as the drive field approaches 0 degrees. At this point in time the current pulse is terminated, the bubble couples to the charged wall on the minor loop tip and is propagated away from the gate area as the drive field continues rotating, completing the transfer We therefore note that three important parameters needed for characterization of the transfer-in (and transfer-out) process are the magnitude of the trapping current I_t , the transfer-in pulse leading edge θ_{i1} , and the transfer-in pulse falling edge θ_{in} .

4.3.1. Trapping Current Amplitude

Independent of the trapping current turn-on and turn-off phases, the most critical parameter for proper gate operation is the amplitude of the trapping current, I_t . The field created by this current must be of sufficient amplitude to "disassociate" the bubble from the charged wall that is propagating the bubble. In Fig. 4-6 we show the simulated bias margins vs transfer-in current, I_t , using the parameters of Table 4-1. In Fig. 4-6, open circles denote successful transfer and the crosses denote failure of the bubble to transfer. We see that there is a current threshold below which transfer will not occur, independent of bias field.

In Fig. 4-7 are the bias field vs transfer-in current amplitude margins as given by Nelson et al.⁸. We also note in the figure the leading and trailing edges of the

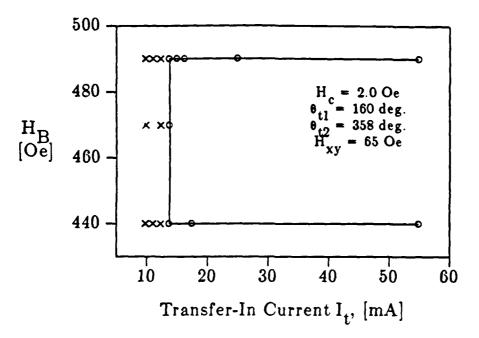


Figure 4-6: Simulated transfer-in current vs bias field margins for the trapping transfer gate. Successful transfer denoted by open circles, failure is shown by the crosses. Here, the current pulse was initiated at $\theta = 160.0$ degrees and was terminated at $\theta = 358.0$ degrees.

transfer current pulse as well as the drive field magnitude of 55 Oe. For transfer current amplitudes greater than 35 mA the margins are relatively independent of transfer current.

In Fig. 4-6 we depicted the simulated transfer-in current vs bias field margins for the transfer-in process, and saw that there was a very sharp threshold in current below which no transfer would occur. Compared with the margins of Nelson et al. in Fig. 4-7, we see that in the experimental devices there is a linear increase in the upper bias margin with transfer current amplitude that saturates at about 457 Oe for a current amplitude of roughly 35 mA. We may attribute differences in the simulated and experimental current margins to a number of factors. First and foremost is the fact that in the simulator described here the effect of the conductor field on the charged wall is not accounted for. Since the fields produced by the conductor may be on the order of the drive field (or greater) the effect of these fields on the charged wall should be included. In our simulated gate design, we do not take into account errors in conductor/implanted pattern registration, which could increase the current required

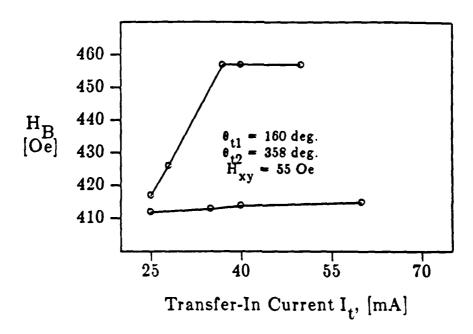


Figure 4-7: Measured transfer-in current vs bias field margins for the trapping transfer gate as given by Nelson et al.⁸

to implement successful transfer. Furthermore, during etching of the conductor pattern in these devices, the actual conductor pattern geometry that results will not be the same as that of the mask pattern. As a matter of fact, due to the isotropic nature of wet chemical etching, typically used in the fabrication of these devices, lateral etching of the mask patterns is on the order of the thickness of the conductor layer being etched. 46 If we refer back to Fig. 4-5, we see that the notch in the conductor responsible for trapping the bubble is 1µm wide. Since the conductor thickness in the experimental device is on the order of 0.5 µm⁸, then we may expect that the resulting gap width in the actual fabricated device may be almost 2µm wide. Given this variation in gate geometry, differences in current amplitude for simulated "ideal" devices and actual devices are not surprising, and experimental margins taken in our laboratory on these devices showed that transfer-in current vs bias field margins were a function of chip position on the wafer, ostensibly due to misregistration between the ion-implanted patterns and the conductor level.⁴⁷ In any case, for both the experimental and simulated bias field margin ve trapping current phase comparisons that are to follow, the transfer current amplitude was held fixed at 35 mA; we see that for both simulated (Fig. 4-6) and experimental (Fig. 4-7) margins

that for this current value the bias margins were constant, allowing us to neglect differences in transfer-in current threshold.

4.3.2. Trapping Current Phases

For a fixed trapping current amplitude, the rising and falling edges of the current with respect to the drive field phase were studied. In Fig. 4-8 we show the simulated margins of bias field vs θ_{t1} , the rising edge of the transfer-in current. Here $\theta=0$ degrees is as depicted in Fig. 4-5, the current amplitude was 35 mA, and the falling edge of the transfer current θ_{t2} was held fixed at 320 degrees. For these margins, we assumed that the bubble material was anisotropic, the bubble/charged wall vs drive field relationship used for the simulation was that given in Fig. 2-22. For the sake of comparison, these same margins were re-simulated assuming that the material was perfectly isotropic; that is, the bubble/charged wall stayed in phase with the drive field for all drive field angles. The results are seen in Fig. 4-9.

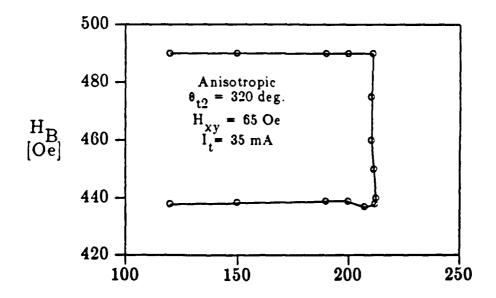
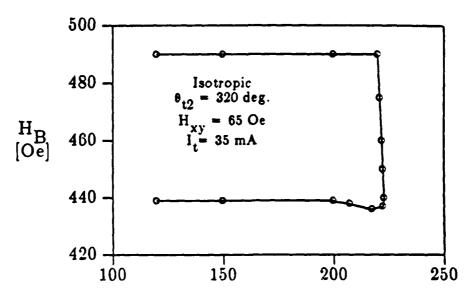


Figure 4-8: Simulated bias field vs transfer current turn-on angle, θ_{t1} margins for the transfer-in process. Simulation parameters are given in Table 4-1.

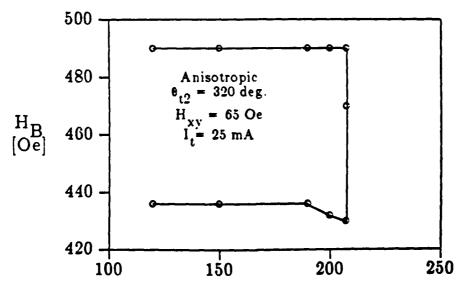
Transfer-In Angle Leading Edge 0₊₁, [degrees]

The margins of Figures 4-8 and 4-9 were then obtained using a lower trapping current amplitude to see its effects on leading-edge phase margin. These results are given in Fig. 4-10 and Fig. 4-11 for anisotropic and isotropic material respectively.



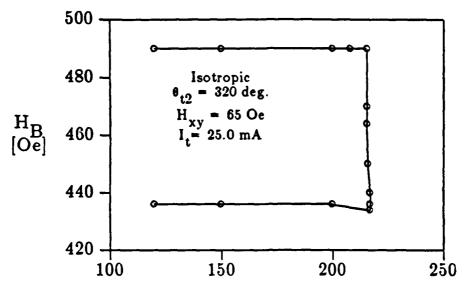
Transfer-In Angle Leading Edge θ_{t1} , [degrees]

Figure 4-9: Simulated bias field vs transfer current turn-on angle, θ_{t1} margins of transfer-in for an isotropic material. These simulations were performed using the same parameters used to obtain Fig. 4-8.



Transfer-In Angle Leading Edge θ_{t1} , [degrees]

Figure 4-10: Simulated bias field vs transfer current turn-on angle, θ_{t1} margins for the transfer-in process.



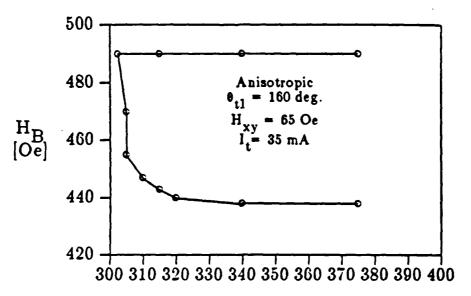
Transfer-In Angle Leading Edge θ_{t1} , [degrees]

Figure 4-11: Simulated bias field vs transfer current turn-on angle, θ_{t1} margins of transfer-in for an isotropic material. These simulations were performed using the same parameters used to obtain Fig. 4-8.

The simulated margins of bias field vs transfer current turn-off angle, θ_{t2} are depicted in Fig. 4-12 for an isotropic bubble material. Here, the trapping current amplitude was 35 mA and the trapping current leading edge occurred at $\theta = 160$ degrees.

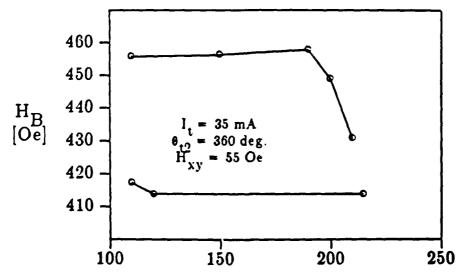
The bias field vs transfer-in current leading and trailing edge margins Nelson et al. measured are given in Fig. 4-13 and Fig. 4-14 respectively. For both figures the transfer current was 25 mA and the drive field frequency was 100kHz; the drive field was 55 Oe in both cases.

In Fig. 4-8 and Fig. 4-9 we showed the simulated bias field vs transfer current turn-on angle margins for an anisotropic and an isotropic bubble material, respectively, and we saw that for the isotropic material successful transfer-in would occur at a greater pulse delay than the anisotropic material. We can see in the anisotropic case of Fig. 4-8 that when θ_{t1} reaches roughly 211 degrees, the bias margin falls precipitously. Failure here was due to the bubble not being trapped by the



Transfer-In Angle Trailing Edge θ_{t2} , [degrees]

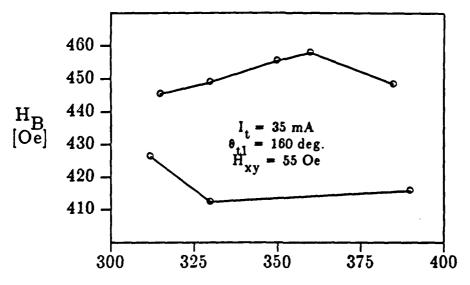
Figure 4-12: Simulated bias field vs transfer-in current turn-off angle, θ_{t2} margins for an anisotropic material.



Transfer-In Angle Leading Edge, θ_{t1} [degrees]

Figure 4-13: Measured bias field vs transfer-in current leading edge angle margins for the trapping transfer gate as given by Nelson et al.8

conductor field; the bubble would usually simply propagate along the major loop. In Fig. 4-9, the isotropic case, the margins do not decay until θ is almost 221 degrees, yielding a margin that is roughly 10 degrees wider than the anisotropic case.



Transfer-In Angle Trailing Edge, θ_{t2} [degrees]

Figure 4-14: Measured bias field vs transfer-in current trailing edge angle margins for the trapping transfer gate as given by Nelson et al.⁸

Bubble motion as a function of time during the transfer-in process is illustrated in Fig. 4-15. Here, the transfer current pulse of 35 mA was initiated at $\theta = 210$ degrees and terminated at $\theta = 320$ degrees. The simulation begins with the bubble on the left-hand-side of the major loop disc as seen in Fig. 4-15(a), and the drive field is rotated in counter-clockwise fashion at a frequency of 100 kHz. For reference, we also give the elapsed time of the simulation in nanoseconds, and the angle of the drive field in degrees for each portion of the simulation that is depicted in the figure; the simulation begins at t = 0 nsec. We see that prior to initiation of the current pulse at $\theta = 210$ degrees that the bubble is some distance away from the notch in the conductor as shown in part (c) of the figure where θ is equal to 209.3 degrees. Once the transfer pulse is initiated, the bubble has to be pulled back into the center of the gate region and held there until an attractive charged wall on the minor loop comes by when θ is in the vicinity of 360 degrees. We see in (d) that the bubble, slightly distorted elliptically, is moving toward the conductor notch, and in (e) it is being held there until the pulse is terminated at $\theta = 320$ degrees and the bubble is able to

propagate away with the aforementioned minor loop charged wall, as seen in (g) and (h) of Fig. 4-15. We should note that to insure reliable gate operation it is not advisable to delay the trapping current pulse as much as was done in Fig. 4-15. Since the portion of the major loop nearest the gate is an unstable bubble position, the bubble velocity here is relatively high as the bubble heads toward the nearest stable position on the disc at $\theta = 240$ degrees. As seen in the plot of bubble/charged wall position vs drive field position that was presented earlier (Fig. 2-22) for anisotropic material, we see that when the drive field position θ_H is equal to 211 degrees, that the bubble/charged wall position θ_W is precisely 221 degrees. For constant trapping current, we expect the bubble position where failure occurs in the isotropic case to be the same as that when failure occurs in anisotropic case, which indeed it is. We should also note that since the bubble/charged wall position vs drive field position is non-linear that the margins in Fig. 4-8 fall more rapidly than in the isotropic case of Fig. 4-9, where the margins fall monotonically.

In Fig. 4-13, we showed the experimental margins of Nelson, et al. 8 for bias field vs transfer-in angle. The margins are relatively flat until θ reaches roughly 190 degrees, at which point the upper margin falls rapidly. Compared to our simulated margins of Fig. 4-8, if we neglect the static offset in bias field explained earlier, we see that the simulated margins display similar behavior except that the angle at which the upper margin decays is roughly 211 degrees, in reasonable agreement with the experimental margins. Given that the experimental margins were taken at a drive field of 55 Oe while the simulated margins are given for a drive field amplitude of 65 Oe this discrepancy is not unexpected. Finally, we must once again note that in our model we did not take the effect of the fields produced by the trapping conductor on charged wall formation and structure into account. With all of these factors considered, the experimental and simulated margins are seen to agree quite well with each other.

The effect of reduced trapping current amplitude on the margins of Fig. 4-8 and Fig. 4-9 is depicted in Fig. 4-10 and Fig. 4-11, respectively, where the current was reduced to 25 mA in the latter cases. We see once again that the isotropic material has better margins than the anisotropic material; margins degrade at $\theta = 207$ degrees in the anisotropic case and $\theta = 215$ degrees in the anisotropic case. Once again

referring back to Fig. 2-22, we see that for the drive field position $\theta_{\rm H}=207$ degrees, $\theta_{\rm W}$, the charged wall/bubble position is 214.5 degrees. We may invoke the same argument used to explain the differences between Fig. 4-8 and Fig. 4-9 to explain the results in the reduced current case under discussion here, and we see that the difference in margin is due to the bubble leading the phase of the drive field in the vicinity of an unstable position.

If we compare bias field vs transfer current leading edge phase margins with respect to current amplitude, that is, compare Fig. 4-8 where the trapping current amplitude was 35 mA with Fig. 4-10, in which a trapping current amplitude of 25 mA was used, we see that the higher current amplitude simulation has wider margins than the lower current simulation. Since this gate works by "trapping" a propagating bubble by a field gradient, and since the field gradient required to trap the bubble is a function of trapping current and position, we expect there to be a correlation between trapping current and maximum permissible leading edge phase margin, assuming a constant bubble diameter. In Fig. 4-16 we give the perpendicular magnetic field contours due to a current of 1 mA applied to the conductor of the transfer gate; each number is in the units of Oe/mA with the positive contours being attractive to the bubble. We see that as a bubble propagates around the major loop past the conductor notch that the field gradient diminishes quite rapidly. This is the reason for the precipitous decay in bias field vs transfer-in leading edge phase margins seen here.

Just as the the leading edge of the trapping current pulse is important for successful transfer, similarly the phase of the trailing edge of the trapping pulse is also important. In Fig. 4-12 the bias field us transfer current pulse trailing edge margins were given. For values of the trailing edge $\theta_{t2} < 305$ degrees, the bubble would simply rotate about in the major loop. Not until θ_{t2} approached 320 degrees did bubbles transfer reliably. This is because when θ is much less than 360 (0) degrees, the nearest attractive charged wall seen by the bubble is the one the bubble was previously dissassociated from on the major loop during the transfer process. Only when θ approaches 360 degrees does the attractive position on the minor loop tip form, insuring bubble transfer to the minor loop.

Compared with the experimental margins of Fig. 4-14, except for the upper bias

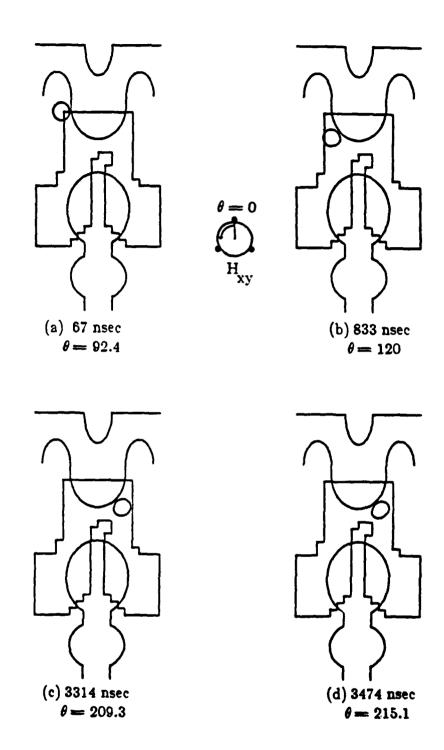
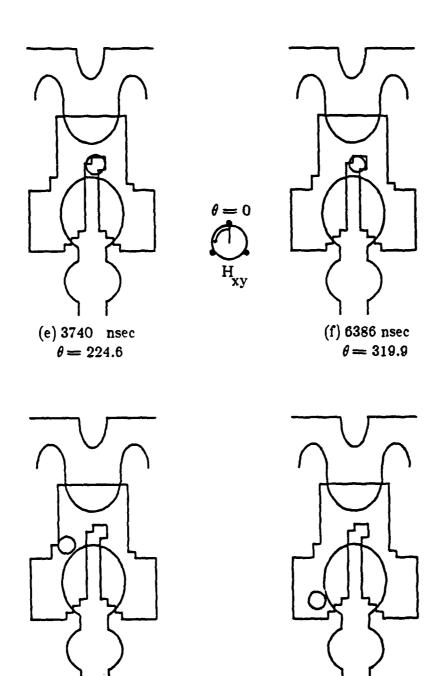


Figure 4-15: The transfer-in process shown as a function of time.



Continuation of Fig. 4-15

(g) 9000 nsec $\theta = 54$

(h) 10852 nsec $\theta = 120.7$

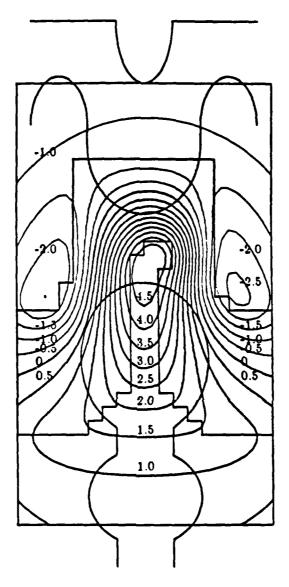


Figure 4-16: Perpendicular magnetic field contours of the trapping transfer gate for a current of 1 mA flowing through the conductor. Each number denotes the contour value in Oe/mA, with the positive contours being a potential minimum for the bubble.

margin, we see that the trends of Fig. 4-12 are quite similar. The experimental margins begin at $\theta = 312$ degrees compared to 305 degrees for the simulated margins, and for both sets of data the margins increase in width (that is, the lower bias margin

decreases) monotonically from the lower bias region for roughly 15 degrees. Thus, we see that the bias field vs transfer-in current leading edge margins for the experimental and simulated margins are in very good agreement.

One of the more interesting failure modes that occurred during transfer-in was due to a combination of low transfer current amplitude and low bias. This is depicted as a function of time in Fig. 4-17. We see that the transfer current, initiated at $\theta = 190$ degrees, is of sufficient amplitude to pin the bubble, but due to low bias and the propagating charged wall on the major loop disc that the bubble elongates into a stripe with one stripehead pinned by the conductor and the other coupled strongly to the charged wall.

4.4. Transfer-Out Simulation

4.4.1. Trapping Current Amplitude

Essentially the same parameters used to characterize transfer-in were used to characterize the transfer-out process. First and foremost of these was the current required to successfully implement transfer-out, and these are shown in Fig. 4-18 as a function of bias field for fixed transfer current pulse rising and falling edges. Once again we use open circles to denote successful transfer and crosses to denote failure.

The experimental bias field vs transfer-out current amplitude margins of the trapping transfer gate are seen in Fig. 4-19. Above current amplitudes of approximately 35 mA, the margins do not vary much with current.

As was found for the transfer-in process it was also seen for transfer-out that there was a very sharp threshold of current amplitude below which no transfer would occur, as depicted in Fig. 4-18. In addition, similar to transfer-in the simulated transfer-out current threshold was much lower than the experimentally obtained transfer-out current as seen in Fig. 4-19. However, in this case, the margins of Fig. 4-19 as published by Nelson, et al. did not extend to values of current below 25 mA, even though transfer may indeed have been successful there, with the implication that our simulated margins may indeed be in better agreement with experiment than they

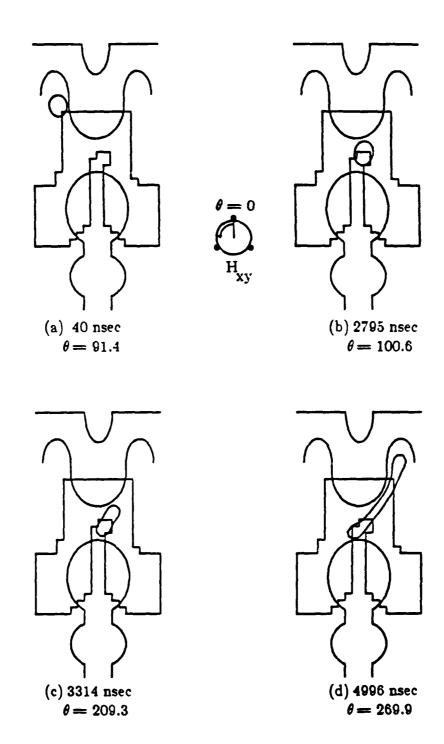


Figure 4-17: Transfer-in failure due to low bias and low trapping current.

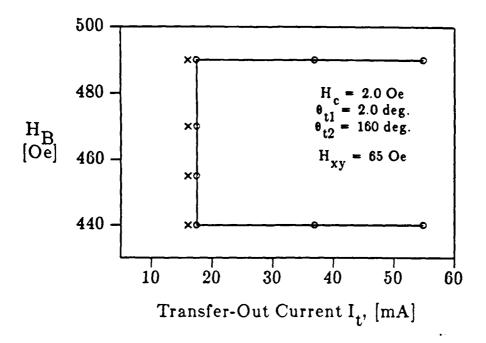


Figure 4-18: Simulated bias field vs transfer-out current margins for the trapping transfer gate. Here, the current pulse was initiated at $\theta = 2.0$ degrees and was terminated at $\theta = 160.0$ degrees. Open circles denote good transfer and crosses denote failure.

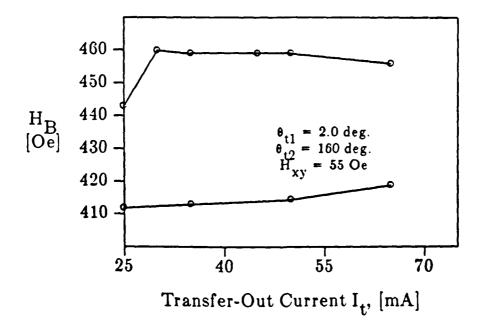


Figure 4-19: Measured bias field vs transfer-out current margins for the trapping transfer gate as given by Nelson et al.⁸

appear to be. As a matter of fact, quasistatic bias field vs transfer-out current amplitude margins taken in our laboratory showed successful transfer at current amplitudes as low as 15 mA.⁴⁷ Given the geometry variations that may occur between the "ideal" gate design used in the simulation and an actual experimental device as well as the simple charged wall model used here, the discrepancy between experimental and simulated margins is reasonable. Since both experimental and simulated margins do not change with current amplitude greater than roughly 30 mA, phase margin simulations as well as experimental margins that will be compared are for current amplitudes greater than 35 mA.

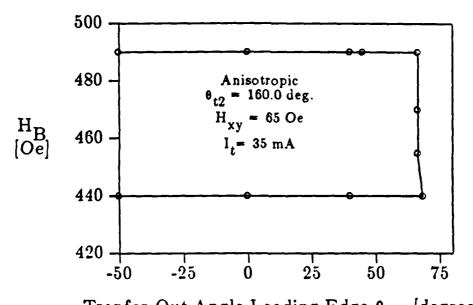
4.4.2. Trapping Current Phases

In Fig. 4-20 we show the simulated bias field margins for transfer-out vs the leading edge of the transfer-out current, θ_{t1} . Here θ_{t2} , the current pulse falling edge, was held fixed at 160 degrees and the current amplitude was 35 mA. The bubble material was assumed to be anisotropic here and results obtained for an ideal isotropic material are given in Fig. 4-21. The margins for the anisotropic material are much wider in θ than those for the isotropic material. This can be explained by the relationship between the drive field angle and the charged wall/bubble position and will be clarified in detail in the discussion to follow.

The simulated transfer-out current trailing edge margins for both anisotropic and isotropic materials are given in Fig. 4-22 and Fig. 4-23, respectively. It is seen that θ_{t2} is not as sensitive to material anisotropy as θ_{t1} for the transfer-out process.

For a trapping current amplitude of 35 mA, the bias field vs transfer-out angle leading edge margins as measured by Nelson et al.⁸ are given in Fig. 4-24. The margins are relatively flat until approximately $\theta = 50$ degrees, after which they fall precipitiously. Regarding the trailing edge margins as depicted in Fig. 4-25, we see that the margins in this case are of the same general form as the leading edge margins.

We saw in Fig. 4-20, the bias field vs transfer-out current pulse leading edge phase margin that bubbles could be successfully transferred for delays up to roughly 66



Transer-Out Angle Leading Edge θ_{tl} , [degrees]

Figure 4-20: Simulated bias field vs transfer-out current leading edge phase, θ_{t1} margins for the trapping transfer gate. Here, the current pulse was terminated at $\theta = 160.0$ degrees with an amplitude of 35 mA for a typical anisotropic material.

degrees at which point the margins decayed rapidly. We recall that there is an easy stripe-out position at $\theta = 0$ degrees on the minor loop tip, so that even though the drive field position may be at a certain angle, the charged wall/bubble will lag the drive field in phase as the drive field rotates through this easy position. Referring to Fig. 2-22, we see that when the drive field position $\theta_{\rm H}$ is 66 degrees, the charged wall/bubble position is only 43 degrees. Comparing to the isotropic margins in Fig. 4-21, we see that the margins decline here at $\theta = 40$ degrees, in reasonable agreement with the argument used to explain similar isotropic/anisotropic margin discrepancies in the discussion above regarding the transfer-in process. It is very interesting to note that transfer-out current pulse leading edge phase vs bias field was the only margin studied in which anisotropic films had better margins than isotropic films, and the magnitude of this difference was greater than any of the margins in which isotropic films performed better than anisotropic films.

Comparing bias field vs transfer-out current leading edge phase margins for

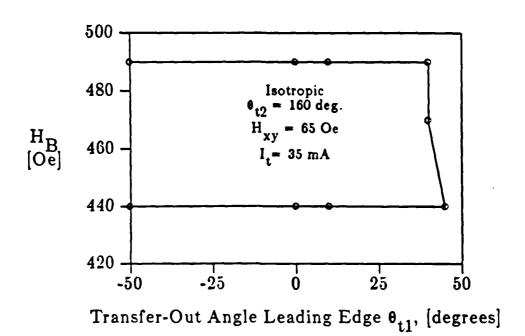
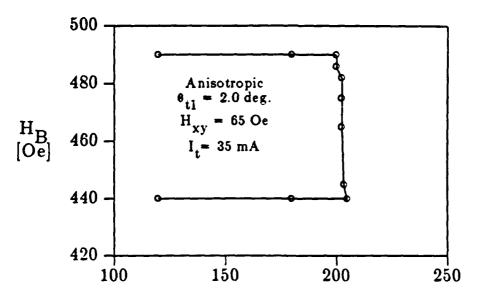


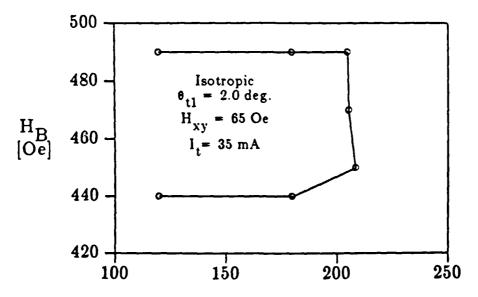
Figure 4-21: Transfer-out margins of Fig. 4-20 for an ideal isotropic material.

simulated and experimental results (Fig. 4-20 and Fig. 4-24, respectively), we see that both sets of data have identical forms; both high and low bias margins are insensitive to θ , the transfer pulse leading edge until a certain threshold, beyond which the margins fall rapidly from the high bias end. The experimental margins in Fig. 4-24 have a threshold value of $\theta = 50$ degrees while the simulated margins do not decay until $\theta = 67$ degrees. However, if we look at the threshold for the isotropic material case given in Fig. 4-21, we see that the threshold occurs at $\theta = 40$ degrees. Given the fact that the anisotropy field value for the material in the simulations was unknown and assumed to be 37 Oe, these results imply that perhaps the material used by Nelson et al.⁸ was more isotropic than the material used in our simulations, based upon the fact that the experimental results are intermediate between the simulated isotropic and isotropic margins. In any case, even though there is not perfect agreement between the experimental and simulated margin decay threshold values here, once again we see that there is at least excellent agreement in the margin trends as predicted by the simulator. Refinements in the charged wall model and more realistic conductor geometries that take into account conductor shape variations due to non-ideal processing effects and mis-alignment between the ion-implanted patterns



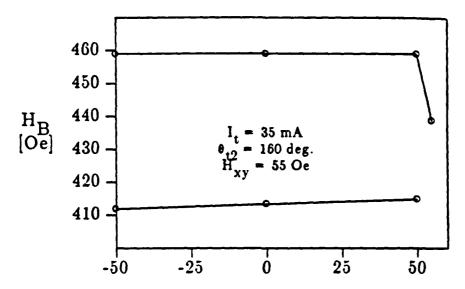
Transfer-Out Angle Trailing Edge θ_{t2} , [degrees]

Figure 4-22: Simulated bias field vs transfer-out current trailing edge phase, θ_{t2} margins for the trapping transfer gate. Here, the current pulse was initiated at $\theta = 2.0$ degrees with an amplitude of 35 mA in a typical anisotropic material.



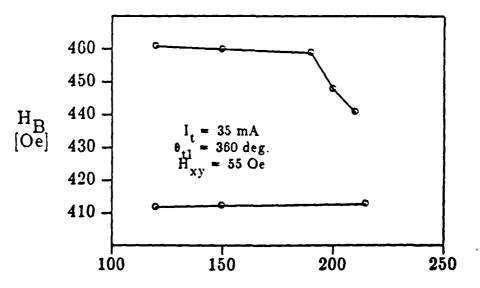
Transfer-Out Angle Trailing Edge θ_{t2} , [degrees]

Figure 4-23: Transfer-out margins of Fig. 4-22 for an ideal isotropic material.



Transfer-Out Angle Leading Edge θ_{t1} , [degrees]

Figure 4-24: Measured bias field vs transfer-out current leading edge angle margins for the trapping transfer gate as given by Nelson et al.⁸



Transfer-Out Angle Trailing Edge θ_{t2} , [degrees]

Figure 4-25: Measured bias field vs transfer-out current trailing edge angle margins for the trapping transfer gate as given by Nelson et al.⁸

and the conductor would be expected to help increase the correlation between the simulated and the experimental results.

The bias field vs transfer-out current pulse trailing edge margins were only slightly sensitive to film anisotropy as seen by comparing Fig. 4-22, the anisotropic case with Fig. 4-23, the isotropic case. The isotropic film had slightly wider margin than the anisotropic film by only about 3 degrees, the anisotropic margins began to decay, rather erratically; at θ_{t2} equal to approximately 202 degrees and the isotropic margins of Fig. 4-23 fall at $\theta_{t2}=205$ degrees. From Fig. 2-22, we see that when $\theta_{\rm H}=203$ degrees, $\theta_{\rm W}=203$ degrees; this is where the bubble charged wall goes from lagging to leading the drive field in phase.

The experimental margins of bias field vs transfer-out angle trailing edge are seen in Fig. 4-25.⁸ Both the upper and lower bias margins are relatively insensitive to trailing edge angle up to a value of θ equal to roughly 190 degrees. As θ increases above this value, the upper margin is seen to decay. Compared to the simulated results of Fig. 4-22 where the margins fall off at $\theta = 202$ degrees, we see that there is good agreement between the experimental and the simulated results.

The transfer-out process as a function of time is given in Fig. 4-26. Here the bias field was 465 Oe, $I_t = 35$ mA, the current pulse was initiated at $\theta = 2.0$ degrees and terminated at $\theta = 202.5$ degrees.

We saw from Fig. 4-20 that successful transfer could be implemented with transfer current pulse leading edge delays of up to roughly 65 degrees. It is illuminating to see the relatively large excursions in position a bubble will undergo during such a process as we show in Fig. 4-27. In this simulation, the leading edge of the transfer pulse was 65 degrees, very close to the value at which failure would occur. The bubble begins on the right-hand-side of the minor loop tip in (a) of the figure, and in (b) we plot the bubble position at $\theta = 63.6$ degrees, noting that the bubble center is almost two bubble diameters away from the center of the notch in the conductor, and the current has not been activated yet. However, we see in (c) that indeed the bubble has been pulled back to the notch of the conductor and does successfully transfer out.

Just as in the transfer-in process, there were a number of different failure modes observed for the transfer-out process, typically failure of the bubble to transfer out for low current pulse amplitudes and bubble collapse at high bias fields. At low bias, the

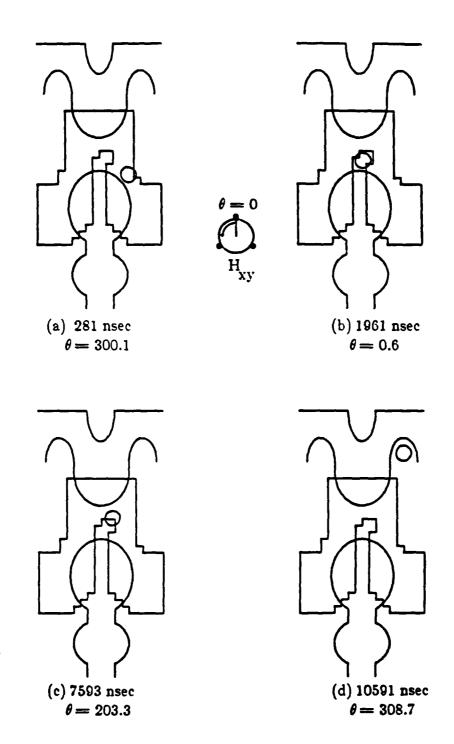


Figure 4-26: The transfer-out process.

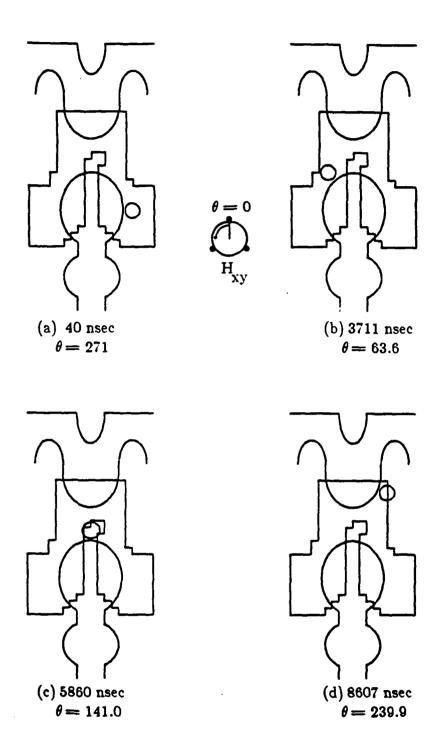


Figure 4-27: The transfer-out process illustrating how the bubble can be "pulled" back into the gate area even though the bubble is a few bubble diameters beyond the conductor notch. The current pulse was activated at $\theta = 65$ degrees here.

most common failure mode was bubble stripe-out as depicted in Fig. 4-28. This is almost the same mode observed in the transfer-in process.

4.5. Summary

In this chapter we have presented some simulations of the operation of, and the failure modes identified in a simple trapping transfer gate for ion-implanted bubble devices. It's successful simulation was an impetus for extending the flexibility of the simulator to model the operation of more complex gates and invent new ones. These results are in the chapters that follow.

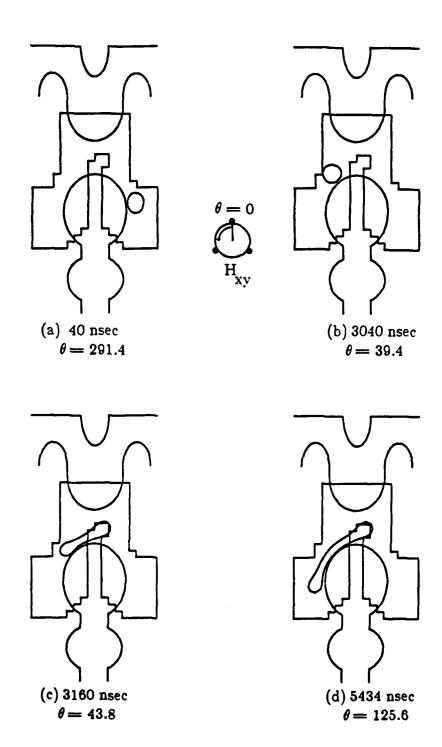


Figure 4-28: A transfer-out failure due to low bias.

Chapter 5 Replicate Gate Simulation

In the previous chapter simulated gate operation was presented for a simple transfer gate, i.e. a gate design that uses only one conductor level and does not require the bubble domain to deform radically during the gate operation process. Here, the use of the simulator for modelling the more complex domain processes that occur during the replicate process is presented, compared to experiments where possible and the results discussed. Once again we also show simulated domain motion during the replicate process as a function of time and some of the many failure modes that were noted to occur.

5.1. Bubble Propagation

Just as was done for the trapping transfer gate of the previous chapter, for the replicate gate to be discussed here bubble propagation margins in the minor loops of the device were simulated prior to simulation of the actual block replicate process. Once simulated, the margins obtained were compared to experimental propagation margins.

In Fig. 5-1 are given the experimental and simulated propagation margins for the minor loops of the replicate gate. The parameters used in the simulation are given in Table 5-1. The solid line is the experimental data of Urai et al.⁹; the diamond, dot and minus sign (-) represent simulated successful propagation, bubble collapse and bubble stripe-out, respectively.

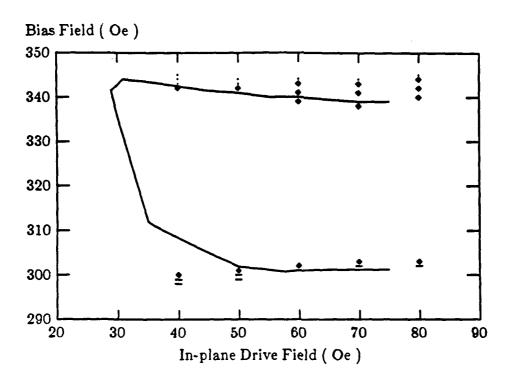


Figure 5-1: Experimental and simulated propagation margins for the minor loops of the block-replicate gate of Urai et al. Parameters used in obtaining the simulated margins are given in Table 5-1. The heavy black line is the published experimental data of Urai et al. and the diamonds denote successful simulated margins. Simulated stripeout and bubble collapse are given by the minus signs (-) and dots, respectively.

Table 5-1: Nominal replicate gate simulation parameters.

Magnetization	$4\pi M_s$	650 G
Anisotropy field	H _k	1750 Oe
Characteristic length	1	0.12 μm
Bubble film thickness	t	1.1 μm
Stripe width	w	1.1 μm
Wall Coercivity	H _c	2.0 Oe
Bubble mobility	$\mu_{\mathbf{w}}$	300 cm/sec-Oe
Saturation velocity	v _s	3800 cm/sec
Operating frequency	f	125 kHz
Drive Field	H _{xy}	70 Oe
Stretching Current	Is	100 mA
Chopping Current	I _c	80 mA
Is Pulse Leading Edge	θ_{s1}	324 Degrees
Is Pulse Falling Edge	θ_{s2}	27 Degrees
Ic Pulse Leading Edge	θ_{c1}	27 Degrees
I _c Pulse Falling Edge	θ_{c2}	39.5 Degrees
Stretcher thickness	t _s	0.6 μm
Chopper thickness	t _c	0.40 μm
Implantation depth	^t d	0.35 μm

Additionally, the effect of the wall coercivity, H_c, on the bubble propagation margin was studied. In Fig. 5-2 is seen how the bias margins deteriorate as the wall coercivity value used for the simulations was increased. In the figure, the thin line, thick line and the broken line represent the simulated propagation margins for values of wall coercivity of 1.0, 3.0 and 3.5 Oe respectively. When the coercivity increases from 1.0 Oe to 3.0 Oe, there is a little margin loss from the low bias end only. When

the coercivity goes from 3.0 Oe to 3.5 Oe however, the high bias margin degrades dramatically, particularly at high drive.

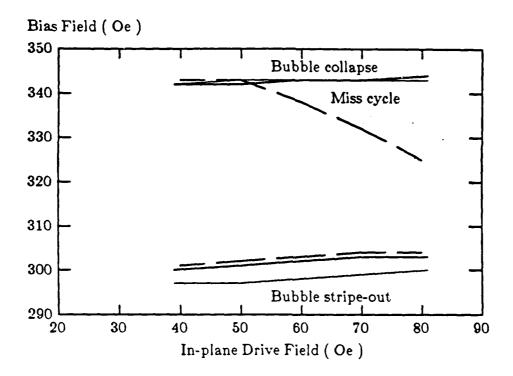


Figure 5-2: Simulated bias field margins for bubble propagation with the wall coercivity as a parameter. Margins degrade from the low bias end as the coercivity is increased from 1.0 Oe (Light line) to 3.0 Oe (Dark line). When $H_c = 3.5$ Oe, the high bias margins fall drastically. (Dashed line.)

5.2. Block Replication Simulation

Since the block replicate gate of Fig. 1-11 consists of two conductor levels, unlike other gates that utilize only one conductor, it was noted that simulation of this gate would require a simulator that was flexible enough to handle a large number of parameters and would be a good test of the utility and accuracy of the simulator. Therefore, the operation of this gate was simulated extensively, and some of the results are given here. Once again, for convenience we have redrawn the gate in question as well as the grid used for its discretization; this is seen in Fig. 5-3 where 4 grid units represent 1µm and the orientation of the gate with respect to the three-fold anisotropy is also denoted.

The parameters used in the simulation of this gate are given in Table 5-1. Simulations were typically run in the following way: The bubble was given an initial position on the minor loop propagation track (X = 47, Y = 51) of Fig. 5-3 and then the bubble position was recorded every 40 nsec as the simulation proceeded. After the designated number of field cycles was completed, the bubble motion as a function of time was displayed and the block replicate process was observed to see if it was successful or not. Additionally, the specific type of failure could also be diagnosed using this method.

5.2.1. Replicate Current Margins

Some of the more important parameters used to characterize gate performance are the currents required to successfully implement block replication. In Fig. 5-4 and Fig. 5-5 are the bias field margins of successful replication for the stretching current I_g and chopping current I_c , respectively. In obtaining these margins, the stretching pulse was initiated when the angle of the drive field, θ , was at 324 degrees and was terminated at $\theta = 27$ degrees, at which time the chopping pulse was initiated. The chopping pulse was then turned off at $\theta = 39.5$ degrees. In the simulations of Fig. 5-4, the chopping current was held fixed at 100 mA; for Fig. 5-5, I_g was equal to 80 mA. In Fig. 5-4, we also include some of the experimental data of Urai et al. and note the excellent agreement between experiment and our model.

Before scrutinizing the specific failure modes that might occur in the process of replicating a bubble, it will be instructive showing as a function of time successful replication as predicted by the simulator. The process is depicted in Fig. 5-6, where we show the bubble position as both a function of time and the position of the drive field, in degrees. The parameters used in this simulation are given in Table 5-1 except here θ_{c2} , the field angle at which chopping current I_c is terminated, was 34.5 degrees. The bias field for the simulation was 340 Oe, and at t=0 nsec., the beginning of the simulation, the bias field was oriented at $\theta=270$ degrees while the bubble was positioned on the upper-right-hand-side of the minor loop; in Fig. 5-6(a) we see the bubble just 40 nsec into the simulation. In (b), we see the bubble at $\theta=323.4$ degrees, just prior to the activation of the stretch current pulse leading edge which is at $\theta=324$ degrees. Only 26 nsec after the stretch pulse leading edge ($\theta=325.2$)

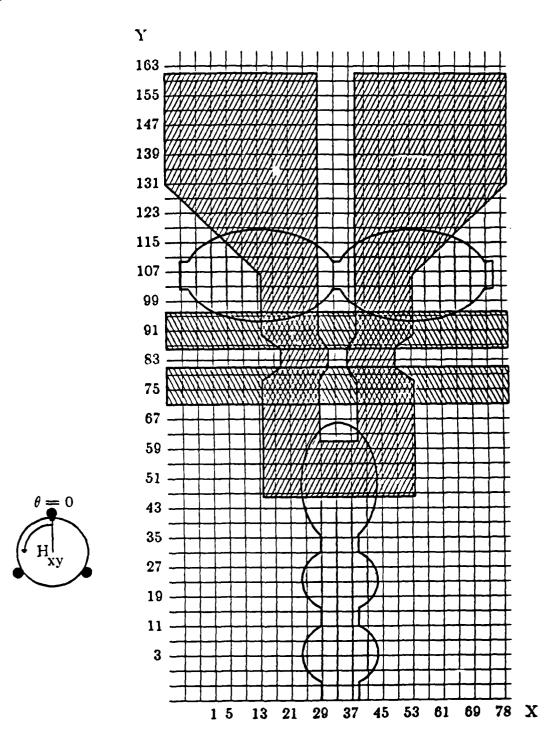


Figure 5-3: Block replicate gate design and grid used to compute fields and bubble wall positions. I grid unit equals $0.25\mu m$ here.

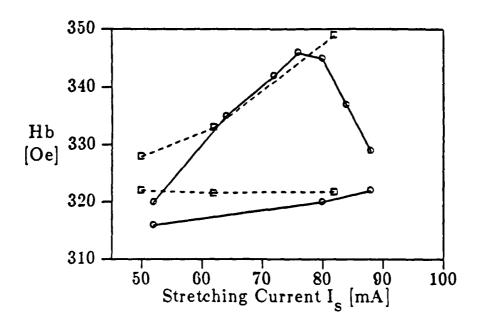


Figure 5-4: Simulated bias field vs stretching current margins for the gate depicted in Fig. 5-3, depicted by the open circles. $I_c = 100$ mA. The experimental margins of Urai et al.⁹ are shown as open boxes.

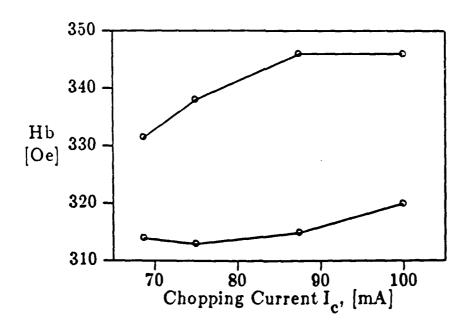


Figure 5-5: Simulated bias field vs chopping current margins for the gate depicted in Fig. 5-3. $I_s = 80 \text{ mA}$.

degrees), we see in Fig. 5-6(c) that the bubble has already begun to stripeout, and in (d) has fully expanded along the entire hairpin channel length ($\theta = 352.0$ degrees). Since the stretch pulse falling edge was specified to occur at $\theta = 27$ degrees, we can see that there is sufficient stretch pulse duration here, even though the bias field is 340 Oe, close to the collapse value of 347 Oe.

In Fig. 5-6(e) is seen the stripe configuration at $\theta=26.0$ degrees, just prior to termination of the stretch pulse and activation of the chopping pulse at $\theta=27$ degrees. Less than 30 nsec after the chopping pulse leading edge, the stripe has been chopped in half as seen in (f), where $\theta=28.3$ degrees. We can see how the original data bubble has not fully contracted back into a cylindrical bubble due to the stray field of the chopping conductor, active until $\theta=34.5$ degrees, which is of such polarity as to expand the domain on the minor loop tip. Furthermore, since the drive field is at 28.3 degrees here, the charged wall is also assisting in the elongation of the domain. Finally, when $\theta=127.3$ degrees, the seed bubble on the minor loop has propagated out of the gate area and the new bubble is beginning to be propagated out of the cusp on the major loop by the attractive charged wall there.

In Fig. 5-4 we see that there is a linear increase in the upper bias margin as I_s increases above a critical value. Below this threshold, which decreases as the coercivity decreases, the failure mode was due to insufficient bubble stripeout. Since the stretching field of the hairpin is directly proportional to I_s, we expect to see linear behavior in this region and the experimental data verifies this. In the high bias field region I_s increases until the stretch current is high enough to induce spontaneous bubble nucleation in the major loop cusp. Urai et al.⁹ also described spontaneous nucleation errors, but at higher current densities than theoretically obtained. This is due in part to our relatively simple model for spontaneous nucleation. Furthermore, Urai's published margins do not include propagation failure on the minor loop, which we have taken into account in our simulations, since we assumed bubble propagation failure would also lead to replication failure. Above this threshold the high bias margin decreases rapidly with increasing I_s. At low bias, the most common failure mechanism was "uncontrolled" bubble stripeout due to high stretching current amplitudes, although successfully replicated bubbles would sometimes stripeout due to

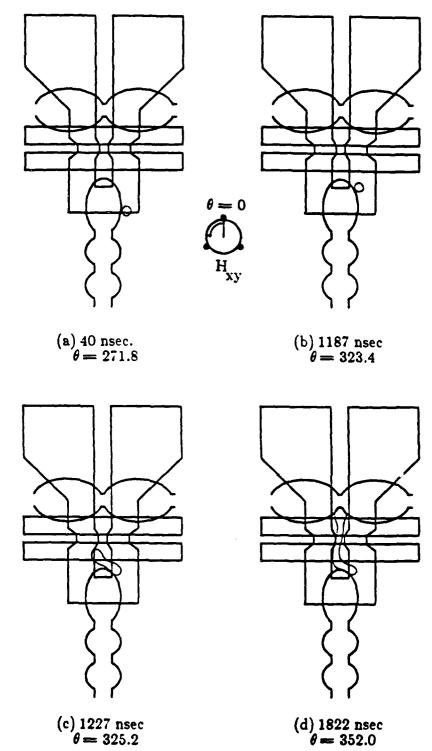
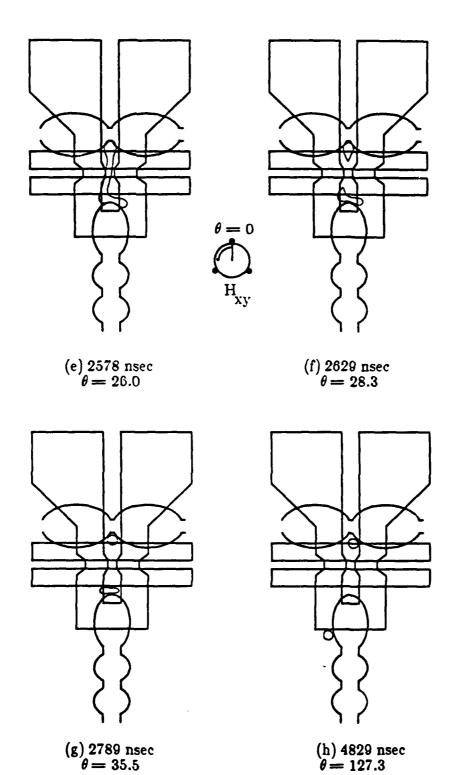


Figure 5-6: The block replicate process shown as a function of time.



Continuation of Fig. 5-6

the stray fields of the relatively long chopping pulse. We should also note that the assumed coercivity value of 2.0 Oe is probably higher than the actual experimental value; for $H_c = 0.5$ Oe we noted that the minimum stretching current decreased to 40 mA, resulting in a widening of the margins of Fig. 5-4.

In Fig. 5-7, we depict the failure that typically occurred due to insufficient stretching current, I_s . Again, the parameters for this simulation are given in Table 1 except that $I_s = 72$ mA here, and the bias field was 346 Oe. In (b) of this figure, when $\theta = 25.2$ degrees, even though the stretch pulse is still being applied to the hairpin the bubble does little more than deform elliptically. In (c) since $\theta = 36.0$ degrees the chopping current is active and at the high bias field of 346 Oe we can see that the bubble diameter is larger than in (a), when no currents were applied. However, the bubble is still rotating around the minor loop tip and by the time $\theta = 73.8$ degrees, as shown in (d), the bubble is being propagated out of the gate area. Here, even though the replication process was not successful, data integrity was maintained due to the fact that the bubble is still in its original position with respect to the rotating field.

For I_c, the chopping current, there was a threshold below which no chopping would occur, independent of bias field. Above this value, at high bias fields, the minimum chopping current increases linearly with bias field until the bubble collapse field is reached, at which point the upper margin remains constant as seen in Fig. 5-5. At low bias the margins are limited by bubble stripeout by the stretching current at low values of chopping current and for higher values of chopping current failure was due to stripeout of successfully replicated bubbles on the minor loop tip due to the stray field of the chopping conductor. This explains the linear increase in the low bias margin for values of I_c greater than 75 mA in Fig. 5-5. This problem can probably be eliminated by modification of the chopping conductor geometry.

In Fig. 5-8(a) through (f) we show the low chopping current failure that occurred at higher bias fields. Here, the $H_B = 346$ Oe and $I_c = 75$ mA. In (c) of the figure we see the successfully stretched bubble just prior to termination of the stretch pulse and the beginning of the chopping pulse, whose leading edge is at $\theta = 27$ degrees. In (d), just before termination of the stretch pulse at $\theta = 39.5$ degrees, we can see that the

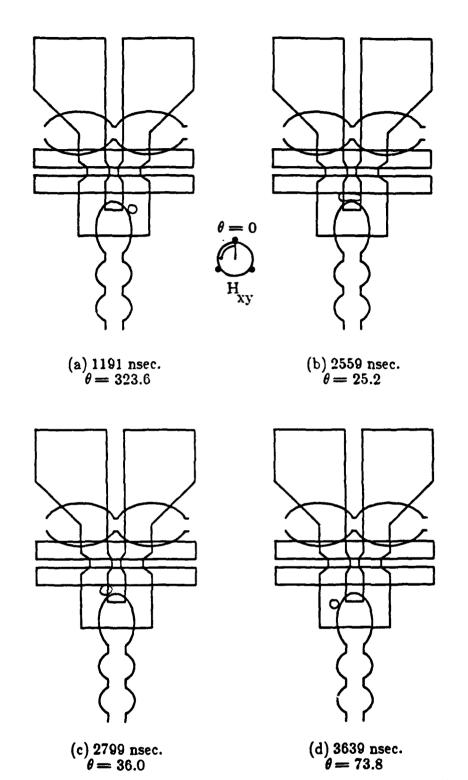


Figure 5-7: Failure mode in the block replicate process due to insufficient stretching current.

stripe has not been chopped successfully, and that the stripe head attached to the minor loop tip is being pulled by the charged wall there. In addition, there are attractive fields on the outer edges of the chopping conductor which are stabilizing the two stripeheads (note the width of the stripeheads here). However, upon cessation of the chopping pulse, at the relatively high bias field (346 Oe), the stripe quickly contracts into a bubble and becomes uncoupled from both the charged wall on the minor loop, which is propagating away from the direction of stripehead contraction, and the major loop cusp. The result is shown in (f) of the figure, where the bubble is seen uncoupled from both propagation patterns. We should point out that if the chopping pulse would have been terminated earlier in phase with respect to the drive field, the stripehead on the minor loop would have remained coupled to the charged wall on the minor loop and the stripe would have simply contracted back into a bubble on the minor loop and propagated away with the drive field.

5.2.2. Replicate Current Phase Margins

In Fig. 5-9 we show the simulated bias field vs stretching current pulse leading edge margins that were measured. Here, the stretch current pulse falling edge was held fixed at $\theta = 27$ degrees, at which point the current pulse was activated. We see that as the drive field angle approaches 355 degrees, the margins begin to decay monotonically from the high bias region; lower bias margins did not change appreciably until θ reached roughly 375 degrees, after which there was no margin.

Another important aspect of gate performance is the sensitivity of successful gate operation with respect to the relative phases of the stretching and chopping currents. In Fig. 5-10 we show the bias field margins obtained as a function of the delay between the falling edge of the stretch current pulse and the leading edge of the chopping current pulse. Here, the stretching current pulse was terminated at $\theta = 27$ degrees as denoted by the arrow, and the chopping pulse length was held fixed at 12.5 degrees. We noted in our simulations that replication was successful even if the chopping pulse was initiated prior to termination of the stretching pulse, indicating a wider range of operation than depicted here. In the figure we also show experimental data; the apparent discrepancy between the experimental and simulated margins is due to the fact that we have included propagation errors in our simulated margins

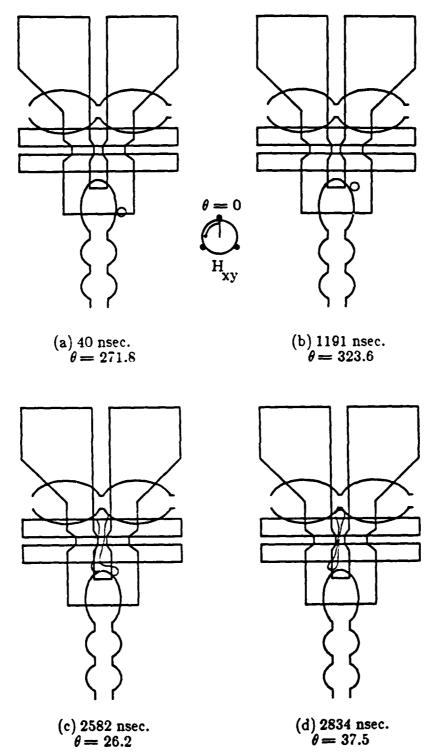
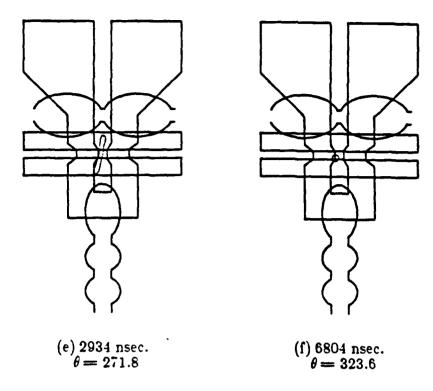


Figure 5-8: Failure mode in the block replicate process due to insufficient chopping current.



Continuation of Fig. 5-8

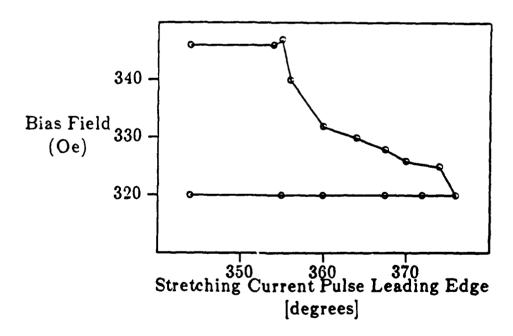


Figure 5-9: Simulated bias field vs stretching current leading edge margins for the gate depicted in Fig. 5-3. $I_s = 80 \text{ mA}$, $I_c = 100 \text{ mA}$.

which the experimental data do not take into account. This will be discussed in greater detail in the following section.

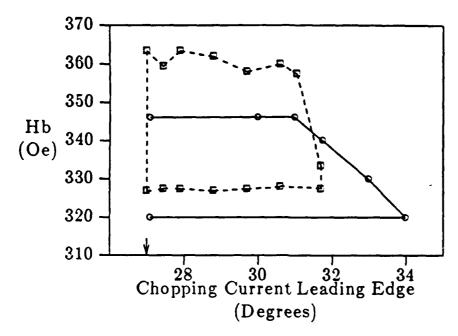


Figure 5-10: Simulated bias field vs chopping current leading edge margins for the gate depicted in Fig. 5-3, shown by the open circles. Experimental margins of Urai et al. given by open boxes. The stretching current turn-off angle, denoted by the arrow, was 27 degrees here.

In Fig. 5-10 we presented the effect of the delay between termination of the stretching pulse and the leading edge of the chopping pulse. For a stretching pulse that terminates at $\theta=27$ degrees, there is no loss in margin until the chopping current leading edge is delayed approximately 4 degrees after termination of the stretch pulse ($\theta=31$ degrees), at which point the bias margin linearly decreases. For a drive field frequency of 125 kHz, this (4 degrees) corresponds to a time delay of roughly 90 nsec. Assuming that the contracting stripe velocity at high bias reaches the saturation value of 3800 cm/sec, then the contracting stripe head will travel 3.4μ m, which is close to half the hairpin channel length of $3.5~\mu$ m, which is also the centerpoint of the chopping conductor channel. Since it is obvious that replication will fail if the stripe has contracted beyond the chopping conductor region, this indicates that our simulator model is reasonably accurate. As the chopping current

leading edge is increased further, we expect successful replication to occur at lower values of H_b , since the effective driving field on the shrinking domain wall is lower at lower bias fields, resulting in lower shrinking velocities. The experimental margins in this figure are seen to be much higher than the simulated margins at high bias fields. This is due to the fact that once again in our simulations we assumed replication would fail if bubble propagation errors occurred; the experimental margins, on the other hand, simply depict successful stretching and cutting of the bubble, independent of the propagation bias field margins, which are seen to reduce the upper bias field limits of Fig. 5-10 by over 10 Oe. The bias margins are seen to be offset by a constant factor, probably due to the difference between the actual experimental implanted layer thickness, which was unknown, and the value used in the simulations, 0.35 μ m.

In Fig. 5-11 is seen one of the errors that resulted when the delay between the falling edge of the stretching pulse and leading edge of the chopping pulse was too long. In this simulation, the stretching pulse was terminated at $\theta=27$ degrees and the chopping pulse was activated at $\theta=32.0$ degrees. Here the bias field was 346 Oe, which is near the collapse limit of the bias margin. The stripe, due to the high bias field, shrinks relatively symmetrically towards the center of the hairpin channel, and becomes uncoupled from the implanted patterns. We noted that at lower bias fields and long chopping current delays, the stretched stripehead would contract back to the minor loop and the bubble would simply propagate around the pattern. It appears that the stray fields from the chopping conductor, which stabilize the stripeheads of the expanded domain, have a pronounced impact on gate performance since they may cause uncoupling of the charged wall and bubble on the minor loop tip.

Even if the stretching current amplitude was of sufficient amplitude, we depicted in Fig. 5-9 that if the leading edge of the stretching pulse was delayed until approximately $\theta = 355$ degrees, the successful operating margins decayed at higher bias fields. Upon further scrutinity, we noted that failure occurred due to lack of bubble stripeout along the hairpin channel; the bubble typically distorted radially and then propagated around the minor loop tip. Since the falling edge of the stretching current was held fixed at 27 degrees here, there was certainly ample time for the

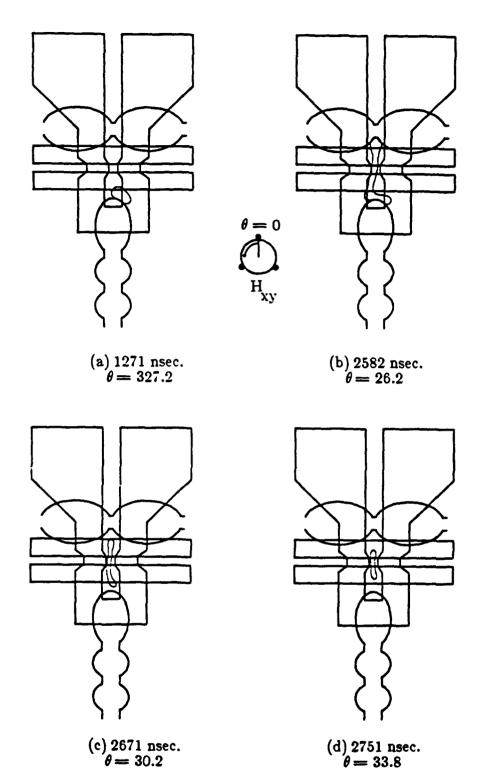


Figure 5-11: Failure mode in the block replicate process due to long delay between termination of the stretching current pulse and beginning of the chopping current pulse.

bubble to stripe out along the entire hairpin channel length which was 7μ m. A simple calculation shows that if we conservatively assume the stretching velocity is only one-half v_s , the sauration velocity, then the drive field would rotate through only 16 degrees in the time required for the expanding stripe head to travel the full hairpin channel length. This confirms independently that in these data failure is not due to insufficient stretch pulse length as the time sequence study of bubble motion here indicated.

In Fig. 5-12 we see the result of waiting until $\theta = 357$ degrees before activating the stretcher. The bubble simply distorts and rotates around the minor loop tip with the drive field. If we look at the field contours of the hairpin stretcher, which we show in Fig. 5-13, we see that possibly due to the necking down of the channel where the stretcher crosses the chopping conductor that the maximum gradient of the stretching field is not directed along the channel length, but perpendicular to it. This explains the shape of the bubble seen in Fig. 5-12(c), where the bubble has striped out parallel to the edge of the chopping conductor, even though at $\theta = 24.8$ degrees here, the chopping conductor has not been activated yet. Of course, the charged wall is assisting in the stretching process, but at such a high bias field (346 Oe here) we expect its contribution to be small. Clearly, we expect stretching to be easiest when the bubble is beneath that section of the stretcher that produces the highest bias field reduction so these results are very surprising when considered from this point of view. Actually, this unexpected behaviour has been observed in experimental devices and its causes not explained. 48 Gal et al., 49 proposed a theory which suggests the perturbing field on an expanding domain is proportional to the domain perturbation, i.e., an already elliptically distorted bubble will more easily distort elliptically than a circular domain. In Fig. 5-12(b) the domain seen is distorted radially since the initial shape of the domain as the bias field acting upon it was applied was radial. When the bias field was reduced (due to the stretcher field) the domain distorted radially since the energy of the radial domain in this case is lower than the energy of a stripe domain even below the bubble stripeout field. Now, when the stretcher is initiated earlier in phase, the bubble is still coupled to the charged wall beneath a portion of the stretch conductor which has a relatively high gradient (see Fig. 5-13). This gradient, in conjunction with the charged wall essentially "pinning" part of the expanding domain

creates an elliptical distortion which overwhelms any other domain distortion modes, such as the radial one. Once the elliptical distortion mode is initiated, the domain easily expands. Therefore, we may conclude that even if the stretching pulse is of sufficient magnitude and duration to cause bubble stripeout, the bubble should be in a high enough gradient to cause elliptical instability in order for it to stripe out.

We have just discussed the results we obtained when the stretching current pulse was delayed with respect to the rotating field, and saw that even if the I pulse was of sufficient duration and amplitude, the replicate process would fail if the stretch pulse was initiated too late in phase with respect to the drive field. We saw in Fig. 5-9 that as long as the stretch pulse was initiated prior to $\theta = 355$ degrees, the bubble would stretch out the length of the hairpin channel, independent of bias field. We therefore should not be surprised to learn that there is also a value of θ prior to which the stretch pulse should be terminated in order to achieve successful replication. Recalling that during the replicate process the drive field rotates propagating the charged wall with it, it is clear that disruption of the bubble/charged wall coupling mechanism may lead to device failure, and in Fig. 5-14 we depict such a failure. In this simulation, the stretcher current was turned on at $\theta = 350$ degrees which, as seen in Fig. 5-9, was seen to lead to successful gate operation as long as I_{z} was terminated at $\theta = 27$ degrees. In Fig. 5-14 however, the stretching pulse was terminated at $\theta = 44$ degrees and although successful replication did occur as seen in (c) of the figure, we note that by (d), in which $\theta = 119.2$ degrees, the bubble on the minor loop has become disengaged from the charged wall on the minor loop and fallen behind the drive field in phase. We can see here that the replicated bubble has been pulled from the major line cusp by the circulating charged wall there and is near an easy stripeout position on the major loop disc ($\theta = 120$ degrees). The attractive nature of this position is also reflected in the relative sizes of the two bubbles in this figure; the seed bubble at $\theta = 0$ degrees on the minor loop tip is smaller in diameter than the bubble on the major loop. Even though $\theta = 0$ is indeed an easy stripeout position, we know from the earlier discussion regarding charged wall behavior in implanted garnets that the drive field breaks up the three-fold symmetry and $\theta = 120$ degrees is the preferred stable charged wall position at this applied field value. The bubble on the minor loop tip, having lost the attractive potential well of the charged wall to which it had been

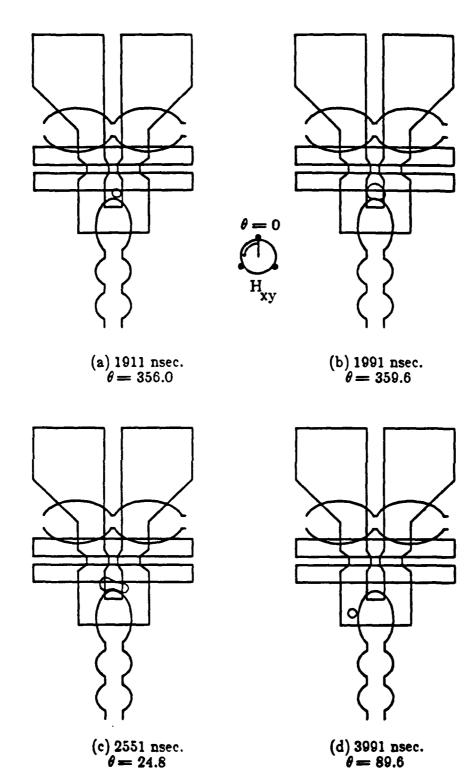


Figure 5-12: Failure mode in the block replicate process due to late stretching current pulse leading edge.

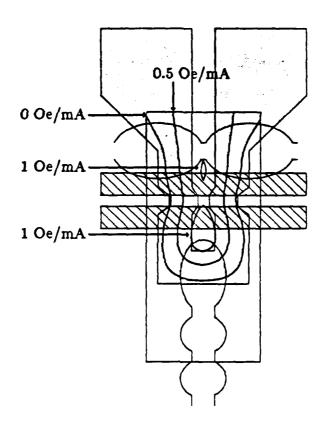


Figure 5-13: Normalized perpendicular magnetic field contours due to a current of 1 mA. in the stretching conductor. The fields are averaged over the height of the bubble film thickness.

previously coupled, feels a stronger net bias field and contracts; at high enough bias fields this bubble will collapse upon formation of a negative charged wall nearby as the drive field approaches $\theta = 180$ degrees. For this particular run the bias field was only 340 Oe and the bubble did not collapse; as the drive field circulated through 360 degrees the bubble was "picked up" by the charged wall passing through this stable position and propagated away, one full rotating field cycle behind its "correct" position. We should point out that the chopping current pulse here was begun at $\theta = 44$ degrees and terminated at $\theta = 46.4$ degrees; at an operating frequency of 125 kHz this corresponds to a pulse width of less than 53 nsec. Thus, we see that the chopping process is very rapid and accounts for only a small fraction of the time required to

implement the replicate process. In the next section, however, we will see the effect of using chopping current pulses of inadequate duration.

Even though stripe chopping is relatively rapid, there is of course a finite amount of time required to actually implement the chopping process due to the fact that the walls of the elongated stripe must be translated roughly one-half the bubble diameter before they coalesce and annihilate one another, resulting in the formation of two disconnected domains. If we assume that both parallel walls of the stripe must move towards each other a distance equal to one half the stripe-width at a velocity equal to the saturation velocity, then we may easily estimate the time required to chop the stripe. This is given as:

$$t_{c} = \frac{w}{2 v_{s} 100}, \tag{5.1}$$

where v_s is the saturation velocity of the material in cm/sec and w is the stripewidth of the material in μ m. Using the parameters given in Table 5-1, from Eqn. (5.1) we can expect that the time required to chop the stripe is on the order of 13 nsec.

We present in Fig. 5-15 the result of applying a chopping pulse of inadequate duration. The simulation parameters are given in Table 1; the chopping pulse commenced at $\theta = 27.0$ degrees and was terminated at $\theta = 27.25$ degrees. The stripe, seen in (d) of the figure, was not chopped and became disconnected from the implanted patterns. This occurred because once the chopping pulse was terminated and the stripe did not get cut, the two stripeheads contracted symmetrically towards the center of the stripe domain. If the stripe chopping process had been successful, the two resulting domains would have contracted into bubbles in similar fashion, but the stripeheads of these two domains nearest the implanted patterns might have remained coupled to these patterns and the replication process might have been successful, as we depict in Fig. 5-16. Actually, as shown in this figure, the expanded stripehead did not even reach the major loop cusp before replication was performed, but replication was still successful. In Fig. 5-16(a), we see the stripe during the chopping process; the stretching current was terminated and the chopping pulse was activated at $\theta = 10$

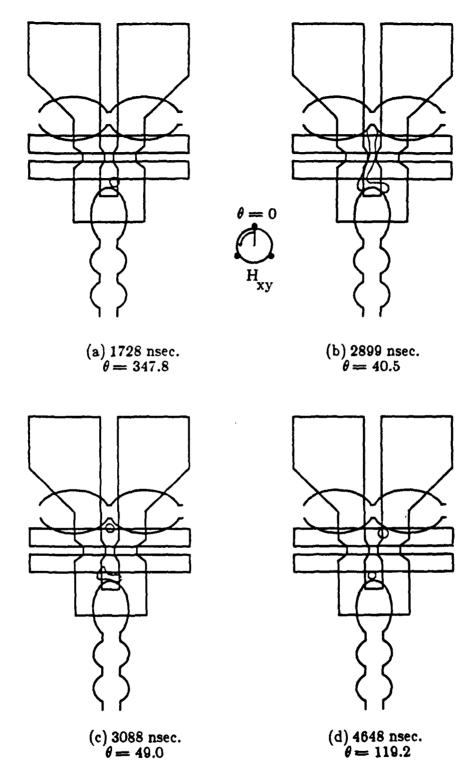


Figure 5-14: Failure mode in the block replicate process due to late stretching current pulse falling edge.

degrees while I_c was terminated at $\theta = 11$ degrees. In contrast to the situation depicted in Fig. 5-15 where the uncut stripe contracts into a bubble whose center is near the center of the hairpin, in Fig. 5-16(b) the replicated bubble, which is under the center of one of the chopping conductors, gets attracted to the major loop cusp within a few hundred nanoseconds, as seen in (d) of Fig. 5-16.

5.2.2.1. High Coercivity Failure

One of the parameters that can be varied to ascertain its effect on device performance is coercivity. In Fig. 5-17, we show the effect of increasing coercivity on the minimum stretching current needed to achieve successful propagation for two different values of bias field which were chosen since these values, 320 Oe and 346 Oe, are near the low and high bias field limits, respectively.

The failure that occurred due to high coercivity in seen in Fig. 5-18, and is very similar to the one that occurred when the stretching current density was too low, as was depicted in Fig. 5-7. For a given coercivity, there is a critical stretching current below which domain stretching will not take place, and this critical current increases as the bias field increases. For a constant bias field, we also saw that the critical stretching current increases linearly with the coercivity. Therefore, the failure depicted in Fig. 5-18 could also be attributed to insufficient stretch current, and not just high coercivity. In short, both low stretching current and high wall coercivity will both contribute to replication failure and a combination of the two will most certainly result in failure.

5.2.2.2. Replicate-In Mode

The block replicate gate under discussion here was also observed in simulation to work in the replicate-in mode, although it was not specifically designed for this purpose. This process involves replication of bubbles on the major loop as they are transferred into the minor loops, and the result of one such simulation is shown in Fig. 5-19. Here, the stretch current was activated at $\theta = 250$ degrees when the major loop bubble was near the stable position at $\theta = 240$ degrees, and it was terminated at 350 degrees.

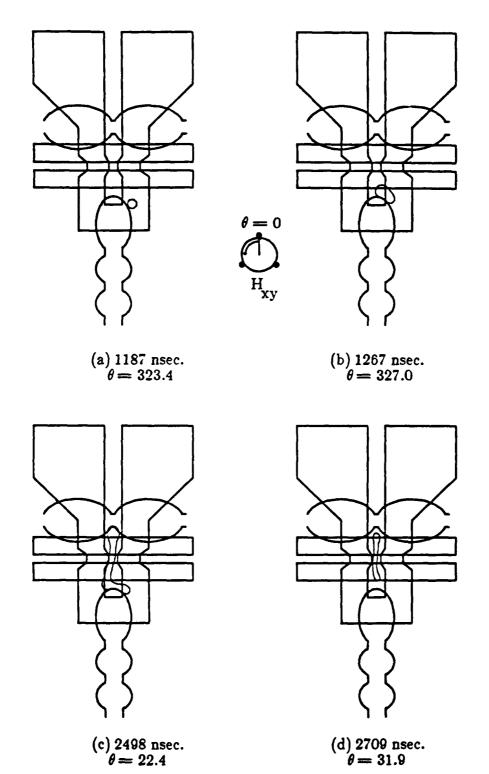


Figure 5-15: Failure in the block replicate process due to short chopping pulse.

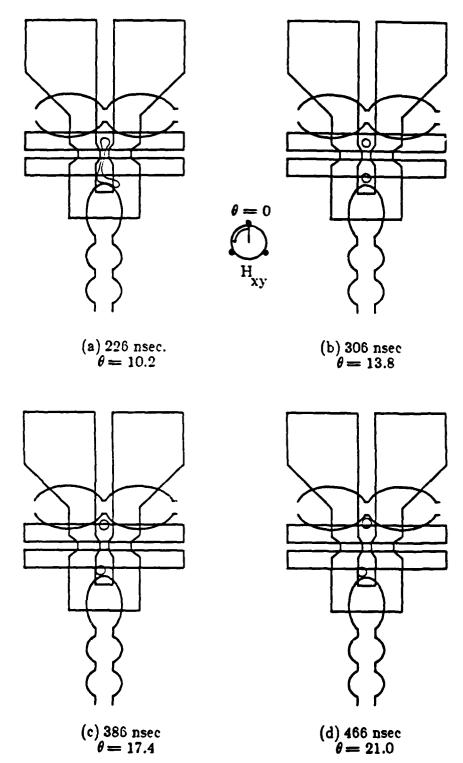


Figure 5-16: Successful replication even though short stretching pulse duration prevented the expanding stripehead from reaching the major loop cusp prior to activation of the chopping conductor.

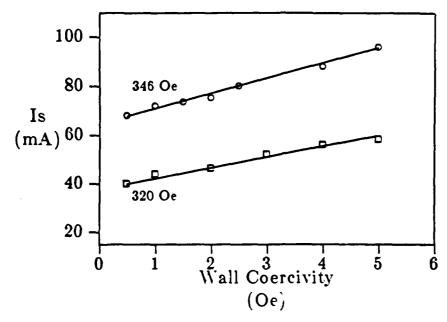


Figure 5-17: Effect of coercivity on minimum stretching current required for successful replication in the gate Fig. 5-3. Squares denote current margin at a bias field of 346 Oe, circles give margin at 320 Oe bias field. $I_c = 100 \text{ mA}$ for both sets of data.

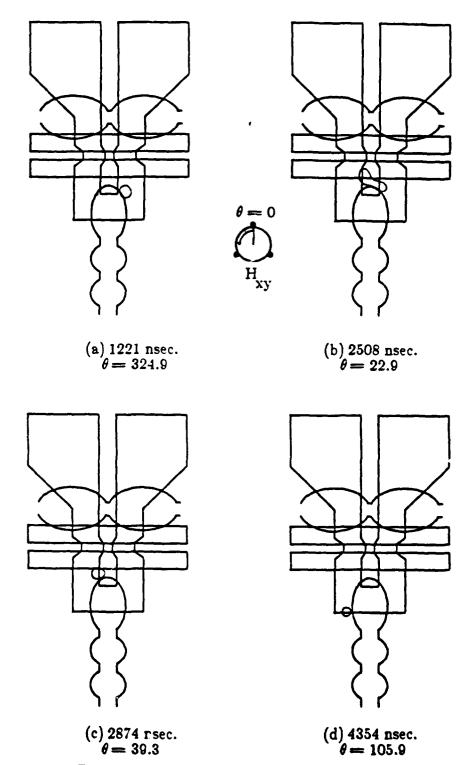


Figure 5-18: Failure mode in the block replicate process due to high coercivity. The assumed value of $H_{\rm c}$ was 3.5 Oe here.

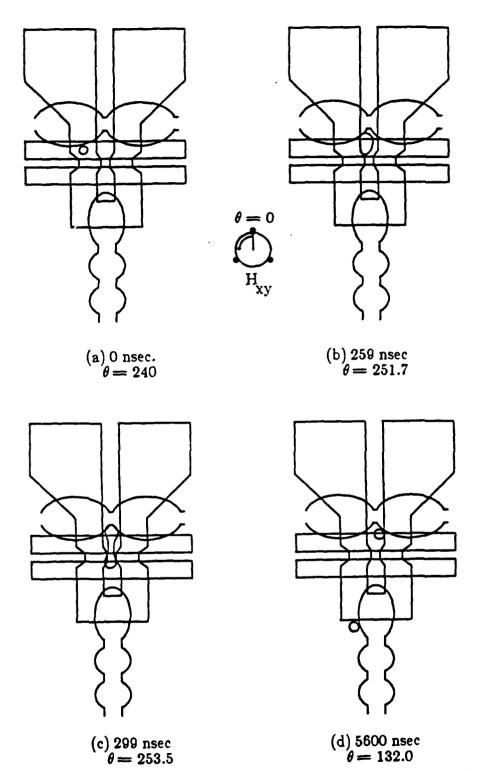


Figure 5-19: Operation of the block replicate gate in the replicate-in mode.

5.3. The Dual Gate

5.3.1. Introduction

In Chapter 1 of this thesis, a design for a combined block replicate and pseudo-swap gate was presented and the operation of the gate in both of these modes explained. The gate was depicted in Fig. 1-13 and is used to either block replicate minor loop data in much the same fashion as the NEC block replicate gate studied in this chapter or erase minor loop data followed by replicate-in of major loop data. This latter function was termed "pseudo-swap" by the inventors of the gate. 13, 14 Both the replicate function and the pseudo-swap function as performed by this design were simulated and the simulated processes are presented below.

5.3.2. The Replication Process

The replicate process as performed by the dual gate is essentially the same as the process that is performed by the NEC block replicate gate, but the conductors of the gates vary in geometry. The dual gate is reproduced in Fig. 5-20.

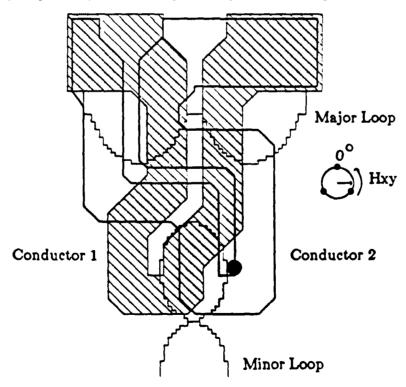


Figure 5-20: Dual gate design that was described in the Introduction.

The parameters that were used to simulate the replicate process as performed by the dual gate are given in Table 5-2, and the replicate process as performed by the simulator is shown in Fig. 5-21. As was done for other replication processes previously presented, the simulation was initiated by placing the bubble on the minor loop pattern and then propagating the bubble into the gate area, followed by pulsing the stretching conductor [the hatched pattern of Fig. 5-21]. Although, as noted in Table 5-2, the stretch pulse was initiated at $\theta = 345$ degrees we see in Fig. 5-21[c] that even at $\theta = 360.9$ degrees that the bubble is just beginning to stretch. In general, it was noted for this gate design that the bubble stretch process was difficult to initiate, and once initiated bubble stripe-out was usually uncontrollable and would lead to stripe-out errors. Of course, this error mode is a function of bias field, stretching current pulse width, pulse amplitude, and stretch pulse leading edge with respect to the phase of the drive field. Although full margins of this gate design have not been simulated at this point in time, preliminary simulations suggest that the bias field vs stretching current margins of the gate may not be very wide.

Table 5-2: Parameters used to simulate the block replicate function as performed by the dual gate of Fig. 5-20.

$4\pi M_s$	650 G
$H_{\mathbf{k}}$	1750 Oe
1	0.12 μm
t	1.1 μm
w	1.1 μm
H _c	1.0 Oe
$\mu_{\mathbf{w}}$	300 cm/sec-Oe
v _s	3800 cm/sec
ſ	100 kHz
H _{xy}	70 Oe
Is	59 mA
I _c	160 mA
$\theta_{\mathtt{sl}}$	345 Degrees
$\theta_{\mathbf{s}2}$	25 Degrees
θ_{c1}	25 Degrees
θ_{c2}	40.0 Degrees
t ₁	0.6 μm
t ₂	0.40 μm
^t d	0.35 μm
	l t w H _c \(\mu_w \) V _s f H _{xy} I _s I _c \(\theta_{s1} \(\theta_{s2} \) \(\theta_{c1} \) \(\theta_{c2} \) t 1 t 2

5.3 3. The Pseudo-Swap Function

The pseudo-swap function is the only function studied in this thesis that requires the use of three current pulses. The first pulse is used to collapse minor loop bubbles and the following pulses are used to implement a replicate-in function in which major loop bubbles are replicated into the minor loops. The function was depicted in the

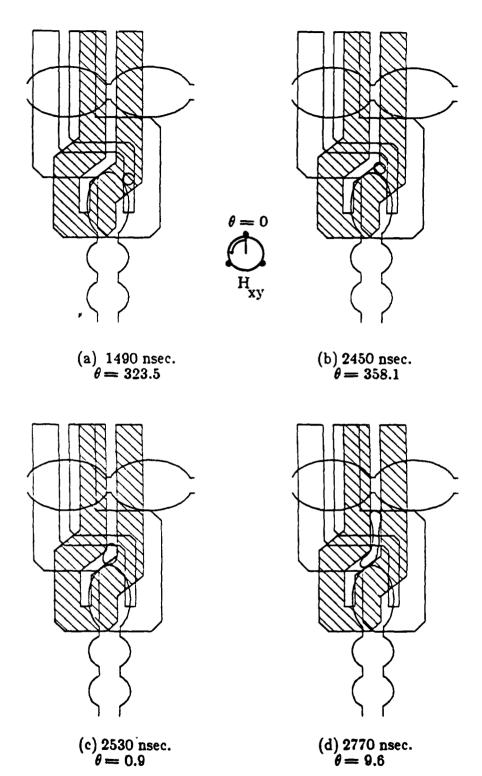
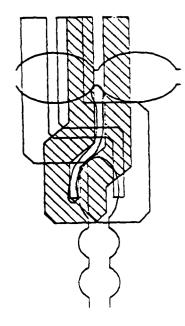
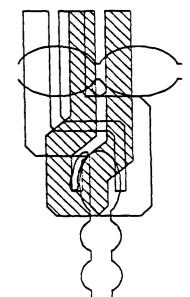


Figure 5-21: Simulated replication process as performed by the dual gate. 13, 14

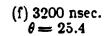
Parameters used in the simulation given in Table 5-2.

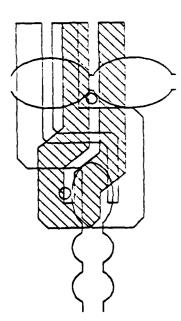






(e) 2950 nsec. $\theta = 16.1$





(g) 4860 nsec. $\theta = 85.0$

Continuation of Fig. 5-21

Introduction; for the reader's convenience we reproduce here the current phases required to implement the pseudo-swap function in Fig. 5-22. The parameters used to simulate the pseudo-swap function are given in Table 5-3.

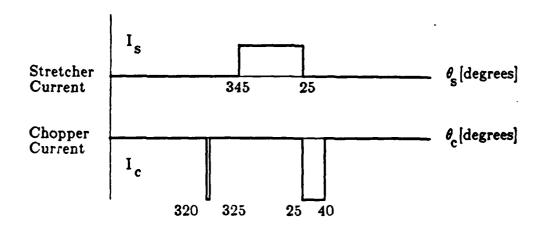


Figure 5-22: Annihilation, stretching, and chopping current phases required for implementation of the simulated pseudo-swap function depicted in Fig. 5-23.

The first pulse activated in the pseudo-swap process is the annihilation pulse and the annihilation current is applied by the chopping conductor as seen in Fig. 5-22. Since bubble collapse can be performed relatively quickly, this pulse need not be very wide when compared to the stretching pulse, but its position with respect to the bubble position should be important since the bubble should be in the vicinity of the maximum annihilation field in order to collapse the bubble. Although the amplitudes of the annihilation and chopping pulses are not equal as depicted in Fig. 5-22, we shall show a simulation of the pseudo-swap process that was performed using the same current amplitudes for these two functions.

Table 5-3: Parameters used to simulate the pseudo-swap function as performed by the dual gate of Fig. 5-20.

Magnetization	$4\pi M_s$	650 G
Anisotropy field	H _k	175∪ Oe
Characteristic length	1	0.12 μm
Bubble film thickness	t	1.1 μm
Stripe width	w	1.1 μm
Wall Coercivity	H _c	1.0 Oe
Bubble mobility	$\mu_{\mathbf{w}}$	300 cm/sec-Oe
Saturation velocity	v _s	3800 cm/sec
Operating frequency	f	100 kHz
Drive Field	H _{xy}	70 Oe
Annihilation Current	Ia	160 mA
Stretcher Current	Is	59 mA
Chopper Current	I _c	160 mA
Ia Pulse Leading Edge	θ_{a1}	320 Degrees
Ia Pulse Falling Edge	θ_{a2}	325 Degrees
l ₁ Pulse Leading Edge	θ_{s1}	345 Degrees
I ₁ Pulse Falling Edge	$\theta_{\mathtt{s}2}$	25 Degrees
I2 Pulse Leading Edge	θ_{c1}	25 Degrees
I2 Pulse Falling Edge	θ_{c2}	40.0 Degrees
Stretcher thickness	t ₁	0.6 μm
Chopper thickness	t ₂	0.40 μm
Implantation depth	td	0.35 μm

The pseudo-swap function as performed by the simulator is depicted in Fig. 5-23. The parameters used for this simulation are given in Table 5-3. We note that the current amplitude for both the annihilation and chopping processes are the same. The

simulation begins with a bubble in the minor loop and a bubble on the major loop as depicted in Fig. 5-23(a) where the drive field is oriented with $\theta = 240$ degrees. When the drive field angle equals 320 degrees, the annihilation pulse is activated, resulting in collapse of the bubble on the minor loop as depicted by the asterisk, *, seen in Fig. 5-23(c). The asterisk actually denotes the coordinates of the bubble center at collapse. Following collapse of the minor loop bubble, the major loop bubble is stretched and chopped (Fig. 5-23(d), (e), and (f)) to complete the pseudo-swap process.

5.4. Summary

The purpose of this chapter was to demonstrate the power and utility of the gate simulator that was developed in the course of this research. The most complex gate that has been proposed for ion-implanted devices, namely the block replicate gate studied in detail here has been successfully simulated, the simulated margins agree well with published experimental margins, and the nature of the gate's failure modes have been studied by scrutinizing wall motion during the replicate process. It should be noted that during the course of the block replicate gate simulations described in this chapter the field contribution of the charged wall was periodically excluded during the replicate process. Then, the result of the simulated replicate process without the charged wall was compared to the simulated replicate process in which the charged wall field was included. Never was an appreciable difference found between the two simulations. Thus, it may be concluded that the simple charged wall model used in this work will not detract from the accuracy of the replicate process simulation. Actually, since the polarity of the in-plane field from the stretching conductor is such as to weaken the charged wall strength it is possible that the simulations performed without the charged wall contribution may be more accurate than those performed that include the charged wall field. In any case, there is not much discrepancy between the two.

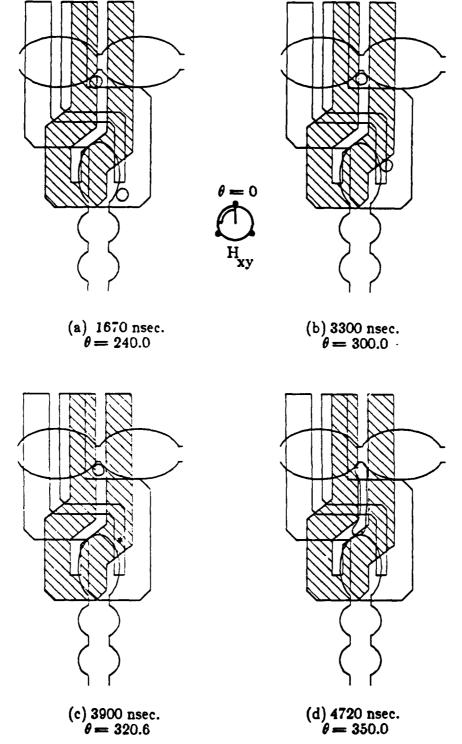
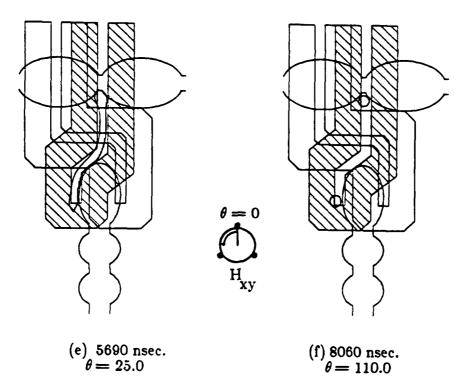


Figure 5-23: Simulated pseudo-swap process as performed by the dual gate. 13, 14

Parameters used in the simulation given in Table 5-3. Asterisk, *, in

(c) of the figure denotes location of the bubble center at collapse.



Continuation of Fig. 5-23.

Chapter 6

New Swap Gate Design and Simulation

6.1. Introduction

The previous chapters were concerned with using a computer simulator to simulate the operation of existing ion-implanted bubble device gates; simulated margins were then compared with experimental margins where possible. Having verified that the simulator can accurately model these gates, it is now possible to design new devices (or improve current device designs) and have confidence in the simulated results. Here, the simulator is used to design a new gate for ion-implanted devices.

In the Introduction to this thesis, an ion-implanted device gate was introduced that was called a "dual gate". Refering back to Fig. 1-14 in which the "pseudo-swap" function is illustrated, it is seen that this process does not actually swap minor loop data with major loop data. Essentially, the process simply replicates-in major loop data into the minor loops following erasure of minor loop data. If future ion-implanted devices must utilize the dual conductor block replicate gate of the type thoroughly simulated in the previous chapter, then a dual conductor true swap gate is a necessary gate to implement and there would be no additional fabrication complexity. Therefore, an attempt was made to design a swap gate that would actually exchange minor loop data and major loop data simultaneously, as is done in permalloy devices as was described in the Introduction. To the author's knowledge, the only other swap gate design for ion-implanted devices to date required impractical drive field rotation reversal in order to implement the swap process. So

6.2. Swap Gate Design

6.2.1. Gate Geometry

Through thorough study of the block replicate gate as was performed in the previous chapter, one notes that bubbles can be stretched in a relatively controlled fashion along the channels of current carrying "hairpin", or parallel conductors. Furthermore, the trapping transfer gate was seen to "disengage" or uncouple a bubble from its driving charged wall while requiring only a modicum of gate current. Based upon these observations, an attempt was made to design a swap gate that utilized "controlled" bubble stretching and "charged wall disengagement" to implement the transfer p ocess, and the first gate design of this type is depicted in Fig. 6-1. In this figure, the shaded conductor is essentially a pair of hairpin conductors, both of which bridge the minor and major loops. The second conductor level, shown as hatched, partially overlaps the shaded conductor, connects to the major loop on the right hand side of the shaded conductor level and to the minor loop on the left hand side of the shaded conductor. Operation of this gate is described in the following section.

6.2.2. New Swap Gate Operation

In Fig. 6-2 the conceptual operation of the gate shown in Fig. 6-1 is depicted. Two bubbles, one on the major loop at position A and one on the minor loop in the vicinity of position B are shown as black circles in Fig. 6-2[a], and are propagating under the influence of the rotating drive field. The goal of the swap operation is to exchange the positions of these two bubbles. [The most complex swap operation, depicted here, is the case where it is desired to swap two bubbles, that is, a logical "1" is to be swapped with another logical "1". In general, there may be zero, one, or two bubbles to be swapped depending on the actual data streams to be exchanged.] In the absence of any applied currents in Conductor 1 or Conductor 2 the bubbles will simply propagate and each bubble will remain on its respective propagation loop. However, as seen in Fig. 6-2[b] when a current I₁ is applied to Conductor 1, the bubbles will elongate into stripe domains due to the influence of the magnetic field created by current I₁. It is seen that the bubble at A has elongated into a stripe domain that extends to A' and that the bubble at position B stretches to position B'. At this point

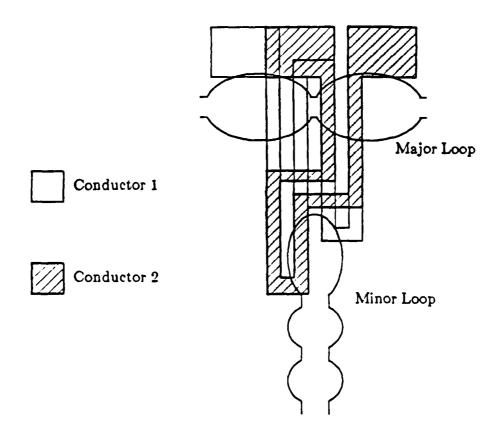


Figure 6-1: New swap gate design for ion-implanted devices. The shaded conductor is a pair of parallel stretching hairpin conductors. The hatched second level conductor is used to shift elongated domains to the nearest implanted pattern.

in time current I_1 is terminated and the current through Conductor 2, I_2 is activated. Due to the magnetic field created by current I_2 , the elongated stripe A-A' becomes detached from position A and elongated stripe B-B' becomes detached from position B as seen in Fig. 6-2[c]. Upon termination of current I_2 , the elongated stripes shrink back into bubble domains at the new positions A' and B' as depicted in Fig. 6-2[d]. The result of this sequence of currents is that the bubbles originally at positions A and B seen in Fig. 6-2[a] are now transferred to positions A' and B' respectively, having undergone the swap operation.

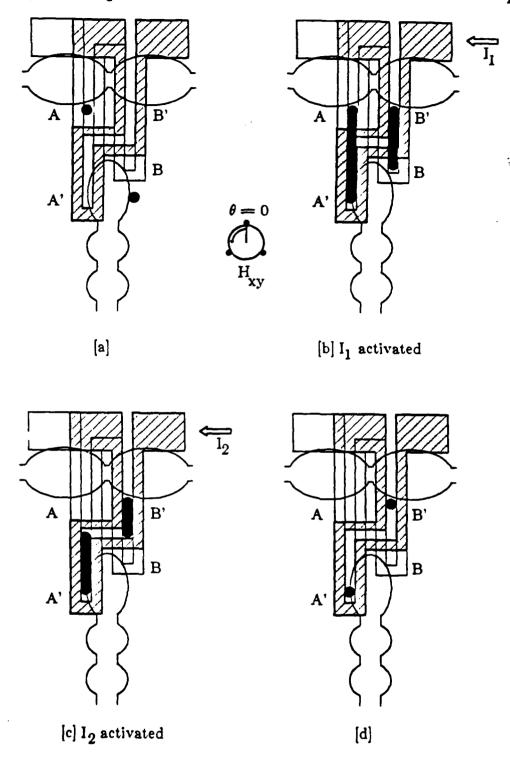


Figure 6-2: Swap operation as performed by the gate depicted in Fig. 6-1. Bubbles at positions A and B are simultaneously transferred to positions A' and B' respectively.

6.3. Swap Gate Simulation

6.3.1. The Simulated Swap Process

As was done for the other gates described in this thesis, the swap gate was simulated in order to ascertain its margins of operation. Unlike the other gates studied and whose failure or successful operation was easy to ascertain since only one bubble at a time was either transferred or replicated (or not), the swap process may be performed on either only one bubble (in either of two initial positions) or two bubbles (in both of two initial positions). In other words, referring back to Fig. 6-2 we see that in order to obtain full gate operation margins we have to ascertain the margins for: 1) Bubble transfer from A to A', 2) Bubble transfer from B to B', and 3) Simultaneous bubble transfer from A to A' and B to B'.

An actual simulated result of the swap gate operation described in Fig. 6-2 is depicted in Fig. 6-3. Parameters for this simulation are given in Table 6-1. In Fig. 6-3(a) we see the two domains, one on the minor loop and the other on the major loop near the beginning of the conductor 1 pulse, which causes the two domains to bridge the major and minor loops. In (b) of this figure it is seen that indeed both domains have bridged the major and minor loops via the hairpin channels. In Fig. 6-3(c), after termination of the second conductor pulse the domains are seen to contract and by (d) of the same figure the bubbles are coupled to the implanted patterns. The bubble originally in the major loop is now in the minor loop and vice versa.

As seen in Fig. 6-3(c), during contraction the two bubbles become disengaged from their respective propagation patterns and are essentially "free" until they couple to a passing charged wall. It was seen during initial simulations at relatively high drive fields (70 Oe) that the bubble being transferred from the minor loop to the major loop (the bubble on the right-hand-side of Fig. 6-3) would not couple to the charged wall on the major loop and remained "stranded" between the minor and major loops. This occurred when only one bubble was used in the simulation. When two bubbles were being swapped their mutual repulsive force insured that the bubbles would separate and be driven closer to their new positions on the implanted patterns. Thus, the use of only one bubble in performing the simulations implied the worst case condition in

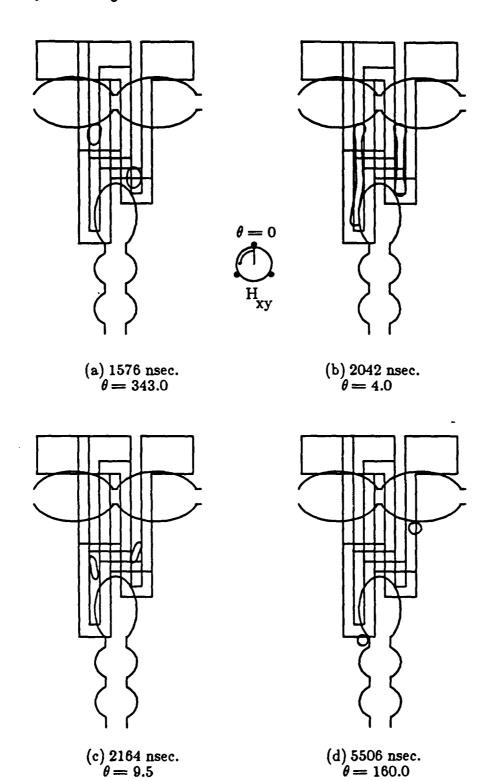


Figure 6-3: Actual simulation of the swap function as performed by the simulator described in this thesis. Nominal simulation parameters are given in Table 6-1.

obtaining the gate margins. This also led to the use of low drive fields in simulating gate operation because at low drive fields the charged wall length is greater than at high drive fields. Optimization of gate geometry should relax this low drive field constraint.

6.3.2. Simulated Gate Current Margins

One of the most important parameters used to characterize gate performance is the bias field vs current amplitude margins. Using the computer simulator the bias field vs current amplitude margins for the gate of Fig. 6-1 were obtained and the results are given in Fig. 6-4 and Fig. 6-5 for currents l_1 and l_2 , respectively. The other nominal parameters used in the simulation to obtain these margins are given in Table 6-1. The material was assumed to be anisotropic here, that is, the drive field-charged wall relationship used in the simulations is that given in Fig. 2-22. In obtaining the data presented in both Fig. 6-4 and Fig. 6-5 successful gate operation was defined as the successful transfer of two bubbles; one bubble was transferred from the minor loop to the major loop and the other bubble was transferred from the major loop to the minor loop. The use of a single bubble was explained above as being the worst case in the swap operation due to the transfer-enhancing effect of bubble-bubble interaction, so gate margins presented here are the mutual overlapping margins of single bubble swapping margins (swap-in and swap-out).

For Fig. 6-4, the upper bias field margin was limited by lack of bubble stripeout. In particular, it was seen that the bubble at position A of Fig. 6-2 would not stripe out at currents that would stripe out the bubble at position B. The asymmetry in the ability to cause the two bubbles to stripeout is due to the asymmetry in the geometry of the stretching conductors. At low bias fields, the margin was limited by the uncontrollable stretching of the bubble at position B. The bias field margins of Fig. 6-5 are due completely to the bubble at position B of Fig. 6-2, that is, the bubble at A of this figure was seen to transfer successfully at all bias fields between stripeout and collapse when I₂ was equal to zero. However, the bubble at B would not transfer at higher bias fields unless I₂ was increased up to about 65 mA, beyond which the margin was limited by bubble collapse. The lower margin was restricted by stripeout of either bubble.

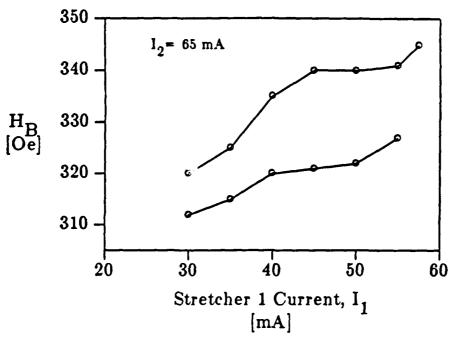


Figure 6-4: Simulated bias field vs Conductor 1 current I_1 margins for the swap gate described in this disclosure. Conductor 2 current $I_2 = 65$ mA here; other parameters are given in Table 6-1.

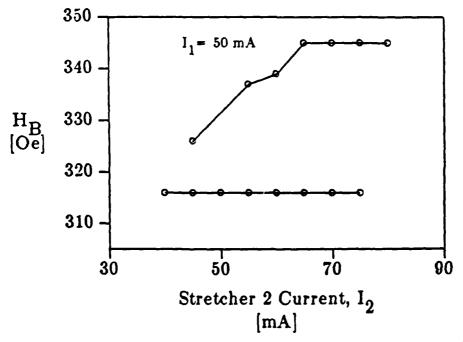


Figure 6-5: Simulated bias field vs Conductor 2 current I_2 margins for the swap gate described in this disclosure. Conductor 1 current $I_1 = 50$ mA here; other parameters are given in Table 6-1.

Table 6-1: Nominal swap gate simulation parameters.

Magnetization	$4\pi M_s$	650 G
Anisotropy field	H _k	1750 Oe
Characteristic length	l i	0.12 μm
Bubble film thickness	t	1.1 μm
Stripe width	w	1.1 μm
Wall Coercivity	H _e	1.0 Oe
Bubble mobility	$\mu_{\mathbf{w}}$	300 cm/sec-Oe
Saturation velocity	v _s	3800 cm/sec
Operating frequency	ı	125 kHz
Drive Field	H _{xy}	40 Oe
Conductor 1 Current	1,	50 mA
Conductor 2 Current	12	65 mA
I ₁ Pulse Leading Edge	θ_{11}	340 Degrees
11 Pulse Falling Edge	θ_{1f}	5 Degrees
I ₂ Pulse Leading Edge	θ_{2l}	5 Degrees
I ₂ Pulse Falling Edge	θ _{2f}	10 Degrees
Conductor 1 thickness	t ₁	0.6 µm
Conductor 2 thickness	t ₂	0.40 μm
Implantation depth	^t d	0.35 µm

6.3.3. Single Bubble Swap Gate Operation

Although the gate introduced and described in this chapter was designed to be a true swap gate, the gate was also seen to operate as a bi-directional transfer gate. Below, both transfer-in and transfer-out modes are depicted. Unlike the A.T.&T. trapping transfer gate that was studied in Chapter 4, the transfer mode of this gate does not utilize bubble trapping. Instead, the bubble is first elongated and allowed to contract; the displaced bubble then couples to a passing charged wall on the

propagation track it is desired to transfer the bubble to. Suprisingly enough, it was found that by judicious selection of the phase of I₁, the transfer process could be implemented without the use of any current in conductor 2. Although complete margins were not taken for single conductor level transfer operations, certain trends and failure modes were noted and depicted below.

6.3.3.1. Transfer-In

This operation was easily performed with only one conductor level current and it is depicted in Fig. 6-6. The current I_1 was terminated at $\theta=5.0$ degrees and the bubble is seen to be never more than one bubble diameter from the minor loop tip and the strong charged wall position in the area of the tip. The bubble relatively quickly couples to the charged wall on the minor loop and propagates away. Compared to the A.T.&T. trapping transfer gate of Chapter 4 in which the trapping current was applied for on the order of 180 degrees, here the transfer current need be applied for only roughly 30 degrees.

The effect of delaying the falling edge of the current pulse is depicted in Fig. 6-7. Here I_1 was terminated at $\theta=85$ degrees and the contracted bubble has not engaged the charged wall that it should have coupled to. In Fig. 6-7(f) since the drive field is oriented to $\theta=121.5$ degrees the charged wall is at approximately $\theta=120$ degrees ($\theta=120$ degrees is an easy stripeout position) while the bubble is still not coupled to the minor loop. The use of current I_2 would help relieve this problem but there is of course a maximum delay beyond which the bubble will not be able to couple to the charged wall. One possible solution to widening this phase delay margin would be to elongate the hairpin channel so that when the bubble contracts upon termination of current I_1 the charged wall to which it should couple is in the vicinity of the bubble.

6.3.3.2. Transfer-Out

The transfer-out function is depicted in Fig. 6-8; I_1 was activated at $\theta = 350$ degrees and terminated at $\theta = 85$ degrees. In this figure it is very easy to see how the bubble being transferred remains uncoupled from any implanted patterns for a relatively long period of time and must await the passage of a charged wall before it is transferred (see Fig. 6-8(e) and (f)). A current in the second level conductor or the presence of another bubble would enhance the transfer process as was explained earlier in this chapter.

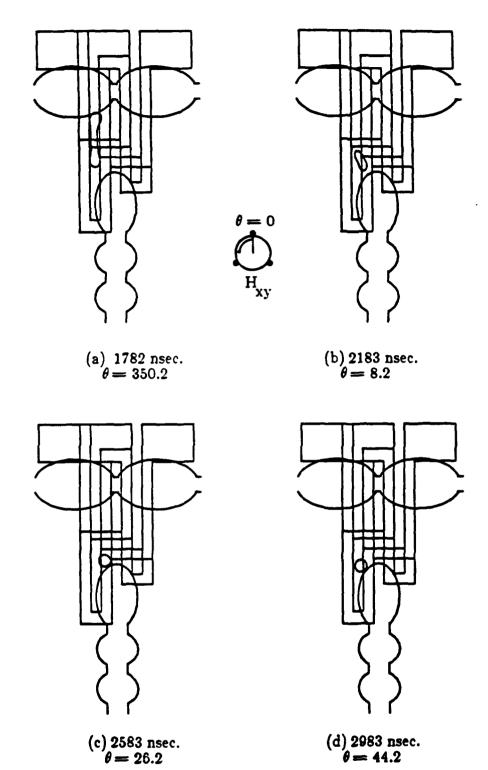
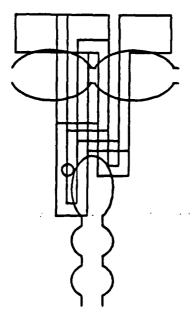
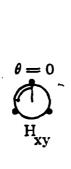
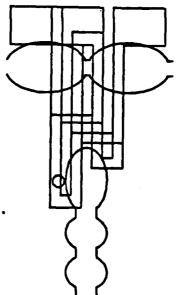


Figure 6-6: Actual simulation of the transfer-in function as performed by the simulator described in this thesis. Nominal simulation parameters are given in Table 6-1, except that $l_2 = 0$ here.

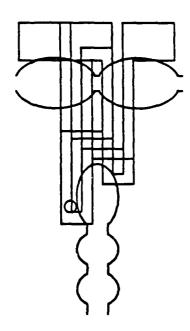


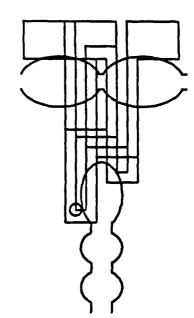




(e) 3543 nsec. $\theta = 69.4$

(f) 3943 nsec. $\theta = 87.4$





(g) 4343 nsec. $\theta = 105.4$

(h) 4743 nsec. $\theta = 123.4$

Continuation of Fig. 6-6

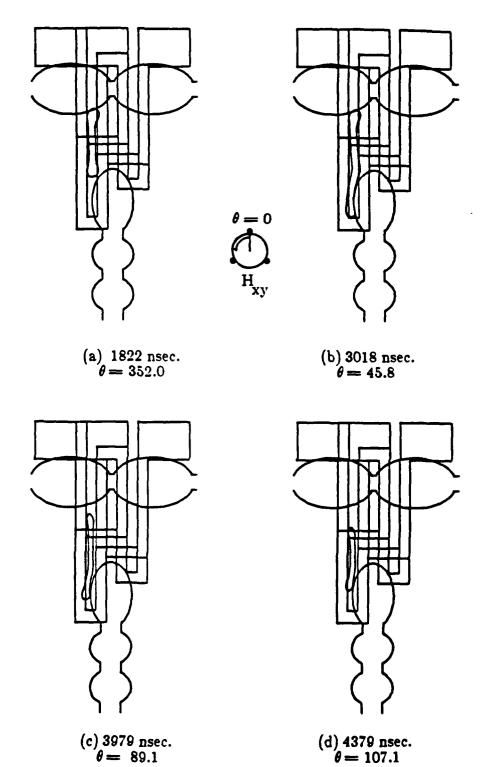
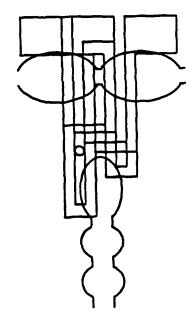
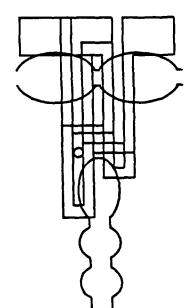


Figure 6-7: Error in the transfer-in process due to long current pulse delay.

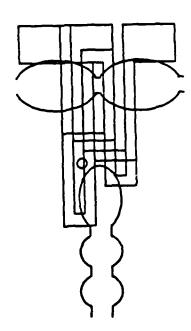




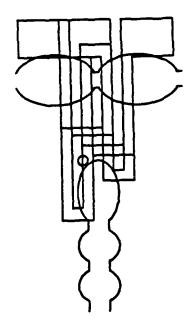


(e) 4539 nsec. $\theta = 114.3$

(f) 4699 nsec. $\theta = 121.5$



(g) 4869 nsec. $\theta = 129.1$



(h) 8021 nsec. $\theta = 270.9$

Continuation of Fig. 6-7

Finally, we show the effect of a long transfer pulse on the transfer-out process. For the simulation depicted in Fig. 6-9 I_1 was started at $\theta = 340$ degrees and terminated at $\theta = 180$ degrees. Although the bubble has stretched and coupled to the major loop, the passing charged wall on the major loop has not been able to attract the bubble, which is seen propagating backwards towards the major loop cusp (Fig. 6-9(c)) and is one rotating field cycle behind the phase of the drive field.

6.4. Summary

In this chapter, a novel swap gate design was introduced and simulated. Its performance, even without optimization, has been shown to be on the order of other ion-implanted gates such as the block replicate gate of Chapter 5. Since the swap function has never been implemented in such fashion as introduced here, its utilization, in conjunction with the dual-conductor block replicate gate should lead to the deployment of an all-ion-implanted bubble device.

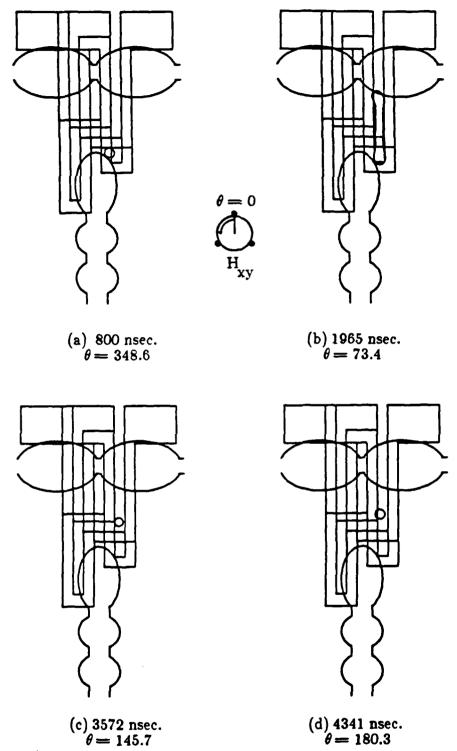
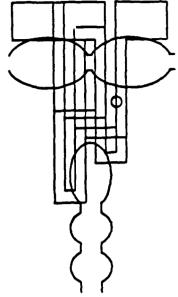
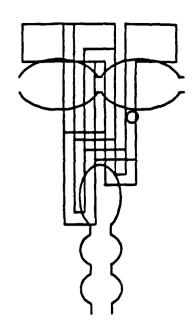


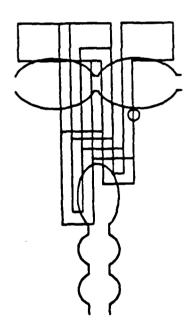
Figure 6-8: Actual simulation of the transfer-out function as performed by the simulator described in this thesis. Nominal simulation parameters are given in Table 6-1, but $I_2=0$ here.



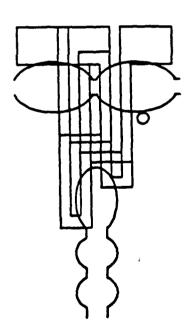
(e) 4501 nsec. θ = 187.5



(f) 4581 nsec. $\theta = 191.1$



(g) 4661 nsec. $\theta = 194.7$



(h) 4821 nsec. $\theta = 201.9$

Continuation of Fig. 6-8

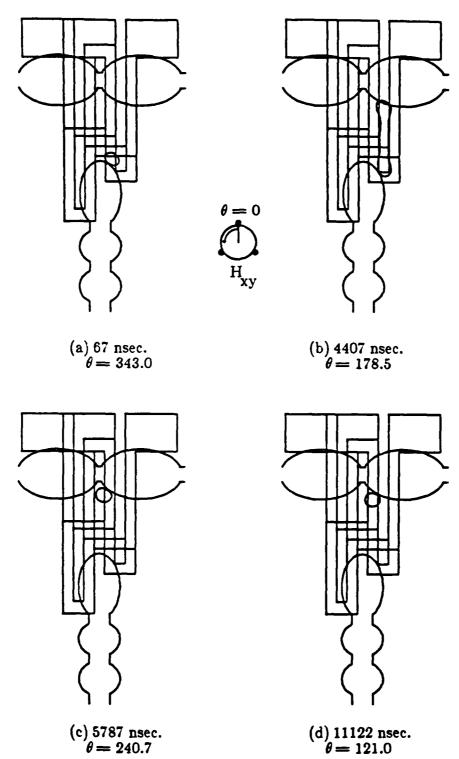


Figure 6-9: Error in the transfer-out process due to long I₁ current pulse.

Chapter 7 Conclusions

7.1. Contributions of This Thesis

In this thesis, a simulator devised to predict the operation of current-activated magnetic bubble gates for ion-implanted devices was introduced. To the knowledge of the author, there has been no report of this type of work being performed to date. Due to the way the simulator has been configured, independent fields arising from different sources are computed independently; this "modular" approach allows design variations and iterations in gate design to be performed with minimum cycle time. Furthermore, parameters that one would like to study independently can truly be varied independently of each other and their impact on gate performance studied. Although not always possible in actual devices, this approach may assist in helping design or analyze a device by keeping certain parameters fixed while others are varied to study the effects of these variations without complicated interactions that may obscure the results or their interpretation. In this thesis for example, certain gate parameters were simulated and compared for an actual bubble material and an assumed "ideal" istropic material. Finally, since the simulator utilizes fields from various sources to compute domain wall motion, there is no reason why it can not be used for current-access, permalloy, and hybrid devices as long as the fields from these propagation elements can be first computed.

A simple model for bubble motion on an unimplanted disc was modified and extended to predict bubble behavior on contiguous disc propagation patterns. Although just devised as a simple method for introducing a bubble into a gate area in order to test gate operation, it was found that simulated bubble behavior on the implanted tracks was very close to experimental margins. Particularly interesting and completely unexpected was the simulation of experimentally observed propagation

errors due to bubbles being trapped in minor loop cusps. In addition, bubble collapse and stripeout errors during propagation were predicted. As is well known, bubble collapse in ion-implanted devices typically occurs in the cusps or tips of the propagation tracks, and both of these modes were observed in the simulations. Simulated propagation margins were seen to correspond very well with experimental margins with only a static offset in bias field being the difference between experimental and simulated margins. This offset is attributed to the difference in implanted layer depth in the experimental devices, which is unknown, and the assumed value used in the simulations.

The simulator was used to predict the margins of both bi-directional trapping transfer gates using one conductor level and a block replicate gate that utilizes two independent conductor levels. In the latter gate, one conductor stretched the bubble whilst the second conductor chopped the elongated stripe in half. For both gates the simulated margins were compared and seen to agree favorably with experimental margins. Where the simulated margins did not agree very closely with experimental margins it at least predicted trends in the experimental margins. In addition, the block replicate gate design, through modification of the stretching and chopping current phases, was also seen to work as a replicate-in gate, even though it was not designed for this function. This implies that the simulator can be used to implement new device designs and functions. When isotropic material margins were compared to anisotropic margins, it was noted that phase margin differences could indeed be attributed to the anisotropy in a predictable manner and that this phase difference could be used as a method to determine the degree of anisotropy of the material.

Beyond ascertaining gate margins, the simulator was also used to identify particular failure modes and, since bubble position is computed as a function of time, these failure modes could also be studied as a function of time. Even for "normal" operation of the gates described herein some interesting bubble behavior was noted. For example, even during successful transfer gate operation, it was observed that bubbles undergo large excursions in position during the transfer process.

Finally the simulator was used to design and test the operation of a new swap gate for ion-implanted devices. Since the use of ion-implanted propagation structures in

Conclusions 191

bubble devices has not been utilized to date due to the lack of replicate and swap gates for these devices, the implementation of this gate may possibly lead to the development of an all ion-implanted bubble memory chip. Simulation of this gate revealed that bubbles could be transferred with relatively short conductor pulses as compared to those required to implement transfer in the A.T.&T. trapping transfer gate. It should be noted that, even in the absence of gate geometry and current pulse phase optimization, simulated gate bias field margins were acceptable.

7.2. Future Work

7.2.1. Simulator Improvement

Based on the results presented here and the conclusions drawn from these results, there are several points to be made regarding the direction this work should take in the future. While it is easy to be idealistic and state what should be done, the emphasis here will be on realistic goals and improvements that may extend from or be appended to the work presented in this thesis.

The major flaw in the simulator at present is the model used for the charged wall. However, computing the charged wall configuration every 30 degrees for a total drive field rotation of 180 degrees (only 7 positions) required up to 560 minutes of CPU time on a HITAC M-200H supercomputer as reported by Fukushima et al. 31 Obviously, this is a difficult problem, to say the least. However, once the the wall configuration is computed given the appropriate material parameters and drive and bias fields, it need not be recomputed. Therefore, given a specific material and field constraints, as in a development environment, there may be some utility in actually computing the charged wall configuration, as time consuming as it may be.

Even if the aforementioned charged wall model is not to be modified radically, it may still be improved upon. For example, in this thesis we assume that $4\pi M$ of the implanted layer is the same as $4\pi M$ of the bubble layer, which should not be assumed. In addition, the charged wall is assumed to be created by a uniaxial anisotropy parallel to the propagation pattern edges that was assumed to be independent of the boundary orientation with respect to the crystalline axes. In other words, the charged

Conclusions 192

wall has the same strength as it rotates through both hard and easy directions, while in reality the strength of the charged wall should be a function of the anisotropy around the pattern which in turn is a function of its orientation with respect to the crystal axes.

7.2.2. New Gate Design

Independent of improving the simulator to enhance its accuracy, the present simulator can be used to either improve upon existing gate designs or devise new gates, as has been shown. Since domain behaviour during the stretching and chopping processes seems to be dominated by the conductor fields as mentioned previously, the simple charged wall model employed for the purpose of this research is adequate in testing new gate designs.

Regarding the new swap gate introduced in Chapter 6, there are a number of geometry variations that could be tested in order to see if gate operation margins could be enhanced. In permalloy devices since the replicate gate and the swap gate are on opposite ends of the minor loop, the margins of the new swap gate on a minor loop tip rotated by 180 degrees from that of Chapter 6 can be simulated. In conjunction with the block replicate gate, the new swap gate design can be used to actually implement an all implanted bubble chip since all required chip functions are thus realized.

Bibliography

- 1. A.H. Eschenfelder, Magnetic Bubble Technology, Springer-Verlag, Berlin, 1980.
- Bobeck, A.H., Fischer, R.F., Perneski, A.J., Remeika, J.P., and Van Uitert, L.G., "Application of Orthoferrites to Domain Wall Devices", I.E.E.E. Trans. Magn., Vol. MAG-5, No. 3, 1969, pp. 544-533.
- 3. T.J. Walsh and S.H. Charap, "Novel Bubble Drive", AIP Conf. Proc., Vol. 23, 1974, pp. 550.
- 4. A. H. Bobeck, S.L. Blank, A.D. Butherus, F.J. Ciak and W. Strauss, "Current-access magnetic bubble circuits", Bell Syst. Tech. J., Vol. 58, 1979, pp. 1453.
- Y.S. Lin, G.S. Almasi, G.E. Keefe and E.W. Pugh, "Self-Aligned Contiguous-Disk Chip Using 1μm Bubbles and Charged-Wall Functions", I.E.E.E. Trans. Magn., Vol. MAG-15, No. 6, 1979, pp. 1642 - 1647.
- 6. Y. Sugita, R. Suzuki, T. Ikeda, T. Takeuchi, N. Kodama, M. Takeshita, R. Imura, T. Satoh, H. Umezaki, and N. Koyama, "Ion-Implanted and Permalloy Hybrid Magnetic Bubble Devices", *I.E.E.E. Trans. Magn.*, Vol. MAG-22, No. 3, July 1986, pp. 239 246.
- Kodama, N., Koyama, N., Umezaki, H., Suzuki, R., Takeuchi, T. and Sugita,
 Y., "Characteristics Of Junctions Between Ion-Implanted And Permalloy
 Tracks In Hybrid Bubble Devices", I.E.E.E. Trans. Magn., Vol. MAG-20, No.
 September 1984, pp. 1075 1077.
- 8. T.J. Nelson, V.J. Fratello, D.J. Muehlner, B.J. Roman and S.E.G. Slusky, "Four-Micron Period Ion-Implanted Bubble Test Circuits", *I.E.E.E. Trans. Magn.*, Vol. MAG-22, No. 2, March 1986, pp. 93 100.
- Urai, H., Mizuno, K., Asada, S., Takada, N., Yoshioka, N., Gokan, H. and Yoshimi, K., "4Mb On-Chip-Cache Bubble Memory Chips With 4μm Period Ion-Implanted Propagation Patterns", I.E.E.E. Trans. Magn., Vol. MAG-20, No. 5, September 1984, pp. 1072 - 1074.
- 10. Mizuno, K., Suga, S. and Urai, H., "Block Replicate Gates for Ion-Implanted Bubble Devices", gth Japanese Applied Magnetics Society Meeting Digest, Vol. 76, 1985, pp. 76, [In Japanese]
- Magnin, J., Poirier, M., Fedeli, J.M. and Delaye, M.T., "Two Conductor Levels Block Replicator For 4μm Period Ion-Implanted Devices", I.E.E.E. Trans. Magn., Vol. MAG-20, No. 5, September 1984, pp. 1087 - 1089.

- 12. Komenou, K., Matsuda, K., Miyashita, T., Ohashi, M., Betsui, K., Satoh, Y. and Yamagishi, K., "Design of a Block Replicate Gate for Ion-Implanted Bubble Devices", *I.E.E.E. Trans. Magn.*, Vol. MAG-18, No. 6, November 1982, pp. 1352 1354.
- 13. T. Sato, T. Toyooka and R. Suzuki, "Dual Gate With Replicate and Pseudo-Swap Functions Using Double Conductor Layers for Ion-Implanted Devices", I.E.E.E. Trans. Magn., Vol. MAG-23, 1987, pp. 2569 2571.
- 14. Sato, T., Toyooka, T., Takeshita, M., and Suzuki, R., "Characteristics of Dual Gate for 16Mb Ion-Implanted Bubble Memory Devices", 11th Japanese Applied Magnetics Society Meeting Digest, Vol. 11, 1987, pp. 184, [In Japanese]
- 15. A.A. Thiele, "The Theory of Cylindrical Magnetic Domains", Bell Syst. Tech. J., Vol. 48, No. 10, 1969, pp. 3287-3335.
- 16. Mark H. Kryder, "Magnetic Bubble Device Scaling and Density Limits", I.E.E.E. Trans. Magn., Vol. MAG-15, No. 3, 1979, pp. 1099-1016.
- 17. C.C. Shir and Y.S. Lin, "Critical Curves For Determining Magnetization Directions in Implanted Films", J. Appl. Phys., Vol. 50, No. 6, 1979, pp. 4246 4258.
- 18. Douglas A. Saunders, Stress-induced Magnetic Anisotropies in Ion-implanted, Contiguous-disk, Magnetic Bubble Devices, PhD dissertation, Carnegie Mellon University, 1987.
- D. A. Saunders And M. H. Kryder, "Stresses And Magnetoelastic Anisotropies At Implantation Edges In Ion Implanted Garnet Films", J. Appl. Phys., Vol. 57, 1985, pp. 4061.
- 20. A. Hubert, "Charged Walls In Thin Magnetic Films", I.E.E.E. Trans. Magn., Vol. Mag-15, 1979, pp. 1251-1260.
- 21. Y. Hidaka and H. Matsutera, "Charged Wall Formation Mechanism In Ion-Implanted Contiguous Disk Bubble Devices", Appl. Phy. Let., Vol. 39, 1982, pp. 116.
- 22. A. Hubert, "The Calculation of Charged Wall Contours In Ion-Implanted Magnetic Bubble Devices", J. of Magnetism and Magnetic Materials, Vol. 31-34, 1983, pp. 976 978.
- 23. A.P. Malozemoss and J.C. Slonczewski, Magnetic Domain Walls in Bubble Materials, Academic Press, New York, 1979.
- 24. A.A. Thiele, "Device Implications of the Theory of Cylindrical Magnetic Domains", Bell Syst. Tech. J., Vol. 50, No. 3, 1971, pp. 725-773.
- Herbert Callen and Richard M. Josephs, "Dynamics of Magnetic Bubble Domains with an Application to Wall Mobilities", J. Appl. Phys., Vol. 42, No. 5, 1971, pp. 1977-1982.
- 26. K. Yamagishi, J. Mada and K. Yamaguchi, "A Method of Approximating

- Bubble Domain Runout Diameter and Bias Magnetic Field", I.E.E.E. Trans. Magn., Vol. MAG-20, No. 4, 1984, pp. 547-549.
- 27. P. Pougnet, H. Jouve, P. Gerard and F.B. Humphrey, "Potential Barrier Study of the Border-line Defined by Ion implantation in Bubble Garnets", J. Appl. Phys., Vol. 53, No. 3, March 1982, pp. 2513 2515.
- 28. Y. Hidaka, "Charged wall formation and propagation analysis in ion-implanted contiguous disk bubble devices", J. Appl. Phys., Vol. 53, No. 8, August 1982, pp. 5815 5822.
- 29. S.C.M. Backerra, W.H. De Roode and U. Enz, "The Influence Of Implantation-Induced Stress Gardients In Magnetic Bubble Layers", *Phillips J. Res.*, Vol. 36, 1980, pp. 112.
- 30. M.H. Kryder and D. Saunders, "The Effects Of Stress Relaxation And Anisotropic Magnetostriction On Charged Walls In Ion-Implanted Garnets", I.E.E.E. Trans. Magn., Vol. Mag-19, 1983, pp. 1817.
- 31. H. Fukushima And N. Hayashi, "Computer Simulation Of Magnetization Distributions In Contiguous-Disk Bubble Devices", *I.E.E.E. Trans. Magn.*, No. 5, 1987, pp. 3364.
- 32. H. Urai, K. Mizuno, Y. Kato, H. Matsutera, H. Gokan and H. Makino, "Roles of a Hard Bubble Suppression Layer in Ion-Implanted Bubble Devices", I.E.E. Trans. Magn., Vol. MAG-23, No. 5, 1987, pp. 3358-3360.
- 33. J.C. DeLuca and A.P. Malozemoff, "Dynamic Method for Characterizing Potential Wells of Bubbles Under Charged Walls", *I.E.E.E. Trans.* Magn., Vol. MAG-15, No. 6, November 1979, pp. 1651 1653.
- 34. H. Urai, "New Method For Potential Well Measurements Using Bubble Runout In Ion-Implanted Bubble Devices", *I.E.E.E. Trans. Magn.*, Vol. Mag-21, 1985, pp. 2676-2679.
- 35. S. J. Zhang and F. B. Humphrey, "Potential Well Of Charged-Walls", I.E.E.E. Trans. Magn., Vol. MAG-18, No. 6, 1982, pp. 1358.
- 36. Calhoun, B.A., "The Motion Of A Charged Wall Coupled To A Bubble", I.E.E.E. Trans. Magn., Vol. MAG-18, No. 6, November 1982.
- 37. B.E. Argyle, M.H. Kryder, R.E. Mundie and J.C. Slonczewski, "Mobility of a Charged Wall Coupled to a Bubble", *I.E.E.E. Trans. Majn.*, Vol. MAG-14, No. 5, September 1978, pp. 593 595.
- 38. F.C. Rossol and A.A. Thiele, "Domain Wall Dynamics Measured Using Cylindrical Domains", J. Appl. Phys., Vol. 41, No. 3, 1970, pp. 1163-1164.
- 39. Abramowitz, M. and Stegun, I.A., Handbook of Mathematical Functions, Dover Publications, New York, 1965.
- 40. T.J. Nelson, Yu-Ssu Chen and J.E. Geusic, "Field Nucleation of Magnetic Bubbles", I.E.E.E. Trans. Magn., Vol. MAG-9, No. 3, September 1973, pp. 289 293.

- Almasi, G.S., Keefe, G.E., Lin, Y.S. and Sanders, I.L., "Nucleation of 1μm Bubbles Via Charged Walls", I.B.M. Research Report, No. RC 7608 (#32932), April 1979.
- 42. Hayashi, N. and Abe, K., "Computer Simulation of Bubble Motion", Japan. J. Appl. Phys., Vol. 14, No. 11, Nov. 1975, pp. 1705 1716.
- 43. Hayashi, N., Mikami, H. and Abe, K., "Computer Simulation of Bubble Motion", I.E.E.E. Trans. Magn., Vol. MAG-13, No. 5, September 1977, pp. 1345 1347.
- 44. N. Hayashi and K. Abe, "Computer Simulation of Magnetic Bubble Domain Wall Motion", Japan. J. Appl. Phys., Vol. 15, 1976, pp. 1683.
- 45. T. Takeuchi, N. Ohta and Y. Sugita, "Origin of Effective Anisotropy Field Change Induced by Ion Implantation in Magnetic Garnet Films", I.E.E.E. Trans. Magn., Vol. MAG-20, No. 5, 1984, pp. 1108.
- 46. M. Alex, "Unpublished Notes".
- 47. J. R. Wullert II, "Analysis And Design Of Ion-Implanted Contiguous Disk Bubble Memory Devices", Master's thesis, Carnegie Mellon University, 1986.
- 48. Toyooka Takashi, Hitachi Central Research Laboratories, "Private Communication".
- 49. L. Gal, G.J. Zimmer and F.B. Humphrey, "Transient Magnetic Bubble Domain Motion Configurations During Radial Wall Motion", *Phys. Stat. Sol.*, Vol. a, No. 30, 1975, pp. 561.
- 50. Kochan Ju, "Passive Swap Gate Designs For Contiguous Disc Devices", I.E.E.E. Trans. Magn., Vol. MAG-18, No. 6, 1982, pp. 1364.